Individual Plasmonic Nanogaps: Controlled Assembly and Detailed Investigation

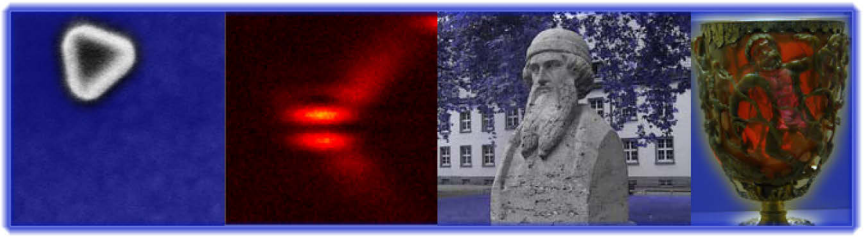

von

Marcus Schmelzeisen

Januar 2011

Max-Planck-Institut

für Polymerforschung

JOHANNES GUTENBERG UNIVERSITÄT MAINZ

Individual Plasmonic Nanogaps:

Controlled Assembly and Detailed Investigation

Dissertation

zur Erlangung des Grades eines

„Doktor der Naturwissenschaften“

im Promotionsfach Chemie

am Fachbereich Chemie, Pharmazie und Geowissenschaften

der Johannes Gutenberg-Universität Mainz

vorgelegt von

Marcus Schmelzeisen

geboren in Eltville am Rhein

Mainz, im Januar 2011

Die vorliegende Arbeit wurde am **Max-Planck-Institut für Polymerforschung in Mainz** unter Anleitung von [in printed version available] in der Zeit von August 2007 bis Januar 2011 angefertigt. Die Projektgruppe wurde finanziell vom Bundesministerium für Bildung und Forschung als Nano-Nachwuchsgruppe (Nr. 03N8702) und der Deutschen Forschungsgemeinschaft (DFG, SFB 625) gefördert.

Dekan: [in printed version available]

1. Berichterstatter: [in printed version available]

2. Berichterstatter: [in printed version available]

Tag der mündlichen Prüfung: 05.04.2011

Für meine Familie

Nach Golde drängt,
Am Gold hängt,
Doch Alles. Ach wir Armen!

Johann Wolfgang von Goethe (1749 – 1832)

Table of Content

Abbreviations

$\perp$	Polarization Perpendicular to the Block
||	Polarization Parallel to the Block
$\|T_{zx}(r_{B1})\|^2$ or $\|T_{zy}(r_{B1})\|^2$	Effective Intensity Contributing to the Excitation in the given Polarization Direction
2D	Two Dimensional
3D	Three Dimensional
AC	Ambient Colloid Model
AE	Auger Electrons
AET	Spacer Molecule: 2-Aminoethanethiol
AFM	Atomic Force Microscopy
ATR	Attenuated Total Reflectance
B1/B2	linear Aperture Blocks under Dark-Field Conditions
BSE	Backscattered Electrons
c	Velocity of Light
CCD	Charged-Coupled Device
d	Diameter
Dark	Background
DLS	Dynamic Light Scattering
DOP	Dielectric-on-Plane
DOS	Density of States
ε	Dielectric Function/Permittivity
EF	Enhancement Factor
fcc	Face Centered Cubic
FEM	Finite Element Method
FIT/FIM	Finite Integration Technique / Finite Integration Method
FS	Feedback System
FWHM	Full Width at Half-Maximum
g	Electron-Phonon-Coupling Constant
G	Electron-Phonon Coupling
h	Planck's Constant
$\hbar$	Dirac Constant
HOMO	Highest Occupied Molecular Orbital
I_0	Laser Energy Flow Density
IR	Infrared
k	Wavevector
λ	Wavelength
LSP	Localized Surface Plasmon (Particle Plasmon)
LSPR	Localized Surface Plasmon Resonance
LUMO	Lowest Unoccupied Molecular Orbital
n	Refractive Index

NA	Numerical Aperture
Nd:YAG	Neodymium Doped Yttrium Aluminum Garnet (Laser)
Obj	Object
PCS	Photon-Correlation Spectroscopy
PDI	Perylene Diimide dye
PDI-G2	Spacer Molecule: Type of Polyphenylene Dendrimer, stands for Perylene-Diimide in Generation 2
Ref	Reference
SAM	Self Assembled Monolayer
SBR	Signal-to-Background Ratio
SCOM	Scanning Confocal Optical Microscopy
SEM	Scanning Electron Microscopy
SE	Secondary Electrons
SERS	Surface Enhanced Raman Scattering
SFM	Scanning Force Microscopy
SOP	Sphere-On-Plane
SP	Surface Plasmons
SPR	Surface Plasmon Resonance
τ	Correlation Time
THF	Tetrahydrofurane
TSG	Template Stripped Gold
TSS	Template Stripped Silver
UV-Vis	Ultraviolet-Visible
W	Working Function
ω	Angular Frequency
Xe	Xenon

1 Introduction

1.1 Motivation and Aims

Nanoplasmonics is an emerging new discipline which deals with the collective oscillation of conduction electrons on surfaces of metal nanostructures, called plasmons. Since the plasmons can be spatially confined in volumes far smaller than the diffraction limit of light, this field of science brings new ways of pushing optics fully into the nanometer-size regime. The plasmons can be present on particulate, smooth or corrugated surfaces of various metals – most importantly on noble metals such as gold and silver. They have enormous potential in the fields of optical computing and recording,[1, 2] sub-wavelength optical devices[3-6] or biological[7, 8] and chemical research.[9, 10] Advanced materials composed of metal structures can have novel optical properties, such as negative refraction[11-14] that are required to realize recent predictions of super lensing.[15]

The plasmonic resonances are accompanied by large electromagnetic fields near such structures. This effect is the basis of surface enhanced Raman scattering (SERS)[16] and optical tweezers.[17] The strongest field enhancements are obtained by nanometer-sized gaps between two metallic objects as they arise between two spheres or between a sphere and a film. These strong electromagnetic fields in small volumes of a few cubic nanometers play an important role in many physical effects which involve the emission and collection of light, such as scanning tunneling microscopy.[18] They are also interesting from a fundamental point of view as they raise the question how the dielectric response of such a geometry compares to the bulk material.[19] The sub-nanometer features associated with these structures determine the characteristics of the localized fields and the enhancement ratio. The key to unlock the full potential of plasmonic nanostructures is to understand these features at the nanoscale. At the same time the resonance wavelength of such structures can be easily tuned, e.g. by changing the sphere diameter. The corresponding large shifts are interesting for biological as well as chemical sensing.[20, 21]

In this work, the plasmonic gaps between metal particles and plane metal surfaces are investigated by dark field microscopy. This sphere-on-plane (SOP) system is selected because of its balance between performance, practicability and theoretical modeling.[22] For a detailed investigation of the involved resonances, single-object spectroscopy is mandatory since big variations between individual resonators are the rule rather than an exception. A new developed scanning confocal dark field mode is presented which takes advantage of the intermediate excitation of surface plasmons in the excitation and in the emission process. This guarantees high quality dark field micrographs through the metal film of a sphere-on-plane system and helps in the spectroscopic investigations of single resonators.

The optical investigations are accompanied by atomic force and scanning electron microscopy to determine the dimensions of the investigated resonators and correlate the optical resonances with their shape and size.

The sphere-on-plane geometries are assembled with both control over the gap distance by thiol chemistry and the particle shape by laser irradiation, which induces quantitative shape transformation of the particles to spheres. This creates well-defined systems which are compared to theoretical calculations. To investigate the influence of the enhancement on the luminescence of a dye, a polyphenylene dendrimer with a perylene in the core is placed with nanometer-size precision in the gap.

The methods developed in this thesis aim at a deeper understanding of the involved electromagnetic resonances and field enhancements. Most experimental work in the past either relied on ensemble measurements,[23, 24] or were performed without the connection of optical spectroscopy and imaging techniques.[25, 26] The single particle approach is, however, necessary to reveal the inherent optical response of the sphere-on plane geometry and remove any inhomogeneous broadening. The correlation with the corresponding particle shape and size is required to estimate the influence of deviations from the models which are used to describe the experimental systems. In this thesis the resonance line widths and positions are to be determined and compared to theoretical calculations. The prepared architectures, which combine ultra-smooth metal surfaces and ideal metal spheres, allow for the first time for quantitative experiments.

The large fields associated with the nanometer-sized gaps can also alter the fluorescence behavior of dyes in close proximity. While the theoretical interpretations of the involved processes were developed in the 1980s,[27] quantitative experiments in these regimes remain rather an exception, because they require samples with controllable metal structures and defined dye position. The selected sphere-on-plane geometry with a perylene loaded polyphenylene dendrimer in the gap appears promising for just this purpose. The aim of this experiment is to study the mechanisms in the strong coupling regime and verify the theoretical concepts.

1.2 Outline

The thesis is organized as follows: First a short introduction of the theoretical basics of metal optics is given in Chapter 2. The properties of surface plasmon modes on planar metal dielectric interfaces and in nanoparticles are discussed. Subsequently the consequences are described when the two couple in a sphere-on-plane system. In Chapter 3 all experimental procedures and utilized methods are explained which are needed to perform the

experiments in the subsequent chapters. The most important ones are scanning confocal microscopy, electron microscopy and atomic force microscopy.

Chapter 4 presents a method to transform suspensions of chemical reduced gold and silver nanoparticles of different diameters into ideal spheres by intense laser pulses. The parameters of the used Nd:YAG laser with wavelengths of 532 and 355 nm are selected in such a way that the particles are irradiated in aqueous suspension under “mild” conditions to obtain shape transformation in principle by particle melting during the pulse. The involved processes of the irradiation and upper limits are discussed in detail by using different theoretical models. The transformed metal spheres possess superior properties over the unirradiated particles like a dramatic decreased plasmon line width and are ideal for the controlled assembly of sphere-on-plane systems which resemble the theoretical models to describe them.

In Chapter 5 the plasmon mediated dark field mode is established. The concept is verified by experimental investigation of the effective point-spread function, the intensity distribution of the scattered radiation and by comparison with classical dark-field geometry. The wavelength-dependence of both the signal strength and the point-spread function are discussed.

The wavelength dependent scattering response of polystyrene spheres with diameters between 200 and 500 nm on a gold film is studied in the following Chapter 6. The system is used as reference to investigate in detail the reproducibility of the presented dark field mode of Chapter 5. The geometry is comparable to a sphere-on-plane metal system, but the dielectric particles do not interact with the metal film through hybridized plasmon modes. The sphere interaction with the metal film leads to an interesting size-dependent modification of the scattering response.

In Chapter 7 all new knowledge is combined to investigate different sphere-on-plane gold systems on a single object basis by confocal, atomic-force and electron microscopy. The gap in all systems is created by a monolayer of 2-aminoethanethiol which acts as spacer layer between the film and the particle. The optical response of chemical reduced gold particles is compared to the resonances of gold spheres created by the laser induced transformation process and variations of the film roughness. The results demonstrate the superiority of single object investigations over ensemble experiments in the past which showed a good qualitative agreement to the theory in spite of big spectral deviations of the individual resonators. Only the systems with the ideal gold spheres show in all cases a defined response which correlates in terms of resonance position with the theoretical calculations. The resonance width is for all investigated cases significantly more than theoretically predicted and could lead to important consequences for theoretical investigations.

In Chapter 8 the fluorescence enhancement of the described perylene diimide loaded polyphenylene dendrimer is investigated which serves both as spacer and chromophore bearing unit in the gap of a silver sphere-on-plane system. The dendrimer in the shell with only phenyl-phenyl linkages accounts for an outstanding rigidity and as such shape persistency, while being optical inactive. The 16 peripheral dithiolane rings establish the necessary affinity for binding to the silver. As such the chromophore in the core can be placed with nanometer precision in the gap between the metallic structures. For such gaps of less than 3 nm, physical effects beyond the weak-coupling regime are expected which can change the spectral fluorescence profile of the dye and represented the main motivation for the work. On a single object basis, the fluorescence from the sphere-on-plane structures is investigated and correlated with the plasmonic resonances and the particle shape obtained by scanning electron microscopy. A strong fluorescence signal is seen from all particles, which is at least 1000 times stronger than the signal from the plane dye-coated metal surface. The fluorescence emission profile varies between the particles and shows light emission at higher energies than the free dye. For the silver sphere-on-plane system two classes of scattering resonators can be distinguished. Up to a significant line-broadening the response of the “sphere-on-plane”-like cases resemble the theoretical prediction for a perfect sphere-on-plane geometry while resonators which deviate strongly from this ideal scenario are also found as seen from the gold case. The strong modifications of the dye emission spectrum finally suggest the presence of physical mechanisms at very small metal/dye separations, which are beyond a simple wavelength-dependent enhancement factor.

The thesis ends with the main results in the concluding remarks (Chapter 9)

1.3 Bibliography

1. Atwater, H. A.; Maier, S.; Polman, A.; Dionne, J. A.; Sweatlock, L., The new "p-n junction". Plasmonics enables photonic access to the nanoworld. *Mrs Bulletin* **2005,** *30* (5), 385-389.

2. Zijlstra, P.; Chon, J. W. M.; Gu, M., Five-dimensional optical recording mediated by surface plasmons in gold nanorods. *Nature* **2009,** *459* (7245), 410-413.

3. Barnes, W. L.; Dereux, A.; Ebbesen, T. W., Surface plasmon subwavelength optics. *Nature* **2003,** *424* (6950), 824-830.

4. Ebbesen, T. W.; Genet, C.; Bozhevolnyi, S. I., Surface-plasmon circuitry. *Physics Today* **2008,** *61* (5), 44-50.

5. Maier, S. A.; Brongersma, M. L.; Kik, P. G.; Meltzer, S.; Requicha, A. A. G.; Atwater, H. A., Plasmonics - A route to nanoscale optical devices. *Adv. Mater.* **2001,** *13* (19), 1501-1505.

6. Chang, D. E.; Sorensen, A. S.; Demler, E. A.; Lukin, M. D., A single-photon transistor using nanoscale surface plasmons. *Nat. Phys.* **2007,** *3* (11), 807-812.

7. Lakowicz, J. R., Radiative decay engineering 5: metal-enhanced fluorescence and plasmon emission. *Analytical Biochemistry* **2005,** *337*, 171-194.

8. Yildiz, A.; Forkey, J. N.; McKinney, S. A.; Ha, T.; Goldman, Y. E.; Selvin, P. R., Myosin V walks hand-over-hand: Single fluorophore imaging with 1.5-nm localization. *Science* **2003,** *300* (5628), 2061-2065.

9. Murphy, C. J.; San, T. K.; Gole, A. M.; Orendorff, C. J.; Gao, J. X.; Gou, L.; Hunyadi, S. E.; Li, T., Anisotropic metal nanoparticles: Synthesis, assembly, and optical applications. *Journal of Physical Chemistry B* **2005,** *109* (29), 13857-13870.

10. Willets, K. A.; Van Duyne, R. P., Localized surface plasmon resonance spectroscopy and sensing. *Annual Review of Physical Chemistry* **2007,** *58*, 267-297.

11. Murray, W. A.; Barnes, W. L., Plasmonic materials. *Adv. Mater.* **2007,** *19* (22), 3771-3782.

12. Pendry, J. B., Negative Refraction Makes a Perfect Lens. *Physical Review Letters* **2000,** *85* (18), 3966-3969.

13. Shelby, R. A.; Smith, D. R.; Schultz, S., Experimental Verification of a Negative Index of Refraction. *Science* **2001,** *292* (5514), 77-79.

14. Smith, D. R.; Padilla, W. J.; Vier, D. C.; Nemat-Nasser, S. C.; Schultz, S., Composite Medium with Simultaneously Negative Permeability and Permittivity. *Physical Review Letters* **2000,** *84* (18), 4184.

15. Fang, N.; Lee, H.; Sun, C.; Zhang, X., Sub-diffraction-limited optical imaging with a silver superlens. *Science* **2005,** *308* (5721), 534-537.

16. Nie, S. M.; Emory, S. R., Probing single molecules and single nanoparticles by surface-enhanced Raman scattering. *Science* **1997,** *275* (5303), 1102-1106.

17. Xu, H. X.; Kall, M., Surface-plasmon-enhanced optical forces in silver nanoaggregates. *Physical Review Letters* **2002,** *89* (24).

18. Johansson, P.; Monreal, R.; Apell, P., Theory for Light-Emission from a Scanning Tunneling Microscope. *Phys. Rev. B* **1990,** *42* (14), 9210-9213.

19. Zuloaga, J.; Prodan, E.; Nordlander, P., Quantum Description of the Plasmon Resonances of a Nanoparticle Dimer. *Nano Letters* **2009,** *9* (2), 887-891.

20. Hutter, E.; Cha, S.; Liu, J. F.; Park, J.; Yi, J.; Fendler, J. H.; Roy, D., Role of substrate metal in gold nanoparticle enhanced surface plasmon resonance imaging. *Journal of Physical Chemistry B* **2001,** *105* (1), 8-12.

21. Lyon, L. A.; Pena, D. J.; Natan, M. J., Surface plasmon resonance of Au colloid-modified Au films: Particle size dependence. *Journal of Physical Chemistry B* **1999,** *103* (28), 5826-5831.

22. Aravind, P. K.; Metiu, H., The effects of the interaction between resonances in the electromagnetic response of a sphere-plane structure - applications to surface enhanced spectroscopy. *Surface Science* **1983,** *124* (2-3), 506-528.

23. Okamoto, T.; Yamaguchi, I., Optical absorption study of the surface plasmon resonance in gold nanoparticles immobilized onto a gold substrate by self-assembly technique. *J. Phys. Chem. B* **2003,** *107* (38), 10321-10324.

24. Tsuboi, K.; Abe, S.; Fukuba, S.; Shimojo, M.; Tanaka, M.; Furuya, K.; Fujita, K.; Kajikawa, K., Second-harmonic spectroscopy of surface immobilized gold nanospheres above a gold surface supported by self-assembled monolayers. *J. Chem. Phys.* **2006,** *125* (17).

25. Hu, M.; Ghoshal, A.; Marquez, M.; Kik, P. G., Single Particle Spectroscopy Study of Metal-Film-Induced Tuning of Silver Nanoparticle Plasmon Resonances. *Journal of Physical Chemistry C* **2010,** *114* (16), 7509-7514.

26. Mock, J. J.; Hill, R. T.; Degiron, A.; Zauscher, S.; Chilkoti, A.; Smith, D. R., Distance-dependent plasmon resonant coupling between a gold nanoparticle and gold film. *Nano Letters* **2008,** *8* (8), 2245-2252.

27. Wokaun, A., Surface Enhancement of Optical Fields Mechanism and Applications. *Molecular Physics* **1985,** *56* (1), 1-33.

2 Theoretical Background

The understanding of the optical properties of metal nanostructures requires the knowledge of both electrodynamics and solid state theory. As this is discussed in most textbooks[1-3] on condensed matter physics, this chapter is intended only as a short overview of the basic concepts involved with metal optics. For further reading, citations to the original literature are given when available. The chapter starts with the description of the optical properties of bulk metals, by using a classical, non-quantum mechanical, model which is usually exact enough in practice over a wide range of frequencies. The second part reviews the properties of metallic structures like films and nanoparticles and the consequences when the two are combined in a sphere-on-plane geometry.

2.1 Optical Properties of Metals

There is a big difference between the optical properties of insulators and conductors of electricity. Insulators and particularly glasses (amorphous or non-crystalline insulators) have a broad window of transparency over the optical spectrum for light with less energy than their band gap. In this window the dielectric function generally has a weak dispersion; therefore, the materials transmit light with very little loss. In contrast conducting materials or metals are dominated by their high reflectivity in the visible and infrared which is the reason that they are often used to reflect optical signals or to shield electromagnetic waves. Conductive coatings commonly serve as mirror surfaces, can be used to detect or emit electromagnetic signals of lower frequencies or transport microwaves and radio frequency waves. In the field of plasmonics these properties of metals together with nanostructuring are required to gain access to all the fascinating applications. The interaction of metals with electromagnetic fields can be firmly understood in the classical framework based on Maxwell's equations,[4] but these equations expect some material properties, like the complex dielectric function ε, as input parameters which are not explained in the context of the electrodynamic theory. These values must either be taken from experimental data or explained by solid state theory. At the end of the 19th century Paul Drude performed intensive studies on the optical properties of a large number of materials. By combining these data with the theory of electrons he could explain the electrical conductivity, the thermal conductivity and also the optical properties of metals.

2.1.1 Drude-Sommerfeld Model

The Drude model regards metals as a classical gas of electrons executing a diffusive motion.[5, 6] The details of the lattice potential and electron-electron interactions are not taken into account. The electrons can move freely until they suffer an instantaneous scattering process

on obstacles like ions, defects or impurities etc. Later Sommerfeld[7] incorporated corrections originating from the Pauli exclusion. This Drude-Sommerfeld model describes successfully many properties of metals despite its drastic assumptions. In the presence of an external electric field **E** the electrons oscillate in response and the equation of motion becomes:

$$m \cdot \ddot{\mathbf{x}}(t) + m \cdot \gamma \cdot \dot{\mathbf{x}}(t) = -q \cdot \mathbf{E} \tag{2.1}$$

where **x** is the displacement of the electron from its equilibrium, *m* is the electron mass and *q* is the magnitude of the electron charge. Their motion is damped via collisions at the collision centers, which occur with a characteristic rate of $\gamma = 1/\tau$. τ is known as the relaxation time of the free electron gas and is typically on the order of 10^{-14} s at room temperature, corresponding to g = 100 THz. After each collision the directional information is completely lost which results in a random orientation of the electron velocity. Small modifications of the electron motion occur due to the band structure of the metals and are incorporated into the model by using an effective mass m^*, which is in general different from the free-electron mass *m*. If we assume a harmonic time dependence $\mathbf{E}=\mathbf{E_0}\, e^{-i\omega t}$ of the driving field, a particular solution to equation (2.1) is

$$\mathbf{x}(t) = \mathbf{x_0} \cdot e^{-i\omega t} = \frac{q}{m^* \cdot \left(\omega^2 + i\gamma\omega\right)} \cdot \mathbf{E_0} \cdot e^{-i\omega t} \tag{2.2}$$

The displaced electrons contribute to the macroscopic polarization **P** explicitly given by

$$\mathbf{P} = \varepsilon_\infty \varepsilon_0 \chi \cdot \mathbf{E} = -nqx = \frac{n \cdot q^2}{m^* \cdot \left(\omega^2 + i\gamma\omega\right)} \cdot \mathbf{E_0} \cdot e^{-i\omega t} \tag{2.3}$$

Here χ is the susceptibility and *n* is the density of the conduction electrons. ε_∞ includes the contribution of the bound electrons to the polarizability and should have the value of 1 if only conduction band electrons contribute to the dielectric function. Solving this equation for the susceptibility gives:

$$\chi = -\frac{1}{\varepsilon_\infty} \cdot \frac{n \cdot q^2}{\varepsilon_0 \cdot m^* \cdot \left(\omega^2 + i\gamma\omega\right)} \tag{2.4}$$

The numerator of this term has the dimension of a frequency squared. Its square root is called the plasma frequency ω_p because it is the oscillation frequency of the free electron gas:

$$\omega_p = \sqrt{\frac{n \cdot q^2}{\varepsilon_0 \cdot m^*}} \tag{2.5}$$

Note that the value of the plasma frequency is dependent only on the number of free electrons and not on the conductivity. The dielectric function of the free electron gas of the metal finally becomes:

$$\varepsilon(\omega) = \varepsilon_\infty \cdot (\chi + 1) = \varepsilon_\infty - \frac{\omega_p^2}{(\omega^2 + i\gamma\omega)} \tag{2.6}$$

The real and imaginary components of this complex dielectric function are given by:

$$\varepsilon(\omega) = \varepsilon_\infty - \frac{\omega_p^2}{(\omega^2 + i\gamma\omega)} = \varepsilon_\infty - \frac{\omega_p^2 \cdot \tau^2}{1 + \omega^2 \cdot \tau^2} + i\frac{\omega_p^2 \cdot \tau}{\omega \cdot (1 + \omega^2 \cdot \tau^2)} \tag{2.7}$$

where $\gamma = 1/\tau$ was used. In the near infrared or in the visible $1/\tau$ is several orders of magnitude smaller then ω and so $\varepsilon(\omega)$ is predominantly real and given in a good approximation by

$$\varepsilon(\omega) \approx \varepsilon_\infty - \frac{\omega_p^2}{\omega^2} \tag{2.8}$$

Thus it is negative as long as $\omega < \omega_p/\varepsilon_\infty$ and a negative value is required to achieve plasmonic resonances. The name plasma frequency originates therefore from the fact that for $\omega = \omega_p$ the electron gas can sustain these charge density oscillations or plasmons. For frequencies larger than ω_p the inertia of the conduction electrons prevents from instantaneous screening of the field and charge density waves are created. A big advantage of the Drude model is that it can easily be incorporated into time-domain based numerical solvers for Maxwell's equation,[4] such as the finite-difference time-domain (FDTD) scheme via the direct calculation of the induced currents using equation (2.1).[8]

2.1.2 Empirical Bulk Values for Silver and Gold

The optical properties of the metals can be determined experimentally by reflection or transmission measurements from the clean metal surfaces under ultra-high vacuum conditions. Today a huge amount of tabulated data[9-14] exists which shows especially in the imaginary part large variations. They arise not only on the basis of systematic errors in the measurements, but also have their origin in the microscopic origin of the macroscopic measured mean values.[15] In Figure 2.1 the tabulated dielectric values from Johnson and Christy[10] are compared for gold to the calculated ones using the Drude model. The model describes the behavior of the metal very good at large wavelengths whereas additional contributions are present at smaller wavelengths, especially for the imaginary part. These deviations have their origin in the limit of the model which describe the dielectric properties of a metal solely as a result from the free electrons in the conduction band. For higher energies or smaller wavelengths electrons from deeper bands can be excited into the conduction band. This leads to increased damping and competition between the two excitations and deteriorate the plasmonic behavior of a metal.

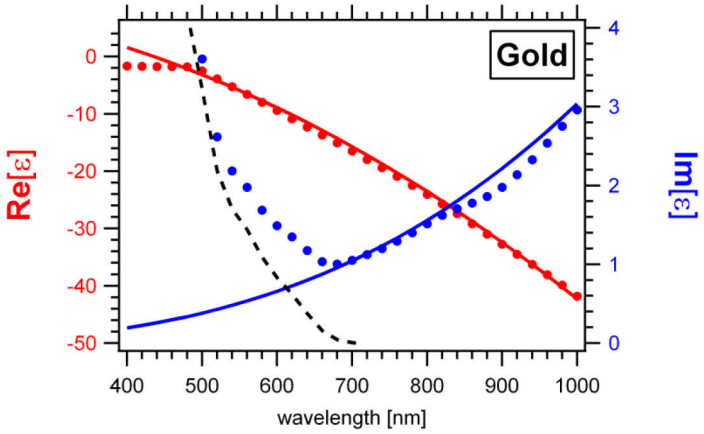

Figure 2.1: *Complex dielectric function of gold with red the real part and blue the imaginary part. The circles show the experimental values taken from Johnson and Christy.[10] The solid lines show the values calculated according to equation (2.7). The interband contribution (black dashed line) is calculated from the difference of the experimental data to the Drude model.*

As they have their origin not in the conduction band, but in a deeper band, they are called interband transitions. In noble metals like gold and silver the electrons originate from completely filled d-bands which are relatively close to the Fermi energy. For gold the interband transitions start to emerge at wavelengths smaller than 700 nm, which is shown for the imaginary part by the black line. For sensing applications it is advisable to stay out of this region.

Silver behaves in the whole visible range better than gold, because the d-band excitation threshold is larger. It is therefore considered to be a better Drude metal. The permittivity down to a wavelength of 400 nm is shown in Figure 2.2.

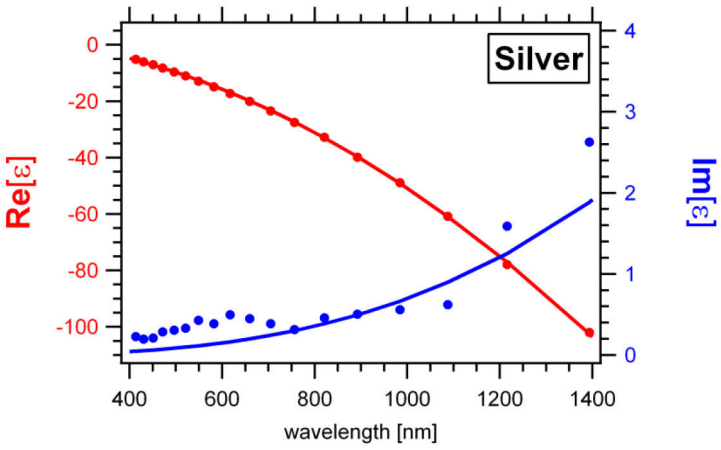

Figure 2.2: *Complex dielectric function of silver with red the real part and blue the imaginary part. The circles show the experimental values taken from Johnson and Christy.[10] The solid lines show the values calculated according to equation (2.7).*

2.1.3 Modifications to the Bulk Dielectric Function

In the derivation of the bulk dielectric function of a metal, the external applied field only varied with time, but was otherwise spatially uniform which led to a frequency dependent

dielectric function $\varepsilon(\omega)$. Modifications will occur if the applied external field varies over distances comparable to the mean free path of the electrons and by the presence of an interface. The properties of the surface is different from the bulk as the metal lattice is terminated which changes the band structure of the material and the screening forces experienced by the electrons. These surface states are strongly localized to the interface, but also extent outside for length scales on the order of 0.1 nm and behave like a dye with corresponding HOMO/LUMO gap at the metal surface. Electrons from occupied surface states can be excited to the conduction band or vice versa electrons from the conduction band can be excited into the empty surface states. A way to see their influence is the application of an electrostatic potential to the surface.[16] The surface then sees a different portion of the potential as the bulk. For spheres the surface to volume ratio changes drastically with decreasing radius and surface effect will correspondingly play an important role in very small nanostructures.

A second modification will occur when the wave-vector of the near field is of order or less than the mean free path of the electrons associated with defect, impurity and phonon-electron scattering. When the field varies on a length scale shorter than this characteristic length scale the response of an electron at one time and place will depend on its velocity. In turn, the electron's velocity depends on the forces acting on it at an earlier time and in another place, hence the expression, non-local.[17] In this regime the dielectric function becomes a function of the wave vector **k**. An example which makes the fields spatially inhomogeneous is the presence of the plasma oscillations in metals. At frequencies greater than the plasma frequency these longitudinal waves propagate inside the metal in addition to the transversal waves of the electromagnetic field contributing to the reflectivity. Methods to calculate the dependence of ε on **k** can be found in the book of Kolb[18] for surfaces and in the review of Fuchs and Claro[19] for small metal spheres.

2.2 Optical Resonances of Metallic Structures

Metal nanostructures attract both fundamentally and technologically considerable attention because of their unique optical properties. As seen from the last section the origin of these effects is attributed to the collective oscillation of conduction band electrons in response to the electric field produced by the radiation with light. These eigenmodes of the electron gas are also called “plasmons”. Since the electrons carry a charge, they are likewise associated with an electromagnetic field and every theoretical description has to include this interplay of fields and charges. Therefore, the occurrence of surface plasmons depends on the boundary conditions for the electromagnetic fields and the cases for the bulk metal, planar/dielectric interfaces and metal particles have to be treated differently. In the

literature these modes are distinguished by speaking of volume, surface and particle plasmons, respectively.[20] The surface plasmons (SP) will be treated next. They are propagating dispersive electromagnetic waves coupled to the electron plasma of a conductor at a dielectric interface and decay exponentially on both sides normal to the surface. An important consequence of the evanescent nature of the SPs is the momentum mismatch between the incident light and the SPs which must be overcome to generate surface plasmons from an incident propagating light beam.

The particle plasmons, also called "*localized surface plasmons*" (LSP), are non-propagating excitations of the conduction electrons in small nanostructures. These modes naturally arise from the scattering problem of small, sub-wavelength conductive nanoparticles in an oscillating electromagnetic field. The curved surface of the particles exerts an effective restoring force on the driven electrons, so that a sharp resonance can arise, leading to fields both inside and in the near-field zone outside the particle. Another consequence of the curved surface is that the resonance can be excited by direct light illumination, in contrast to propagating SPs. The particle plasmons will be discussed in the second part while the final section will focus on the interaction of the two in a sphere-on-plane system.

2.2.1 Surface Plasmons on Metal-Planes

More than 100 years ago, R. W. Wood observed strong, angular dependent variations in the intensity of light that was reflected from an optical metal grating.[21] He simply called them anomalies, because he could not understand their origin. Later they were explained by Fano.[22] Twenty years later, the possibility that metals support surface waves was revisited in the context of inelastic electron scattering experiments.[23] At this time the term surface plasmon was born[24] due to the connection of the energy losses with the plasma oscillations of the conduction electrons. Turbadar[25] was the first one to observe them on non-corrugated metal plane layers in multilayer systems. He introduced a glass prism to couple the light momentum to the excitation in the metal. This coupling technique is known as the Kretschmann configuration due to Kretschman[26] who developed the same mechanism twelve years later without being familiar with the previous work. He and Otto[27] are together regarded as the pioneers of surface plasmon spectroscopy as they were not only the first to fully understand the underlying physical mechanism of these surface waves at metal dielectric interfaces, but also recognized their huge sensitivity to all different surfaces processes. The principle of surface plasmon spectroscopy will be discussed briefly in Chapter 3.2.4, but the principle of surface plasmons and their applications are also described in many textbooks.[28-30] To understand the evanescent nature of surface plasmons the Maxwell's equation[4] under the appropriate boundary conditions have to be solved for an ideal 2D model interface with Cartesian coordinate system as depicted in Figure 2.3.[31]

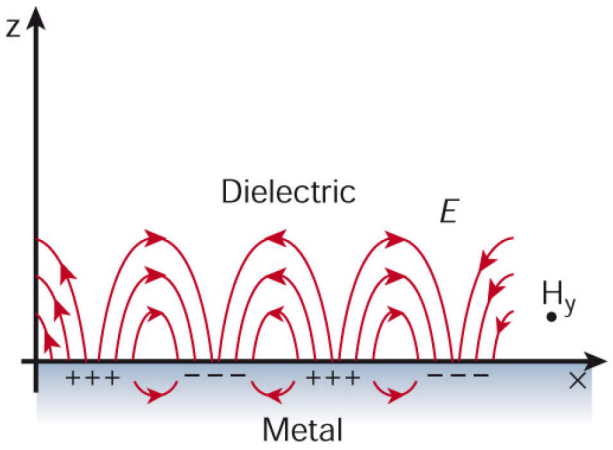

Figure 2.3: *Interface between two media. The interface is defined by z = 0. In each half space the transverse electric fields normal to the interface are considered.*[31]

For a p-polarized wave the transverse electric fields normal to the surface plane inside the dielectric (z >0), E_z^d and inside the metal substrate (z <0), E_z^m are considered:

$$E_z^d = E_0^d \cdot \exp\left(ik_z^d z\right) \cdot \exp\left(ik_{sp} x\right) \tag{2.9}$$

$$E_z^m = E_0^m \cdot \exp\left(ik_z^m z\right) \cdot \exp\left(ik_{sp} x\right) \tag{2.10}$$

The main result is a relation of the wave vector of the surface plasmons along the interface, k_{sp}, also called dispersion-relation

$$k_{SP} = \frac{2\pi}{\lambda} \cdot \sqrt{\frac{\varepsilon_d \cdot \varepsilon_m}{\varepsilon_d + \varepsilon_m}} = \frac{\omega}{c} \cdot \sqrt{\frac{\varepsilon_d \cdot \varepsilon_m}{\varepsilon_d + \varepsilon_m}} \tag{2.11}$$

where ε_d and ε_m are the dielectric functions of the dielectric and the metal, and λ is the free-space optical wavelength. The pre-factor with the wavelength of the incident light can be substituted by the ratio of the angular frequency ω and the speed of light c. The surface plasmon is also characterized by a wave vector k_z, which accounts for its extension normal to the surface on either side of the interface. That complex wave vector, describing the field in the dielectric (d) or metal (m), respectively, is determined by

$$k_z^{d,m} = \sqrt{\left(\frac{2\pi}{\lambda}\right)^2 \cdot \varepsilon_{d,m} - k_{sp}^2} = \frac{\omega}{c} \cdot \sqrt{\frac{\varepsilon_{d,m}^2}{\varepsilon_d + \varepsilon_m}} \tag{2.12}$$

The detailed derivation of equation (2.11) and (2.12) is long and can be found in literature.[28, 32, 33] For an interface wave that propagates along the interface, a real k_{sp} value is required. This condition is fulfilled for equation (2.11) if the sum and the product of the dielectric functions are on one hand either both positive or both negative. In order to obtain an exponentially decaying wave in both media the wave vector normal to the surface k_z has on the other hand to be purely imaginary. This can only be achieved if the sum $\varepsilon_d + \varepsilon_m$ in the

denominator of equation (2.12) is negative. From this the conditions the existence of a surface plasmon phenomenon at an interface are derived as:

$$\varepsilon_m(\omega) \cdot \varepsilon_d(\omega) < 0 \tag{2.13}$$

$$\varepsilon_m(\omega) + \varepsilon_d(\omega) < 0 \tag{2.14}$$

which means that one of the dielectric functions must be negative with an absolute value exceeding that of the other. This is satisfied by several metals in the visible and near-infrared of the spectrum for which ε_m has a large negative real part and a small positive imaginary part. As an example the surface plasmon wave vector k_x for a silver–air interface in the red part of the visible spectrum is found to be $k_{SP} > 1.03\ \omega/c$ This increase in momentum is associated with the binding of the surface plasmons to the surface, and the resulting momentum mismatch between the incident light and surface plasmons of the same frequency must be bridged by proper methods to generate them, see Chapter 3.2.4.

2.2.2 Particle Plasmons in Metal Spheres

The particle plasmon resonance of tiny gold and silver particles is located in the visible rendering these nanoparticles brightly colored upon excitation with light. These optical properties have fascinated people for many centuries. They used them for example to stain glass by adding gold and silver to the melt.

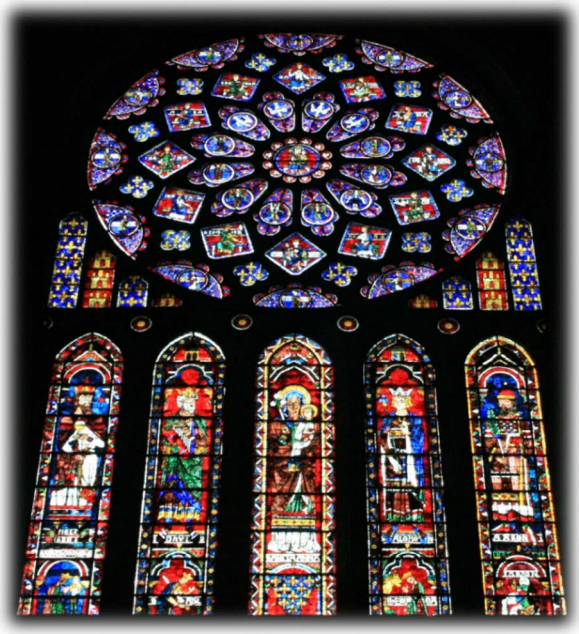

Figure 2.4: *Rose window of the Cathedral of Notre Dame, Chartres*[34]

When the melt solidifies this approach leads to tiny metal inclusions in the glass and gives it a bright permanent color that does not bleach or cease. These glasses were often used in church windows and can look differently in reflection and transmission. An example for such

a window is depicted in Figure 2.4[34] where the rose window in the cathedral of Notre Dame in Chartres is shown. If the included nanoparticles are for example large enough to scatter predominantly green light, the glass will look green in reflection or at some angle. However, in direct transmission the glass will look red, as all of the green light has already been scattered in other directions. The colors of these metal nanoparticles are a result of the particle plasmon resonance. Figure 2.5 (a)[35] shows how this effect can be pictured in a very simple way. The electric field of an incoming light wave induces polarization of the free electrons with respect to the much heavier ionic core of a spherical nanoparticle. The net charge difference occurs at the nanoparticle surface which in turn acts as a restoring force. In this manner, a dipolar oscillation with the same phase is created in the simplest case. This is demonstrated in (b)[36] for the example of a 60 nm gold particle in water.

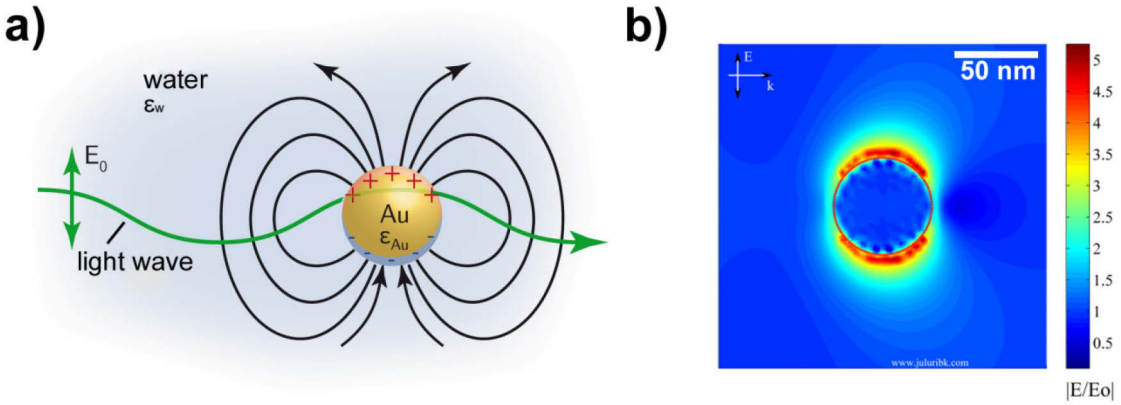

Figure 2.5: *(a) schematic of the excitation of a particle plasmon in a metal gold particle by an external oscillation field[35], (b) electric field distribution inside and outside of a 60 nm gold particle in water at a wavelength of 532 nm using DDSCAT 7.[36]*

The surface plays obviously a very important role for the observation of this phenomenon as it alters the boundary conditions for the polarizability of the metal and does not require the same strict matching conditions as its surface plasmon counterpart. Since the transverse momentum is not conserved in this spherical geometry, a particle plasmon exhibits a distinct resonance frequency, depending on its shape and size of the metal as well as on the dielectric constant of the metal itself and of medium surrounding it.[20, 37] The plasmon resonance is strongest and shifted into the visible part of the electromagnetic spectrum for the noble meals copper, silver and gold which is the reason why these metals have historically fascinated scientists dating back to Faraday.[38] The resonance enhances both the field inside and outside of the particle which can be used to enhance nonlinear optical effects such as surface enhanced Raman Scattering (SERS).[39, 40] As particle plasmons do not propagate they are not characterized by a propagation length, but rather by a decay of the particle plasmon over time. The main loss mechanisms are a radiative decay process into photons and absorption.[41]

The principle problem of electromagnetic scattering by a homogenous, isotropic sphere is commonly referred to as *Mie theory*, although Gustav Mie[42] was not the first to formulate this scattering problem. Before him both Alfred Clebsch, solving the elastic point source scattering problem of a perfectly rigid sphere using potential functions[43] and Ludvig Lorenz[44, 45] contributed to this problem. In 1909 Peter Debye[46] considered the related problem of the radiation pressure on a spherical particle utilizing two scalar potential functions. Therefore plane wave scattering by a homogenous isotropic sphere is sometimes also referred to as *Lorenz-Mie* or even *Lorenz-Mie-Debye theory*.

Dating back to 1908 Mie was the first to explain the red color of gold nanoparticle solutions. He solved the Maxwell equations[4] for an electromagnetic light wave interacting with a small sphere having the same macroscopic dielectric properties as the bulk metal. The solution to this electrodynamic calculation is performed in spherical polar coordinates using usual boundary conditions for the field at the surface of the particle. The boundary is defined by the electron density, which is assumed to have a sharp discontinuity at the surface of the sphere. This leads to a series of multipole oscillations for the extinction cross-section of the nanoparticle.[20, 37, 47] By series expansion of the involved fields into partial waves, the following expression for the extinction and scattering cross sections are obtained:[20]

$$\sigma_{ext} = \frac{2\pi}{\left|\vec{k}\right|^2} \sum_{L=1}^{\infty} (2L+1)\,\mathrm{Re}\left[a_L + b_L\right] \tag{2.15}$$

$$\sigma_{sca} = \frac{2\pi}{\left|\vec{k}\right|^2} \sum_{L=1}^{\infty} (2L+1)\left(\left|a_L\right|^2 + \left|b_L\right|^2\right) \tag{2.16}$$

with the absorption cross section as the difference between the two processes $\sigma_{abs} = \sigma_{ext} - \sigma_{sca}$ and a_L and b_L the corresponding Mie expansion coefficients for a plane wave in spherical harmonics:

$$a_L = \frac{m\psi_L(mx)\psi'_L(x) - \psi'_L(mx)\psi_L(x)}{m\psi_L(mx)\eta'_L(x) - \psi'_L(mx)\eta_L(x)} \tag{2.17}$$

$$b_L = \frac{\psi_L(mx)\psi'_L(x) - m\psi'_L(mx)\psi_L(x)}{\psi_L(mx)\eta'_L(x) - m\psi'_L(mx)\eta_L(x)} \tag{2.18}$$

The coefficient $m=n_m/n_d$ is the ratio of the complex refractive index of the particle n_m and the real refraction index of the surrounding medium n_d, k is the wave vector and x is the size parameter with $2\pi r n_d/\lambda$ and r the radius of the nanoparticle. ψ_L and η_L are the Ricatti-Bessel cylindrical functions. The dash indicates differentiation with respect to the argument in the brackets. The summation index L gives the order of the partial waves, described by vector spherical harmonic functions for the electric and magnetic field and thus is the order

of spherical multipole excitations in the particle. Figure 2.6[37] shows as an example the electric and magnetic field lines of the electric multipoles for *L* up to three. *L*=1 corresponds to dipole fields as in Figure 2.5 (b), *L*=2 to quadrupole, *L*=3 to octupole fields and so on.

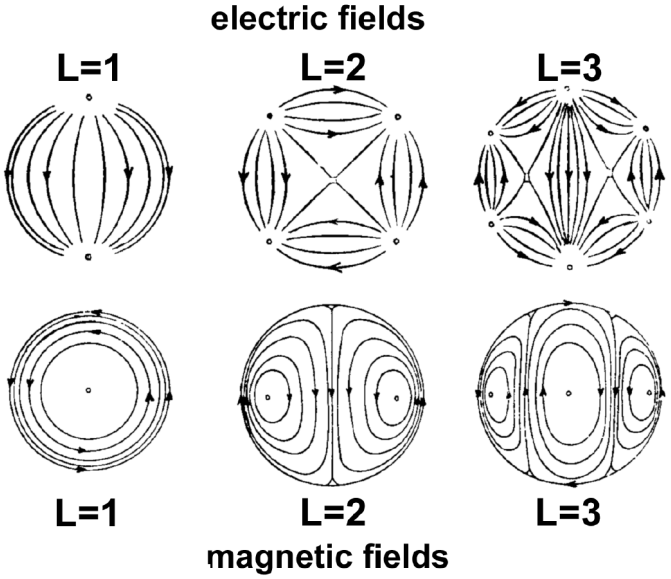

Figure 2.6: *Electric and magnetic fields far away from the particles, of the L=1, 2 and 3 electric partial waves, i.e. the electric dipole, quadrupole and octupole mode. The same field distributions hold for the magnetic partial waves, if electric and magnetic fields are interchanged.*[37]

It is sometimes useful for comparison to describe the cross sections as dimensionless efficiencies which are normalized with respect to the area of the scatterer projected perpendicular to the direction of the incoming wave:

$$Q_{abs/sca} = \frac{C_{abs/sca}}{\pi \cdot r^2} \tag{2.19}$$

In a normal absorption experiment the sum of scattering and absorption processes is measured. This extinction cross section is related to the measured attenuation of light of intensity I_0 over path-length d in the presence of a dilute colloidal solution containing N particles per volume by:

$$A = \log_{10}\left(\frac{I}{I_0}\right) = -\frac{N \cdot \sigma_{ext} \cdot d}{\ln(10)} \tag{2.20}$$

where A is the absorbance and I is the intensity of the transmitted light. If the number of particles is measured in terms of a molar metal atom concentration, the molar extinction coefficient ε_{LB} of a solution is measured according to Lambert-Beer's law in units of $M^{-1}cm^{-1}$ and the quantity is related to the extinction cross section through the Avogadro constant N_A by:

$$\varepsilon_{LB}\left[\frac{L}{mol \cdot cm}\right] = \frac{N_A}{1000 \cdot \ln(10)} \cdot \sigma_{ext} \tag{2.21}$$

For nanoparticles much smaller than the wavelength of light ($x << 2\pi$ or $2r << \lambda$) retardation over the whole particle volume becomes negligible and then only the dipole oscillation (L=1) significantly contributes to the cross-sections. In this case they simplify to the following relationships:

$$\sigma_{ext}(\lambda) = 9\left(\frac{\omega}{c}\right)\cdot\varepsilon_d^{3/2}\cdot V\cdot\frac{\mathrm{Im}\left[\varepsilon_m(\omega)\right]}{\left(\mathrm{Re}\left[\varepsilon_m(\omega)\right]+2\varepsilon_d\right)^2+\mathrm{Im}\left[\varepsilon_m(\omega)\right]^2}\propto V \tag{2.22}$$

$$\sigma_{sca}(\lambda) = \frac{3}{2\pi}\left(\frac{\omega}{c}\right)^4\cdot\varepsilon_d^2\cdot V^2\cdot\frac{\left(\mathrm{Re}\left[\varepsilon_m(\omega)\right]-\varepsilon_d\right)^2+\mathrm{Im}\left[\varepsilon_m(\omega)\right]^2}{\left(\mathrm{Re}\left[\varepsilon_m(\omega)\right]+2\varepsilon_d\right)^2+\mathrm{Im}\left[\varepsilon_m(\omega)\right]^2}\propto V^2 \tag{2.23}$$

where V is the particle volume, ω the angular frequency of the exciting light, c the speed of light. ε_m and ε_d are the dielectric functions of the metal and the surrounding medium, respectively. Within this dipole approximation the particle plasmon resonance is independent of the particle size. The resonance condition is fulfilled when the denominator gets small. This condition is fulfilled for $\mathrm{Re}[\varepsilon_m(\omega)]=-2\,\varepsilon_d$. under the assumption that $\mathrm{Im}[\varepsilon_m(\omega)]$ is small or only weakly depending on the angular frequency ω (the *Fröhlich mode*).

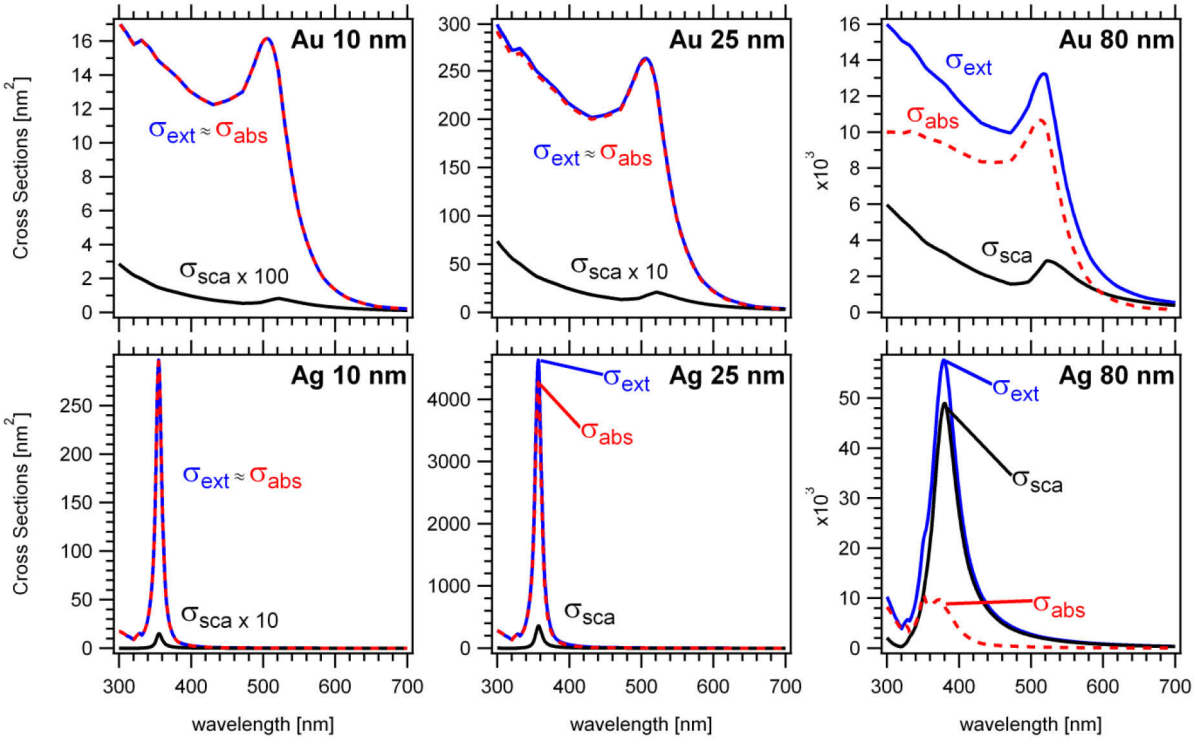

Figure 2.7: *Extinction, absorption and scattering cross sections for gold and silver nanoparticles with diameters of 10, 25 and 80 nm in vacuum, using values from Johnson & Christy.[10] Note the different scaling.[37, 48]*

For these small particles the participation of the scattering cross section is due to the dependency from the volume V^2 ($\propto r^6$) very weak and the measured optical response of a particle is primary made from the absorption cross section as can be seen for gold and silver nanoparticles with diameters of 25 nm and smaller in Figure 2.7.[37, 48]

For larger nanoparticles scattering processes become important, as can be seen for the silver particles with a diameter of 80 nm, but also the dipole approximation is no longer valid. In this regime the plasmon resonance depends explicitly on the particle size as the size parameter *x* is a function of the particle radius *r*. The larger the particles are, the more important the higher orders modes become, because the incoming light can no longer homogenously polarize the particles. These higher order modes peak at lower energies with increases particle size, which can be very well seen in the example of the absorption cross section for the largest silver particles in Figure 2.7. At the same time the plasmon bandwidth increases because of the radiation damping. The coherent oscillations of the electrons are able to decay directly into photons and this broadens the resonance.[20, 49, 50] As the optical absorption spectra depend directly on the size of the particles, this is regarded as an "*extrinsic size effect*".[20]

For nanoparticles on the order of a few nanometers the situation concerning the size dependence of the optical absorption spectra is a little more complicated as derived from the dipole approximation. For 5 nm gold nanoparticles the plasmon band is strongly damped and its absorption becomes weak and broad. For 2 nm particles it completely disappears.[51, 52] The electron density in the "conduction band" becomes very small and the assumption of bulk-like electronic and optical properties of the nanoparticle cannot be justified any longer. This is another example of a non-local effect. These nanoparticles are better treated as molecular clusters with discrete electronic states and with a dielectric function that is size dependent $\varepsilon(\omega,r)$. The mean free path of the electrons in silver and gold is of the order of 40-50 nm and in most theoretical models it is assumed that the dielectric function of the material becomes size dependent below an average particle diameter of 20 nm.[20] Since the electrons reach faster the surface, the coherence of the plasma oscillation is lost more quickly and with it the band width increases with decreasing particle size.[53-55] This size effect is regarded as an "*intrinsic size effect*",[20] because in this case the material dielectric function itself depends on the size.

When the nanoparticles become elongated at one axis the plasmon resonance splits into two bands. The optical absorption spectrum of these spheroidal particles can be qualitatively described by Gans theory,[37, 56] which is an extension of the Mie theory. The Gans theory calculates a depolarization factor along each axis of the spheroid based on the aspect ratio of the semi-major and semi-minor axis. In both Gans theory and experimental measurements on gold nanorods the longitudinal mode of the major axis shifts to the red, while the transverse resonance of the minor axis slightly blue shifts.

2.2.3 Sphere-on-Plane Systems

In a system of a metal particle placed very close to a plane metal surface, the electromagnetic interaction between the particle plasmon[37] and the surface plasmon mode[28] gives rise to various interesting optical phenomena and creates a special type of electromagnetic normal mode, the so-called "*gap mode*", which is strongly localized in the space between the sphere and the surface. This coupling is not linear and can neither be described in terms of the isolated resonance of the sphere nor the plane. The gap modes were suggested to be the source of the light emission from tunnel junctions[57-59] and play a central role in surface enhanced Raman scattering (SERS) spectroscopy as the source of large field enhancements.[39, 60, 61]

The optical response of this so-called sphere-on-plane (SOP) system can be calculated by neglecting retardation and solving the Laplace equation to obtain the scalar potentials in the surrounding medium, metal substrate and sphere. It was solved by Rendel[62] to explain experiments with tunnel junctions, by Wind[63] to explain the behavior of island films and by Aravind[64] as first step to understand SERS. Ruppin *et al.*[65] solved the equation to describe systems of small metal particles deposited on a substrate. The mathematical procedure is not repeated here, but can be briefly summarized in the following way: (1) First the required potentials are expanded in bispherical coordinates. (2) By imposing the boundary conditions the unknown coefficients of the expansions are determined. The frequencies of the electromagnetic normal modes are given by the conditions for the existence of nontrivial solutions. (3) The detailed characteristics of the normal modes such as the field distribution can be calculated from the determined potentials. In this electrostatic approximation the response of the system is a function of the dielectric property of the materials, of the sphere radius R and of the gap distance d from the film. The system is scale-invariant[66] and the interaction only depends on the ratio of d/R, but not on the sphere size itself. For systems composed of silver and gold Figure 2.8 shows the calculated extinction efficiencies for various ratios of the gap distance to the sphere radius, using the model from Wind[63] with the dielectric functions from Johnson and Christy[10] in a homogenous dielectric environment with ε =1. The sphere or the metal particle with a diameter of 20 nm is illuminated under an incident angle of 60° with p-polarized light.

The electromagnetic interaction of the sphere alone results in a single resonance band, appearing for gold and silver around 520 nm and 360 nm respectively, shown in Figure 2.8 with the black curves. The position is given by the dipole approximation (2.22).

By adding a plane or a metallic film in a large distance, the observed resonance is red-shifted, as shown in gray. The interaction can be regarded as a dipole on mirror interaction. The field emitted by the sphere is reflected by the plane and interacts again with itself

producing a shift in the resonance wavelength of the system compared with the resonance of the sphere alone.

When the plane distance d is very small compared with the sphere radius, the sphere can no longer be regarded as a dipole and due to the charge distribution multipoles have to be considered. At these distances, huge red-shifts and a significant increase in the extinction efficiencies are seen. The resonance wavelength of these gap modes shifts to longer wavelength as the ratio decreases, which is shown in blue for d/R=0.05, green for d/R=0.03 and red d/R=0.01.

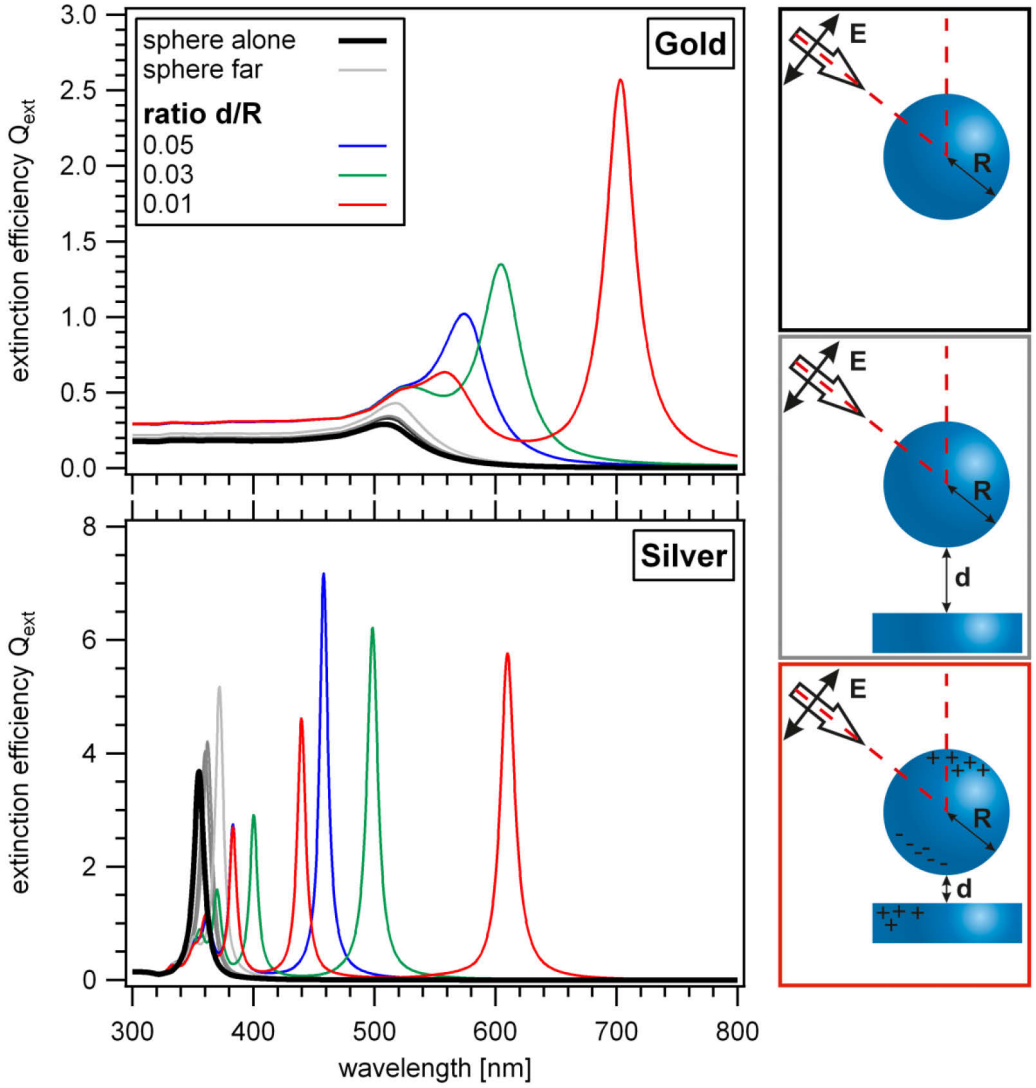

Figure 2.8: *Calculated extinction efficiencies of a particle above a substrate for gold and silver and various ratios of the gap distance to the particle radius in vacuum. A p-polarized beam at an incident angle of 60° is assumed. The sphere diameter is 20 nm. For the calculation the dielectric values from Johnson and Christy[10] were used.*

For s-polarized light the red-shifts are negligible[67] since the lateral components are not so effective in exciting the structure. The resonances of the silver sphere-on-plane system are sharper and shift stronger to the red. Already for distance to sphere ratios smaller than of

0.05 resonances from higher order modes can clearly be distinguished on the blue side of the spectrum from the fundamental on the red side.

Theoretical calculations predict a large electric field in the nano-gap at resonance condition. Figure 2.9[68] shows a calculation taken from Aravind *et al.*[64] for systems using gold and silver. The field enhancement which is defined as the ratio between the field in the gap E^2 and the incident field E_0^2 is in the order of 10^4 for gold and $5x10^4$ for silver.

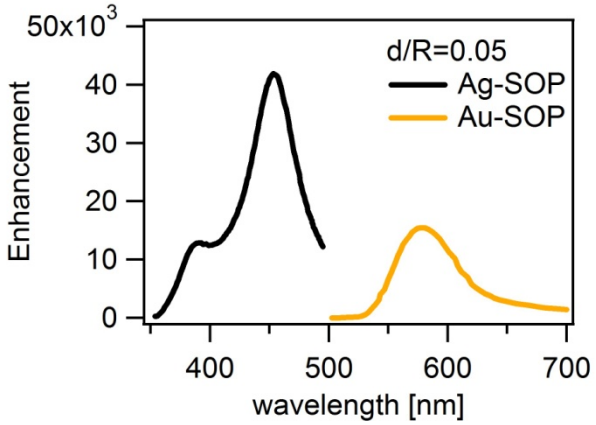

Figure 2.9: *Maximum Enhancement of the field in the gap for a silver (Ag) and gold (Au) sphere-on-plane system (SOP)*[64, 68]

Apart from the obvious potentials in different applications these enhancements are also interesting from a fundamental point of view. The appearance in such small volumes raises the questions of the applicability of the macroscopic description of matter at the nanoscale. The near fields can interact with the surface states of the metal or make the system sensitive to non-local effects which are normally not included in the description by a bulk dielectric function.

A problem arises when experiments are compared to these analytical theories as a spacer layer is needed to adjust the distance between the particle and the metal surface. A detailed overview of the literature involved with sphere-on-plane resonators is given in Chapter 7. For gold and silver systems usually the widespread thiol chemistry is exploited. This layer constitutes only a small part of the environment surrounding the sphere, but due to the occurring high fields in the gap the dielectric environment in this region plays an important role for the optical response of the whole system. The importance of this layer was shown in Raman scattering experiments[69, 70] and models which include this layer have also been developed with numerical calculations.[71, 72] Recently the group of Nordlander[73] presented a simple and intuitive model the plasmon hybridization concept, that can be used to describe the coupling of complex plasmonic nanostructures of arbitrary shape. In this approach, the plasmon resonances of complex nanostructures are expressed in terms of the interaction between plasmon resonances of its elementary components. The resulting hybridized

plasmon modes are formed in rigorous analogy with molecular orbital theory where the wave functions of the individual atoms overlap in a molecule and form bonding and antibonding molecular orbitals. The plasmon modes in the sphere-on-plane system can then be viewed as being formed by the interaction and hybridization of the discrete nanoparticle and continuum delocalized surface film plasmon modes.[74, 75] Since the surface plasmons have a finite interaction with all sphere plasmons, they mediate an indirect (hybridization) between sphere plasmons of different angular momentum. The interactions are schematically shown in Figure 2.10 (b).

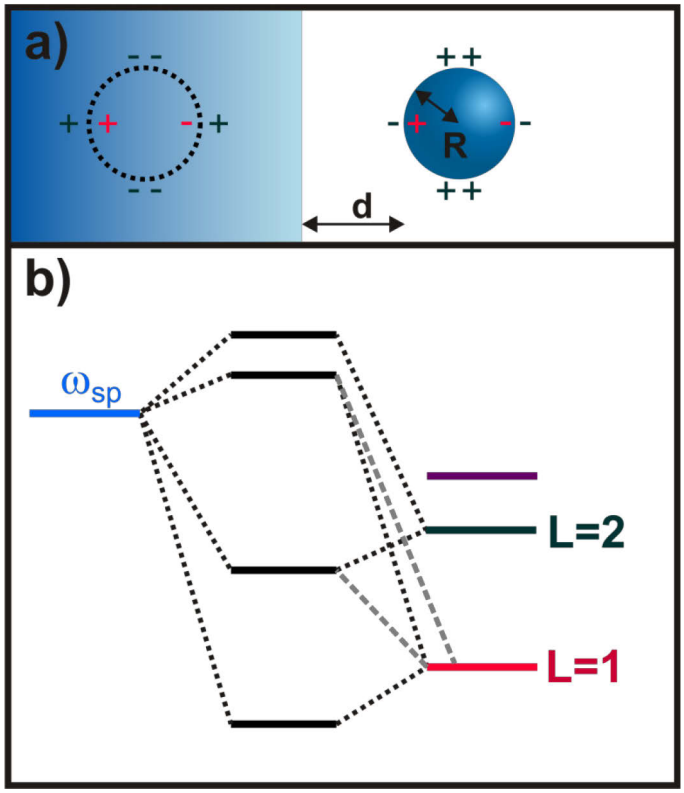

Figure 2.10: *(a) schematic showing the image response of the surface to the L=1 and L=2 particle plasmons. The surface mediates an interaction between the plasmons of different L, resulting in a distance-dependent hybridization of the particle plasmons, (b) plasmon hybridization principle for the nanoparticle-metal system.*

They are identically to what is expected from a simple image model of the surface in which the sphere plasmons interact both with its own image and with the images of the other sphere plasmons of the same azimuthal symmetry as shown in Figure 2.10 (a). The picture is similar to the formation of dimer plasmons from individual nanoparticle plasmons.[76]

2.3 Bibliography

1. Ashcroft, N.; Mermin, D., *Solid State Physics*. 1st ed.; Brooks Cole: 1976.
2. Jackson, J. D., *Klassische Elektrodynamik*. 2nd ed.; de Gruyter: Berlin, 1982.
3. Kittel, C., *Introduction to Solid Sate Physics*. 8th Edition ed.; John Wiley & Sons: New York, 2005.

4. Maxwell, J. C., A Dynamical Theory of the Electromagnetic Field. *Philosophical Transactions of the Royal Society of London* **1865,** *155*, 459-512.

5. Drude, P., Zur Ionentheorie der Metalle. *Physikalische Zeitschrift* **1900,** *1*, 161-165.

6. Drude, P., Zur Elektronentheorie der Metalle. *Annalen der Physik* **1900,** *306* (3), 566-613.

7. Sommerfeld, A.; Bethe, H., *Elektronentheorie der Metalle*. Springer Verlag: Heidelberg, 1933; Vol. 24-2.

8. Kashiwa, T.; Fukai, I., A Treatment by the FD-TD Method of the Dispersive Characteristics Associated with Electron Polarization. *Microwave and Optical Technology Letters* **1990,** *3* (6), 203-205.

9. Gray, D. E., *American Institute of Physics Handbook*. 3rd ed.; Mc-Graw Hill: 1972.

10. Johnson, P. B.; Christy, R. W., Optical Constants of Noble-Metals. *Phys. Rev. B* **1972,** *6* (12), 4370-4379.

11. Lynch, D. W.; Huttner, W. R., *Handbook of Optical Constants of Solids*. Academic Press Inc.: 1985; p 275-367.

12. Otter, M., Optische Konstanten Massiver Metalle. *Zeitschrift für Physik* **1961,** *161* (2), 163-178.

13. Schulz, L. G., The Optical Constants of Silver, Gold, Copper, and Aluminum .1. The Absorption Coefficient-K. *Journal of the Optical Society of America* **1954,** *44* (5), 357-362.

14. Schulz, L. G.; Tangherlini, F. R., Optical Constants of Silver, Gold, Copper, and Aluminum .2. The Index of Refraction-N. *Journal of the Optical Society of America* **1954,** *44* (5), 362-368.

15. Aspnes, D. E., Optical Properties of Thin-Films. *Thin Solid Films* **1982,** *89* (3), 249-262.

16. Henglein, F.; Kolb, D. M.; Stolberg, L.; Lipkowski, J., Electroreflectance Spectroscopy of Au(100) Covered by Adsorbed Pyridine Molecules. *Surface Science* **1993,** *291* (3), 325-336.

17. Barnes, W. L., Fluorescence near interfaces: the role of photonic mode density. *J. Mod. Opt.* **1998,** *45* (4), 661-699.

18. Kolb, D. M., *Spectroelectrochemistry: Theory and Practice*. Plenum: New York, 1988.

19. Fuchs, R.; Claro, F., Multipolar Response of Small Metallic Spheres - Nonlocal Theory. *Phys. Rev. B* **1987,** *35* (8), 3722-3727.

20. Kreibig, U.; Vollmer, M., *Optical Properties of Metal Clusters,*. Springer-Verlag: Berlin, 1995.

21. Wood, R. W., On a remarkable case of uneven distribution of light in a diffraction grating spectrum. *Philosophical Magazine* **1902,** *4* (21), 396-402.

22. Fano, U., On the theory of the intensity anomalies of diffraction. *Annalen der Physik* **1938,** *32* (5), 393-443.

23. Ritchie, R. H., Plasma Losses by Fast Electrons in Thin Film. *Physical Review* **1957,** *106* (5), 874-881.

24. Ritchie, R. H.; Marusak, A. L., Surface Plasmon Dispersion Relation for an Electron Gas. *Surface Science* **1966,** *4* (3), 234-240.

25. Turbadar, T., Complete absorption of light by thin metal films. *Proceedings of the Physical Society of London* **1959,** *73* (469), 40-44.

26. Kretschmann, E., Determination Of Optical Constants Of Metals By Excitation Of Surface Plasmons. *Zeitschrift für Physik* **1971,** *241* (4), 313-324.

27. Otto, A., Excitation of Nonradiative Surface Plasma Waves in Silver by Method of Frustrated Total Reflection. *Zeitschrift für Physik* **1968,** *216* (4), 398-410.

28. Raether, H., *Surface Plasmons on Smooth and Rough Surfaces and on Gratings*. Springer-Verlag: New York, 1988.

29. Homola, J.; Dostalek, J.; Jian, S.; Ladd, J.; Löfas, S.; A., M., *Surface Plasmon Resonance Based Sensors*. Springer: Berlin, 2006; Vol. 4.

30. Homola, J.; Koudela, I.; Yee, S. S., Surface plasmon resonance sensors based on diffraction gratings and prism couplers: sensitivity comparison. *Sensors and Actuators B-Chemical* **1999,** *54* (1-2), 16-24.

31. Barnes, W. L.; Dereux, A.; Ebbesen, T. W., Surface plasmon subwavelength optics. *Nature* **2003,** *424* (6950), 824-830.

32. Novotny, L.; Hecht, B., *Principles of Nano-Optics*. Cambridge University Press: New York, 2006.

33. Knoll, W., Interfaces and thin films as seen by bound electromagnetic waves. *Annual Review of Physical Chemistry* **1998,** *49*, 569-638.

34. Borchert, A. http://de.wikipedia.org/wiki/Kathedrale_von_Chartres (accessed 20.12.2010).

35. Raschke, G. Molekulare Erkennung mit einzelnen Gold-Nanopartikeln. Dissertation, Ludwig-Maximilians-Universität, München, 2005.

36. Juluri, B. http://juluribk.com/ (accessed 03.01.2011).

37. Bohren, C. F.; Huffman, D. R., *Absorption and scattering of light by small particles*. Wiley-VCH: New York, 1983.

38. Faraday, M., The Bakerian Lecture: Experimental Relations of Gold (and Other Metals) to Light. *Philosophical Transactions of the Royal Society of London* **1857,** *147*, 145-181.

39. Moskovits, M.; Jeong, D. H., Engineering nanostructures for giant optical fields. *Chemical Physics Letters* **2004,** *397* (1-3), 91-95.

40. Nie, S. M.; Emory, S. R., Probing single molecules and single nanoparticles by surface-enhanced Raman scattering. *Science* **1997,** *275* (5303), 1102-1106.

41. Link, S.; El-Sayed, M. A., Optical properties and ultrafast dynamics of metallic nanocrystals. *Annual review of physical chemistry, Volume 54, 2003* **2003**, 331-452.

42. Mie, G., Beiträge zur Optik trüber Medien, speziell kolloidaler Metallösungen. *Annalen der Physik, Vierte Folge* **1908,** *25* (3), 377-445.

43. Clebsch, A., Über die Reflexion an einer Kugelfläche. *Journal für Mathematik* **1863,** *61* (3), 195-262.

44. Lorenz, L. V., Lysbevaegelsen i og uden for en af plane Lysbolger belyst Kugle. *Det Kongelige Danske Videnskabernes Selskabs Skrifter, 6. Raekke, 6. Bind* **1890,** *1*, 1-62.

45. Lorenz, L. V., *Sur la lumière réfléchie et réfractée par une sphère (surface) transparente*. Libraire Lehmann & Stage: Kopenhagen, 1898.

46. Debye, P., Der Lichtdruck auf Kugeln von beliebigem Material. *Annalen der Physik Vierte Folge* **1909,** *30* (1), 57-136.

47. Kerker, M., *The Scattering of Light and Other Electromagnetic Radiation*. Academic Press: New York, 1969.

48. Mätzler, C. *Mie Matlab Code*, 2009.

49. Wokaun, A.; Gordon, J. P.; Liao, P. F., Radiation Damping in Surface-Enhanced Raman Scattering. *Physical Review Letters* **1982,** *48* (14), 957-960.

50. Sonnichsen, C.; Franzl, T.; Wilk, T.; von Plessen, G.; Feldmann, J., Plasmon resonances in large noble-metal clusters. *New Journal of Physics* **2002,** *4*.

51. Alvarez, M. M.; Khoury, J. T.; Schaaff, T. G.; Shafigullin, M. N.; Vezmar, I.; Whetten, R. L., Optical absorption spectra of nanocrystal gold molecules. *Journal of Physical Chemistry B* **1997,** *101* (19), 3706-3712.

52. Schaaff, T. G.; Shafigullin, M. N.; Khoury, J. T.; Vezmar, I.; Whetten, R. L.; Cullen, W. G.; First, P. N.; GutierrezWing, C.; Ascensio, J.; JoseYacaman, M. J., Isolation of Smaller Nanocrystal Au Molecules: Robust Quantum Effects in Optical Spectra. *Journal of Physical Chemistry B* **1997,** *101* (40), 7885-7891.

53. Doremus, R. H., Optical Properties of Small Gold Particles. *J. Chem. Phys.* **1964,** *40* (8), 2389-2396.

54. Kreibig, U.; Vonfrags.C, Limitation of Electron Mean-Free Path in Small Silver-Particles. *Zeitschrift für Physik* **1969,** *224* (4), 307-323.

55. Kreibig, U.; Zacharia.P, Surface Plasma Resonances in Small Spherical Silver and Gold Particles. *Zeitschrift für Physik* **1970,** *231* (2), 128-143.

56. Gans, R., The state of ultramicroscopic silver particles. *Annalen der Physik* **1915,** *47* (10), 270-284.

57. Hansma, P. K.; Broida, H. P., Light-Emission from Gold Particles Excited by Electron-Tunneling. *Applied Physics Letters* **1978,** *32* (9), 545-547.

58. Johansson, P.; Monreal, R.; Apell, P., Theory for Light-Emission from a Scanning Tunneling Microscope. *Phys. Rev. B* **1990,** *42* (14), 9210-9213.

59. Lambe, J.; McCarthy, S. L., Light-Emission from Inelastic Electron-Tunneling. *Physical Review Letters* **1976,** *37* (14), 923-925.

60. Hill, R. T.; Mock, J. J.; Urzhumov, Y.; Sebba, D. S.; Oldenburg, S. J.; Chen, S.-Y.; Lazarides, A. A.; Chilkoti, A.; Smith, D. R., Leveraging Nanoscale Plasmonic Modes to Achieve Reproducible Enhancement of Light. *Nano Letters* **2010,** *10* (10), 4150-4154.

61. Pettinger, B.; Krischer, K.; Ertl, G., Giant Raman-Scattering Cross-Section for an Adsorbed Dye at Ag Colloids Associated with Low EM Field Enhancement. *Chemical Physics Letters* **1988,** *151* (1-2), 151-155.

62. Rendell, R. W.; Scalapino, D. J., Surface-Plasmons confined by Microstructures on Tunnel-Junctions. *Phys. Rev. B* **1981,** *24* (6), 3276-3294.

63. Wind, M. M.; Vlieger, J.; Bedeaux, D., The Polarizability of a Truncated Sphere on a Substrate I. *Physica A: Statistical and Theoretical Physics* **1987,** *141* (1), 33-57.

64. Aravind, P. K.; Metiu, H., The effects of the interaction between resonances in the electromagnetic response of a sphere-plane structure - applications to surface enhanced spectroscopy. *Surface Science* **1983,** *124* (2-3), 506-528.

65. Ruppin, R., Surface-Modes and Optical-Absorption of a Small Sphere Above a Substrate. *Surface Science* **1983,** *127* (1), 108-118.

66. Nordlander, P.; Le, F., Plasmonic structure and electromagnetic field enhancements in the metallic nanoparticle-film system. *Applied Physics B-Lasers and Optics* **2006,** *84* (1-2), 35-41.

67. Okamoto, T.; Yamaguchi, I., Optical absorption study of the surface plasmon resonance in gold nanoparticles immobilized onto a gold substrate by self-assembly technique. *J. Phys. Chem. B* **2003,** *107* (38), 10321-10324.

68. Rueda, A. Optical resonances of sphere-on-plane geometries. Dissertation, Johannes Gutenberg Universität, Mainz, 2008.

69. Futamata, M.; Maruyama, F.; Ishikawa, M., Adsorbed sites of individual molecules on Ag nanoparticles in single molecule sensitivity-surface-enhanced Raman scattering. *Journal of Physical Chemistry B* **2004,** *108* (35), 13119-13127.

70. Futamata, M.; Maruyama, Y.; Ishikawa, M., Critical importance of the junction in touching Ag particles for single molecule sensitivity in SERS. *Journal of Molecular Structure* **2005,** *735*, 75-84.

71. Leveque, G.; Martin, O. J. F., Tunable composite nanoparticle for plasmonics. *Optics Letters* **2006,** *31* (18), 2750-2752.

72. Leveque, G.; Martin, O. J. F., Optical interactions in a plasmonic particle coupled to a metallic film. *Optics Express* **2006,** *14* (21), 9971-9981.

73. Prodan, E.; Radloff, C.; Halas, N. J.; Nordlander, P., A hybridization model for the plasmon response of complex nanostructures. *Science* **2003,** *302* (5644), 419-422.

74. Le, F.; Lwin, N. Z.; Steele, J. M.; Kall, M.; Halas, N. J.; Nordlander, P., Plasmons in the metallic nanoparticle - Film system as a tunable impurity problem. *Nano Letters* **2005,** *5* (10), 2009-2013.

75. Nordlander, P.; Prodan, E., Plasmon hybridization in nanoparticles near metallic surfaces. *Nano Letters* **2004,** *4* (11), 2209-2213.

76. Nordlander, P.; Oubre, C.; Prodan, E.; Li, K.; Stockman, M. I., Plasmon hybridizaton in nanoparticle dimers. *Nano Letters* **2004,** *4* (5), 899-903.

3 Materials and Methods

3.1 Materials

3.1.1 Gold Nanoparticle Synthesis

Gold nanoparticles were prepared by chemical reduction in aqueous solution. The method was originally described by Turkevitsch *et al.*[1] and then refined by Frens.[2] In the reaction sodium citrate acts both as reducing agent and ligand for the stabilization of the created nanoparticles in water.

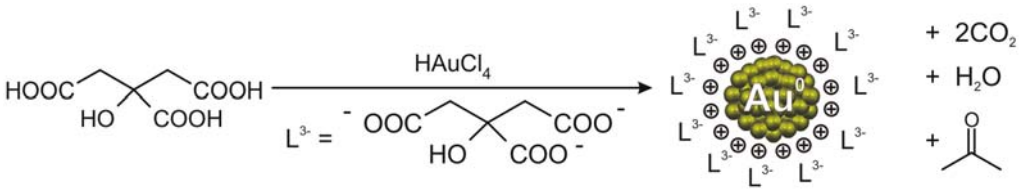

Figure 3.1: *Reaction scheme[3] for the synthesis of citrate stabilized gold nanoparticles*

The amount of reductant adjusts the particle diameter and particles can be produced over a wide range of sizes. To produce larger particles less citrate is added. This reduction decreases the amount of available citrate ions for stabilizing the particles, and this causes the small particles to aggregate into bigger ones until the total surface area of all particles becomes small enough to be fully covered by the existing citrate ions. This is also the reason that larger particles are obtained on costs of their monodispersity and shape. In most cases elongated and irregular spheroidal forms are observed. The negatively charged citrate layer creates then the necessary long-time stabilization of the particles by electrostatic repulsion. In the following, an exemplary procedure for the synthesis of particles with a diameter of 60 nm is described:

100 ml of a 0.3 mM aqueous solution of hydrogen tetrachloroaurate(III) trihydrate (*$HAuCl_4 \cdot 3\ H_2O$, 99.995%,* Sigma-Aldrich) was heated under reflux and stirring to the boiling point. Then, 2 ml of 17 mM aqueous solution of trisodium citrate dihydrate (*$HOC(CO_2Na)(CH_2CO_2Na)_2 \cdot 2\ H_2O$,* Sigma-Aldrich) was injected quickly. The suspension changed color from black to dark red in the first few minutes. After keeping the mixture boiling for another 10 minutes the heating source was removed and the suspension was allowed to slowly cool down to room temperature while stirring. The size and shape distributions of the particles prepared were determined by scanning electron microscopy (SEM, *Gemini 1530,* Zeiss-LEO, Oberkochen, Germany) after drying some drops of the colloidal suspension on a freshly cleaned silica wafer. For the preparation of different sizes the following amounts of the two chemicals were added to the described amount of water:

Table 3.1: Amounts of chloroauric acid and citrate for different sizes of nanoparticles

diameter	amount of HAuCl4	amount of citrate
20 nm	10,0 mg (0,025 mmol)	60 mg (0,204 mmol)
40 nm	10,0 mg (0,025 mmol)	15 mg (0,051 mmol)
60 nm	12,0 mg (0,030 mmol)	10 mg (0,034 mmol)
80 nm	12,0 mg (0,030 mmol)	7,8 mg (0,026 mmol)
100 nm	12,0 mg (0,030 mmol)	6,0 mg (0,020 mmol)
120 nm	12,0 mg (0,030 mmol)	5,0 mg (0,017 mmol)

The color of the suspensions changed with increasing size from dark-red to orange-brown. For particles with a size larger than 60 nm the Tyndall effect becomes visible where a look at scattered light shows another color than a look at the absorbed light.

3.1.2 Silver Nanoparticle Synthesis

For silver nanoparticle suspensions, a common method is the Lee–Meisel method,[4] which is a variation of the Turkevich method[1] in that $AgNO_3$ is used as the metal source, but unlike the Turkevich method, the Lee–Meisel method produces a broad distribution of particle sizes. Therefore, silver particles were synthesized following a procedure published by Suber.[5] In this synthesis the size and shape of the particles is determined by the ratio of silver-nitrate to ascorbic-acid and by the pH-value which is adjusted by adding concentrated nitric acid. By varying the reaction conditions, both isometric and anisotropic silver particles like hexagons or wires can be obtained. The formation of the metallic silver phase in solution is a direct result of the electron transfer from the ascorbic acid to the silver ions according to Figure 3.2:

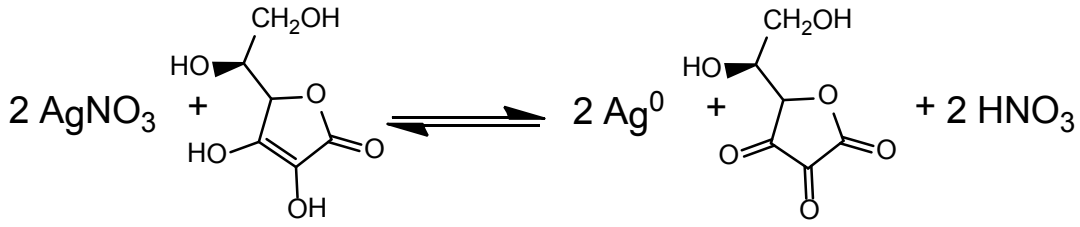

Figure 3.2: *Reaction scheme for the synthesis of silver nanoparticles*

Under acidic conditions the ascorbic acid is a powerful reducing agent and has the ability to completely convert the silver ions into metallic silver. However, at sufficiently high concentrations of the nitric acid, produced by the reaction above, the freshly formed silver seeds will re-dissolve, especially at elevated temperatures. Therefore, the formation of larger stable silver particles cannot take place unless the surface of the metal is somehow protected. As a protection agent the sodium salt of a naphthalene sulfonic acid/formaldehyde copolymer (Daxad 19) is used which is also an extremely powerful dispersant in highly acidic aqueous solutions. The protecting effect is attributed to the strong

interaction of the sulfonic groups with the surface of the silver. For isometric silver particles the following procedure was used:

850 mg silver nitrate ($AgNO_3$, for analysis, 99,8%, Honeywell Riedel-de Haen, Seelze, Germany) and 150 mg Daxad-19 (sodium salt of polynaphtalene sulfonate formaldehyde condensate, mol wt. 8000 g/mol, GEO Specialty Chemicals, Deer Park, USA) were dissolved in 25 ml of ultra-pure water in a 50 ml round flask. After heating the solution under stirring to 40 °C, 2.8 ml of concentrated nitric acid (69.7 wt%, Honeywell Riedel-de Haen, Seelze, Germany) were added. Then a solution of 1300 mg ascorbic acid in 5.5 ml ultra-pure water was added drop wise within 10 minutes. During this process the suspension changed from light brown to olive and to brown green. The suspension was allowed to cool down and stirred further for 60 minutes. The resulting silver particles were centrifuged three times at 8000 rpm for 10 minutes (relative centrifugal force RCF=8200 g, Centrifuge 5810 R with fixed angle rotor F-34-6-38, Eppendorf, Hamburg, Germany). After each cycle, the supernatant liquid was removed and the solid dispersed again in 45 ml of ultra-pure water. The particles and size distributions were determined by scanning electron microscopy (SEM, Gemini 1530, Zeiss-LEO, Oberkochen, Germany). The suspensions were stable for months.

3.1.3 Synthesis of the Perylene Diimide Loaded Polyphenylene Dendrimer in Generation 2 (PDI-G2)

The complete synthesis route to the polyphenylene dendrimer PDI-G2 was developed by [in printed version available] at the MPI-P. The preparation of the dendrimer used in this work was done by [in printed version available] in the synthetic chemistry group of [in printed version available] at the MPI-P. The following information was provided:

The perylene diimide (PDI) core (**1**) was prepared according to a procedure described here.[6, 7] Starting from this fluorescent core the first generation dendrimer (**3**) bearing ethynyl groups was prepared by Diels-Alder reaction with an excess of cyclopentadienone (**2**) substituted with ethynyl groups deactivated by silyl substituents followed by deprotection.[8] For building up the second generation an eightfold Diels-Alder cycloaddition of the methoxy-functionalized tetraphenylcyclopentadienone (**4**) was done to obtain the dendrimer having 16 methoxy-groups at its periphery. The same solvents as for the formation of the first generation were employed. Subsequently these methoxy groups underwent a multiple ether cleavage reaction in the presence of an excess of BBr_3 leading to the sixteen fold hydroxyl-functionalized polyphenylene dendrimer (**6**). The latter was then used in a dicyclohexylcarbodiimide-coupling sequence together with the lipoic acid (5-[1,2]dithiolan-3-ylpentanoic acid) (**7**) leading to the final target molecule (**8**).

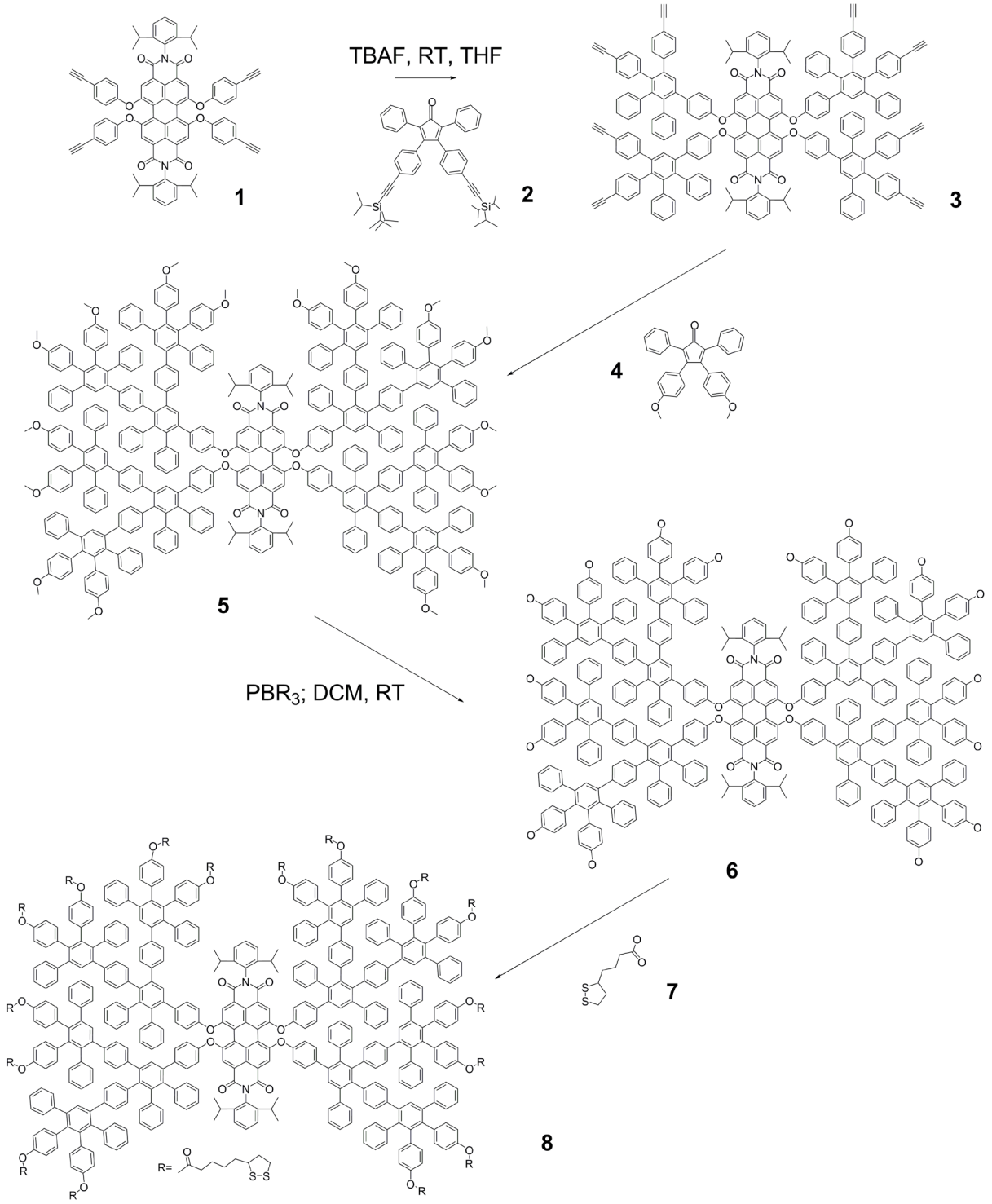

Figure 3.3: *Synthesis of the polyphenylene dendrimer ($PDIG_2$) with a PDI core and 16 dithiolane units R at the periphery.*[9]

All final compounds and intermediates resembled the characteristic properties of polyphenylene dendrimers and were unambiguously identified by the routine analytical methods.

The fluorescence emission spectrum of the PDI-G2 were obtained in a solution of 1 µM tetrahydrofuran (THF, puriss, p.a., stabilized, Sigma Aldrich, Steinheim, Germany) by using a fluorescence spectrometer (Tidas Fl-3095 S spectrometer, J&M Analytik AG, Aalen,

Germany). The excitation wavelength was changed from 400 nm to 705 nm in a step size of 5 nm with an integration time for each emission spectrum of 5 s.

For the single molecule fluorescence measurements, a solution of PDI-G2 in THF was diluted from 1 µM to 0.1 pM in steps of 1:100. An aliquot of 50µL of each concentration was spin coated at 2500 rpm on freshly cleaned cover glasses and analyzed by the in-house built confocal microscope in fluorescence mode and an excitation wavelength of 532 nm(pumped solid state Nd:YAG, GCL-005-L, Crysta-Laser, Reno, USA).

3.1.4 Glass Cleaning Procedure:

Microscope glass slides (clean white, 1 mm thick, Menzel Gläser GmbH, Braunschweig, Germany) were cleaned by immersion in a 2% detergent solution (Helllmanex, Hellma GmbH & Co KG, Müllheim, Germany) in ultra-pure water (milli-Q: 18.2 MΩ cm, Millipore, Billerica, USA), followed by extensive rinsing with ultra-pure water and ethanol (HPLC grade, Fisher Scientific, Leicestershire, United Kingdom). The slides were then heated to 550 °C under a nitrogen atmosphere in a tube furnace.

3.1.5 Silicon Wafer Cleaning Procedure:

Silicon wafers (precut, p-type, Crystek GmbH, Berlin, Germany) were deprotected from the adhesive foil on both sides and cleaned by immersion in a mixture of 50 ml of ultra-pure-water, 10 ml of ammonium hydroxide solution (25 wt%, Fluka Chemie GmbH, Buchs, Switzerland) and 10 ml of hydrogen peroxide solution (35 wt%, p.a., Acros Organics, Geel, Belgium). The mixture was heated to 75 °C for 90 minutes. After cooling to room temperature the slides were rinsed 10 times with ultra-pure water and one time with ethanol (HPLC grade, Fisher Scientific, Leicestershire, United Kingdom). They were stored in ethanol until further use.

3.1.6 Metal Evaporation

The cleaned cover glasses were directly installed in a thermal evaporation chamber (Balzers BLS 500, Balzers, Lichtenstein). First, a 1.5 nm thin chromium layer (99.9%, Unicore Materials, Balzers, Liechtenstein) was deposited followed by a 50 nm thick gold layer (99.99% granulate 2.0–3.0 mm, Balzers). The chromium layer serves as adhesion promoter. The evaporation rate was kept between 0.8 and 1 Å/s at a pressure of 5×10^{-6} mbar. These samples will be called in the following evaporated gold samples. The same method can also be used to evaporate 50 nm of silver (99.99% granulate 2.0–3.0 mm, Balzers) on the thin chromium layer.

3.1.7 Template Stripped Gold Preparation (TSG)

This procedure is a method to fabricate much smoother surfaces than those achieved by evaporation alone. It takes advantage of the poor adhesion between the evaporated material and an atomically flat template surface like mica or silicon single crystals which allows the material to be easily stripped after evaporation and leaving the surface in contact with the template uncovered. The method was first developed by Butt *et al.*[10] for carbon surfaces to image bio-molecules immobilized at a surface. They applied the same technique later to Pt/C and gold layers.[11] Around the same time Hegner experimented also with smooth gold layers. He investigated the stability of different glues in solution showing that they were stable enough to assemble monolayers of alkanethiols by dipping. He introduced the term template stripped gold for the fabricated surfaces.[12] Stamou *et al.*[13] were the first to use silicon templates instead of mica.

For the fabrication of TSG the cleaned silicon wafers were dried under a nitrogen stream and 50 nm of gold were deposited by electrothermal evaporation (0.8-1 Å/s; 5×10^{-6} mbar). The evaporated gold surfaces on the silicon wafers were immediately glued onto thin clean covers slides either using the epoxy glue EPO-Tek 353ND-4 or EPO-TEK 377 (Epoxy Technology Inc., Billerica, USA)) respectively. The glued slides were cured for 2 h at 150 °C and stored until further use. Directly prior to the self-assembly the gold surface was mechanically separated from the silicon wafers using a scalpel as a lever. When necessary the removal was supported by putting the silicon wafers in liquid nitrogen for a few seconds. These samples will be called in the following the TSG (template-stripped gold) samples. The same method can be used to prepare template stripped silver (TSS) surfaces, but this is not part of this work.

3.1.8 Self-Assembled Monolayers (SAMs)

For the gold sphere-on-plane systems in the dark-field scattering experiments the substrates were immersed in a 1 mM ethanol solution of 1-aminoethanethiol hydrochloride (AET) (*$HSCH_2CH_2NH_2{\cdot}HCl$*, Sigma Aldrich) for 2 hours. In this process, the thiol group of the AET attaches to the gold surface and forms a monolayer. Afterwards the substrates were rinsed with a mixture of 1:1 ethanol/water and dried in a nitrogen flow.

For the silver sphere on plane systems in the fluorescence measurements, the perylene diimide loaded polyphenylene dendrimer in generation 2 (PDI-G2) served both as a spacer and chromophore bearing unit. For its deposition the glass substrates with the evaporated silver film were immersed in a 2.5 µM PDI-G2 dendrimer solution in tetrahydrofuran (THF, puriss, p.a., stabilized, Sigma Aldrich, Steinheim, Germany) for 1.5 h. The substrates were subsequently rinsed with tetrahydrofuran (THF, puriss, p.a., stabilized, Sigma Aldrich,

Steinheim, Germany) and dried with nitrogen. The films have a thickness of around 2-3 nm[14] and were stable for weeks.

3.1.9 Particle Deposition

For the dielectric spheres on clean evaporated gold films the following steps were performed in a clean room: Stock solutions of polystyrene (PS) colloids (Nanobead NIST, Polysciences Inc, USA) stored at 4 °C were allowed to warm to room temperature. The dispersion was sonicated for 2 minutes to distribute the colloids. A suitable particle density on the surface was obtained by diluting a volume of the stock suspension with ethanol depending on the diameter of the spheres. The final concentrations of the suspensions were 0.005 wt% for the spheres with diameter between 200 and 300 nm; 0.01 wt% between 300 and 400 nm and 0,05 wt% between a diameter of 400 and 500 nm. A fraction of 70 µL was drop-cast from each suspension on the gold substrates and the surface dried with a stream of nitrogen before the solution evaporated.

For the gold sphere-on-plane systems the gold substrates with the self-assembled monolayer of cysteamine were immersed in a freshly prepared colloidal gold suspension for a time between 10 s and 60 s. All samples were afterwards rinsed with distilled water and dried with nitrogen. The gold nanoparticles were strongly immobilized by this process.

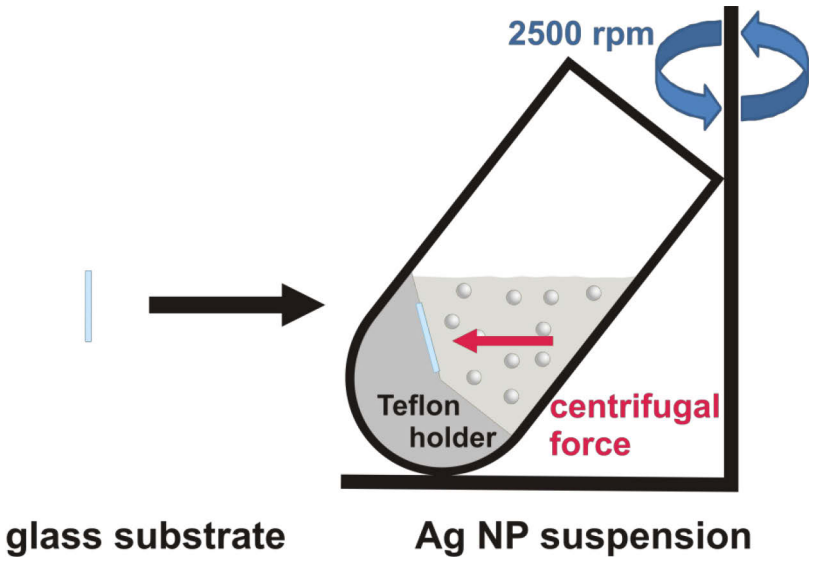

Figure 3.4: *Sketch of the centrifugation procedure with Teflon holder and position of the glass substrate*

For the silver sphere-on-plane systems with the PDI-G2 spacer the particles were deposited by centrifugation of the substrates with the prepared silver suspension at 2500 rpm for 2 min. (relative centrifugal force RCF=800 g, Centrifuge 5810 R with fixed angle rotor F-34-6-38, Eppendorf, Hamburg, Germany). For this purpose, the substrates were placed one by one in a custom made Teflon holder inside a metal centrifugation tube (∅=37 mm) and the

suspension was added. The angle for the sample support was 15° relative to the vertical when built into the rotor. A sketch of the setup is shown in Figure 3.4. This method was necessary due to the hydrophobic nature of the surface after addition of the PDI-G2 in conjunction with the aqueous silver suspension and subsequently brings great advantages both in time and surface coverage when compared to particle deposition by long time immersion under constant movement in a shaker. A comparison is given in Figure 3.5.

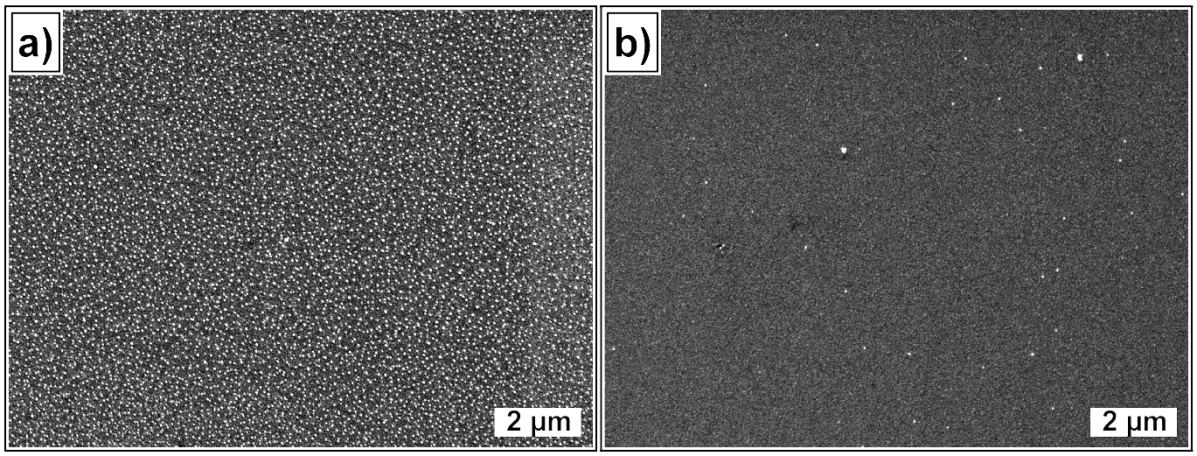

Figure 3.5: *(a) Particle deposition by centrifugation (2 x 4000 rpm for 5 minutes) and (b) by shaking for 48 hours. After each process the substrates were rinsed with ultra-pure water. The white spots are surface bound silver particles.*

The white spots are surface-bound silver particles. After the particle deposition all substrates were rinsed with ultra-pure water and dried with nitrogen.

3.2 Methods

3.2.1 Laser Irradiation of Noble Metal Particles

The interaction of light with colloidal metal particles has been of major interest since Faraday's pioneering experiments.[15] Their optical response is characterized by an absorption band related to the localized surface plasmon resonance (SPR)[16, 17] which depends on the size and shape of the nanoparticles. A useful way of studying these properties is time-resolved spectroscopy[18-20] as it allows following the electron-phonon relaxation dynamics.[19, 21-24] In these experiments a pump laser is used to excite the metal's electron distribution.[25] The electrons subsequently equilibrate with the phonon modes and the time scale for this process provides information about the electron-phonon coupling constant.[26, 27] The temperature of the lattice is normally raised only by a few tens of degrees as usually low excitation powers are used. In particular silver[23, 28, 29] and gold[21, 22, 24] nanoparticles with their plasmon band in the visible region have been studied intensively. However, if the laser pump power is significantly increased the temperature of the metal nanoparticle lattice can be raised to values well above the melting temperature within a few picoseconds when ultra-

short laser pulses are used while the surrounding non-absorbing media remains cool. This approach has widely been used for noble metals to change the dimensions, shape and size of nanoparticles via melting and evaporation. While the extent of the temperature increase depends on the irradiated laser power[19, 30] and the absorption coefficient at the used laser wavelength,[31] there is also a dependency of the pulse width of the laser light since the time constant of heat dissipation from the particles to the surrounding plays a role. All the involved effects during the laser irradiation will be discussed in detail in a later chapter. The experimental studies area mainly carried out on the basis of observed spectral changes and electron microscopy images taken before and after irradiation.

Irradiation Setup: For the experiments presented here the second (λ_{Ex}=532 nm) and third harmonic (λ_{Ex}=355 nm) of a pulsed Nd:YAG laser (PL2143B, Ekspla, Vilnius, Lithuania) was used with a custom designed optical setup. The diameter of the laser beam was 7-8 mm, the pulse duration about 30 ps and the pulse frequency 10 Hz. The light from the laser was directed onto the sample by a suitable combination of appropriate dielectric flip-mirrors for the second (M1-M3) and the third harmonic (M4-M6). After passing the cuvette with the nanoparticle suspension the remaining light was blocked by an aperture. The white light beam from the cold light source perpendicular to the laser pathway was adjusted by two lenses and directed to the spectrometer. The iris diaphragm was used to adjust the beam diameter to the same width as the cuvette wall. A schematic of the optical setup for the irradiation is shown in Figure 3.6.

In a typical irradiation procedure an aliquot of 7 ml from the colloid suspension was placed in a fluorescence cuvette (20x10 mm, 101-QS, Hellma GmbH & Co KG, Müllheim, Germany) with an optical path for the laser beam of 20 mm and irradiated by the second (λ_{Ex}=532 nm) or third harmonic (λ_{Ex}=355 nm). A magnetic stirrer with a speed of 3500 rpm was used to keep the suspensions homogeneous during the laser irradiation. The pulse energy of the laser was determined with a radiometer (RM 3700 with head RjP 735, Laser Probe Inc, Utica, USA) by the back reflection at a fused silica plate. For in situ monitoring of the process the absorbance of the sample was measured in 2 s time intervals with a fiber-optics spectrometer (S1024DW, Ocean Optics Inc., Dunedin, USA) attached to an A/D converter (ADC 1000-USB, Ocean optics Inc.) and a cold light source (KL1500, Carl Zeiss MicroImaging GmbH, Jena, Germany). The integration time was 300 ms and an average of three in-situ spectra was used for each time. The probe beam ran perpendicular to the laser beam and crossed the cuvette 3 mm above.

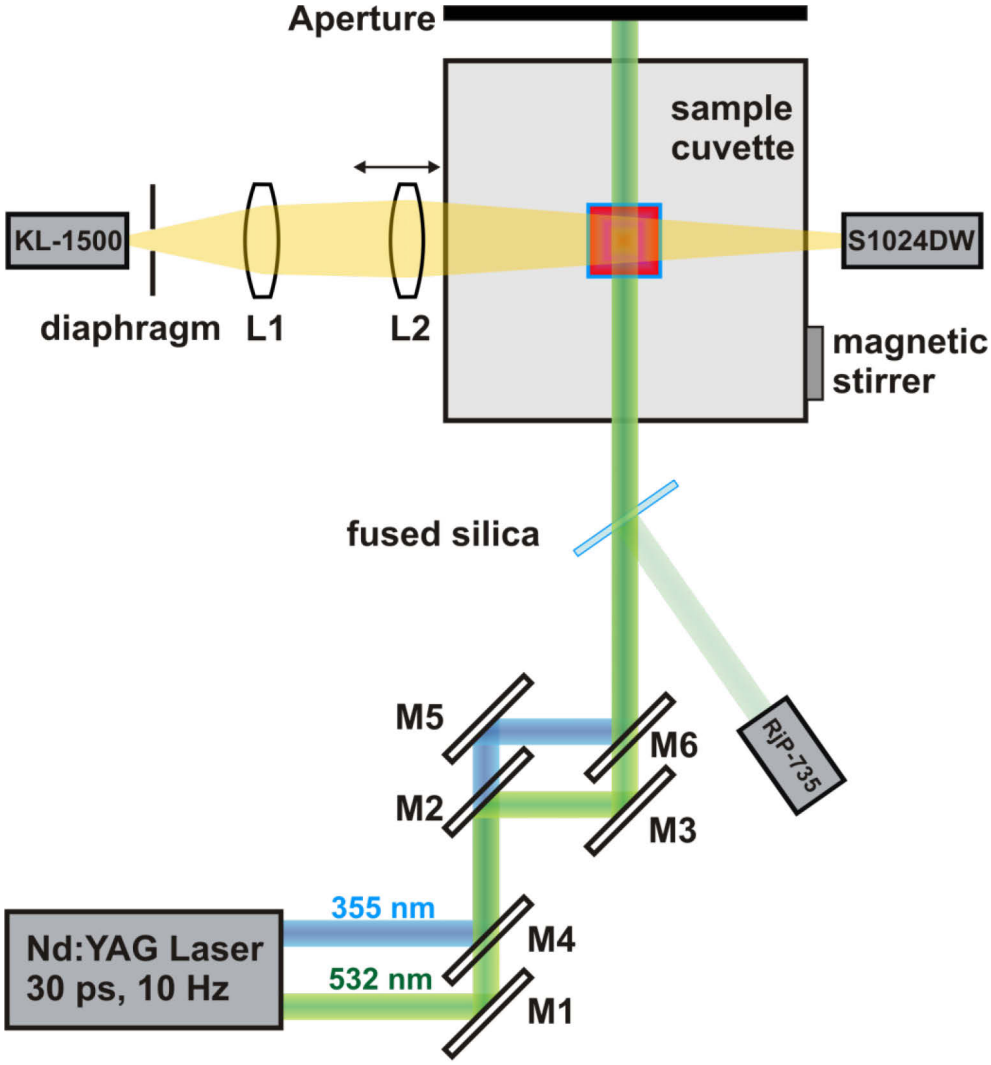

Figure 3.6: *optical setup for the irradiation of metal colloid suspensions with the second (λ_{Ex}=532 nm) and third harmonic (λ_{Ex}=355 nm) of a picosecond Nd:YAG laser*

Data Acquisition: The in-situ spectra for each time were saved by the spectrometer in ASCII format. The data was afterwards imported and automatically displayed by Igor Pro (Version 5.02, Wavemetrics Inc., Portland, USA) using a self-written procedure.

3.2.2 Dynamic Light Scattering (DLS)

Dynamic light-scattering (DLS), also known as photon-correlation spectroscopy (PCS), has become a mature and popular method to characterize the dynamics of particulate materials either in solution or suspension.[32, 33] By determining the diffusion rate information regarding the size distribution of small particles, the conformation of macromolecular chains or various interactions among the constituents in a solution or suspension can be obtained without the need for a calibration. In a typical dynamic light scattering experiment the intensity fluctuations of coherent monochromatic laser light scattered by molecules or particles in a medium is recorded as a function of time at a fixed position and analyzed in the correlation delay time domain. A modern DLS apparatus often utilizes fiber optics guides to both deliver

the light to the sample and collect the scattered light and direct it to the detector. The scatterers can be anything that has a different refractive index than the medium and is stable throughout the duration of the experiment. If all scatterers in the medium were stationary the amount of light scattered in all directions would be constant over time. However all of them are executing Brownian thermal motion so that their relative positions randomly change in relation to the fixed position of the detector. This motion causes different magnitudes of constructive and destructive interference called a speckle pattern on the detector. Since the particles continuously rearrange their configurations fluctuations in the speckle and thus in the scattering intensity arises. The faster the scatterers diffuse, the faster the intensity will change. Since the diffusion rate is determined by their sizes in a given environment information about their size is also contained in the fluctuations. The scattered intensity itself is a stochastic signal and in order to extract useful information its time correlation function has to be computed. This is usually done using an autocorrelator and this is the reason that the method is also called photon-correlation spectroscopy (PCS). For a given scattering angle ϑ with a given scattering vector **q** the normalized intensity time autocorrelation function of the scattered light $g^{(2)}(q,\tau)$ may be written as

$$g^{(2)}(q,\tau) = \frac{\langle I(q,t)\, I(q,t+\tau)\rangle}{\langle I(q,t)\rangle^2} \tag{3.1}$$

with

$$\langle I(q,t)\, I(q,t+\tau)\rangle = \lim_{T\to\infty} \tfrac{1}{T} \int_0^T I(q,t)\, I(q,t+\tau)\, dt \tag{3.2}$$

where $I(q,t)$ and $I(q,t+\tau)$ are the scattering intensities at time t and $t+\tau$ respectively, q is the magnitude of the scattering vector **q** and the angle brackets indicate averaging over t. The scattering vector is defined as the difference between the incident wave vector $\mathbf{k_i}$ and the scattered wave vector $\mathbf{k_s}$ and its magnitude depends on the scattering angle ϑ and the wavelength λ of the light in the scattering medium:

$$q = \left(\frac{4\pi \cdot n}{\lambda}\right) \cdot \sin\left(\frac{\theta}{2}\right) \tag{3.3}$$

In most cases of practical interest the intensity time autocorrelation function may also be expressed in terms of the field time autocorrelation function $g^{(1)}(q,\tau)$ as

$$g^{(2)}(q,\tau) = 1 + \gamma\left[g^{(1)}(q,\tau)\right]^2 \tag{3.4}$$

with $g^{(1)}(q,\tau)$

$$g^{(1)}(q,\tau) = \frac{E\langle I(q,t)\, E^*(q,t+\tau)\rangle}{\langle E(q,t)\, E^*(q,t)\rangle} \tag{3.5}$$

where $E(q,t)$ and $E(q,t+\tau)$ are the scattered electric fields at time t and $t+\tau$ respectively and γ is a factor that depends on the experimental geometry. This relation between the two autocorrelation functions is known as the Siegert-relation.[33] In an ideal apparatus, the constant γ, often called the *"coherence factor",* is equal to 1, so that, in such a case the normalized intensity autocorrelation function starts at a value of 2 at zero time delay and eventually decays to 1. In practice, γ is usually < 1,[34] but by performing light scattering experiments with single mode fiber detection it is almost 1. In this case only one speckle is observed.

In the simplest case of monodisperse particles in dilute solution the field correlation function decays exponentially, $g^{(1)}(q,\tau)=\exp(-\Gamma\tau)$ with a decay rate of $\Gamma=Dq^2$, where D is the diffusion coefficient of the particles. When the viscosity of the liquid η is known, D gives the hydrodynamic radius r_h of the spherical particles by the Stokes-Einstein relation:

$$D = \frac{k_B T}{6\pi\eta r_h} \tag{3.6}$$

where k_B is the Boltzmann constant and T the absolute temperature of the system. In more general cases for polydisperse samples $g^{(1)}(q,\tau)$ can no longer be represented as a single exponential function and must be represented as a sum or an integral over a distribution of decay rates. For solving this problem inverse Laplace-transformation (ITS) is used which can be analyzed by different existing algorithms (e.g. CONTIN[35, 36] or NNLS). For the interpretation of the quality of the measured samples the autocorrelation functions are often normalized with the help of a stretched exponential function in the form of:

$$g^{(1)}(q,\tau) = \left(\exp\left(-Dq^2\tau\right)\right)^{\beta} \tag{3.7}$$

where the parameter β with $0 < \beta \leq 1$ describes the deviation to the mono-exponential decay. This is called the Kohlrausch-Williams-Watts (KWW) analysis.[37, 38]

DLS Setup: All DLS experiments in this thesis were performed by [in printed version available] on a setup built in-house at the MPI-P. The setup is briefly described in the following: The intensity auto-correlation functions $g^{(2)}(q,\tau)$ were recorded by an ALV-5000E digital full correlator (ALV, Langen, Germany) at a scattering angle of ϑ=90° using a Helium-Neon laser (JDS Uniphase, Milpitas, USA) operating at λ=633 nm and 2 mW intensity on the sample. The detection was performed in pseudo-cross-correlation mode using two avalanche photodiodes (SPCM-AQR-14, Perkin-Elmer) in order to remove unwanted contributions from correlated after-pulses inherent in this type of detector. The main underlying assumption is the statistical independence of the nonlinear effects in both detectors. The scattered light from the sample was directed to the photo detectors by a Y-single mode fiber forming a 50/50 fiber beam splitter (Schäfter+Kirchhoff – SuK, Hamburg,

Germany). The incident and detected light were polarized both vertical to the scattering plane. A schematic of the whole setup is shown in Figure 3.7.

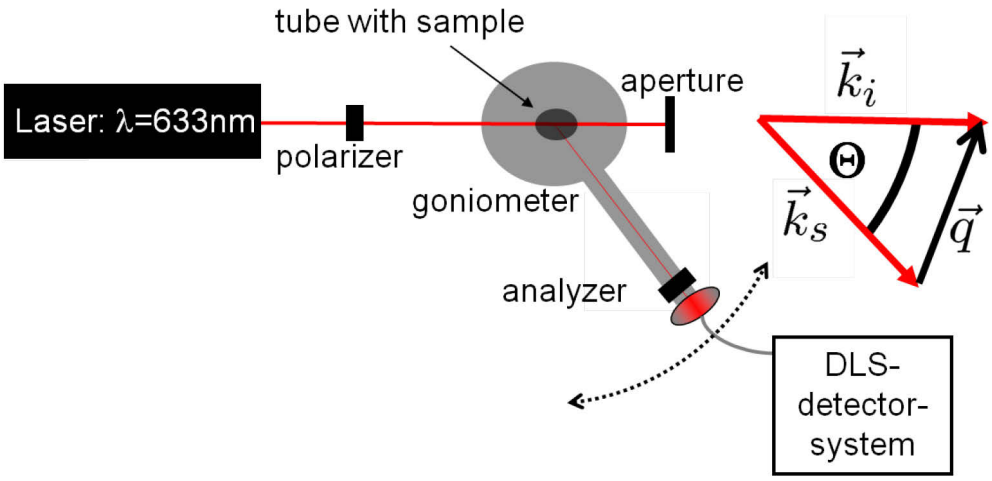

Figure 3.7: *Schematic presentation of the in-house built DLS setup.*[39]

All sample solutions for DLS were prepared by filtering the nanoparticle suspensions with a 0.25 µm PTFE syringe-filter (Millipore, Billerica, USA). The suspensions were equilibrated to 20 °C. Literature values for the refractive index and viscosity were used.[40]

DLS Data Acquisition: Data analysis was performed using the CONTIN[35, 36] inverse Laplace fitting routing and the KWW method[37, 38] in the correlator software from ALV (Version 3.025). The $g^{(2)}(q,\tau)$ curves were normalized to a contrast of 1. The processed data was exported in ASCII format and loaded into Igor Pro (Version 5.02, Wavemetrics Inc., Portland, USA).

3.2.3 Scanning Confocal Optical Microscopy (SCOM)

Optical Microscopy is widely used in several scientific areas where the domain of interest lies in the sub-micrometer to micrometer range. Since the important length-scales are in the order of the visible light, microscopy provides a powerful inexpensive tool to obtain real-space and real-time information of the investigated systems. The ease of sample preparation at room temperature and atmospheric pressure are further advantages. However, certain drawbacks exist for complex sample structures that interact with the light; the most prominent one being multiple scattering. Light coming from the image plane is clouded by aberrant rays of light coming from other point of the sample out of focus resulting in blurriness of the image which is shown in Figure 3.8 (a, c, e).

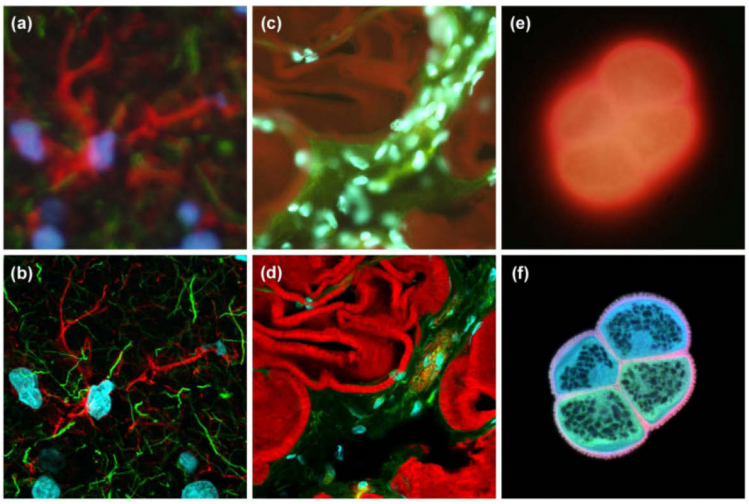

Figure 3.8: *(a,c,e) Widefield fluorescence microscopy and (b,d,f) corresponding laser scanning confocal microscopy*[41]

Marvin Minsky found in 1955 a simple and elegant solution for this problem as he tried to visualize the way nerve cells connected in the human nervous system: the confocal arrangement.[42, 43] First a light source is spatially filtered by an illumination pinhole and imaged onto a diffraction-limited spot on the sample. Second the multiple scattering of some extra rays coming from different points of the sample is filtered by a detection pinhole so that only light from the focal spot reaches the detector. The principle is depicted in Figure 3.9[44] for the example of the symmetric configuration with two lenses.

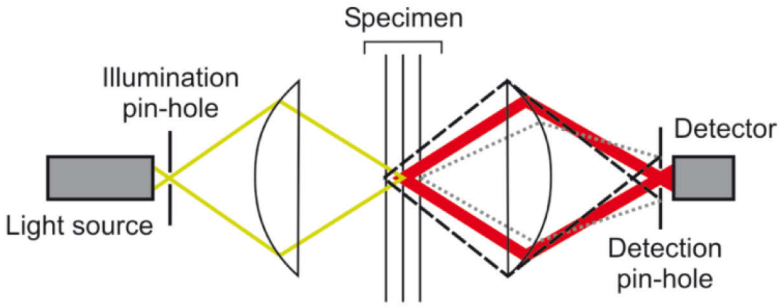

Figure 3.9: *Confocal principle*[44]

As a consequence the amount of light in the specimen is reduced by orders of magnitude, without reducing the focal brightness which is important in fluorescence experiments to prevent photo-bleaching. The word "*confocal*" seems to have been first used by Brakenhoff[45] and others in 1979 to take into account that the focal planes of the illumination and imaging systems are coincident contrary to conventional wide-field microscopy where the foci of illumination and imaging are usually in each other's conjugated planes. A comparison between the typical illumination cones of a widefield and point scanning confocal microscope is presented in Figure 3.10.[41]

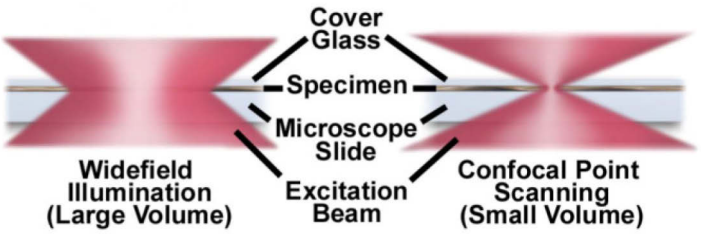

Figure 3.10: *Widefield versus confocal microscopy illumination volumes, demonstrating the difference in size between point scanning and widefield excitation light beams*[41]

In widefield microscopy the entire depth of the specimen over a large volume is illuminated, while the sample is illuminated in confocal microscopy with a finely focused spot of illumination that is centered in the focal plane. As only one spot in the sample is illuminated at a time, the sample needs to be scanned point-by-point to increase the field of view and obtain an image. The result of this arrangement is shown in in Figure 3.8 (b, d, e). The scanned images have less haze and better contrast than that of the conventional microscope and represent a thin cross-section of the specimen. This approach does not only produce images of exceptional resolution, but also allows the user to collect optical slices of the object and use them to create a three dimensional representation of the sample. If the plane of focus is changed, or the object moved, a series of images at different positions can be produced through the thickness of the object. Confocal microscopes are usually classified by the method in which the scanning is performed. The alternatives are either to scan the sample mechanically across a stationary focused light spot, or to scan the focused light beam across a stationary sample. In the first case scanning is really slow, but as the optical path remains stationary, undistorted images of very high quality are produced. Stage scanning confocal microscopes have evolved into instruments that are used traditionally for materials science applications such as the microchip industry. In the second case scanning is very fast compared to the first case and many images per second can be acquired, which is more practical for imaging biological samples.

In optical microscopy the relationship between contrast and resolution with regard to the ability to distinguish two closely space specimen features implies that resolution cannot be defined without reference to contrast. Resolution is one of the clean concepts in physics that can be described, measured and manipulated according to rules derived from geometry of the system. Contrast, on the other hand, is related to the reality of real measurements that limits the ability to use the available resolution. The well-known Rayleigh criterion[46] for resolution states that under the best circumstances two closely spaced points can be distinguished when the lateral distance R_{Airy} between the two in the image plane is larger than:

$$R_{Airy} = \frac{0.61 \cdot \lambda}{n \cdot \sin\theta} \tag{3.8}$$

where λ is the wavelength of the illumination in the space between object and objective lens, n is the corresponding refractive index and θ is the half angle of the cone of light converging to an illuminated spot or diverging from one. The term in the denominator is also called the "*numerical aperture*" *NA*. *NA* describes the angular behavior of the light cone, and it is that which governs the imaging. The Rayleigh criterion separation distance corresponds to a contrast value of 26.4 percent.[47] The confocal approach slightly improves the resolution, but the dramatic difference in resolution enhancement has more to do with the fact that with point-wise illumination and detection the image is formed from the convolution of the two diffraction patterns. This gives rise to a sharpened central peak and weaker outer rings, as shown in Figure 3.11.[47]

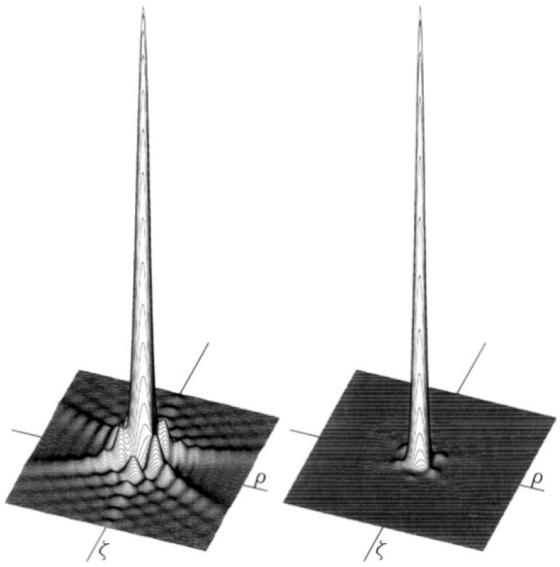

Figure 3.11: *(left) Diffraction pattern in conventional microscopy, (right) diffraction pattern in confocal microcopy*[47]

The actual extent of improvement depends on the size of the pinhole. Near-maximal axial resolution is obtained with a pinhole radius of $\sim 0.7 \times R_{Airy}=R_{confocal}$, whereas optimal lateral resolution is obtained with a pinhole smaller than $0.3 \times R_{Airy}$. However, a pinhole smaller than $\sim 0.7 \times R_{Airy}$ significantly reduces the total signal, a sacrifice that may not be worth the gain in resolution, especially when imaging dim samples. There are various types of confocal microscopes, and the most popular ones are reflection microscopes, dark-field microscopes and fluorescence microscopes. The principle of dark-field microscopy will be explained in detail in Chapter 5 while in Figure 3.12[48] a schematic of a confocal microscope in fluorescence operation mode is shown. Coherent light emitted by a laser system passes through a pinhole aperture that is situated in a conjugate plane with a scanning point on the specimen and a second pinhole aperture positioned in front of a photomultiplier tube. As the laser is reflected by a dichromatic mirror and scanned across the specimen in a defined

focal plane, secondary fluorescence emitted from points on the specimen (in the same focal plane) passes back through the dichromatic mirror and is focused as a confocal point at the detector pinhole aperture. Light reflected by the sample and coming directly from the laser is blocked by a fluorescence filter in front of the detector.

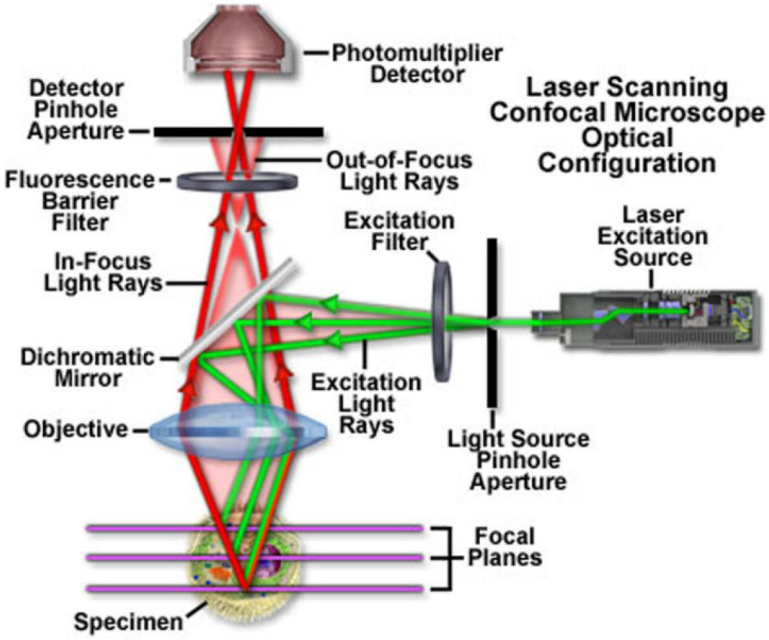

Figure 3.12: *Schematic of a fluorescence confocal microscope.*[48]

In the last years scanning confocal microscopy has become an invaluable tool for a wide range of investigations in the biological and medical sciences for imaging thin optical sections in living and fixed specimens ranging in thickness up to 100 micrometers. This includes for example the live imaging of cells or tissue where the green fluorescent protein (GFP)[49-51] or other dyes can be used to track intracellular protein movement by attaching them to the proteins of interest.

Confocal Microscope Setup: The confocal microscope was designed and constructed by Fernando Stefani[44] to perform fluorescence and light scattering experiments and is depicted in Figure 3.13.[44] A number of light sources can be used to supply excitation light. The light is coupled into a fiber, collimated and then focused onto the samples by an oil-immersed high NA objective. The sample is studied at one spot at a time and in order to make an image, the sample needs to be raster scanned over the focus pixel by pixel. The scattered light is collected by the same objective and then directed through a confocal arrangement to the detector or the spectrometer. The details of its performance and design can be found in his dissertation.[44] If not otherwise indicated all measurements were performed in this configuration.

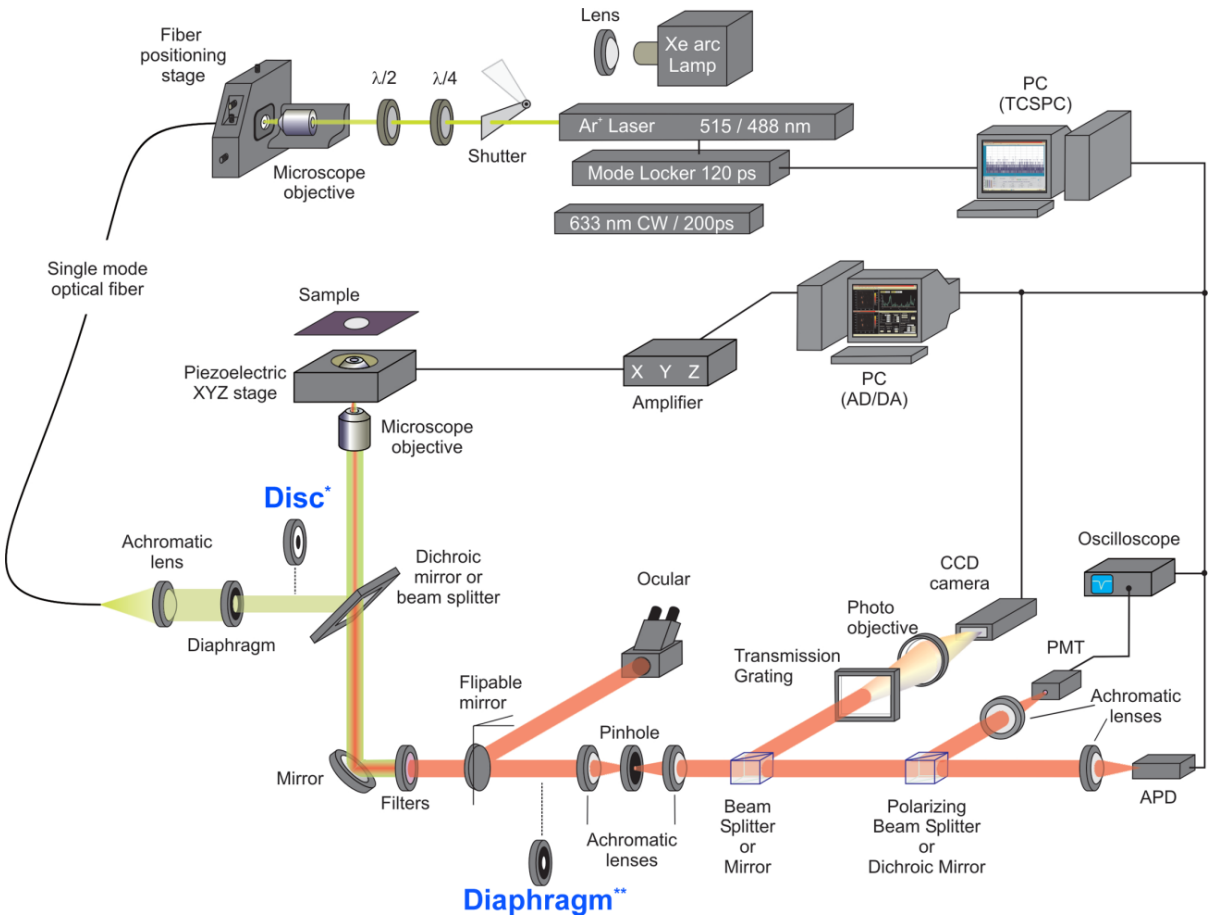

Figure 3.13: *Schematic of the home-built confocal microscope*[44]

However, this original design had some flaws in terms of thermal and mechanical stability which resulted in problems during measurements. The main reasons for the instabilities were the use of highly floating optical elements with aluminum rods screwed to the optical table and non-orthogonal beam adjusters.[52]

Therefore these adjustment elements were separated for the excitation and detection and a rail based system (Owis Sys 65, Owis GmbH, Staufen, Germany) was chosen as the basic mechanical setup. This system comes with 65 mm broad and 22 mm thick rails. The beam height is 65 mm over the mounting area of the rails. Optics up to 40 mm diameter can be integrated. The rails were mounted on massive aluminum blocks of 120 mm height to maintain the compatibility both with the existing light sources and detectors. Only materials with similar thermal expansion coefficient were used to minimize strain. A photography of the whole setup after the re-design is shown in Figure 3.14

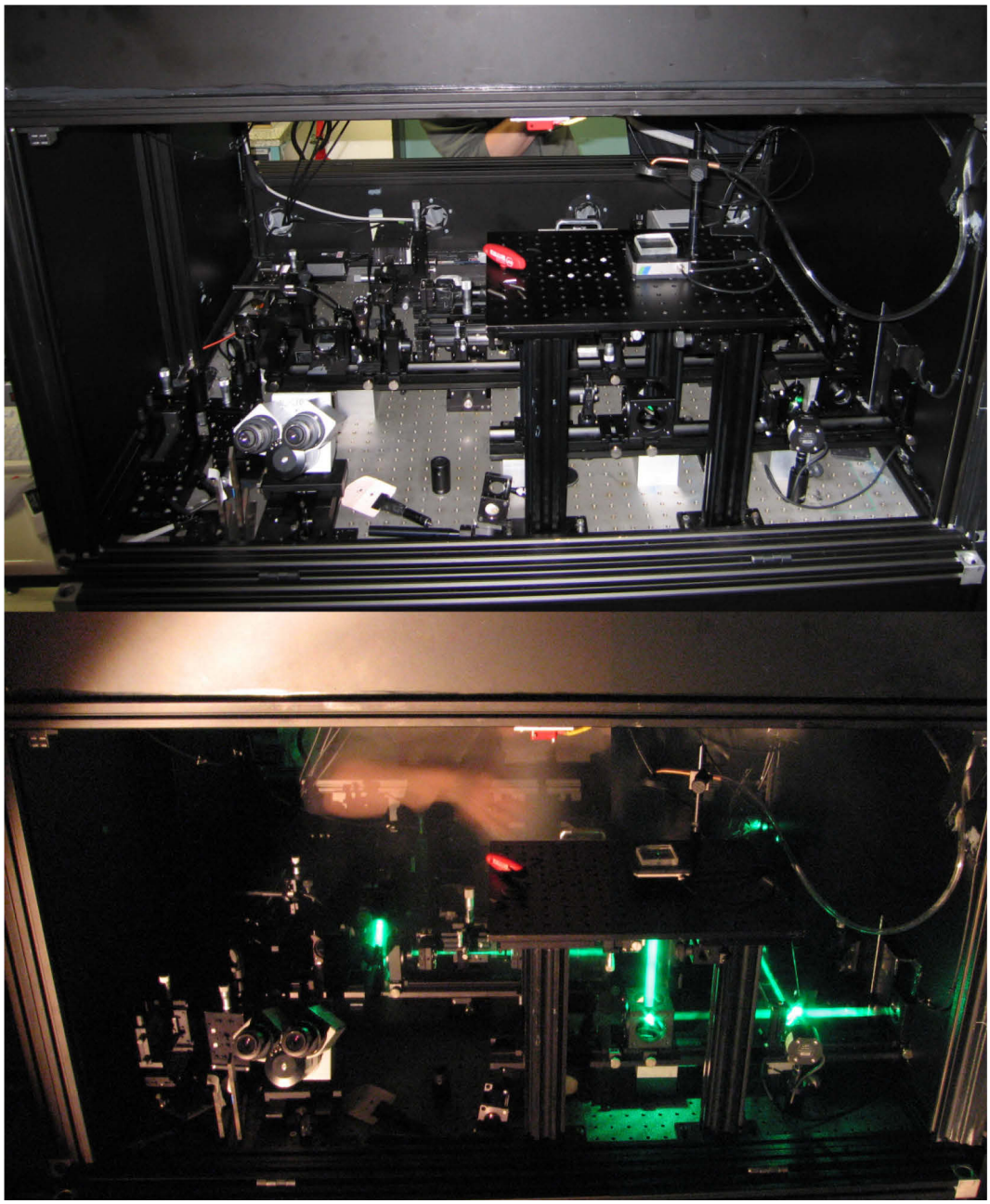

Figure 3.14: *(top) Photography of the optimized confocal microscope, (bottom) same picture under laser illumination, the whole setup is covered in a box to shield the sensitive detectors from stray light.*

The photography can be directly compared with the schematic in Figure 3.15.[52] The colored lines show the different beam paths with red the excitation, blue the visible detection and orange the infrared (IR) detection path which was not used in this work. The dark green path is used for spectroscopy. The remaining colors are additional path which are either not used in this work. The dashed lines are beam diagnosis path which are used for alignment of the instrument. The linear block for the dark-field experiments was placed in the light path directly after the beam-splitter with the number 5 and the optics with the number 3 and 7 was not used in this work.

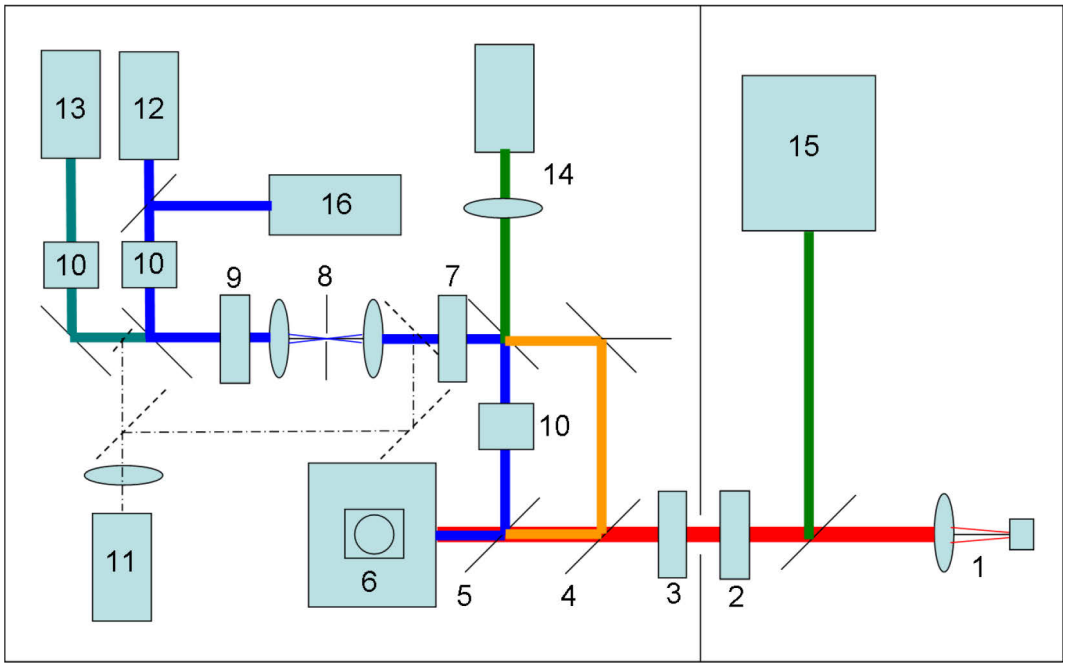

Figure 3.15: *Arrangement of components for the re-designed confocal microscope (roughly to scale, the size of the optical table is 2x1.5m)*[52]

The numbered components in Figure 3.15 correspond to:

1. fiber coupler and collimator for fiber coupled light sources (lasers and arc lamp)
2. Glan-Thompson polarizing prism (PGT 2.20)
3. spatial beam shaping (e.g. for annular illumination)
4. IR beam-splitter
5. VIS/NIR beam-splitter
6. microscope table with piezoelectric scanner and microscope objective
7. spatial beam shaping optics (e.g. iris aperture to block direct light)
8. confocal pinhole
9. Glan-Thompson polarizing prism (PGT 2.15)
10. spectral filtering
11. ocular for monitoring and diagnosis of all beam paths
12. avalanche photodiode for scanning
13. fiber coupler to the grating spectrometer
14. CCD for wide field imaging
15. ultrafast laser system, free space coupled
16. NIR photomultiplier tube for NIR scanning

Sample Preparation: The metal films of the prepared samples were scratched directly before a measurement with a cannula (0.6 x 50 mm) in the shape of an asymmetric cross with an opening angle of approx. 30° and scratch thickness of 20 µm to facilitate alignment of the optical, electron and atomic force images. A schematic of the scratched substrate together with a photography of an exemplary sample is presented in Figure 3.16. The gold point in (b) originated from the sample holder of the evaporation machine and was used as a guide for the further orientation of the sample in all microscopic methods.

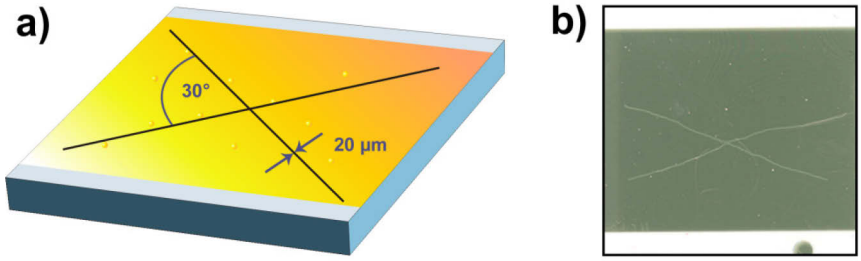

Figure 3.16: *(a) Cartoon of the scratches, (b) photography of real sample*

For sample alignment in the confocal microscope the beam diameter of the He-Ne laser coming from the fiber was reduced with a pinhole to a small spot while the sample was illuminated at the same time from the top with a white light in Köhler illumination. After a support with a millimeter paper was introduced into the beam between objective and beam splitter both the scratches in the metal film and the laser spot from the illumination source were imaged on the paper by eye.

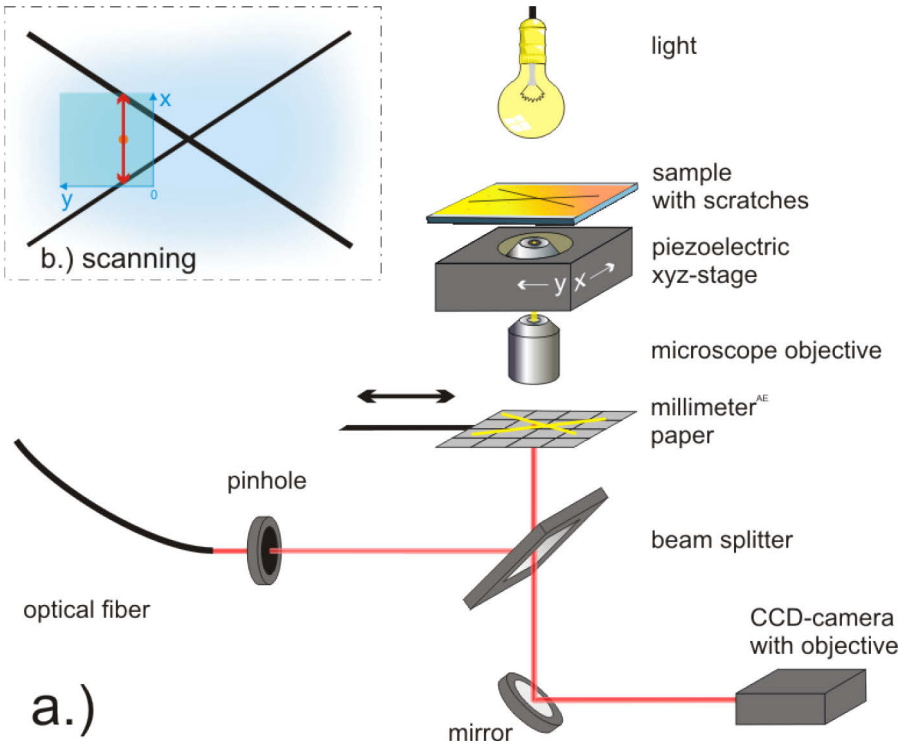

Figure 3.17: *(a) Demonstration of the sample alignment, (b) maximal scan range in blue; the piezo scanner follows the red line and after sample alignment the laser hits the scratches on both sides*

The piezoelectric stage was started to perform a line scan with the maximum possible scan range in x direction at approximately one third of the possible scan range in y-direction. In this way the movement of the scratches in relation to the laser spot was observed and the sample could be aligned such that both scratches on each side are just met by the laser. If necessary the result could be controlled with the CCD camera in the detection pathway imaging the focal plane of the confocal microscope. The whole process is depicted in Figure 3.17. After the process was finished successfully all samples were either investigated by dark-field or fluorescence microscopy.

Dark-field spectroscopy: For dark-field spectroscopy, a plasmon mediated dark field mode was used with a fiber-coupled CCD spectrometer (Andor Shamrock SR303i, Andor Technology, Belfast, Northern Ireland). This operation mode is described in detail later. Light from a He-Ne laser (633 nm) or a Xenon lamp (Osram XBO 150) was coupled into an optical single mode fiber, acting as a point-like light source and providing a divergent beam with an approximately Gaussian profile (TEM_{00}-mode). The illumination beam was collimated by an achromatic lens (f=100 mm) and directed to an oil immersion ($n_{glass}=n_{oil}=1.503$) microscope objective (60x, NA=1.4, Plan-Apo, Nikon GmbH) by a 50/50 beam splitter (Owis GmbH, Staufen, Germany). In the focus of the objective the sample was mounted on top of a piezoelectric stage (Tritor 101 CAP, Piezosystems GmbH, Jena, Germany). The scattered light from the sample was collected by the same objective and separated from the illumination beam by the splitter. After its way through a confocal arrangement (2x lenses, f=100 mm, 100 µm pinhole) the remaining light was focused (lens, f=30 mm) for scanning onto an avalanche photo diode (APD) (Perkin Elmer, Optoelectronics Inc., USA) or into a fiber connected to the CCD spectrometer for spectral analysis.

For light scattering measurements in the original setup, two blocks were symmetrically inserted into the beam before the beam splitter and the confocal arrangement to realize dark field conditions. The light was polarized in directions perpendicular or parallel to the block in the illumination pathway by a thin sheet polarizer (LINOS Photonics GmbH & Co. KG, Göttingen, Germany). In order to image the radiation patterns of the scattering objects the confocal pinhole was removed and the back focal plane of the microscope objective was imaged in the block plane and again on the chip of a CCD device (uEye UI-2250-M-GL, IDS Imaging Development Systems GmbH, Obersulm, Germany) by a suited combination of lenses.

In the new designed setup only one block between the microscope objective and a broadband beam splitter plate (LINOS Photonics GmbH & Co. KG) was used. The polarizer in the illumination was replaced by a Glan-Thompson polarizing prism (PGT 2.20, Bernhard Halle Nachfolger GmbH, Berlin, Germany) and a second polarizer (PGT 2.15, Bernhard Halle

Nachfolger GmbH) was added in the detection pathway after the confocal arrangement which polarized the light during the spectroscopy measurements of individual particles perpendicular to the one in the illumination pathway.

For taking particle spectra, Xenon illumination was used coming from a multimode fiber. The piezoelectric stage of the confocal microscope was moved to a position of an identified particle and the light of this position *I(*Obj*)* analyzed for suitable time by the spectrometer. As a reference for the gold film *I(*Ref*)* the procedure was repeated with the same time for a clean position in the vicinity of the particle. After measuring all selected particles the background count *I(*Dark*)* was determined with a closed lamp shutter and the lamp spectrum *I(*Xe*)* with a mirror as sample. From this, spectra for an object

$$\sigma_O = \frac{I(\text{Obj}) - I(\text{Dark})}{I(\text{Xe}) - I(\text{Dark})} \tag{3.9}$$

and the associated reference

$$\sigma_R = \frac{I(\text{Ref}) - I(\text{Dark})}{I(\text{Xe}) - I(\text{Dark})} \tag{3.10}$$

were obtained, yielding a scattering strength of one particle σ

$$\sigma = \sigma_O - \sigma_R = \frac{I(\text{Obj}) - I(\text{Ref})}{I(\text{Xe}) - I(\text{Dark})} \tag{3.11}$$

Fluorescence Spectroscopy: For fluorescence spectroscopy, light from a 532 nm diode laser (pumped solid state Nd:YAG, GCL-005-L, Crysta-Laser, Reno, USA) in combination with a 532 nm line filter (XL08 532NB3, Omega Optical Inc., Brattleboro, USA) and 620 nm short-pass filter (3RD620SP, Omega Optical Inc.) was used for illumination. In the detection pathway, a 532 nm notch (RazorEdge NF01-532U-25, Semrock, Rochester, USA) and 532 nm long pass filter (RazorEdge LP03-532RU-25, Semrock) blocked all of the illumination light. The remaining fluorescence light was analyzed by the same fiber-coupled CCD spectrometer. During measurement, the sample was exposed to a constant flow of nitrogen in order to avoid oxidation of the dye.

Data Acquisition: The obtained data from the spectrometer was saved in ASCII format and afterwards analyzed by a self-written procedure in Igor Pro (Version 5.02, Wavemetrics Inc., Portland, USA). Spikes in the raw data were removed by careful smoothing using a box function which simply replaces each data value with the average of neighboring values.

3.2.4 Surface Plasmon Spectroscopy

Surface plasmon resonance (SPR) spectroscopy[53-55] is a surface sensitive optical reflection technique which non-invasively monitors changes in the local index of refraction at a metal

surface. The high sensitivity of up to 10^{-5} RIU[54] (refractive index unit) in combination with the label free detection makes it a prominent method in the field of bio-sensing for studying binding events. The detection principle relies on an electron charge density wave oscillation, also called surface plasmon (SP) that arises at the interface between a metal and a dielectric when light is reflected at the film under specific conditions. The surface plasmons have combined electromagnetic wave and surface charge character as shown in Figure 3.18 (a).[56]

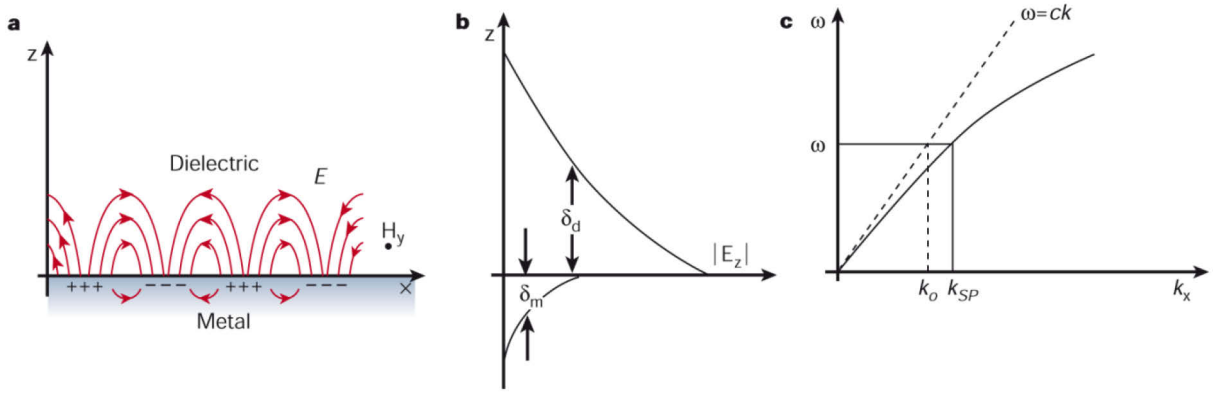

Figure 3.18: *(a) Schematic drawing of the electric field lines and charge distribution associated with a surface plasmon, (b) decay of the electric field in z-direction with distance from the interface, (c) dispersion relation of free photons and surface plasmons*[56]

They are transverse magnetic in character since for the generation of surface charges an electric field normal to the surface is required. The field of the SP is evanescent perpendicular to the surface and decays exponentially into the metal on one side and into the dielectric on the other, see Figure 3.18 (b) In the dielectric medium above the metal, typically air or glass, the decay length of the field δ_d is of the order of half the wavelength of light involved, whereas the decay length into the metal δ_m is much smaller due to the screening effect of the free charges.

Any change in refractive index of the bulk or binding events lead to a shift in the SPR resonance. The excitation of surface plasmons requires a special geometry. It turns out that it is impossible to excite a surface plasmon within a simple reflection experiment. The dispersion curve for a SP mode in Figure 3.18 (c) shows the momentum mismatch problem that must be overcome in order to couple light and SP modes together, with the SP mode always lying beyond the incident light line. A trick helps to fulfill the conditions. If light is incident in a media with a higher refractive index than air the slope of the straight line is decreased and an intersection between the plasmon dispersion relation may occur. This is utilized in the so-called Kretschmann configuration[57, 58] which is shown in Figure 3.19. Angular resolved techniques using a prism in an attenuated total reflectance (ATR) configuration are the most common arrangements, the other methods use grating coupling.[53]

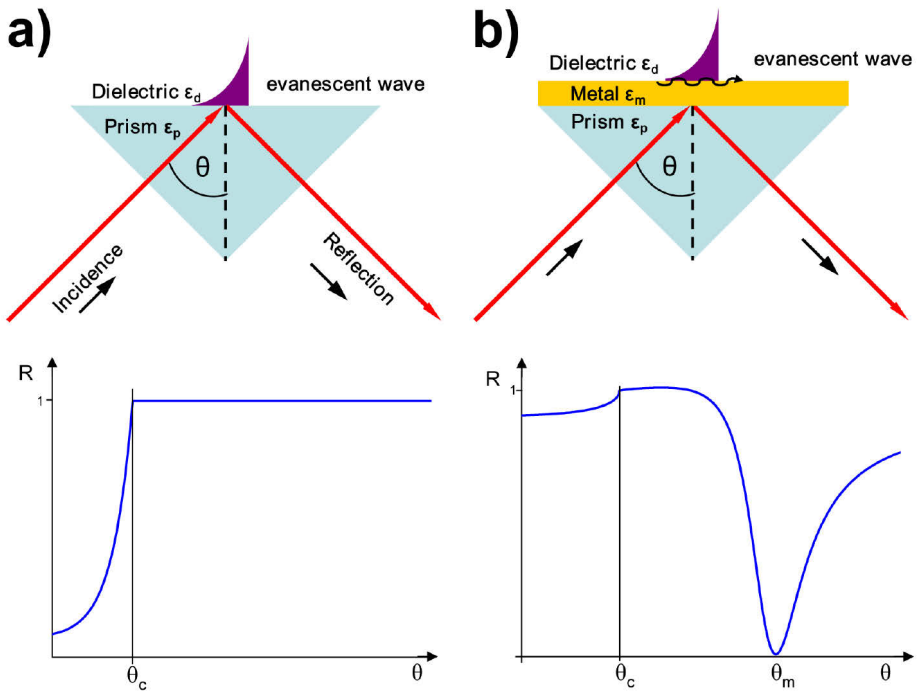

Figure 3.19: *(a) Total internal reflection at a glass prism in contact with a dielectric, (b) attenuated total internal reflectance at a metal film.*[59]

The metal layer is at the base of a prism and the photons are coupled to the metal/dielectric interface via the evanescent light tail of light at the base of a high-index prism. The created evanescent wave propagates along the metal-dielectric interface with a propagation constant that can be adjusted to match that of the surface plasmons by controlling the angle of incidence θ. If parallel monochromatic light is used, reflection under certain incident angles is strongly decreased, because the surface plasmons absorb the irradiated energy. The variation of the incident angle of light shows that the position, width and depth of the characteristic reflection minimum of the surface plasmon resonance strongly depends on the refractive index and the layer thickness of the system.

SPR Setup: For a spectrum of the whole ensemble of a gold sphere-on-plane system the specular reflectivity $R(\theta)$ was measured by [in printed version available] in a home-made surface plasmon spectrometer in Kretschmann configuration[57, 58] at the MPI-P. A halogen lamp and a monochromator (Chromex 250SM scanning monochromator) served as a tunable light source. The beam divergence was controlled by the use of two aperture holes. At the sample position the beam had a divergence of 0.24° and a diameter of 6 mm. The incident light was transverse-magnetically polarized as required for surface plasmon excitation. The reflected light was detected with a photomultiplier (Hamamatsu H6240-01) in photon counting mode. For each wavelength an angular scan was taken. The sample reflectivity $R(\theta)$ was determined by normalizing the reflected light intensity with the incident light intensity which was measured without sample.

SPR Data Acquisition: The analysis of the data based on the fitting of the experimental reflectivity curves to the ones that were modeled by a transfer-matrix algorithm[60] and deduced the dielectric function $\varepsilon_f(\lambda)$ and the thickness d_f of an effective film. Assuming an effective layer of induced dipoles with a polarizability α occupying an area *A*, the Clausius-Mossotti equation[61] was then applied to calculate a polarizability per area. The data analysis was performed in Igor Pro (Version 5.02, Wavemetrics Inc., Portland, USA using a self-written procedure. Each step is described in detail here.[9]

3.2.5 Scanning Electron Microscopy (SEM)

Scanning electron microscopy[62-64] (SEM) is nowadays a standard technique to characterize any nanostructured material. It forms an image of a microscopic region of a specimen surface by the interaction of a probe of electrons with matter. Owing to the great depth of focus, relatively simple image interpretation, and ease of sample preparation, SEM is the preferred technique for viewing specimen details at a resolution well exceeding that of a light microscope. The resolution limit *d* for any microscopic technique is given by Abbe's theory.[65]

$$d = \frac{\lambda}{2 \cdot NA} \tag{3.12}$$

where λ is the wavelength of the illumination in the space between object and objective lens and *NA* is the numerical aperture of the objective lens. For best resolutions, large values of *NA* and short wavelength radiations λ are required. The wavelength of the electrons generated by an electron gun, consisting of an electron source (cathode) and an accelerating anode is given by the de Broglie wavelength

$$\lambda = \frac{h}{m \cdot v} \tag{3.13}$$

where *h* is Planck's constant, *m* the electron mass, and *v* its velocity. The electron velocity is related to the applied electrostatic potential ϕ through which it has been accelerated at the anode by equating the kinetic energy to potential energy:

$$v = \sqrt{\frac{2 \cdot e \cdot \phi}{m}} \tag{3.14}$$

where *e* is the electron charge. Hence the electron wavelength allows with

$$\lambda = \frac{h}{\sqrt{2 \cdot e \cdot m \cdot \phi}} \tag{3.15}$$

for extraordinary high resolution as the electrostatic potential ranges between 0.1 to 30 kV and the obtained wavelengths are far smaller than that of light. Increasing the accelerating

voltage shortens the wavelength and thus increases the resolution. However, the cross-section for electron interaction with matter is greater at lower electron energies and thus one generally gets better image contrast at lower acceleration voltage.

The main function of the SEM illumination system is to produce a high intensity, finely focused beam of a small diameter, which is subsequently scanned over the specimen surface. This is accomplished by reducing an image of the electron source onto the specimen surface using objective lenses in the microscope column. The focused beam is scanned sequentially over the specimen surface in a regular raster under the control of electromagnetic scan coils. The image is formed by collecting a particular type of signal as a function of the two dimensional beam position on the sample.

When the incident electron beam impinges on the sample, a large number of secondary electrons (SE) are produced by removing bound electrons from the solid. This inelastic process causes the primary beam to lose energy, but since the energy required for secondary-electron production is very low, the cascade from a primary electron can produce a large number of secondary electrons. Secondary electrons have energies lower than 50 eV and can therefore leave the sample surface only within a very thin layer at the surface (1-10 nm). This results in a high resolution, both laterally and in depth, and is used for topographic images of the specimen. A second signal arises from Rutherford scattering of the primary beam when the incident electron interacts with the nucleus of an atom in the specimen. A fraction of the primary electrons undergoing Rutherford scattering is deviated through angles sufficiently large to travel back toward the surface of the specimen and escape with energy close to that of the primary beam (backscattering). These backscattered electrons (BSE) have much higher energies (> 50 eV) and are measured with a different detector. BSE contain information about the material composition and show atomic number contrast. The backscattering coefficient has a positive relationship with the atomic number. Most polymers are not suitable for BE studies because they have a poor contrast due to containing only carbon and hydrogen atoms. The BSE do not show the parts of the specimen surface that are shielded from the collector. This effect can be used to study the topography of rough surfaces. However, the resolution is overall inferior when compared to SE. A third image technique is x-ray elemental mapping, which relies on characteristic x-ray emission (X) from excited atoms. This occurs when an inner shell electron is removed from an atom by a high energy electron and the excited atom return to its ground state by emission of a photon in the x-ray region. Alternatively Auger electrons (AE) can be ejected when the superfluous energy is transferred to another electron. The wavelength and hence the energy of the x-ray photon or the Auger electron is characteristic of the excited atomic species. By setting the detector to a particular energy, the spatial variation of the concentration of that element in the object can be imagined.

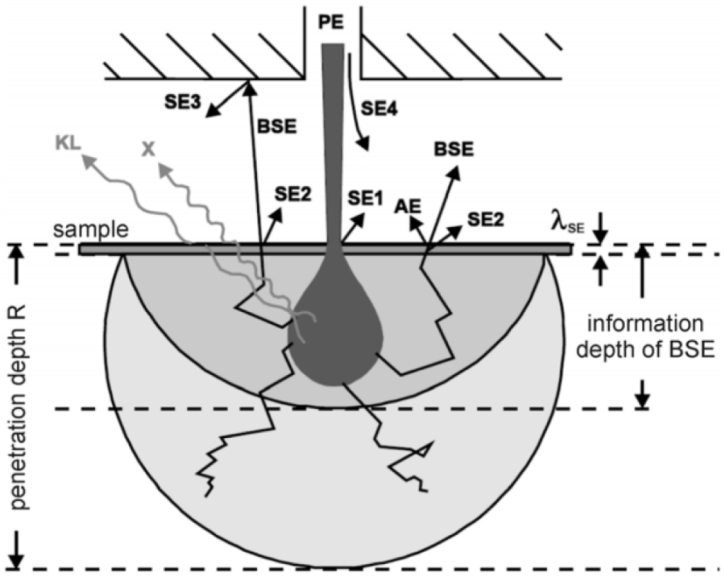

Figure 3.20: *A high electron beam hits the sample surface. Secondary electrons (SE), backscattered electrons (BSE) and Auger electrons (AE) are generated by the interaction with the surface. Cathode luminescence (KL) and X-rays (X) are also present.*[66]

The incident beam penetrates to a significant depth in the specimen before its energy falls below the threshold for the production of the various types of signals. The size and shape of this signal generation depends on the primary beam energy, the electron probe size, and the average atomic number and density of the material. The essential features are depicted in Figure 3.20.[66] Secondary Electrons (SE) of first order (SE1) are generated by the interaction with the primary beam, while larger orders (SE2, SE3, SE4) are only created by backscattered electrons. As this is not limited to the surface they normally are responsible for background noise. Depending on the applied voltage a distinction between conventional and low voltage SEM (< 5 kV) can be drawn.[67] Measurements at low accelerating voltages have the advantage that this drastically reduces both the background noise due to the beam spreading effects and charging artifacts. Furthermore it minimizes beam damages to the sample.

SEM Image Acquisition: SEM images were recorded on a LEO Gemini 1530 (Zeiss, Oberkochen, Germany) using an In-Lens detector system[68] to gain mainly information about the dimensions and shapes of nanoparticles. The low-energy secondary electrons generated at the impact point of the primary beam are intercepted by the weak electric field at the sample surface, then accelerated by the field of the electrostatic lens and focused on the annular SE detector inside the beam booster located above the objective lens, see Figure 3.21.

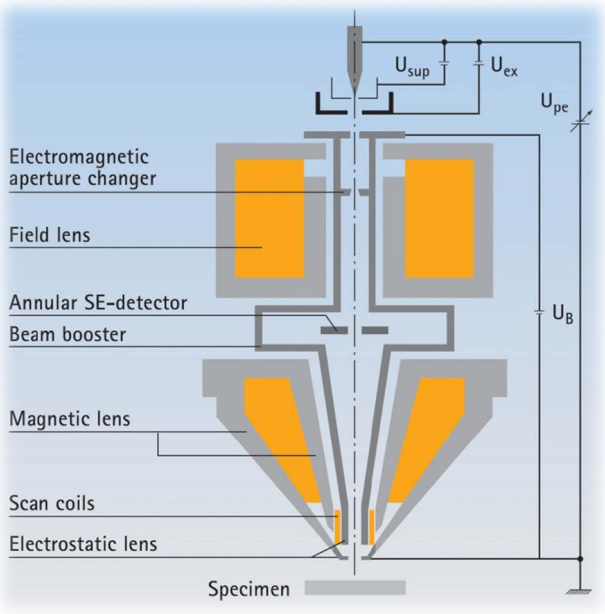

Figure 3.21: *Main electron optical components in the Gemini column*[69]

As a result high contrast images are easily achieved, even from the lowest secondary electron escape depth and energy. Another characteristic of the Gemini system is the before mentioned beam booster[68] in the column which maintains a beam energy in the 10 kV range throughout the full length of the column, even if much lower probe energies are selected. Only after passing through the scanning system located in the pole-piece gap of the objective lens, the beam is decelerated to its final landing energy. This approach provides several advantages such that the sensitivity to the environment is minimized and the beam broadening is further reduced by intercepting all superfluous electrons. The instrument has therefore an outstanding resolution, particularly at low beam energies (3 nm achievable at 1 keV).[68] In all cases native, non-sputtered samples were used while the acceleration voltage ranged from 0.5 to 2 kV. For nanoparticle identification images were first taken at lower magnification of approximate 6000x to locate the region of interest at the scratches of the sample surface and align the SEM field with the optical dark field, atomic force or fluorescence images. Once the locations of the nanoparticles were confirmed the magnification was increased up to 361000x in order to capture high-resolution images of the desired particles.

SEM Particle Evaluation: The dimensions of each particle was determined by manual picture evaluation using the quick selection tool and the analysis function of the software Photoshop CS4 (Adobe, San Jose, USA). Together with other parameters the particle dimensions are determined by counting the pixels representing the particle in the 8-bit gray scale image and multiplying it with the pixel size in nanometers squared provided by the SEM.

3.2.6 Atomic Force Microscopy (AFM)

Atomic force microscopy (AFM) invented by Binning *et al.*[70] has evolved into a useful tool to image and measure the surface morphology of materials down to the nano-scale as it can be used in a broad spectrum of applications such as electronics, chemistry, biology and material science.[71-74] The AFM working principle is the measurement of the interactive force between a tip and the sample surface using special probes made by an elastic cantilever with a sharp tip on the end. The whole cantilever usually made from silicon or silicon nitride acts as a type of spring with a very low spring constant and is fabricated by semi-conductor processing techniques. The local attractive or repulsive force between the tip and the sample is converted into a positive or negative bending of the cantilever which is detected by the deflection of a laser beam focused on the backside of the cantilever and hitting a photodiode with four quadrants. The laser spot position is then calculated in the lateral and vertical direction by comparing the signals in the different quadrants.

If the tip is in analogy to SEM scanned over the sample surface the deflection of the cantilever can be recorded as an image, which represents in its simplest form the three dimensional shape of the sample surface. Alternatively, it is possible to maintain a constant force on the cantilever by a feedback system (FS) by using Hooke's law and adjusting the z-position of the sample. As the tip is raster-scanned over the surface this technique is also termed scanning force microscopy (SFM). A simplified AFM setup is shown in Figure 3.22 (a)[75] while a picture of rectangular and triangular cantilevers with corresponding tips are presented in Figure 3.22 (b).[75]

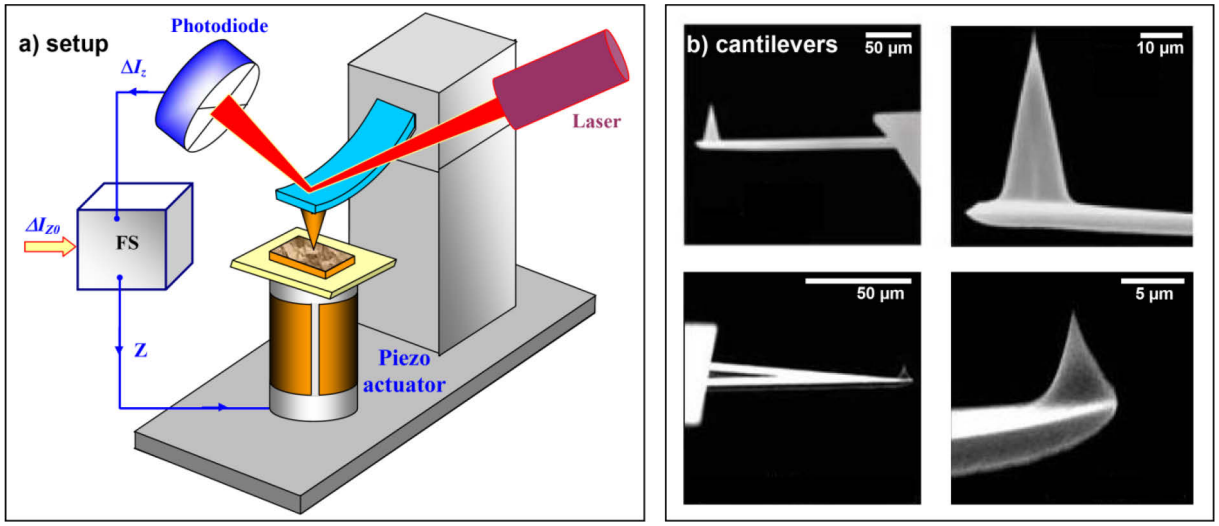

Figure 3.22: *(a) Simplified scheme of the important components of an AFM setup. Laser light is reflected by the cantilever and detected by a photodiode. The position of the cantilever is adjusted by an electronic feedback system (FS), (b) electron microscopy images of rectangular and triangular cantilevers with the tip in large magnification*[75]

Since the tip is in constant contact with the sample this mode of operation is called "*contact mode*", see Figure 3.23 (a). All of the first AFMs were operated in this mode. The resolution

depends on the condition of the sample and the properties of the AFM tip, mainly on the sharpness which can be manufactured with an end radius of a new nanometers. For rare cases such as relatively robust and periodic samples atomic resolution is obtained. Soft samples however, particularly biological samples, provide a more difficult surface to image, because the forces exerted by the tip during imaging can cause deformation or even destruction of the sample. Another drawback is that the tip can be altered by the friction and that it can break very easily, it has the advantage that it is comparably insensitive to perturbations through the environment.

The problems involved with imaging soft samples have been largely overcome by the introduction of dynamic operation modes[76, 77] where the cantilever is actively oscillated normal to the surface at or close to its resonance frequency by a small piezoelectric element mounted in the AFM tip holder. In the "*non-contac*t" mode the cantilever tip is not in direct contact with the surface, but hovers in close proximity. Since the attractive forces like van-der-Waals forces from the sample are substantially weaker than the forces used by contact mode, the tip must be given a small oscillation (< 10 nm) in order to detect them by measuring the change in amplitude, phase, or frequency. During a scan the feedback loop maintains a constant frequency and amplitude of the cantilever by adjusting the distance between tip and sample. This distance is mapped at each data point and an image of the surface is obtained. This mode is shown in Figure 3.23 (b). Since the method does not suffer from tip or sample degradation effects it is usually used for very soft samples like cells. In many cases under ambient conditions a fluid contaminant layer is present on the surface which can also be thicker than the range of the attractive force gradient. Any attempt to image the true surface fails then as the probe either becomes trapped in the liquid layer or hovers beyond the effective range of the forces. Any changes in the environment during the measurements are also influencing the images. For best imaging usually ultra-high-vacuum conditions are required. Under this conditions this method was the first AFM technique to provide true atomic resolution.[72]

A method which combines the advantages of both operation modes is the "*intermittent-contact mode*", also termed "*tapping mode*". It represented the key advancement in AFM technology and overcomes problems such as friction and adhesion. In this mode the cantilever is again oscillated at or near its natural resonant frequency, but now with larger amplitude. The tip is moved so close to the surface until it starts to slightly tap it and due to the energy loss caused by the intermittent contacting of the tip with the surface, the amplitude of vibration changes according to the surface topography of the sample. During tapping operation the oscillation amplitude and hence the tip-sample interaction is kept constant through the feedback loop. This operation mode is presented in Figure 3.23 (c). Since the tip is only in contact with the surface for a very short time, the lateral forces which

are mainly responsible for most of the sample damages are greatly reduced. At the same time the method is due to the stronger oscillation less susceptible to perturbations through the environment. The tapping mode is gentle enough for the visualization of adsorbed single polymer molecules under liquid conditions. With proper scanning parameters, the sample surface can remain unchanged for hours.

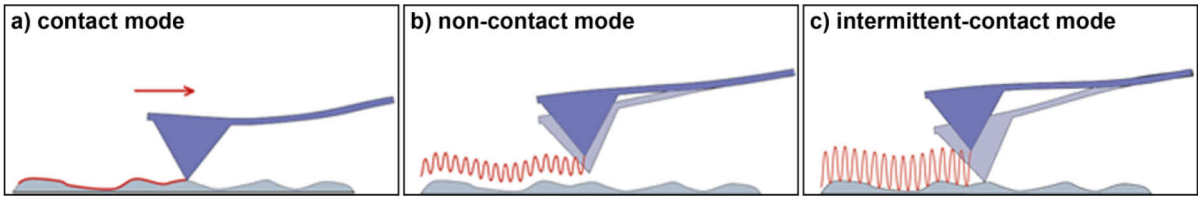

Figure 3.23: *AFM operation modes with (a) contact mode, (b) non-contact mode and (c) intermittent-contact mode.*[78]

Furthermore there is a second information available which is often recorded simultaneously with the height images. The interaction with the sample can not only result in a frequency, but also in a phase shift of the cantilever. Phase images provide the best contrast of fine morphological and nanostructural features due to their sensitivity to surface imperfections such as steps, cracks and the like. On surfaces with local variations of the mechanical properties, the phase changes are even more informative and can allow a compositional analysis, giving sometimes a contrast where non was anticipated from the material properties before.

There are some significant advantages of AFM as an imaging tool when compared with complimentary techniques such as scanning electron microscopy (SEM) which require vacuum conditions and contaminate the samples. Not only does AFM achieve molecular or atomic resolution in three dimensions, it also requires almost no sample preparation and, most importantly, can be performed under fluids, permitting biologic samples to be imaged in near native conditions. The fluid may be exchanged or modified during imaging and therefore there is potential for observing biological processes in real time. The instruments are also capable of manipulating molecules and measuring the strength of interactions with piconewton sensitivity. A disadvantage of AFM is the single scan size. In one pass, SEM can image an area on the order of square millimeters with a depth of field on the order of millimeters, whereas AFM can only image a maximum height on the order of micrometers and a maximum scanning area of about hundred micrometers.

AFM Image Acquisition: All images in this work were taken on a Dimension 3100 (connected to a Nanoscope IV-controller, Veeco Instruments Inc., Santa Barbara, USA) atomic force microscope with silicon cantilevers from Olympus (OMCL-AC 160TS-W2) in tapping mode. The height calibration of the microscope was checked with a calibration standard (Veeco Instruments, 3D reference, 200 nm deep, 10 µm pitches). The height of the optical

characterized nanoparticles from the confocal microscope was directly imaged by AFM after the optical measurements to avoid contamination from the SEM. The substrates were aligned in such a way that the slow scan axis (y) of the instrument followed the bisecting line of the two scratches on the metal film. In this way the distance between the two scratches can be measured right from the beginning by a large scan of the area in order to find the region of interest. After this area was found various high-resolution pictures of the interesting particle areas were made.

AFM Image Processing: Images were processed using Gwyddion data analysis software (Version 2.18, free SPM software from http://gwyddion.net). Images were flattened in first order and point and horizontal error lines removed. The axial dimension of each particle was determined as the height difference between the gold film at the base of the particle to its maximum height. For presentation the processed images were afterwards saved in ASCII format and imported into Igor Pro (Version 5.02, Wavemetrics Inc., Portland, USA) using a self-written procedure.

3.3 Bibliography

1. Turkevich, T.; Stevenson, P. C.; Hillier, J., A study of the nucleation and growth processes in the synthesis of colloidal gold. *Discussions Faraday* **1951,** *11* (55-75).

2. Frens, G., Controlled Nucleation for the Regulation of the Particle Size in Monodisperse Gold Suspensions. *Nature Physical Science* **1973,** *241*, 20-22.

3. Ercolessi, F.; Andreoni, W.; Tosatti, E., Melting of Small Gold Particles - Mechanism and Size Effects. *Phys. Rev. Lett.* **1991,** *66* (7), 911-914.

4. Lee, P. C.; Meisel, D., Adsorption and Surface Enhanced Raman of Dyes on Silver and Gold Sols. *Journal of Physical Chemistry* **1982,** *86* (17), 3391-3395.

5. Suber, L.; Sondi, I.; Matijevic, E.; Goia, D. V., Preparation and the mechanisms of formation of silver particles of different morphologies in homogeneous solutions. *J. Colloid Interface Sci.* **2005,** *288* (2), 489-495.

6. Herrmann, A.; Weil, T.; Sinigersky, V.; Wiesler, U. W.; Vosch, T.; Hofkens, J.; De Schryver, F. C.; Müllen, K., Polyphenylene Dendrimers with Perylene Diimide as a Luminescent Core. *Chemistry - A European Journal* **2001,** *7* (22), 4844-4853.

7. Qu, J.; Pschirer, N. G.; Liu, D.; Stefan, A.; De Schryver, F. C.; Müllen, K., Dendronized Perylenetetracarboxdiimides with Peripheral Triphenylamines for Intramolecular Energy and Electron Transfer. *Chemistry - A European Journal* **2004,** *10* (2), 528-537.

8. Ito, S.; Wehmeier, M.; Brand, J. D.; Kubel, C.; Epsch, R.; Rabe, J. P.; Mullen, K., Synthesis and self-assembly of functionalized hexa-peri-hexabenzocoronenes. *Chemistry-a European Journal* **2000,** *6* (23), 4327-4342.

9. Rueda, A. Optical resonances of sphere-on-plane geometries. Dissertation, Johannes Gutenberg Universität, Mainz, 2008.

10. Butt, H. J.; Wang, D. N.; Hansma, P. K.; Kuhlbrandt, W., Effect of surface roughness of carbon support films on high-resolution electron diffraction of two-dimensional protein crystals. *Ultramicroscopy* **1991,** *36* (4), 307-318.

11. Butt, H. J.; Müller, T.; Gross, H., Immobilizing Biomolecules for Scanning Force Microscopy By Embdding in Carbon. *Journal of Structural Biology* **1993,** *110* (2), 127-132.

12. Hegner, M.; Wagner, P.; Semenza, G., Ultralarge atomically flat template-stripped Au surfaces for scanning probe microscopy. *Surf. Sci.* **1993,** *291* (1-2), 39-46.

13. Stamou, D.; Gourdon, D.; Liley, M.; Burnham, N. A.; Kulik, A.; Vogel, H.; Duschl, C., Uniformly flat gold surfaces: Imaging the domain structure of organic monolayers using scanning force microscopy. *Langmuir* **1997,** *13* (9), 2425-2428.

14. Rueda, A.; Stemmler, M.; Bauer, R.; Mullen, K.; Fogel, Y.; Kreiter, M., Optical resonances of gold nanoparticles on a gold surface: quantitative correlation of geometry and resonance wavelength. *New J. Phys.* **2008,** *10*, 113001/1-113001/21.

15. Faraday, M., The Bakerian Lecture: Experimental Relations of Gold (and Other Metals) to Light. *Philosophical Transactions of the Royal Society of London* **1857,** *147*, 145-181.

16. Link, S.; El-Sayed, M. A., Shape and size dependence of radiative, non-radiative and photothermal properties of gold nanocrystals. *International Reviews in Physical Chemistry* **2000,** *19* (3), 409-453.

17. Bohren, C. F.; Huffman, D. R., *Absorption and scattering of light by small particles*. Wiley-VCH: New York, 1983.

18. El-Sayed, M. A., Some Interesting Properties of Metals Confined in Time and Nanometer Space of Different Shapes. *Accounts of Chemical Research* **2001,** *34* (4), 257-264.

19. Link, S.; El-Sayed, M. A., Spectral Properties and Relaxation Dynamics of Surface Plasmon Electronic Oscillations in Gold and Silver Nanodots and Nanorods. *The Journal of Physical Chemistry B* **1999,** *103* (40), 8410-8426.

20. Zhang, J. Z., Ultrafast Studies of Electron Dynamics in Semiconductor and Metal Colloidal Nanoparticles: Effects of Size and Surface. *Accounts of Chemical Research* **1997,** *30* (10), 423-429.

21. Ahmadi, T. S.; Logunov, S. L.; El-Sayed, M. A., Picosecond Dynamics of Colloidal Gold Nanoparticles. *The Journal of Physical Chemistry* **1996,** *100* (20), 8053-8056.

22. Hodak, J. H.; Henglein, A., Size dependent properties of Au particles: Coherent excitation and dephasing of acoustic. *Journal of Chemical Physics* **1999,** *111* (18), 8613.

23. Hodak, J. H.; Martini, I.; Hartland, G. V., Spectroscopy and Dynamics of Nanometer-Sized Noble Metal Particles. *The Journal of Physical Chemistry B* **1998,** *102* (36), 6958-6967.

24. Link, S.; Burda, C., Electron dynamics in gold and gold-silver alloy nanoparticles: The influence of a nonequilibrium. *Journal of Chemical Physics* **1999,** *111* (3), 1255.

25. Del Fatti, N.; Vallée, F., Ultrafast optical nonlinear properties of metal nanoparticles. *Applied Physics B: Lasers & Optics* **2001,** *73* (4), 383.

26. Elsayed-Ali, H. E.; Norris, T. B.; Pessot, M. A.; Mourou, G. A., Time-resolved observation of electron-phonon relaxation in copper. *Phys. Rev. Lett.* **1987,** *58* (12), 1212.

27. Sun, C. K.; Vall; eacute; e, F.; Acioli, L. H.; Ippen, E. P.; Fujimoto, J. G., Femtosecond-tunable measurement of electron thermalization in gold. *Physical Review B* **1994,** *50* (20), 15337.

28. Del Fatti, N.; Flytzanis, C.; Vallée, F., Ultrafast induced electron-surface scattering in a confined metallic system. *Applied Physics B: Lasers & Optics* **1999,** *68* (3), 433.

29. Roberti, T. W.; Smith, B. A.; Zhang, J. Z., Ultrafast electron dynamics at the liquid–metal interface: Femtosecond studies using surface plasmons in aqueous silver colloid. *Journal of Chemical Physics* **1995,** *102* (9), 3860.

30. Takami, A.; Kurita, H.; Koda, S., Laser-Induced Size Reduction of Noble Metal Particles. *The Journal of Physical Chemistry B* **1999,** *103* (8), 1226-1232.

31. Link, S.; El-Sayed, M. A., Spectroscopic determination of the melting energy of a gold nanorod. *The Journal of Chemical Physics* **2001,** *114* (5), 2362-2368.

32. Berne, B. J.; Pecora, R., *Dynamic Light Scattering with Applications to Chemistry, Biology and Physics*. Dover Publications Inc.: Minola, 2000.

33. Schärtl, W., *Light Scattering from Polymer Solutions and Nanoparticle Dispersions*. Springer: Berlin, 2007.

34. Pecora, R., Dynamic Light Scattering Measurement of Nanopeter Particles in Liquids. *Journal of Nanoparticle Research* **2000,** *2*, 123-131.

35. Provencher, S. W., A Constrained Regularization Method for Inverting Data Represented by Linear Algebraic or Integral-Equations. *Computer Physics Communications* **1982,** *27* (3), 213-227.

36. Provencher, S. W., CONTIN - A General Purpose Constrained Regularizaton Program for Inverting Noisy Linear Algebraic and Integral-Equations. *Computer Physics Communications* **1982,** *27* (3), 229-242.

37. Lindsey, C. P.; Patterson, G. D., Detailed Comparison of the Williams-Watts and Cole-Davidson Functions. *Journal of Chemical Physics* **1980,** *73* (7), 3348-3357.

38. Williams, G.; Watts, D. C., Non-Symmetrical Dielectric Relaxation Behaviour Arising from a simple Empirical Decay Function. *Transactions of the Faraday Society* **1970,** *66* (565P), 80-85.

39. Plum, M. Messung der Dynamik von Materie an Grenzflächen. Dissertation, Johannes Gutenberg Universität, Mainz, 2010.

40. Lide, D. R., *CRC Handbook of Chemistry and Physics, 90th Edition (Internet Version 2010)*. CRC Press/Taylor and Francis: Boca Raton, Fl., 2010.

41. Claxton, N. S.; Fellers, T. J.; Davidson, M. W. www.olympusfluoview.com/theory/LSCMIntro.pdf (accessed 10.12.2008).

42. Minski, M., Memoir on inventing the confocal scanning microscope. *Scanning* **1988,** *10*, 128–138.

43. Minski, M. Microscopy Apparatus. US Pat. 3,013,467, 1961.

44. Stefani, F. D. Confocal Microscopy applied to the Study of single entity Fluorescence and Light Scattering. Dissertation, Johannes Gutenberg Universität, Mainz, 2004.

45. Brakenhoff, G. J.; Blom, P.; Barends, P., Confocal Scanning Light-Microscopy with High Aperture Immersion Lenses. *Journal of Microscopy-Oxford* **1979,** *117* (NOV), 219-232.

46. Born, M.; Wolf, E., *Principles of Optics: Electromagnetic Theory of Propagation, Interference and Diffraction of Light*. 6 ed.; Cambridge University Press;: 1997.

47. Webb, R. H., Confocal optical microscopy. *Reports on Progress in Physics* **1996,** *59* (3), 427-471.

48. Olympus http://www.olympusconfocal.com/theory/confocalintro.html (accessed 10.12.2008).

49. Chalfie, M.; Tu, Y.; Euskirchen, G.; Ward, W. W.; Prasher, D. C., Green FLuorescent Protein as Marker for Gene-Expression. *Science* **1994,** *263* (5148), 802-805.

50. Cormack, B. P.; Valdivia, R. H.; Falkow, S., FACS-optimized mutants of the green fluorescent protein (GFP). *Gene* **1996,** *173* (1), 33-38.

51. Tsien, R. Y., The green fluorescent protein. *Annual Review of Biochemistry* **1998,** *67*, 509-544.

52. Unger, A. Refractive index sensing with localized plasmonic resonances – Theoretical description and experimental verification. Dissertation, Universität Mannheim, Mannheim, 2010.

53. Knoll, W., Interfaces and thin films as seen by bound electromagnetic waves. *Annual Review of Physical Chemistry* **1998,** *49*, 569-638.

54. Homola, J.; Dostalek, J.; Jian, S.; Ladd, J.; Löfas, S.; A., M., *Surface Plasmon Resonance Based Sensors*. Springer: Berlin, 2006; Vol. 4.

55. Pitarke, J. M.; Silkin, V. M.; Chulkov, E. V.; Echenique, P. M., Theory of surface plasmons and surface-plasmon polaritons. *Reports on Progress in Physics* **2007,** *70*, 1-87.

56. Barnes, W. L.; Dereux, A.; Ebbesen, T. W., Surface plasmon subwavelength optics. *Nature* **2003,** *424* (6950), 824-830.

57. Kretschmann, E., Determination Of Optical Constants Of Metals By Excitation Of Surface Plasmons. *Zeitschrift für Physik* **1971,** *241* (4), 313-324.

58. Turbadar, T., Complete absorption of light by thin metal films. *Proceedings of the Physical Society of London* **1959,** *73* (469), 40-44.

59. Vockenroth, I. K. Investigations of tethered bilayer lipid membranes for their potential use in biosensing devices Ph.D. thesis, Universität of Bath, Mannheim, 2007.

60. Yeh, P., *Optical Waves in Layered Media*. John Wiley & Sons Inc: Hoboten, 1988.

61. Schnatterly, S. E.; Tarrio, C., Local fields in solids: microscopic aspects for dielectrics. *Reviews of Modern Physics* **1992,** *64* (2), 619-622.

62. Egerton, R., *Physical principles of electron microscopy: an introduction to TEM, SEM, and AEM*. Springer Science+Business Media: 2005.

63. Goldstein, J.; Newbury, D.; Joy, D.; Lyman, C.; Echlin, P.; Lifshin, E.; Sawyer, L.; Michael, J., *Scanning Electron Microscopy and X-ray Microanalysis*. 3rd ed. ed.; Plenum Publishers: New York, 2003; p 689.

64. Reimer, L.; Pfefferkorn, G., *Raster-Elektronenmikroskopie*. 2. ed. ed.; Springer: Berlin, 1977.

65. Abbe, E., A Contribution to the Theory of the Microscope and the Nature of Microscopic Vision. *Proceedings of the Bristol Naturalists' Society* **1876,** (Bd. 1).

66. Retsch, M. Complex Materials via Colloidal Crystallization. Dissertation, Johannes Gutenberg Universität, Mainz, 2009.

67. Vezie, D. L.; Thomas, E. L.; Adams, W. W., Low-voltage, high-resolution scanning electron microscopy: a new characterization technique for polymer morphology. *Polymer* **1995,** *36* (9), 1761-1779.

68. Jaksch, H.; Martin, J., High-resolution, low-voltage SEM for true surface imaging and analysis. *Fresenius' Journal of Analytical Chemistry* **1995,** *353* (3), 378-382.

69. Zeiss http://www.zeiss.de (accessed 20.08.2010).

70. Binnig, G.; Quate, C. F.; Gerber, C., Atomic Force Microscope. *Phys. Rev. Lett.* **1986,** *56* (9), 930.

71. Butt, H. J.; Berger, R.; Bonaccurso, E.; Chen, Y.; Wang, J., Impact of atomic force microscopy on interface and colloid science. *Advances in Colloid and Interface Science* **2007,** *133*, 91-104.

72. Giessibl, F. J., Advances in atomic force microscopy. *Reviews of Modern Physics* **2003,** *75* (3), 949.

73. Jalili, N.; Laxminarayana, K., A review of atomic force microscopy imaging systems: application to molecular metrology and biological sciences. *Mechatronics* **2004,** *14* (8), 907-945.

74. Magonov, S. N.; Reneker, D. H., Characterization of polymer surfaces with atomic force microscopy. *Annu. Rev. Mater. Sci.* **1997,** *27*, 175-222.

75. Mironov, V. L., *Fundamentals of Scanning Probe Microscopy*. The Russian Academy of Sciences: Nizhniy Novgorod, 2004.

76. Albrecht, T. R.; Grutter, P.; Horne, D.; Rugar, D., Frequency-Modulation Detection Using High_Q Cantilevers for Enhanced Force Microscope Sensitivity. *J. Appl. Phys.* **1991,** *69* (2), 668-673.

77. Martin, Y.; Williams, C. C.; Wickramasinghe, H. K., Atomic Force Microscope Force Mapping and Profiling on a Sub 100-A Scale. *J. Appl. Phys.* **1987,** *61* (10), 4723-4729.

78. JPK http://www.jpk.com/imaging-mode-practicalities.434.html (accessed 21.05.2010).

4 Laser-Induced Shape Transformation of Gold and Silver Nanoparticles in Aqueous Suspensions

4.1 Introduction

Small metal nanoparticles have been attracting considerable attention due to their unique optical, electrical and magnetic properties[1-3] and their potential applications as novel catalysts,[4, 5] sub-wavelength optical devices,[6-8] surface enhanced Raman spectroscopy (SERS)[9-11] or optical recording.[12, 13] Their small size (< 100 nm) causes strong confinement of the electrons and gives rise to fascinating effects not observed in bulk material.

The chemical and physical properties of the nanoparticles are determined by a set of parameters that include their size, shape, composition, environment and structure. In principle any of these parameters can be controlled to fine-tune their properties. The interaction of gold and silver nanoparticles with light is dominated by the localized surface plasmon resonance (LSPR) which is highly sensitive to the shape and can be tuned accordingly from the visible to the near infrared.[1, 14] The last decade has witnessed the successful synthesis of a variety of shapes like cubes and prisms,[15, 16] plates and disks[17-19] and rods and wires.[20, 21] However, ideal spherical particles still play a unique role as the only type for which the classical Mie[22] theory provides an analytical solution to Maxwell equations.[23] In the case of the sphere-on-plane system ideal spheres are correspondingly used as model particles in the calculations.[24]

Realistic experiments[25] normally rely on nanoparticles which are synthesized by chemical reduction of their metal salts and hardly resemble the spheres of the model systems. As observed with macroscopic metal surfaces[26] the surface topography of the particles also plays an important role in their optical response. Halas[27] and Mulvaney[28] with co-workers could show that nanoscale surface corrugations on gold nanoparticles induces a very significant red-shift and broadening of the particle plasmon resonance, along with damping of the higher modes. Recently, ultra-short pulsed laser sources are used more frequently for size reduction and reshaping of these metal nanoparticles leading to changes in their surface topography and thus compensating the shortcomings of the chemical synthesis.

The effect of intense laser light on metal particles in aqueous solution has first been studied by Eckstein and Kreibig[29] who reported the aggregation of 10 nm gold particles under irradiation of a 514 nm continuous wave Argon ion laser. In 1996 Takami *et al.*[30] studied for the first time the influence of nanosecond pulsed laser light on aqueous suspensions of silver nanoparticles. They demonstrated that the irradiation caused particle size reduction and shape transformation and resulted in a narrower size distribution, though the involved

mechanism remained unsolved. Later, the group[31, 32] explained the results by the slow heat transfer of the deposited laser energy into the surrounding solvent. This then leads to the melting and/or vaporization of the nanoparticles depending on the deposited laser energy. To confirm this model they measured the temperature of gold nanoparticles by recording the emission spectra of gold with a photon counter system and found that 0.2 µs after the laser pulse the particle temperature was 2500 ± 100 K, which is much higher than the gold melting temperature. Inasawa *et al.*[33, 34] could later show that the transformation of the particles starts at the surface and involves the formation of a thin liquid layer at temperatures well below the melting point. This melting point reduction occurs due to the surface tension difference between the liquid and solid phases. Plech[35] used ultrafast X-ray diffraction for monitoring the lattice expansion and cooling of 100 nm diameter gold nanoparticles. At elevated temperatures a loss of long-range lattice order was observed which was attributed to the pre-melting of the particles. At the bulk melting point, complete melting was observed within 100 ps after the excitation. Phase transitions were also observed in the temperature dependent elastic properties of the particles by employing pump-probe spectroscopy.[36] Gold particles showed femtosecond laser induced acoustic oscillations. The reported breathing mode was attributed to the softening of the elastic properties due to the laser-induced heating and its period depended on the pump-laser intensity.[36]

However, Mafune and co-workers[37, 38] detected photoelectrons ejected from gold nanoparticles irradiated by nanosecond laser pulses and thereby, seemed to confirm a mechanism proposed by Kamat[39] and theoretically derived by Grua[40] The initial ejection of the photoelectrons after excitation causes the particles to become positively charged and the repulsion between the charges leads then to fragmentation. The ionization efficiency was highest when the interband transition of gold particles was resonantly excited whereas intraband excitation contributed hardly to the ionization. Giammanco *et al.*[41] developed a theoretical model which allowed for a quantitative treatment of the involved phenomena and compared it to experimental results of gold particles with a radius of 1.75 nm. Under the selected irradiation conditions with a focused laser beam evaporation did not play a relevant role and their photo-fragmentation was due to the interplay of thermionic emission and photon-assisted ionization.

The entire discussion shows that the primary interaction of the laser beam with the particles starts through the absorption of the laser photons by the particle electrons, while the subsequent processes can develop in different ways depending on the selected irradiation conditions like laser fluence, pulse length, environment, particle material or particle size. Therefore the first part of this chapter deals with a detailed description of the involved processes during the laser interaction and roughly evaluates their influence in the irradiation

of gold and silver particles for the typical involved laser intensities and wavelengths of the used Nd:YAG laser. In the following experimental part the derived parameters were then selected in such a way that gold and silver nanoparticles of different diameters could be irradiated in aqueous suspensions under "mild" conditions to obtain shape transformation mainly by melting. The effect of the laser irradiation on the shape and size of the nanoparticles was characterized by UV-Vis absorption and photon correlation spectroscopy (PCS) as well as scanning electron microscopy (SEM). The introduced procedure represents a simple and rapid method to obtain spherical particles with defined shape and low surface roughness and narrow size distribution. The metal spheres possess superior properties over their un-irradiated predecessors and are suitable for single-particle-experiments in several applications since they possess a very defined reproducible optical response. [in printed version available] from the MPI for the science of light in Erlangen used them to measure the field distribution of light in the focal plane of a high numerical aperture microscope objective. A short summary of their work will also be presented at the end of the chapter.

4.2 Theoretical Study of Laser Irradiation of Particles

The interaction of a low intensity ultra-short laser pulse with metal nanoparticles results in a perturbation of the electron distribution in the metal, which is normally given by a Fermi distribution. The initially created electron distribution with energies up to the pump energy above the Fermi level is highly non-thermal and the first relaxation step is internal thermalization by electron-electron scattering until a new Fermi electron distribution with a higher electron temperature is reached. The process of internal thermalization is a non-radiative process and can be regarded as the coupling of the excited electrons with a reservoir of free electron kinetic energy modes forming a continuum.[42, 43] This is extremely fast in bulk metals (500 fs for gold[44] and 350 fs for silver[45]). Since the electron heat capacity is much smaller than the lattice heat capacity, the resulting electron temperature can reach several thousand degrees Kelvin depending on the pump fluence.[46, 47] In case of nanoparticles, the heating of the electron gas leads to spectral broadening and a decrease in the maximum intensity of the particle plasmon absorption[48, 49] and therefore, a transient bleach of the plasmon band is observed in a difference spectrum.[50]

After the electrons are thermalized, they lose their energy further by exchanging their heat with the lattice through electron-phonon coupling. This process is independent of the size and shape of gold particles in the size range from 2 to 120 nm.[51] The measured relaxation times for the electron-phonon-scattering depend on the laser pump power and are on the order of a few picoseconds (1-5 ps). They compare well with the values measured for bulk metals.[44]

As the electronic gas cools, it heats the lattice until both temperatures are equilibrated. Due to the much larger heat capacity of the lattice, the final temperature of the whole system is now only a few tens of degrees higher than before the laser pulse. Finally the lattice exchanges heat with its surroundings by phonon-phonon interaction, and with that a complete relaxation of the initially absorbed photon energy is achieved. The time to reach ambient temperature depends on the heat capacity of the environment and the thermal conductivity of the ligand molecules, but is in general on the order of 100 ps. Superimposed on this lattice cooling is a back-and-forth expansion and contraction of the entire particle volume. This coherent breathing mode has a period on the order of 10 ps, depending on the size and shape of the affected particles.[36] The processes for the response of a metal nanoparticle to an incident laser pulse are summarized in Figure 4.1.

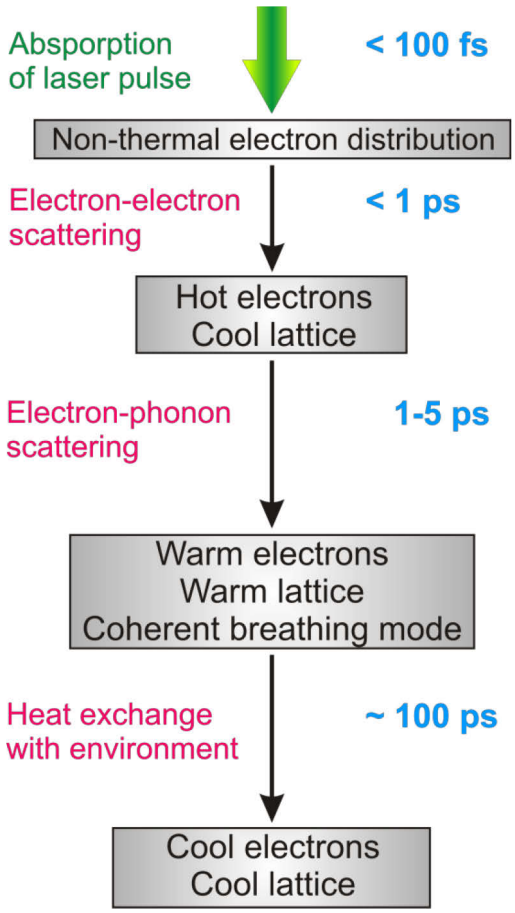

Figure 4.1: *Flow chart of the involved processes for the response of a metal nanoparticle to an incident laser pulse*

When the power of the laser is increased or the beam is highly focused, both the electrons and the lattice can reach very high temperatures within one pulse. Depending on the parameters the subsequent mechanisms can then develop in two ways:

(i) The electrons can rapidly accumulate sufficient energy to leave the particle either by thermionic emission and/or photo-ionization which leads to fragmentation of the nanoparticles by Coulomb explosion.

(ii) Alternatively, the energy of the electrons will transfer to the crystal lattice due to the efficient heat transfer between the electrons and phonons followed by particle melting and/or evaporation.

One of the important points that determine the type of mechanism is the pulse length of the laser. In case of the irradiation with a laser pulse shorter than the time constant for electron-phonon-scattering, only the electrons are excited to extremely high-energy states by the absorption of photons, resulting in electron ejection. In case of a longer pulse width than the time constant for the relaxation to the lattice, absorbed photon energy transfers to the phonons during the irradiation of a pulse and electrons are not in high-energy states. In this case, electron ejection is less efficient and the photo-thermal processes become dominant. For femtosecond pulses the number of electrons that are required for the size reduction of gold particles by Coulomb explosion is enormously high. Link[52] reported that the required energy has to be three orders of magnitude higher than the energies used in this study. This means that the related process is not very efficient. For nanosecond laser pulses the size reduction requires nearly the same energy, because the absorbed laser energy is lost by the heat dissipation from the particles. The most efficient method for particle transformation is therefore the irradiation by picosecond laser pulses. The size reduction is also caused by a photo-thermal process, but the heat dissipation is negligible.

In the following discussion a system composed of monodisperse spherical silver or gold nanoparticles suspended in pure water is considered in detail during the irradiation with the second (λ_{Ex}=532 nm) and third harmonic (λ_{Ex}=355 nm) of a picosecond Nd:YAG laser. Particle sizes are varied from 10 to 100 nm. The pulse duration τ_0 of the laser is adopted from the experimental part as equal to be 30 ps with a laser beam diameter D_0 of 8 mm. The maximum pulse energy, $(A_0)_{max}$ is equal to 10 mJ/pulse for the second harmonic and 5 mJ/pulse for the third harmonic. Those values correspond to a threshold that was not exceeded in most part of this work and under these conditions the following laser energy flow densities can be calculated by:

$$I_0 = \frac{4 \cdot A_0}{\pi \cdot \tau_0 \cdot D_0^2} \tag{4.1}$$

For the second harmonic a value of I_0=6.6 x 10^{12} W/m^2 is calculated while the value is equal to I_0=3.3 x 10^{12} W/m^2.for the third harmonic. In the now following discussion the numbers serve as reference energies to estimate the influence of the different mechanisms during the irradiation. If a process is not occurring up to this value it can be completely neglected for all lower energies. First the possibility of electron ejection is considered in our system.

4.2.1 Electron Ejection

Ionization of a metal particle by electron emission can be caused by a photoelectric or by a thermal effect. The former is roughly calculated by evaluating the ratio of involved electrons in the conduction band to the number of photons from the laser. The influence of the latter is estimated by a set of differential equations which roughly estimate the efficiency of the lattice heating and by a calculation of the absorbed energy.

4.2.1.1 Photoemission

At ambient electron temperatures the photoelectric effect is efficient if the photon energy of incident light is larger than the so-called work function value W of the metal (extraction energy from Fermi level). As the potential for polycrystalline gold is as high as W_{Au}=5.1 eV[53] and for silver W_{Ag}=4.3 eV[53], either single-photon excitation of the interband with the third harmonic (λ_{Ex}=355 nm or 3.5 eV) or single-photon excitation of the intraband with the second harmonic (λ_{Ex}=532 nm or 2.3 eV) cannot reach the ionization threshold. The work function of single crystalline gold or silver particles with low-index planes should be slightly different, but the deviations are assumed to be small.[40] In this reference photoemission induced by intraband absorption of gold particles is also assumed to be negligible compared to the one related with the interband absorption. These theoretical findings were later experimentally proven by Yamada.[38] The result can be transferred to silver particles, because the interband gap for silver exceeds the one for gold. Note that recent work[54, 55] has revealed that water cavities or bubbles are already formed around the irradiated metal below the boiling point of gold. Such a formation of a vapor layer should prevent the reduction of the work function by considering the electron affinity of the surrounding water molecules (-0.8 eV)[56]. As a result, at least two or three photons are required to ionize the nanoparticles. For a numerical estimation of the influence for multi-photon excitation in our system the photon density of the laser beam n_{Ph} is compared with the density of conduction electrons in a metal particle n_e[57] Assuming that multi-photon processes become essential then this ratio X exceeds 1, the related formula is given for this critical ratio by

$$X_{cr} = \frac{n_{Ph}}{n_e} = 1 \tag{4.2}$$

On one hand, the density of the photons in the laser beam n_{Ph} is given by the quotient of the laser flow density I_0 and the energy of one photon:

$$n_{Ph} = \frac{I_0}{\omega \hbar c} \tag{4.3}$$

In this formula $\hbar$ is the reduced Planck constant or Dirac constant, ω is the angular frequency of the photon and c is the velocity of light.

On the other hand, the density of conduction electrons n_e for gold and silver is given by the quotient of the number of electrons N_e in a particle and the particle volume $V_P=\pi\, d^3/6$ where d is the particle diameter:

$$n_e = \frac{N_e}{V_p} \tag{4.4}$$

Silver and gold have only one conduction electron for each atom and therefore the number of related electrons in a particle is equal to the number of atoms. Both metals crystallize in a face-centered cubic crystal lattice (fcc) with a similar cell constant of $a_{Au}\approx a_{Ag}$=0.408 nm[58] and with four atoms in a unit cell the number of atoms N_a or number of conduction electrons N_e, respectively, is equal to:

$$N_e = N_a = \frac{2\cdot\pi}{3}\left(\frac{d}{a}\right)^3 \tag{4.5}$$

The electron density is then given by $n_e=4/a^3$ ≈59 electrons(atoms)/nm^3 and the introduced parameter X_{cr} is therefore equal to:

$$X_{cr} = \frac{n_{Ph}}{n_e} = \frac{a^3\cdot I_0}{4\cdot\omega\hbar c} \tag{4.6}$$

Assuming a value of 1 for X_{cr} as the critical limit where multi-photon processes can become important, the formula (4.6.) can be rearranged to calculate the corresponding critical laser flow densities:

$$\left(I_0\right)_{cr} = \frac{4\cdot\hbar c}{a^3}\cdot X_{cr}\cdot\omega = \frac{4\cdot hc^2}{a^3\cdot\lambda} \tag{4.7}$$

For the second harmonic and third harmonic values of 6.59 x 10^{18} W/m^2 and 9.88 x 10^{18} W/m^2 are calculated respectively which are six orders of magnitude higher than the maximum applied values of the Nd:YAG laser in this work. Hence, multi-photon processes can be neglected in the limit of the applied energies. The authors in this reference[33] conclude that even more intensive laser light must be used for a participation of the photoelectric effect. They excited gold nanoparticles with picosecond pulses up to 35 mJ/cm^2 of the third harmonic of a Nd:YAG laser and monitored the subsequent changes by two probe lasers at wavelengths of 488 nm and 635 nm. In the theoretical model of Grua[40] photoemission via the excited state does not play an important role either, because the lifetime of the excited state is very short.

4.2.1.2 Thermal Emission

The efficiency of the thermal emission of electrons depends on the temperature of the electron gas. The described behavior during the interaction with the laser pulse with the fast

heating of the electrons and the slow heating of the crystal lattice can be modeled by two coupled diffusion equations. Both equations are connected by a term that is proportional to the electron-phonon coupling constant *G* and the temperature difference between electrons and lattice, original proposed by Anisimov.[59] This Two-Temperature-Model (TTM) is commonly accepted to describe such systems[40, 44, 51, 57] and the governing equations are:

$$c_e \frac{dT_e}{dt} = -\frac{G}{V_p}\left(T_e - T_l\right) + \frac{L}{V_p} \tag{4.8}$$

$$c_l \frac{dT_l}{dt} = -\frac{G}{V_p}\left(T_e - T_l\right) + \frac{S}{V_p} \tag{4.9}$$

where T_e and T_l are the heat temperature of the electrons and the lattice, c_e and c_l are the related heat capacities and V_p is the particle volume. L is the laser power adsorbed by the conduction electrons per unit time, and S is the particle heat loss per unit time. The two equations can be combined to:

$$\frac{d\left(T_e - T_l\right)}{dt} = -\frac{G}{V_p}\left(\frac{1}{c_e} - \frac{1}{c_l}\right)\cdot\left(T_e - T_l\right) + \frac{1}{V_p}\cdot\left(\frac{L}{c_e} - \frac{S}{c_l}\right) \tag{4.10}$$

The electron heat capacity, $c_e=\gamma T_e$ with γ=63 J/(K^2 m^3), is much smaller than that of the lattice c_l for all temperatures considered here and so the latter can be neglected in this equation. Heat loss should be considered next. Since the time constant for the heat dissipation from the particles is larger (100-200 ps[46]) than the pulse width of the laser (20 ps), it can also be disregarded. Under these assumptions and with the introduction of $\Delta T=T_e-T_l$ one obtains:

$$\frac{d\left(\Delta T\right)}{dt} = -\frac{G}{V_p \cdot \gamma T_e}\cdot\Delta T + \frac{L}{V_p \cdot \gamma T_e} \tag{4.11}$$

Taking into account that for the initial period $T_l<<T_e$, and thus $T_e\approx\Delta T$, this equation has the following analytical solution:

$$\ln\left(1 - \frac{G}{L}\cdot\Delta T\right) + \frac{G}{L}\cdot\Delta T = -\frac{G^2}{V_p \cdot \gamma \cdot L}\cdot t \tag{4.12}$$

It shows almost an exponential growth of ΔT to its maximum value:

$$\left(\Delta T\right)_{\max} = \frac{L}{G} \tag{4.13}$$

In this equation, the laser power L absorbed by a particle per unit time is given by:

$$L = I_0 \cdot \sigma_{abs}^{\lambda}\left(d_p\right) \tag{4.14}$$

where I_0 is the laser intensity defined by (4.1) and $\sigma^{\lambda}_{abs}(d_p)$ is the absorption cross section of the particle for a given wavelength. The latter can be calculated for a water environment using Mie Theory[22] with a free available program code[14, 60] and is displayed in Figure 4.2 (a) and (b) for gold and silver and the two wavelengths of the Nd:YAG laser. For comparison the absorption efficiencies of the two metals – a dimensionless ratio of the absorption cross section to the geometric cross section of the particle – are displayed in (c) and (d).

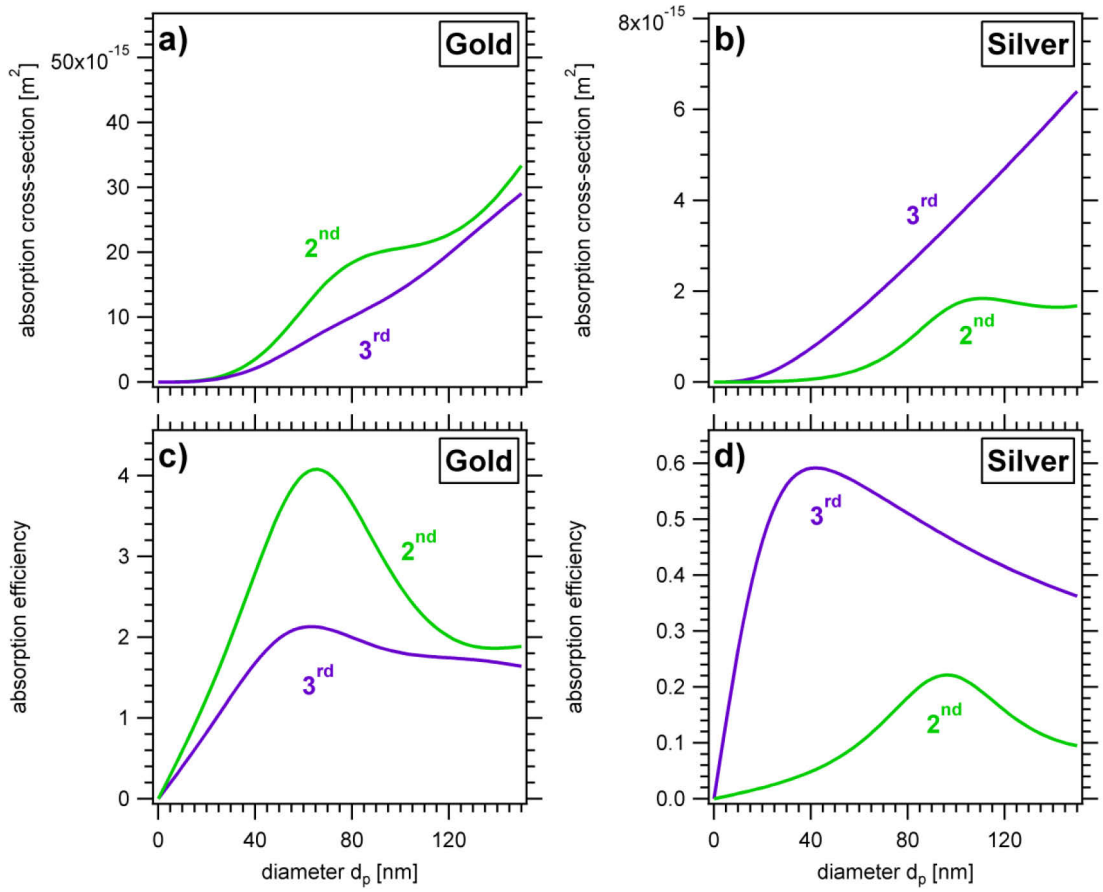

Figure 4.2: *Absorption cross sections of spherical gold (a) and silver (b) particles as a function of the particle diameter d_p for the second (2^{nd}) and third (3^{rd}) harmonic, absorption efficiencies of gold (c) and silver (d)*[60]

It should be noted that there are substantial differences between experimental data on the complex refractive index values for gold and silver by distinct authors. For all calculations in this chapter the values from Johnson and Christy[61] were used while the data from Hale *et. al.*[62] were adopted for the refractive index of water. The maxima in the absorption efficiencies are determined by the first dipole term in the Mie expansion. At these positions the values for gold are compared to silver by a factor of 19 higher for the second harmonic and by a factor of around 4 for the third harmonic, but silver is not by definition a poor absorber; the cross sections are only quite more wavelength dependent. Figure 4.3 shows the absorption efficiencies for three different diameters of gold and silver particles.

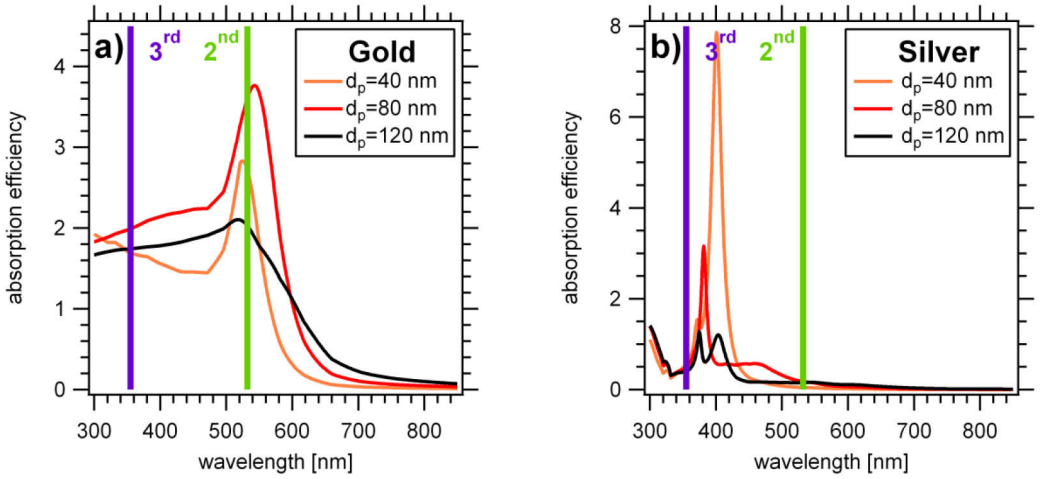

Figure 4.3: *Absorption efficiencies as a function of the wavelength for gold (a) and silver (b) particles with diameters of 40, 80 and 120 nm, the available wavelengths of the Nd:YAG laser are displayed for comparison*[60]

While gold shows a strong absorption through nearly the whole visible spectrum and the interaction is almost size-independent, silver absorbs preferentially in a narrow wavelength range around 400 nm and the cross-section at this position strongly depends on the size. Both available wavelengths of the Nd:YAG laser correspond to minima positions for silver particles and, as a consequence, the absorption cross-sections appear so small.

The electron-phonon coupling G in equation (4.13) can be calculated by using $G=g\,V_P$. Experimentally determined values for the electron-phonon coupling constant g are already available for gold $g_{Au}=(3.0\pm0.5)\times10^{16}$ W/(K m^3) and silver $g_{Ag}=(3.5\pm0.5)\times10^{16}$ W/(K m^3) in the literature.[63] The intensive heating of the electron gas in the first initial phase is then described by

$$\left(\Delta T\right)_{\max} = 6\cdot\frac{I_0}{g\cdot\pi\cdot d_p^3}\cdot\sigma_{abs}^{\lambda}\left(d_p\right) \tag{4.15}$$

After this first period, the slow heating of the crystal lattice becomes the dominant part with the temperature of the electron gas slowly increasing to keep the temperature difference to the lattice constant. Under intensive laser irradiation, the lattice temperature can first reach the melting point of the metal and then also the boiling point, that is $T_b(Au)$=3129 K for gold and $T_b(Ag)$=2435 K for silver, respectively.[64] Under the assumption that the heat transfer and the electron-phonon coupling constant g between the electrons and the particle lattice keeps constant after the melting, the maximum possible temperature of the electrons can be estimated as:

$$\left(T_e\right)_{\max} = T_b + \left(\Delta T\right)_{\max} \tag{4.16}$$

with the second term $(\Delta T)_{max}$ determined by equation (4.15). The solution to this equation strongly depends on the determined laser energy flow density I_0 from (4.1) at the beginning of this chapter. For these values, Figure 4.4 shows the maximum electron gas temperatures

as a function of the diameter of gold and silver particles for the two different wavelengths of the Nd:YAG laser.

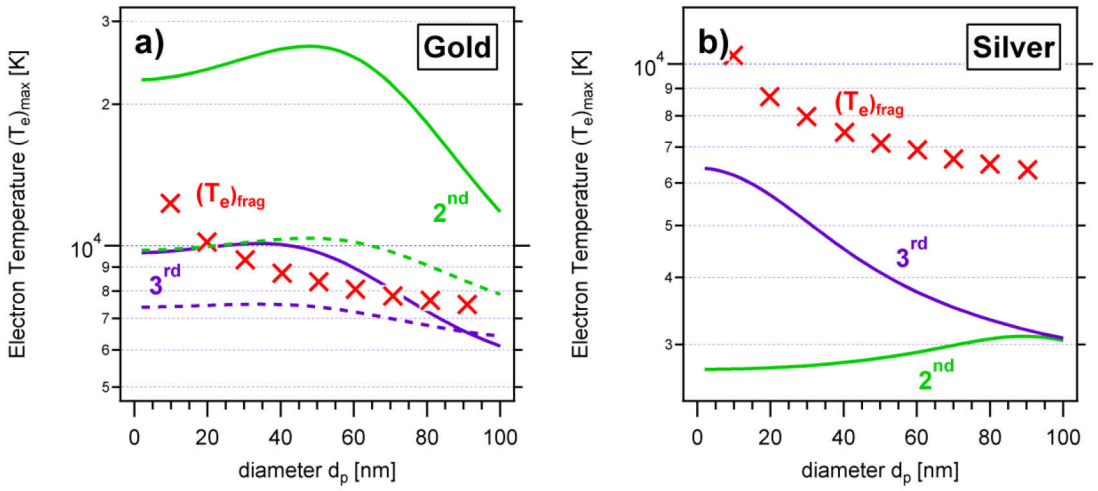

Figure 4.4: *Maximum temperatures of the electron gas in gold (a) and silver (b) nanoparticles of different diameters when irradiated by the second (2^{nd}) and third (3^{rd}) harmonic of a Nd:YAG laser. For gold the temperature dependence of the electron phonon-constant is considered in the dashed lines. The fragmentation temperatures[57] are displayed as red crosses for comparison*

As displayed, these temperatures strongly depend on the particle diameter, the laser wavelength and finally the particle material. For silver, the maximum possible electron temperature remains below 6500 K for all parameters, while for gold all calculated temperatures constantly reach very high values above 6500 K. In this regime the approach assuming a constant electron-phonon coupling is not valid any longer and processes become effective which lead to an increase of the electron-phonon coupling constant *g* with temperature.[40, 65] As a consequence, the maximum possible temperature is decreased. For gold, this effect becomes noticeable when the electron temperature exceeds 3000 K.[65] Figure 4.5 shows the course of the electron-phonon coupling factors with the electron temperature for gold (a) and silver (b). The values were determined by computational analysis based on electron structure calculations of the electron density of states and directly taken from the author's homepage.[65] The dashed horizontal lines show the experimentally determined constants[63] in the low temperature regime. The deviations for silver are very small for all calculated temperatures and so no correction is taken into account for this case. For gold the opposite is true for the whole temperature range that needs to be considered.

As a correction the calculated electron-phonon coupling factor is fitted in the interesting range between 3000 and 30000 K as a quadratic polynomial in *T*. The three fitting terms are shown in the inset of Figure 4.5 (a). As such, the constant *g* is replaced in equation (4.15) by this polynomial. The equation is then transformed into a cubic equation in *T*:

$$CT^3 + BT^2 + AT - 6 \cdot \frac{I_0}{\pi \cdot d_p^3} \cdot \sigma_{abs}^{\lambda}\left(d_p\right) = 0 \tag{4.17}$$

The equation is divided by the term *C,* followed by the application of the method of Cardano[66] which finds three solutions to the temperatures for each diameter. One solution is negative and the other one is even higher than the already calculated value assuming a constant value of *g.* Only the last possible solution provides the expected physical meaning. The obtained values are corrected by the boiling point of gold from equation (4.16) and plotted in Figure 4.4 (a) for each wavelength of the Nd:YAG laser as dashed lines.

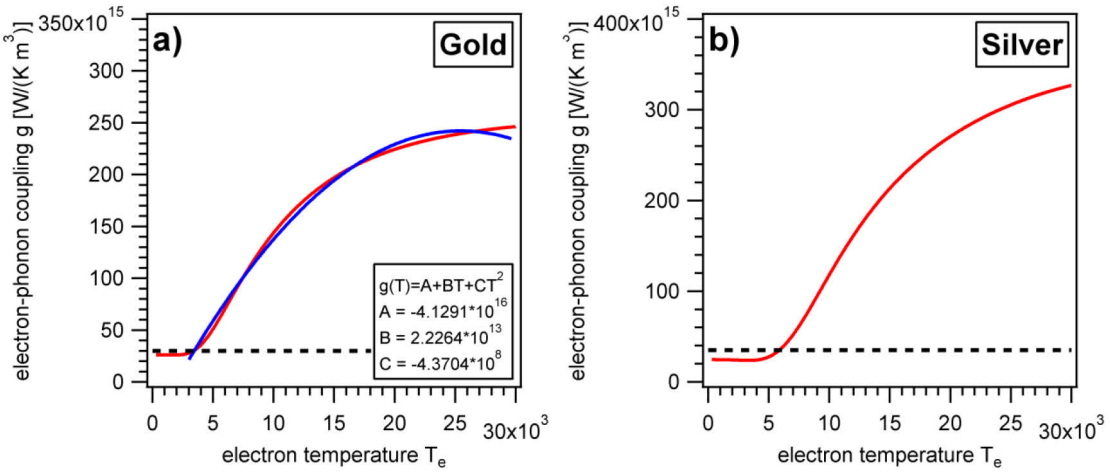

Figure 4.5: *Calculated[65] electron temperature dependence of the electron-phonon coupling constant for gold (a) and silver (b), horizontal line represents the experimental determined values in the low temperature regime[63]*

These upper limits of the electron temperatures permit to estimate the possibility of thermionic emission by calculating first the critical fraction of ejected electrons which can lead to particle fission. This is done by using the "liquid drop" model[67, 68] which was initially developed for small gaseous clusters of different metals. It was later adopted by Yamada[37, 38] to investigate the fragmentation of nanoparticles. In this model the cluster fission is treated as competition between Coulomb and surface forces. A highly charged particle becomes unstable when the disruptive Coulomb force exceeds the attractive cohesive force. The criterion for the Coulomb explosion is expressed by a ratio of fission *Y*:

$$Y = \left(\frac{q^2}{N}\right) / \left(\frac{16 \cdot \pi \cdot \sigma_S \cdot r_{WS}^3}{e^2}\right) = \left(\frac{q^2}{N}\right) / \left(\frac{q^2}{N}\right)_{crit} \tag{4.18}$$

Here, q is the number of charges per cluster, N is the number of atoms in the cluster, e is the elementary charge and σ_S is the surface tension. The parameter r_{WS} is the Wigner-Seitz radius, a parameter frequently used in condensed matter physics for describing the density of a system. It is the radius of a ball which contains the same volume as the volume per particle in the system under consideration. The index "*crit*" is the critical ratio where multiply charged nanoparticles are expected to readily dissociate into smaller ones when

$Y = 1$ (Rayleigh limit). The evaporation and Coulomb explosion competitively occur in the range $0.3 < Y < 1$ and only evaporation takes place when $Y < 0.3$. Accordingly, the created charges q at a ratio of $Y = 0.3$ are calculated for nanoparticles of different diameters by adopting the literature values $(q^2/N)_{crit}$ for silver 0.91 and gold 1.11[67] and considering equation (4.5) for the number of atoms in the particle. The charges are equal to the number of ejected electrons from the particle n_e^{ej}, hence a critical ratio (n_e^{ej}/N_e) for each particle diameter can be calculated which is equal to the minimum fraction of electrons to cause the particle fragmentation.

The fraction of electrons with energy ε that can be ejected by thermionic emission if their energy is above the sum of the Fermi energy E_F and the work function W can be calculated for each temperature from the equation:

$$\frac{n_\varepsilon}{N}(T) = \frac{\int_{\varepsilon}^{\infty} f_E \cdot \sqrt{E}\ dE}{\int_{0}^{\infty} f_E \cdot \sqrt{E}\ dE} \quad \text{with } f_E = \frac{1}{1 + \exp\left[\frac{E - E_F}{kT}\right]} \tag{4.19}$$

where the function f_E is the Fermi-Dirac distribution and $\sqrt{E}$ originates from the density of states around the energy E. For gold and silver the Fermi energy E_F is under consideration of equation (4.5) and the particle volume $V_P = \pi d^3/6$ given by:

$$E_F = \frac{\hbar^2}{2 \cdot m_e} \cdot \left(\frac{3 \cdot \pi^2 \cdot N_e}{V_p}\right)^{2/3} = \frac{\left(12 \cdot \pi^2\right)^{2/3} \cdot \hbar^2}{2 \cdot m_e \cdot a^2} = 8.87x10^{-19}\ \text{J} = 5.54\ \text{eV} \tag{4.20}$$

Here, N_e is the number of electrons in a particle obtained by (4.5), and m_e is the electron mass. The numeric integration of equation (4.19) delivers the fraction of electrons for every electron temperature which can be thermally ejected from a particle. The results can directly be compared to the results of equation (4.18) where the minimum fraction of electrons causing the particle fragmentation has been calculated. By comparison, the minimum electron temperature $(T_e)_{fr}$ at which the fragmentation processes starts to emerge is obtained. The results have been adopted from Pyatenko *et al.*[57] and are shown for different diameters of silver and gold particles in Figure 4.4 as a comparison to the calculated electron temperatures.

In case of silver, the difference between the maximum reachable temperature $(T_e)_{max}$ for the given laser flow densities I_0 and the fragmentation temperature $(T_e)_{fr}$ is too large to achieve particle fragmentation at any point. The same holds true when gold particles are irradiated with the third harmonic (λ_{Ex}=355 nm) of the Nd:YAG laser. The situation changes for the second harmonic (λ_{Ex}=532 nm) where particle fragmentation due to thermionic emission followed by Coulomb Explosion is possible for all particles with a diameter larger than

20 nm. By further increasing the laser intensity, thermionic emission can also emerge for the third harmonic in small silver and all gold particles while the second harmonic is not suitable in silver for all possible parameters without laser focusing. Beam focusing increases the laser intensity and raises the electron temperature. Since this creates different electron temperatures in different particles along the beam, the experimental results are more difficult to interpret. In the performed experiments, these high values for the energy flow density were only used for gold particles with a diameter of 20 nm, where the results of the calculation are not explicit under all the applied assumptions. For larger particles, the intensity in a typical experiment was normally decreased to 3-4 mJ/pulse, so that thermionic emission should be excluded for these cases. Please also note that the authors in this work[33] ruled out the possibility of thermionic emission up to a laser energy flow density of I_0=5.7 x 10^{12} W/m^2 when gold particles of 36 nm diameter were irradiated with the third harmonic of a Nd:YAG laser, the same type used in the experiments in this thesis. They used transient absorption spectroscopy with probe lasers at 488 nm and 635 nm and up to this value they were not able to detect any contribution of solvated electrons showing a strong broad absorption in the red.[69] Above this limit, strong absorption was observed, but by calculating the number of electrons from the absorbance change at 635 nm and the absorption coefficient of solvated electrons they could also exclude the influence of Coulomb explosion for even higher intensities in their experiment. In the end, the influence of thermionic emission followed by Coulomb explosion is negligible for most of the applied parameters in this work.

4.2.2 Melting and Evaporation

At low laser intensities morphological changes in metal particles are caused by photothermal processes which prevail in this regime over all described phenomena induced by ionization. The energy absorbed by a metal particle while irradiated with a laser pulse is then transformed into particle heating, melting and vaporization. Since the time constant for the melting occurs on a time scale of 30 ps[70] and the vaporization is considered to happen afterwards, the transformations do not occur during the pulse duration of the picosecond laser. However, all the processes including the complete re-cooling of the particles are fast enough and complete within the time period of 100 ms (10 Hz) between two consecutive laser pulses. Pyatenko[71] calculated characteristic time ranges of 2 x 10^{-6} s to 2 x 10^{-5} s for radiation cooling and 10^{-5} s to 10^{-4} s for conductive/convective cooling when the particle diameter is varied between 10 and 100 nm. Takami[32] could not detect any blackbody radiation of gold particles with a diameter of 25 nm after 100 µs of the pulse. All these times are negligible compared to the 100 ms interval between two pulses. As heat loss was

excluded in the previous chapter, all the energy absorbed by a particle is spent on its heating and melting and the absorbed energy of a single laser pulse is equal to:

$$Q_{abs}\left(d_p\right) = \frac{4 \cdot A_0^{soft}}{\pi \cdot D_0^2} \cdot \sigma_{abs}^{\lambda}\left(d_p\right) = J_0^{soft} \cdot \sigma_{abs}^{\lambda}\left(d_p\right) \tag{4.21}$$

where J_0^{soft} is the laser fluence as defined in equation (4.21). The index "*soft*" defines a laser power where the particles are heated and melted by a single pulse, but are not evaporated at all. The energy needed to accomplish complete melting until the boiling point of the metal is given by the energy balance equation:

$$Q_{abs}\left(d_p\right) = \rho_p \cdot \frac{\pi \cdot d_p^3}{6} \cdot \left[c_p^s \cdot \left(T_m - T_0\right) + \Delta H_m + c_p^l \cdot \left(T_b - T_m\right)\right] \tag{4.22}$$

Here, ρ_p is the density of the metal, $c_p^{\,s}$ and $c_p^{\,l}$ is the heat capacity for the solid and the liquid metal, respectively, and ΔH_m is the enthalpy of fusion. T_m and T_b are the melting and boiling points of the metal with T_0 the initial temperature (293 K). For particles of different diameters d_p the combination of both equations offers the possibility to calculate the required laser fluences J_0^{soft} that heat a solid particle up to the melting point (1st term, blue), to complete melting (2nd term, red) and heat the liquid particle further to the boiling point (3rd term, green) by one laser pulse. In this model the photon densities for different laser widths are not taken into consideration. All physical constants used in the equation are adopted from bulk values[64, 72] and are summarized in the following table:

Table 4.1: Relevant physical constants for gold and silver

physical constants	silver	gold
metal density ρ_p [64]	10.5 g/cm^3	19.3 g/cm^3
heat capacity $c_p^{\,s}$ [72]	0.235 J/g K	0.129 J/g K
heat capacity $c_p^{\,l}$ [72]	0.318 J/g K	0.149 J/g K
heat of fusion ΔH_m [64]	104.76 J/g	63.71 J/g
melting point T_m [64]	1235 K	1337 K
boiling point T_b [64]	2435 K	3129 K

The temperature estimation for the melting and boiling point of the metals with bulk physical constants are justified by the fact that the melting point of gold particles only decreases drastically when the particle size is less than 5 nm.[73] For silver the same fact is assumed. The required energy to heat and melt the particles up to the boiling point by considering all terms on the right side in equation (4.22) is shown for the second and third harmonic in Figure 4.6 (a) and (b) as a function of particle diameter. One laser pulse with higher energy than the calculated threshold in the corresponding curve will start particle evaporation and size reduction. For gold (a) the second harmonic is more efficient than the third harmonic and thus, less energy is required to heat the particles to the boiling point.

The critical energies are for both wavelengths on the order of milli-joules and increase with diameter. They have a small broad minimum at a diameter of around 47 mm for the second and 34 nm for the third harmonic. For gold particles larger than 100 nm laser pulse energies for the second harmonic are higher than 10 mJ/pulse and by using picosecond laser pulses with their high photon densities the colloids may simultaneously be affected by ionization phenomena. The heating of silver particles with the Nd:YAG laser in (b) is by far not as efficient, mostly because of the small absorption cross sections at these wavelengths. The required energies to heat the particles to the boiling point are basically around one order of magnitude higher than for gold and the third harmonic is more efficient than the second. While the curve for the third harmonic continuously increases with diameter, the second harmonic has a profound minimum at a diameter of around 90 nm. If the laser fluence for this wavelength is lower than 0.2 J/cm^3, the calculation indicates that no particles can be evaporated. For picosecond laser pulses both wavelengths are in the range where ionization effects may play a role during irradiation.

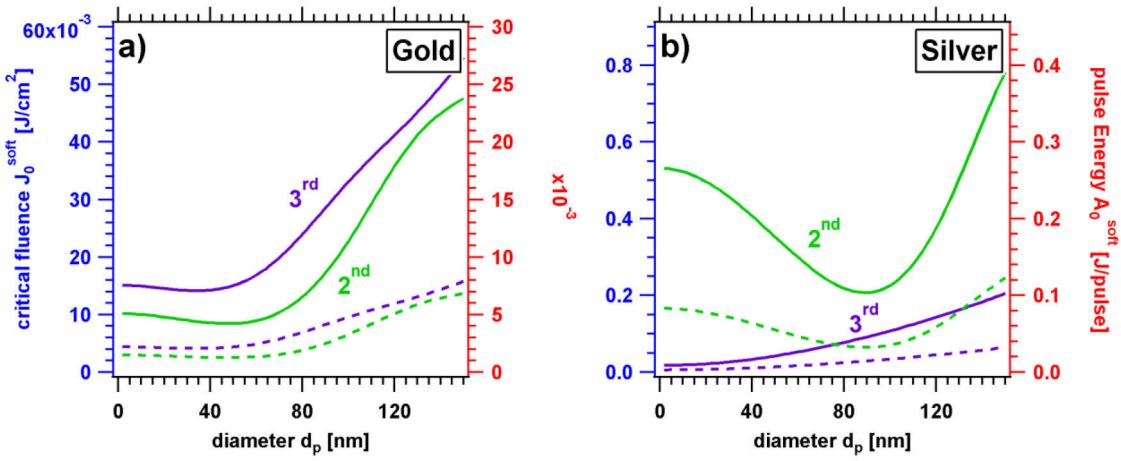

Figure 4.6: *Minimum fluence and pulse energy needed to initiate the process of evaporation for gold (a) and silver (b) particles of different diameters, calculations for the second (2nd) and third (3rd) harmonic of a Nd:YAG laser, dashed lines are the required values for heating up the particles only to the melting point*

It should be pointed out that these estimations were made for bare particles while the experiments were performed with gold particles covered by a citrate layer and with silver particles covered by a polymer shell. These additional layers slightly increase the particle absorption cross section and decrease the necessary intensities. Furthermore, it is well known that the melting of the nanoparticles starts at their surfaces at reduced temperatures.[74-77] A liquid layer on a rigid metal core was directly observed for 100 nm lead particles in a SiO matrix by dark-field electron microscopy[75] while the surface melting of gold nanoparticles was studied by in-situ transmission electron microscopy.[78] In computational simulations Wang *et al.*[79] observed shape transformations of gold nanorods consisting of 10^3 to 10^4 atoms below the melting point of gold. In view of all these results the actual shape transformations of the investigated particles should already occur well below their melting

point due to the occurrence of surface melting. The temperature at which these changes start should decrease with a decrease in the particle size. Inasawa *et al.*[34] calculated the actual temperature and the thickness of the corresponding liquid surface layer for ellipsoidal gold particles with a mean diameter of the major axis of 38 nm by using both the heat balance and the surface melting model.[80] The calculations based on laser heating and thermally induced heat experiments suggest that shape transformations start to occur at 1208 K which is by more than 100 K lower than the melting point for the bulk. The corresponding thickness of the liquid layer to reduce the initial aspect ratio of the ellipsoids from 1.29 to smaller than 1.1 for spheres was calculated to be between 1.2 nm and 1.4 nm. The described effects originating from surface melting are taken into account in the model above by calculating the required energy to heat up the particles only to the melting point. The results are shown in Figure 4.6 (a) and (b) as dashed lines. In the approximate energy range between the dashed and associated solid lines particle transformation by particle melting can occur without the unwanted size reduction due to evaporation. For gold the new values are well below 10 mJ/pulse and ionization phenomena should emerge by a limited extent only for the third harmonic. For silver this rather occurs for the second harmonic. The total energies for both metals are quite lower compared to the previous cases, especially for very small and very large particles.

The induced changes after exposure to low-energy femtosecond and nanosecond laser pulses were investigated in detail for short gold nanorods in colloidal solution with high resolution transmission-electron-microscopy by Link[81] and Wang[82] The originally prepared nanorods with aspect ratios of 3-7 were defect free single crystals with {100}, {111} and {110} facets and contained no volume dislocations, stacking faults or twins while the relatively unstable {110} facets were absent in nanospheres. The sphere structure was dominated by lower energy {111} and {100} facets with shapes of truncated octahedral, icosahedral and decahedral and contained planar defects. After these observations the authors proposed a mechanism where the rod-to-sphere rearrangement during laser illumination starts in the interior of the rod by the creation of point and line defects which serve as nuclei for the formation of twins and stacking faults. This is only possible if melting occurs at the defect sites before. Surface diffusion with surface melting takes place almost simultaneously and enhances the growth of the twinned crystals. This process is driven by surface energy reduction where the {111} surface area grows on costs of the {110} surface. A continuation growth of the twinned crystal finally eliminates the unstable {110} surface completely and the entire particles is then enclosed by the more stable {111} and {100} faces.

4.3 Results and Discussion

The theoretical evaluation of the necessary energies with the objective to completely transform the shape of colloidal particles through the interaction with laser light based on some a priori assumptions, like mono-disperse ideal spherical particles. Therefore, the calculated energies can only serve as guidance to the experiment. Chemical reduction methods produce broader size distributions of lower particle qualities with irregular ellipsoidal shapes and corrugations on the surfaces and add some impurities to the solvents. For experiments under soft irradiation conditions the most efficient wavelength for each metal promises the best results and avoids unwanted auxiliary processes. For gold the second harmonic (λ_{Ex}=532 nm) is most efficient, although the difference to the third harmonic (λ_{Ex}=355 nm) is not big and some authors report successful results for both wavelengths.[32, 52] For silver literature is as well available for both cases,[30, 83] but the calculations indicate that the third harmonic (λ_{Ex}=355 nm) is strongly preferred, especially when very small or very large particles are irradiated. In one of the first experiments the second harmonic (λ_{Ex}=532 nm) was tested, but the result in terms of complete shape transformation and surface roughness reduction was not very satisfying. Therefore, the wavelength for the irradiation in the following experiment was changed to the third harmonic (λ_{Ex}=355 nm).

4.3.1 Irradiation of Gold Particles

For gold various experiments were performed with different sizes of particles to determine the required threshold under soft irradiation conditions. The size of the particles in each section is continuously reduced to a diameter of 20 nm.

4.3.1.1 Determination of the Optimum Pulse Energy for Large Particles

In the first experiment, gold particles with a mean diameter of 169 nm and a mean aspect ratio of 1.25 were irradiated by a Nd:YAG laser with a wavelength of 532 nm using pulse energies (fluences) between 1.5 mJ (3 mJ/cm^2) and 10 mJ (20 mJ/cm^2). The results of the energy balance equations (4.21) and (4.22) which characterize the melting process indicate that the experimentally determined energy for melting these large particles should serve as an upper threshold for all other sizes in the range between 20-150 nm. Since the chemical methods for this case provide also a broad distribution of particle sizes the efficiency of the irradiation method to change the shape of the whole ensemble can be demonstrated. An optical absorption spectrum of the root suspension before the irradiation is shown in Figure 4.7 (a) with the corresponding electron micrograph in (b) and the distribution of the aspect ratios in (c). The absorption spectrum exhibits a single band in the visible region which can

be assigned to intraband transitions (particle plasmon band) occurring within the conduction band derived mainly from the gold $6s^1p$ hybridized atomic orbitals. For the large particles presented here the dipole approximation is no longer valid. The incident light can no longer polarize the nanoparticles homogenously and higher-order modes are excited. These modes depend on the particle radius r and peak at lower energies. Therefore, the plasmon band is red shifted with respect to the dipole mode and has a maximum at around 570 nm. These retardation effects also broaden the plasmon band since different multipole modes can be excited simultaneously and peak at different energies.[14]

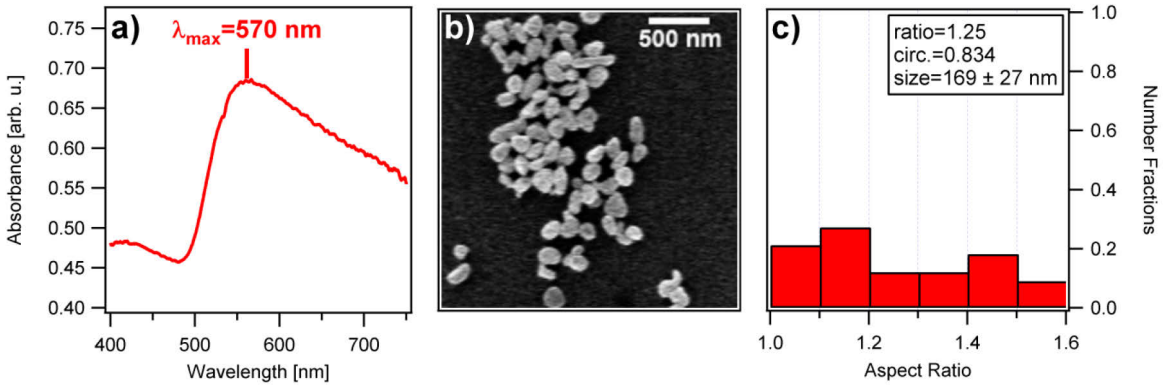

Figure 4.7: *(a) Optical absorption spectrum of gold particles before the irradiation, (b) corresponding scanning electron micrograph, (c) distribution of the aspect ratios obtained by SEM images.*

Contributions of interband transitions, occurring between the d-band and the unoccupied states of the conduction band (5d → 6sp), start to emerge for gold particles at a wavelength of 750 nm and continuously increase their proportion to the whole absorbance towards the ultraviolet region.[48, 84] Between 400 and 500 nm the spectra is dominated by these interband transitions. Thus, an increase in absorbance is detected for short wavelength. As gold nanorods show an absorption spectrum with two peaks, one at around 530 nm (transverse plasmon band) and the other at around 800 nm (longitudinal plasmon band),[52, 85] the initial particles with ellipsoidal shapes are also considered to show the transverse and longitudinal absorption. Due to their low mean aspect ratio, as shown in Figure 4.7 (b), those two peaks are not separated, but overlap with each other. Therefore, the absorption band in (a) is further asymmetrically broadened towards the red side as it actually consists of two peaks, one at a shorter wavelength for the transverse mode and one at longer wavelength for the longitudinal mode. The ellipsoidal shapes of the un-irradiated nanoparticles are clearly visible in the corresponding SEM image in (b). The particles have an oblate geometry and some even possess more irregular shapes with sharp edges, corrugations and different visible planes on the surface. A detailed analysis of the measured electron micrographs in (c) reveals a broad distribution of aspect ratios up to a maximum value of around 1.6. The average circularity for the particles which is the proportion of the area and the perimeter (4π

area/perimeter^2) has a value of 0.834. For an ideal circle the factor should be 1. The results of the irradiation experiments with different laser energies are shown in Figure 4.8. The absorption spectra of the sample suspension before and after the irradiation together with the respective pulse energy and irradiation time are displayed on the left side (a-d). The laser pulse energies increase from top to bottom.

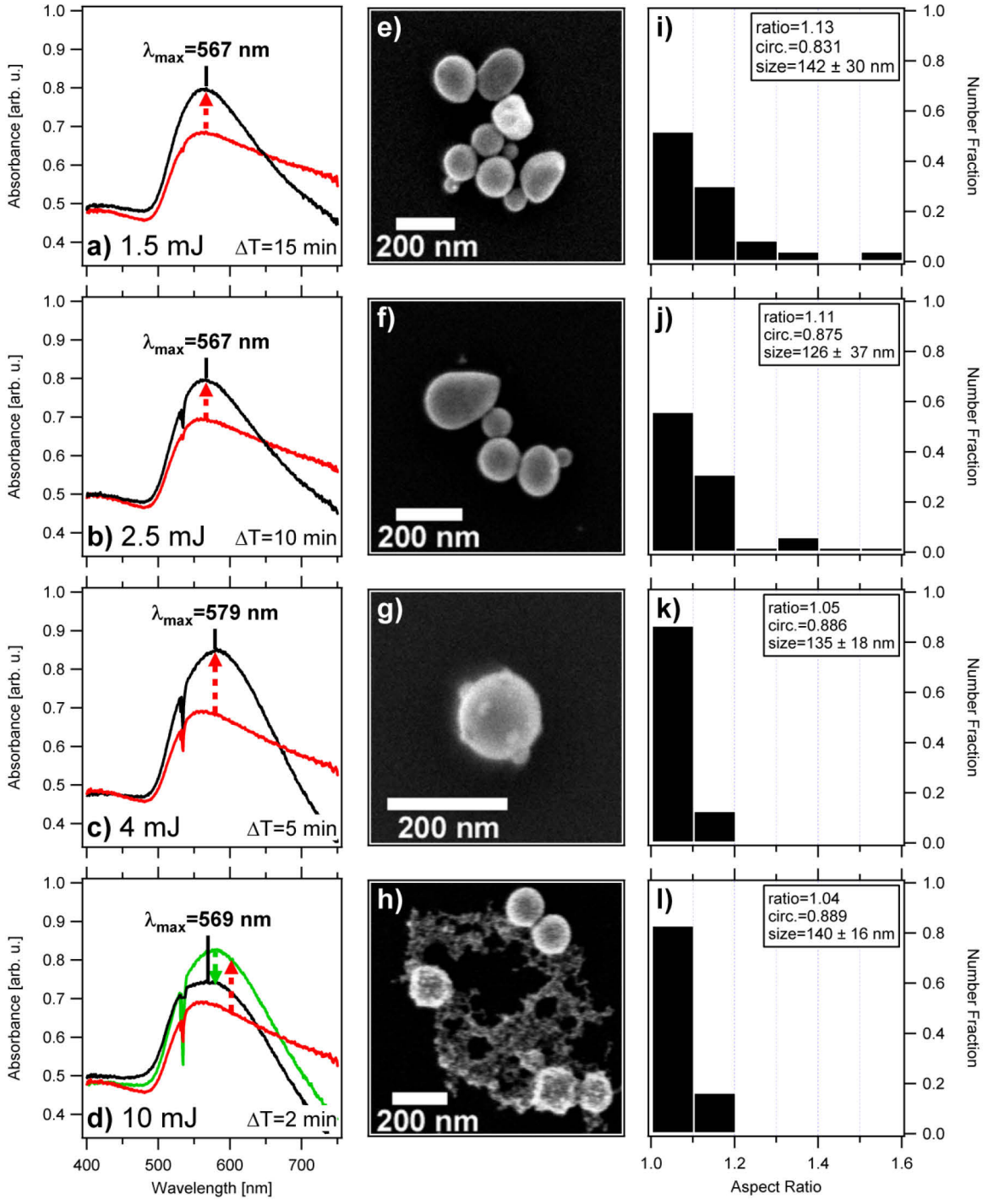

Figure 4.8: *Shape and size dependence of gold nanoparticle irradiation on the laser pulse energy. Optical absorption spectra before and after the irradiation are shown on the left side (a-d). Representative SEM images corresponding to the laser energy to the left are shown in the center of the figure (e-h). Please note that the magnification is not the same for all pictures. The aspect ratio distributions determined from the SEM images are given in the statistical plots on the right side (i-l).*

The irradiation time depends on the induced changes in the in-situ absorption spectra recorded every 2 s by the spectrometer. As long as the spectra were modified by the laser, the irradiation was continued. Since the total absorbance decreased untypically for a pulse energy of 10 mJ after 4 s or around 40 pulses the procedure was interrupted after 2 min, although changes in the recorded spectra were still occurring. The SEM images (e-k) corresponding to the final irradiation product for each pulse energy are displayed to the right of the optical absorption data while the statistical plots (i-l) show the aspect ratio distributions of the produced particles.

For a pulse energy of 1.5 mJ the absorption shows compared to the initial spectrum a clear shift to a shorter wavelength and an increased peak intensity. These changes in the absorption are consistent with previous reported work[30, 83, 86, 87] and indicate that the laser induced shape transformation has started. The changes in peak intensity and line width are consistent with the removal of the rods with higher aspect ratios absorbing on the red edge of the absorption band and an increase in the number of spherical particles. The absorbance below 500 nm is almost unmodified because it originates mainly from the interband transition (5d → 6sp)[84] which is insensitive to the size and shape of the nanoparticles.[52, 88] Both the corresponding electron micrograph and the distribution of the aspect ratios confirm these observations. The shape transformation of the particles in the SEM images has commenced, but is far from being completed. The mean aspect ratio of the particles is reduced to a value of 1.11 while the average circularity value remains with 0.831 nearly constant compared to the root suspension. The crystal surfaces show still minor corrugations, but with most of the sharp edges flattened or disappeared. Together with the shape transformation size reduction seems to happen and the average size of the particles is reduced from 169 nm to 142 nm. This effect is caused by the 2-dimensional (2D) imaging of a 3-dimensional (3D) particle in the SEM. While the visible lateral dimensions of the oblate spheres are reduced, the invisible height in a sphere-like particle is increased. This is later confirmed in Chapter 7 by atomic force microscopy.

The pulse energy of 2.5 mJ (fluence 5 mJ/cm^2) is for this particle diameter still below the calculated energy threshold to reach the melting point of bulk gold in Figure 4.6, but the shape transformation has progressed further. The sharp peak at a wavelength of 532 nm in the black curve of the absorption spectrum (b) originates from the irradiation laser whose light is scattered by the particles and detected by the spectrometer perpendicular to it. A suitable notch filter would have blocked the excitation light, but it does not influence the measurement. In the SEM image the particle surfaces are now completely smooth without any detectable faces or edges. The average values for size (126 nm) and aspect ratio (1.11) are further decreasing while the circularity goes up to a value of 0.875. However, the energy is still not large enough to transform all ellipsoidal particles completely into spheres.

This changes for a pulse energy of 4 mJ or a fluence of 8 mJ/cm^2, even though the value is still below the threshold for reaching the bulk melting point of gold in Figure 4.6. The combination of equations (4.21) and (4.22) calculates for spherical particles with diameters between 120 and 170 nm a gold temperature between 1096 and 827 K, which is up to 40% below the melting point of 1337 K for the bulk metal. These values strongly depend on the exact beam diameter in the experiment, but comparable values for the melting point reduction at a gold surface can be found in literature.[89, 90] In any case, the measured SEM images together with the detailed shape analysis suggest that after an irradiation of 5 minutes all particles are transformed into nearly ideal spheres. The statistic plot shows a very narrow distribution of aspect ratios with a mean value of 1.05 and the circularity increases further to 0.886. The condensed gold droplets on the particle surface in the SEM image (g) provide further evidence that the applied photon energy in the experiment is not only sufficient to melt the gold on the surface, but even high enough to vaporize it to some amount. According to classical thermodynamics the vapor pressure at a liquid interface in equilibrium for a given temperature is expressed by the Clausius-Clapeyron relation,[91] but the curvature effect should give about a 10% larger pressure[92] when the Kelvin equation[91] is taken into consideration. In other words the important factor which determines the evaporation of nanoparticles is not the temperature itself, but the vapor pressure at the liquid interface. These effects support the formation of gold vapor even when the absorbed photon energy is insufficient to reach the boiling point. The surrounding water is not considered to disturb the vaporization process, because a water vapor layer around the hot liquid gold particles should first be formed[54] and the amount of gold vapor depends on the vapor pressure at the interface. After being cooled down again, the vaporized gold most probably goes back to the “parent” particle and condensates on the surface in the shape of the drops.[31, 34] With sufficient laser energy the vaporized gold atoms should also be able to leave the heated particle and condensate as additional small particles. This would result in a bimodal size distribution which is not observed here. This exact behavior with reproducible droplet creation on the particle surface has not been reported in literature to the author’s best knowledge. The effect is not only reproducible for different particles, but also for different laser experiments with different suspensions as long as the same excitation energy is used.

For a pulse energy of 10 mJ which heats the particles already to temperatures between the melting and boiling point according to Figure 4.6 (a) the absorbance spectrum (d) shows the same spectral changes only in the first 4 s or around 40 laser pulses (green curve) observed for all lower used energies. The maximum peak intensity goes up and the line width gets narrower. After this time the maximum intensity continuously decreases with every new pulses indicating that the total amount of absorbing material diminishes. These absorbance

changes are caused by size reduction of gold nanoparticles with the formation of a bimodal size distribution. Aggregation to very large clusters not absorbing in the visible could be a second reason. Therefore, the irradiation was stopped after two minutes. The SEM measurement (g) clearly confirms the assumption of size reduction while the statistic plot (l) shows no further improvement in the shape of the remaining "mother" particles. For this statistics only the remaining large particles were counted, since the interest in this work lies purely in shape transformation and not size reduction. The laser energy is now high enough that both liquid and vapor can coexist at the boiling stage and so gold vapor can also be formed inside the liquid gold particles. Gold bubbles in the liquid gold drops move then to the surface which results in the projection of some volume of liquid gold around the bubble.[92] Therefore after being cooled, particles with gold strings are formed. Such gold strings can also turn into smaller particles by additional pulses. The diameters of these small particles are almost independent of the irradiated laser energy[92] and the condensation kinetics of gold vapor are thought to be one of the main factors for the formation of small particles with downward limited size restriction. Small particles generated by size reduction are less expected to reduce their size, because the time constant of heat dissipation is proportional to the square of the radius (10 ps for 5 nm, 50 ps for 15 nm and 270 ps for 40 nm diameters).[93] Hence, though small particles absorb photon energy as well, they are not heated to high temperature due to the heat dissipation.

Summarizing, the pulse energy for gold nanoparticles of that size should be kept between 2.5 mJ and 4 mJ. This ensures that nearly all particles are transformed to nearly ideal spheres with a smooth surface and avoids the unwanted effects from the liquid gold droplets on the particle surfaces or size reduction.

In a second experiment gold nanoparticles with an average size of 83 nm were irradiated with a pulse energy of 3 mJ for 240 s. The original colloids before the irradiation are shown in the SEM image (a) of Figure 4.9 while the result after the irradiation is shown in (c). The shape transformation is completed and all particles are transformed into nearly ideal spheres without any side-effects. As the pulse energy is adjusted to the previously determined optimal value, but the particles are in average 90 nm smaller, the dependency of the pulse energy on the diameter cannot be as strict as indicated by Figure 4.6. In the related curve the energy for particles of that size is sufficient to heat the particles at least to the melting point (heat of fusion neglected). For particles of 150 nm this would correspond already to a pulse energy of around 7.5 mJ which is above the previous experimentally determined critical value where problems with particle evaporation started to emerge. The irradiation induced modifications with time are illustrated in the absorption spectra of Figure 4.9 (c) and show the same changes and features as described before. The maximum intensity shifts from 560 nm to 534 nm and the full width at half-maximum (FWHM) decreases from

around 100 nm to 30 nm. In the first 40 s (around 400 pulses) most of the changes are already completed and in the rest of the time (200 s or 2000 pulses) only minor modifications occur.

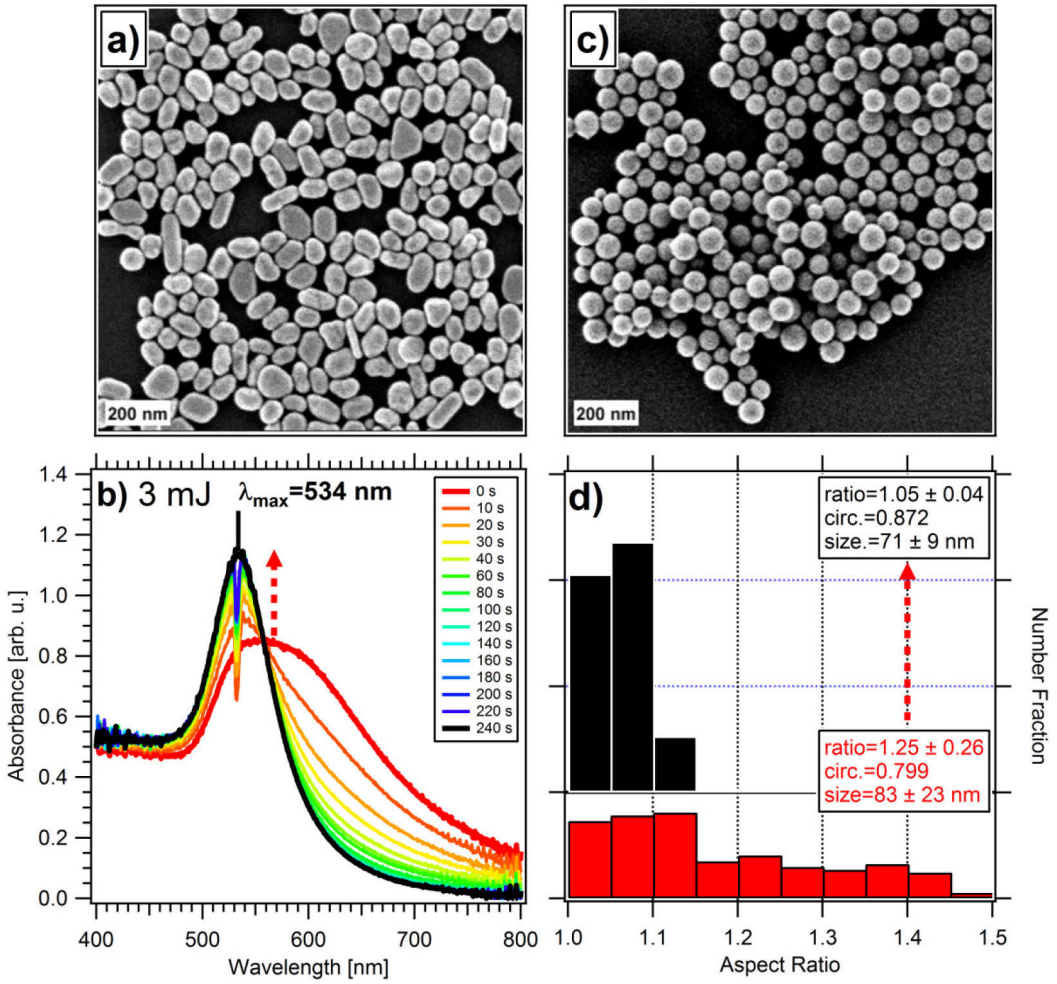

Figure 4.9: *SEM images of gold colloids before (a) and after the irradiation (c) with the second harmonic of a Nd:YAG laser, spectral changes during the irradiation (b) and distribution of the aspect ratios before (red) and after (black) the laser treatment (d)*

For an energy where shape transformation is dominant, the process seems to stop after all particles are converted to spheres and more spectral changes can only be induced by a higher pulse energy which would cause size reduction. This is very convenient for the experiment since the end of the process is defined. In the statistics plot (d) a very narrow distribution of aspect ratios is reached after the transformation. The mean aspect ratio decreases from 1.25 to 1.05 with the circularity increasing from 0.799 to 0.872. As the height of the oblate particles apparently increases, the size reduces from 83 to 71 nm.

4.3.1.2 Laser Irradiation of Medium Sized Particles

In the following experiment the size of the nanoparticles is further decreased to a diameter of 33 nm which is around the minimum of the curve for the second harmonic in Figure 4.6

(a) required to initiate shape transformation under soft irradiation conditions. This suspension was irradiated with pulse energies (fluences) between 0.5 mJ (1 mJ/cm^2) and 4 mJ (8 mJ/cm^2) where the last value is near the limit for soft irradiation conditions in Figure 4.6. The results are summarized in Figure 4.10.

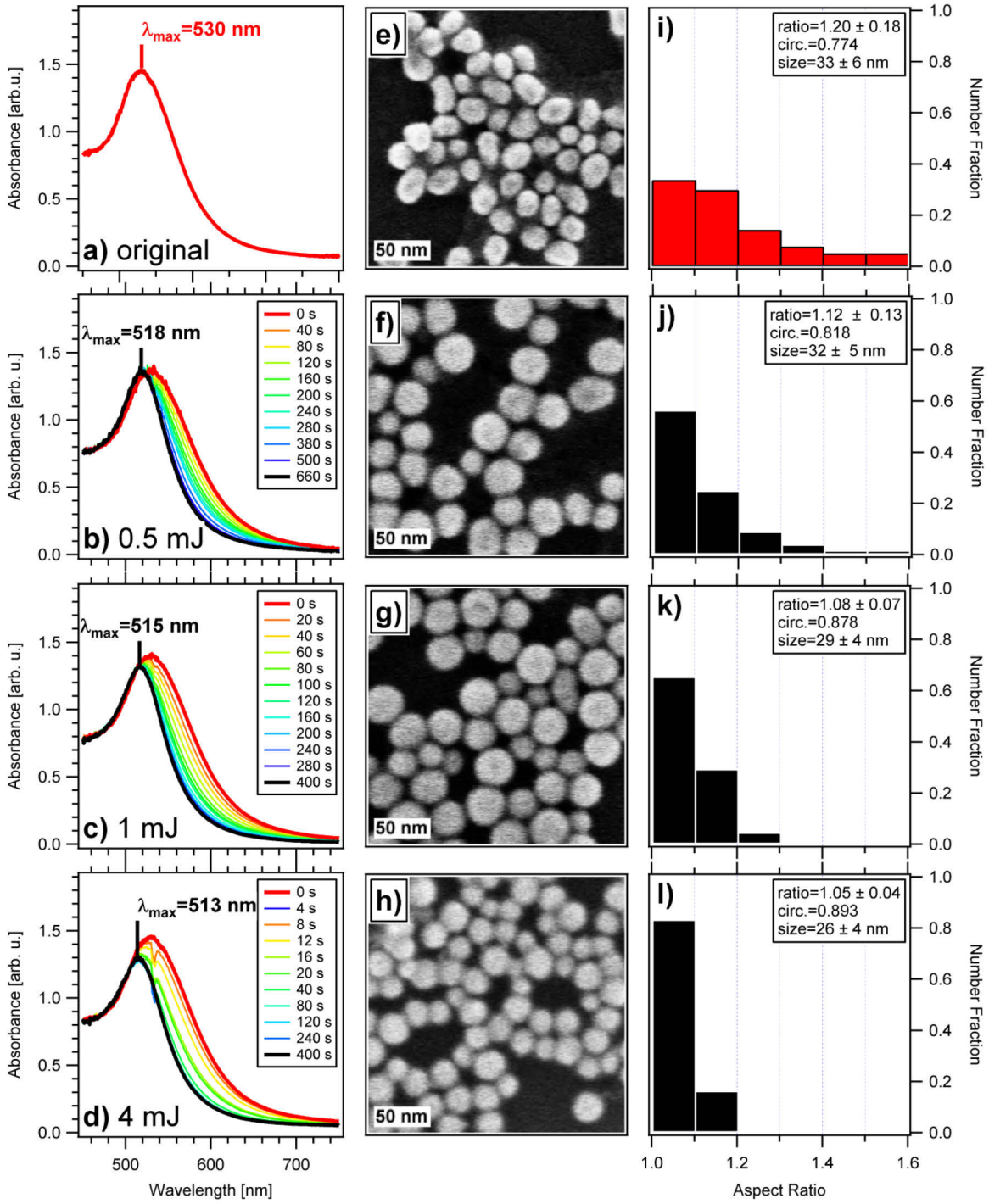

Figure 4.10: *Shape and size transformation in relation to the applied pulse energy for gold particles with a diameter of 40 nm. Optical absorption spectra (a-d) show the shift of the maximum intensity position with time, SEM images (e-h) give an impression of the results and the corresponding statistic plots (i-l) show the distribution of aspect ratios for each experiment.*

The position of the maximum absorbance consequently shifts with increasing laser energy in (a-d) from 530 nm to 513 nm for the highest energy, while the FWHM decreases from 80 nm to 66 nm. The absorbance intensity maximum is not increasing as observed in the previous cases for larger particles. The signal is nearly constant for a pulse energy of 0.5 mJ and decreasing for energies higher than 1 mJ/pulse. Since a bimodal size distribution cannot be imaged by the SEM measurements for all energies and the energy is still very low in (c) this behavior is not associated to laser induced size reduction. The FWHM is also getting continuously smaller for all presented energies in contrast to Figure 4.8 (d) which shows an increase in the FWM as size reduction occurs. One possible explanation could be that the size of the particles is close to the quasi-static regime where retardation effects can be neglected and the resonance in the dipole approximation is not depending on the particle size. For gold, this regime is reached for diameters of around 25 nm.

For larger particles the higher order modes shift to smaller wavelength when shape transformation proceeds and contribute to the absorption at the resonance position of the sphere and therefore, the corresponding absorbance intensity maximum increases.

For smaller particles these retardation effects can be neglected and the signal gets weaker during the transformation.[94] The statistics plots (j-k) show that the shape transformation is incomplete for the lower pulse energies. Only for the highest energy a comparable aspect ratio and circularity is reached as observed from the previous experiments. From (i-l) the mean aspect ratio and the average size are getting smaller while the circularity is increasing. On one hand laser assisted transformation starts for these smaller particles at lower energies, but on the other hand they are more stable against higher laser energies when the pulse energy relative to their size is considered in Figure 4.6. Please note that in Figure 4.10 (d) for an energy of 4 mJ/pulse no droplets on the particle surfaces are visible.

As a control measurement the irradiation was repeated for a gold particle suspension with an average size of 38 ± 6 nm, a mean aspect ratio of 1.08 ± 0.08 and a circularity of 0.807. This time, the energy range around 4 mJ/pulse is probed to determine the evaporation threshold and re-check the particle stability. The results for energies with a value of 3, 4 and 6 mJ per pulse are summarized together with the statistics in Figure 4.11. Please note that the absolute absorbance in (a-c) is higher than in the previous experiment, because a larger cuvette (20x20 mm, QG-101) with an optical pathway of 20 mm for both the laser and the white light was used to test the irradiation of larger suspension volumes. During the irradiation procedure the position of the absorption band continuously shifts from 534 nm to 515, 514 and 513 nm with the subsequent next higher applied energy.

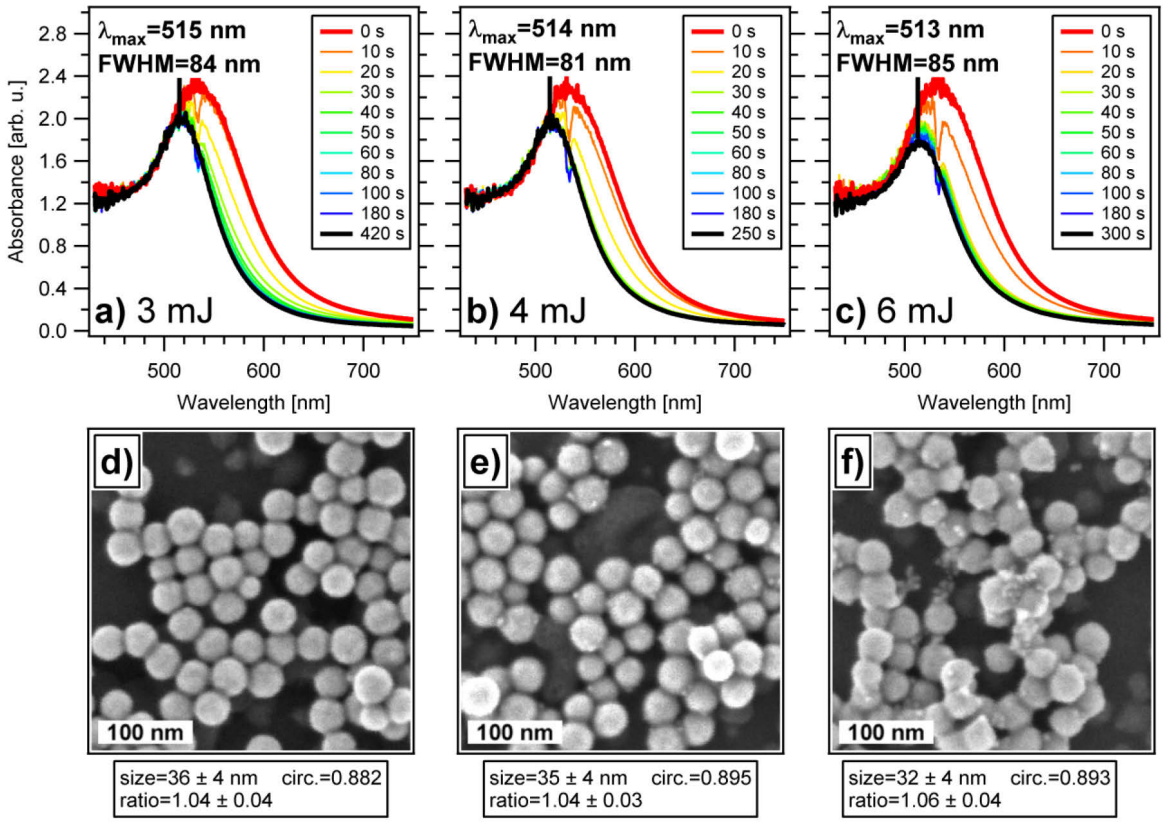

Figure 4.11: *(a-c) In-situ absorption spectra for pulse energies of 3, 4 and 6 mJ respectively, (d-f) corresponding SEM images with extracted statistical data*

Even with the smaller shifts in the maximum intensity the irradiation induced changes in the whole suspension are still so large, that they are visible with the bare eye; see Figure 4.12 for a comparison of the original suspension before the irradiation with the one after irradiation from Figure 4.11 (b) and 4 mJ/pulse.

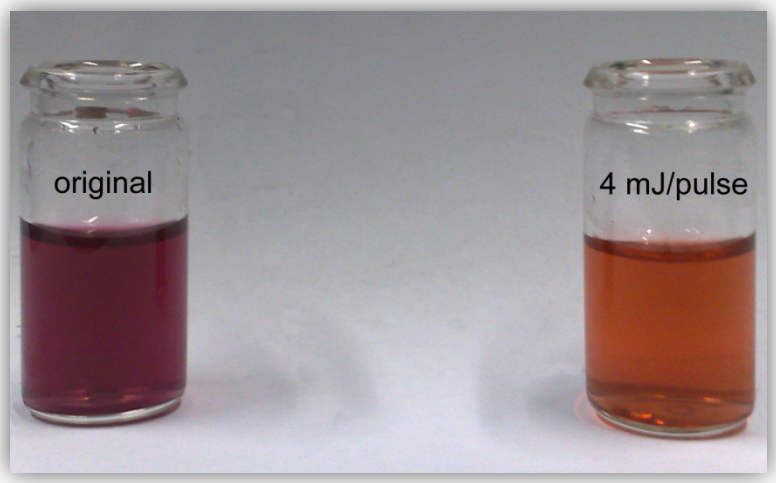

Figure 4.12: *Color change of the suspension before and after irradiation*

The rate of the spectral changes in the first minute improves when the energy is increased. After this time only limited changes in the spectra are visible and the process stops

automatically. While the maximum absorption for the two lower energies is comparable it decreases further for the highest energy with 6 mJ/pulse. The FWHM for the two lower energies decreases from 95 nm to 84 and 81 nm, respectively, whereas it increases again for the 6 mJ/pulse. For this case a very long irradiation time was selected to ensure the stability of the absorption spectrum during irradiation. As stated before the broadening of the FWHM is an indication that evaporation has started. The corresponding SEM micrograph in (f) confirms this and shows a bimodal size distribution which is typical for size reduction from evaporation. In the SEM images (d) and (e) all particles are transformed into nearly ideal spheres which is supported by the statistical values presented on the bottom. In contrast to the first experiment in this size range the SEM image (e) for a pulse energy of 4 mJ shows droplets on most of the particle surfaces. Since the determination of the beam diameter and the pulse energy is afflicted with some error it is most likely that the relative laser fluence differed slightly compared to the previous experiment. As the applied absolute pulse energy is also very close to the threshold energy for this effect, droplet creation can be easily induced in this case by accident.

4.3.1.3 Laser Irradiation and Dynamic Light Scattering of Small Particles

In the next experiment the mean particle diameter of the suspension is further reduced to 20 ± 2 nm. The particles aspect ratios are comparable to the previous irradiated samples. For these dimensions the SEM resolution is no longer sufficient to image all particle details like the crystal faces or surface roughness. Thus, transmission electron microscopy (TEM) would be the method of choice, but since the spectral changes in the absorbance are now well understood and the shape transformation can be handled quite well, electron microscopy in general would not provide new information of the involved processes. Furthermore, imaging methods only allow an impression of a small fraction of the whole suspension and the necessary picture analysis for the statistics can only be performed on an even smaller part. However, dynamic light scattering (DLS) as an alternative choice has the advantage that it is very efficient and sensitive in the determination of size distributions for the whole suspension through the Stokes-Einstein relation and considers all involved particles in the data analysis.

The results of the irradiation with energies between 2 and 12 mJ/pulse are presented in Figure 4.13. In (a) and (b) the progress of the irradiation is shown for two representative cases with the lowest and highest energy while the recorded UV-Vis spectra in (e) with the magnification in (f) compare the results for all energies with additional values of 3, 4, 5 and 8 mJ/pulse to the unirradiated suspension. Both of the intermediate recorded spectra in (a) and (b) undergo the same changes during the irradiation as previously described.

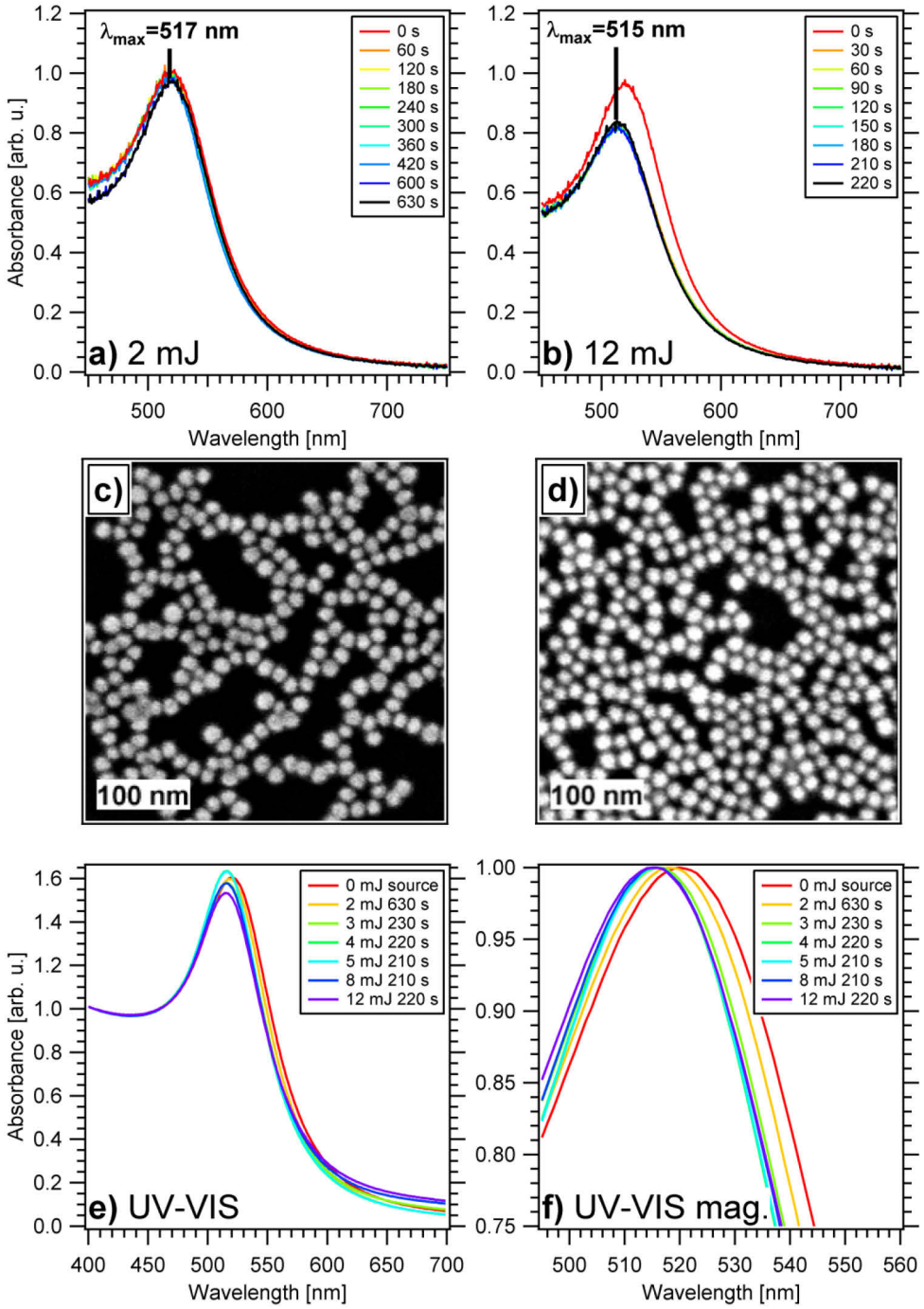

Figure 4.13: *(a-b) In-situ absorption spectra for 2 and 12 mJ pulse energies, (c-d) corresponding SEM images, (e-f) UV-Vis absorption spectra after irradiation for all energies compared to the original suspension*

The maximum absorbance shifts to a smaller wavelength while the width of the resonance at half-maximum (FWHM) shrinks. The highest applied energy (fluence) of 12 mJ/pulse (24 mJ/cm^2) is both exceeding the threshold value where thermionic emission followed by Coulomb explosion may play a role in Figure 4.4 and where the soft irradiation condition for gold is considerably exceeded in Figure 4.6. Under the presented experimental conditions thermionic emission should not play a role while evaporation is a possibility. In experiments[92] where gold particles with a diameter of 25 nm and an aspect ratio of 1.3 were irradiated with the less effective third harmonic TEM images already showed a bimodal size

distribution for laser fluences of 23 mJ/cm^2. Transient absorption spectroscopy by the same author[33] one year later indicated that for particles with a diameter of 36 nm the evaporation already starts at laser fluences larger than 17 mJ/cm^2. In this second experiment the same laser conditions with the same Nd:YAG laser was used as in the first experiment. In spite of the theoretical predictions all these experiments demonstrate that gold particles become more stable against fragmentation the smaller they get and the particles shown in Figure 4.13 have only a diameter of 20 nm. Hence, they should be quite stable against fragmentation. The representative SEM image in Figure 4.13 (d) with a low particle resolution does not show any evidence of such processes. The micrograph in (c) for the lowest pulse energy shows identical particles, but for this energy all the effects initiating size reduction can be excluded. An analysis of the resonance position at the absorption maximum and the full width at half-maximum (FWHM) for each suspension for the UV-Vis spectra in (e) give some more evidences for the possible processes. The data is summarized in Table 4.2.

Table 4.2: Resonance position and full width at half-maximum for the absorbance after irradiation with different pulse energies

Energy	0 mJ	2 mJ	3 mJ	4 mJ	5 mJ	8 mJ	12 mJ
λ_{max}	519 nm	517 nm	515 nm	515 nm	515 nm	515 nm	515 nm
FWHM	81 nm	77 nm	73 nm	69 nm	69 nm	72 nm	74 nm

The relative height of the absorption bands in the UV-Vis measurements does not correspond to the ones from the intermediate absorption spectra during the irradiation, because the employed UV-Vis cuvettes were rinsed with water after each measurement. These water residues most probably changed the concentration of the suspensions to such a degree that the small differences in the maxima disappeared, although attempts were made to dry them with a nitrogen stream as far as possible. Therefore, all UV-Vis spectra in (e) are normalized at a wavelength of 405 nm, where the absorption does not depend on the particle size, and the ones in (f) are normalized at the position of the maximum intensity to compare the width and position of the resonances. The resonance position in the spectra shifts from 519 nm to a smaller wavelength of 515 nm until a pulse energy of 3 mJ is reached, for all higher energies the trend is apparently stopped. The width of the resonances reaches a minimum between pulse energies of 4 and 5 mJ. The decrease of the maximum intensity together with the broadening of the particle plasmon peak has been previously assigned to fragmentation phenomena, but with diameters below 25 nm the particles are now smaller than the electron mean free path of gold. In this intrinsic size region the width of the resonance also increases and its height decreases when the particle diameter decreases, because the frequency of the electron scattering at a particle boundary in the electronic excited state increases with a decrease in the diameter.

Since the resolution of the SEM images is too low and the recorded UV-Vis spectra are not conclusive, the suspensions with a pulse energy of 4 mJ and 12 mJ were investigated by dynamic light scattering at an angle of 90° between the laser and the detector. For the suspension with 4 mJ fragmentation is excluded by considering all previous experiments and also the FWHM reaches a minimum in the UV-Vis spectra. For the irradiation with 12 mJ size reduction initiated by all described mechanism is a possibility and resonance broadening has already occurred. The results from the DLS experiment are presented in Figure 4.14.

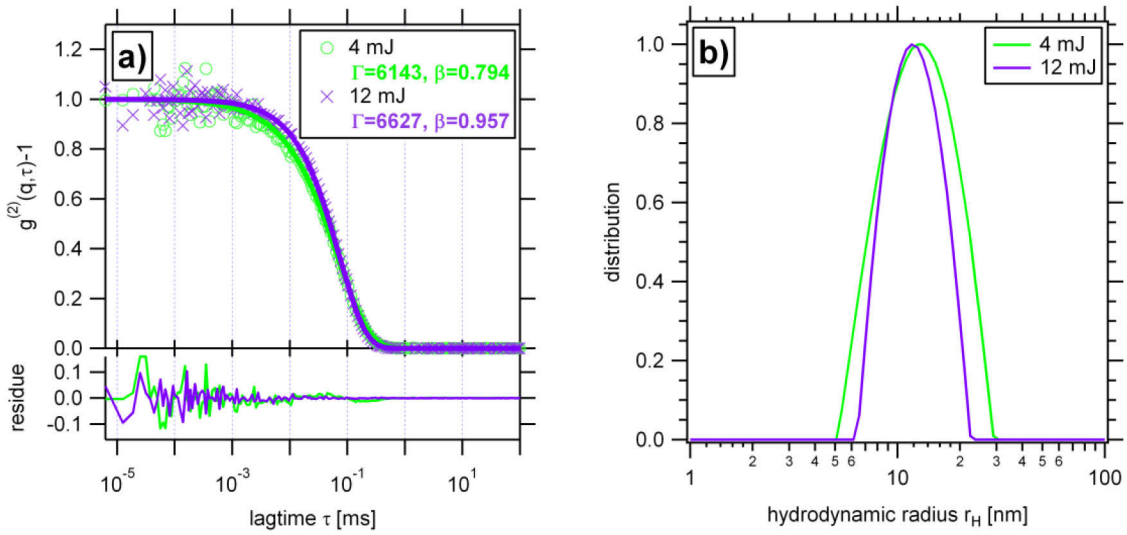

Figure 4.14: *(a) Normalized intensity time autocorrelation function $g^{(2)}(q,\tau)$ for suspensions irradiated with 4 mJ and 12 mJ/pulse, spectra recorded at 90° (q=0.0186 nm^{-1}), (b) CONTIN-fits for the data from (a)*

For fitting, the measured intensity time autocorrelation functions $g^{(2)}(q,\tau)$ from the DLS experiment in (a) the Kohlrausch-Williams Watts[95] (KWW) analysis was used. It is related to the field correlation function $g^{(1)}(q,\tau)$ by the Siegert-relation. For a one decay process it is calculated by the square root of $g^{(2)}(q,\tau)$-1. In the fits the decay Γ and the parameter β increase for the higher pulse energy. While the decay rate is inversely proportional to the hydrodynamic radius through the Stokes-Einstein relation the parameter β describes a better mono-exponential decay. This can be interpreted as particle size reduction with a narrower size distribution. The CONTIN[60, 96, 97] fits in (b) confirm this interpretation with the hydrodynamic radius decreasing from 13.4 nm to 12.3 nm and the FWHM decreasing from 15.2 to 10.7 nm. At this point it is important to note that the size determined by the DLS is normally the size of an equivalent sphere that moves in the same manner as the detected scatterer and is termed the hydrodynamic radius. The particles appear in the DLS larger than in the SEM, because in its size determination the hydrated citrate layer on the surface is included, while the SEM does not "see" this layer.

The size reduction after the laser irradiation seems to be moderate and related to shape transformation. There is no indication of a bimodal size distribution in the DLS, though very

small particles created by fragmentation would most probably not appear in the DLS since their relative scattering signal is too weak. There is a downward limited size restriction for the fragmentation since the smallest particles produced by laser induced fragmentation are independent of the applied laser energy[92] which depends on the condensation kinetics of gold vapor and the heat capacity of the solvent. This means that the created particles from the fragmentation are considered to be not smaller than 6 nm[92] which is above the "quantum size effect" limit[98] for gold. Accordingly these particles should still show a plasmon band and appear in one of the characterization methods when created in high enough concentrations.

Another explanation related to the detected size reduction from the DLS experiment may be the laser induced separation of aggregates to single particles during the irradiation with high energies. One characteristic of the Turkevitsch synthesis[99] is that small particles aggregate into bigger ones until the surface is totally covered with citrate ions. This is the reason for the elongated shapes and this also leads to dimers etc.

Looking for the upper stability limit for the irradiation of particles with diameters of around 20 nm the energy range was further increased in the last experiment to a maximum pulse energy of 22 mJ or a laser fluence of 44 mJ/cm^2. For these high energies all previous described mechanisms are a possibility. Figure 4.15 shows the UV-Vis spectra of the suspensions before and after the irradiation. The spectra are presented as originally measured with no normalization applied. The graph in (b) shows only the region around the maximum of the plasmon band.

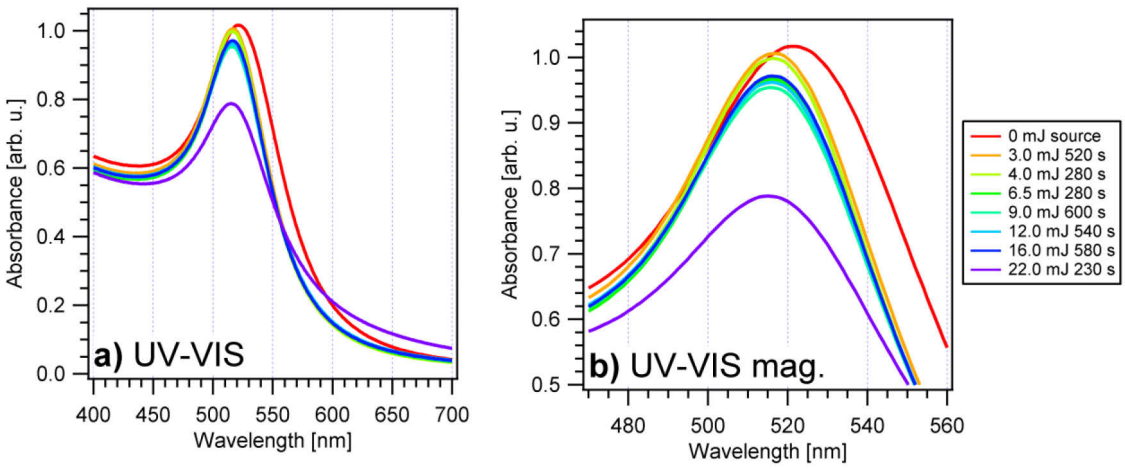

Figure 4.15: *(a-b) UV-Vis spectra of all irradiated suspensions*

All the important parameters in the spectra including the position, height and width of the resonance are quite stable for energies up to 16 mJ/pulse, suggesting that no particle fragmentation occurred. The resonance position at the maximum slowly shifts from originally 519 nm to a smaller wavelength of 513 nm. The FWHM for the original suspension

is with a value of 92 nm by 11 nm larger than the one for the previous suspension and gives a hint for a broader initial size distribution. The resonance width after the irradiation slowly decreases and reaches a minimum of 82 nm for a pulse energy of around 4 mJ, which is still 13 nm larger than in Figure 4.13. For higher energies up to 16 mJ/pulse the spectral changes are quite constant with the FWHM increasing to 84nm. The situation is completely different for the highest value with a pulse energy of 22 mJ where significant resonance broadening together with a weaker absorption signal is observed, indicating the contributions of evaporation or thermal emission followed by size reduction during the irradiation. The data extracted from the UV/VIS measurements are summarized in the first half of the following Table 4.3.

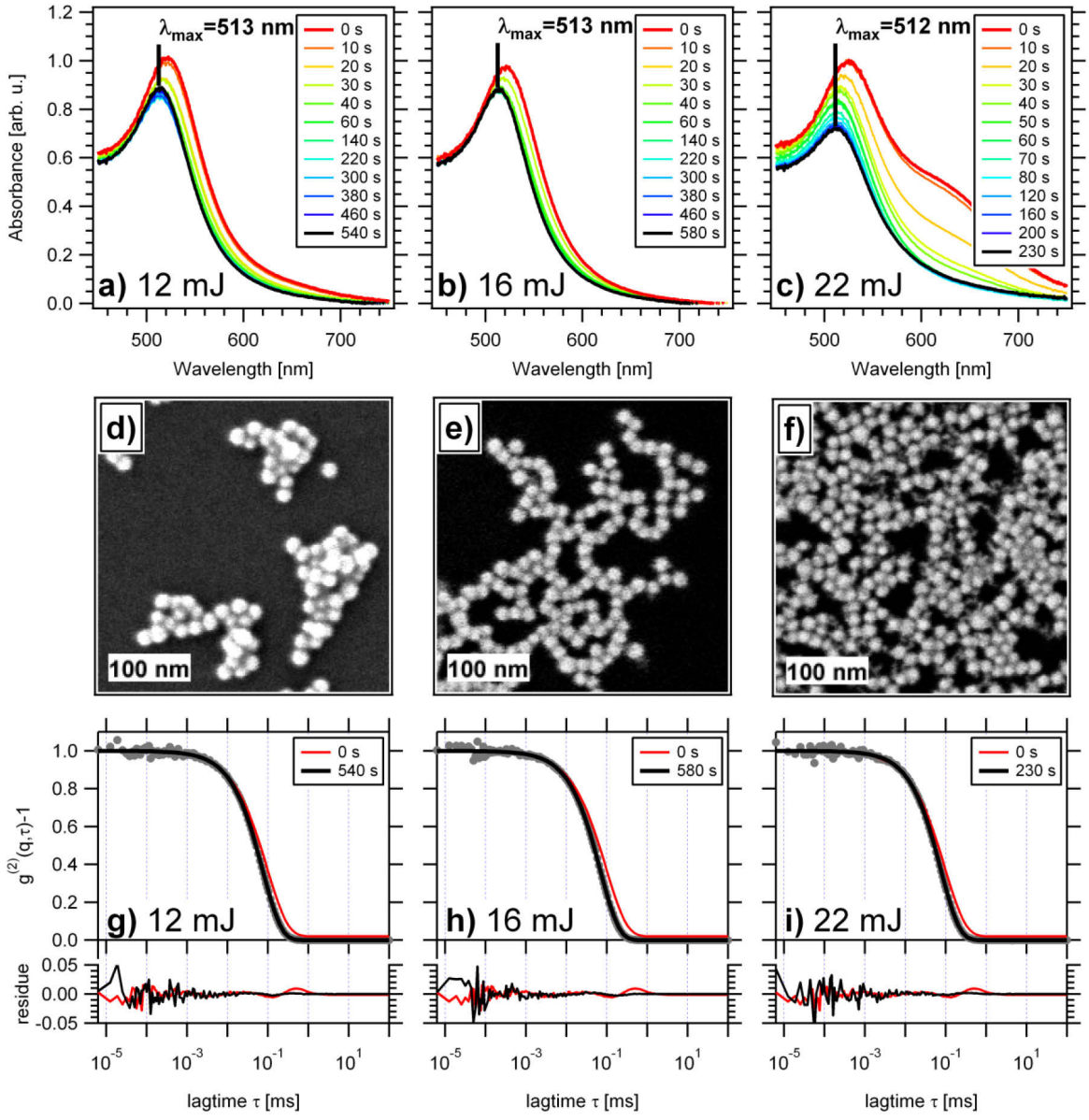

Figure 4.16: *(a-c) in-situ absorption spectra for pulse energies of 12, 16 and 22 mJ respectively with (d-f) showing the corresponding SEM images and (g-i) the DLS spectra with raw data from $g^{(2)}(q,\tau)$ shown as gray full circles and fits as black lines, spectra recorded at 90° (q=0.0186 nm^{-1})*

For the three highest energies with 12, 16 and 22 mJ/pulse which are most interesting for the estimation of the particle stability, Figure 4.16 shows detailed information of the irradiation progress in terms of in-situ absorption spectra (a-c), representative SEM images (d-f) and results from the DLS measurements (g-i). The red and black curves in the spectra describe the initial and final condition of the suspension, respectively. The times in the insets indicate the irradiation duration. In the DLS spectra the raw data from the intensity correlation function $g^{(2)}(q,\tau)$ is shown in gray full circles and the fits obtained by the KWW analysis in black. The resulting decay rates Γ and the parameters β are shown in in the second half of Table 4.3. The determined values from the correlation functions and fits which are used in this overview, but are not displayed in Figure 4.16 are presented in Appendix 10.1 in Figure 10.1

Table 4.3: resonance position and full width at half-maximum for the absorbance from UV-Vis and the decay rate and the β parameter from DLS after irradiation with different pulse energies

Energy	0 mJ	3 mJ	4 mJ	6.5 mJ	9 mJ	12 mJ	16 mJ	22 mJ
λ_{max}	519 nm	514 nm	514 nm	514 nm	513 nm	513 nm	513 nm	512 nm
FWHM	92 nm	83 nm	82 nm	83 nm	85 nm	85 nm	84 nm	102 nm
Γ	4648	-	-	-	5278	6481	6984	6373
β	0.850	-	-	-	0.910	0.948	0.949	0.965

The irradiations with 12 and 16 mJ/pulse show the previously described features. In the absorbance spectra the induced spectral modifications from the light interaction accelerate with increasing energy in the first minute, then slow down and stop automatically when all particles have been transformed. After the irradiation with 12 mJ/pulse the particles in the electron micrograph in (d) look larger than the ones in (e) for the 16 mJ/pulse, but this is mostly a consequence of the large brightness and sharpness differences in the two images. Apart from that there is no evidence for fragmentation or the existence of a bimodal particle size distribution. The DLS measurements show a profound increase for both the decay rate Γ and the β-value relative to the initial suspension, which again is a sign of a smaller size distribution and a moderate size reduction. Both of the considered values with Γ=6481 and β=0.949 for the 16 mJ/pulse are even very similar to the first experiment with the largest step between 9 and 12 mJ/pulse. This large difference could be an indication that something else except from the shape transformation of the particles is happening, but there is no data in the UV-Vis or the SEM images which would prove this.

The situation is completely different for the irradiation with a pulse energy of 22 mJ. The SEM image in (f) clearly shows fragments of small particles next to the larger “mother” particles and proves finally that fragmentation processes can be detected even within these dimensions. The origins of the process is most probably related to the applied pulse energy, but the new shoulder above 580 nm on the red side of the plasmon band in the absorption

spectra (c) before the irradiation could be another explanation. The feature was not seen in all previous irradiations with this suspension and is most probably an indication that spontaneous particle aggregation occurred due to some external influence. Under normal circumstances the suspensions, especially those of the smallest particles, are long-term stable in a fridge. These large particle aggregates are far away from being as stable to the laser as the smaller ones and most probably fragment and so the shoulder disappears completely during the irradiation. However, the maximum absorbance in the in-situ spectra continuously decreases further without any slowdown. Therefore, the irradiation was interrupted after 230 s. Together with the larger resonance width and a FWHM of 102 nm this makes particle fragmentation for all existing sizes most probable. The decay rate from the DLS fit after the irradiation is smaller than the one for the 16 mJ/pulse and comparable to the 12 mJ/pulse while the β value reaches a maximum. The determined particle distribution in the DLS apparently gets narrower, while the average size of it increases due to the particle aggregates from the beginning. Since all samples for the DLS measurements were filtered into the light scattering cell any traces of available particle aggregates are removed and do not influence the spectra. There is obviously no detectable signal from the small fragmented particles due to their weak scattering intensity compared to the "mother" particles, which was predictable, but with the β value near 1 these particle suspensions are nevertheless an ideal material for various applications in the field of light scattering, for example for probing the diffusion in the pores of hydrogels.[100]

The final Figure 4.17 summarizes all irradiation results for the different sized gold nanoparticles. The red lines show the experimental determined energy ranges in which the irradiation started, but no evaporation occurred. It shows only the available data for the used energy steps in this work. If the pulse energy is modified in a smaller step-sizes at the extremes this values can extend in individual cases.

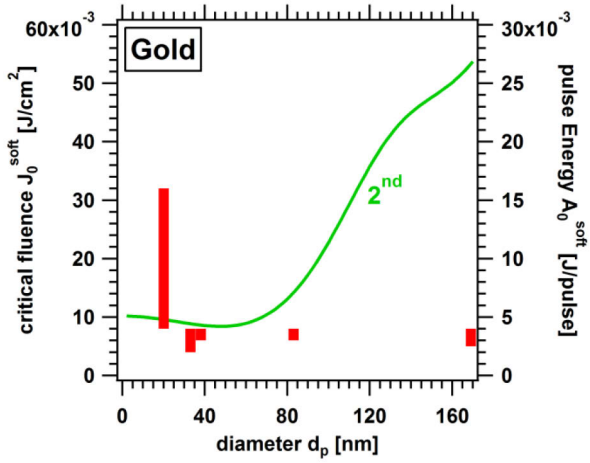

Figure 4.17: *Overview of all irradiation results in relation to the theoretical calculated energies for the second harmonic of the Nd:YAG laser.*

It is obvious that nearly a constant pulse energy for nearly a complete transformation is required for all measured particles and that the particles get more stable with smaller sizes.

4.3.2 Irradiation of Silver Particles

The energy balance equations (4.21) and (4.22) predict for the shape transformation of silver particles under soft irradiation conditions very large energies which are one magnitude higher than for gold. At this level of laser energies all described mechanisms would contribute to the irradiation of silver particles. However, the model is very simple and does not even consider the different laser flow densities. The high energies are overall a direct consequence of the small absorption cross sections from the silver at the selected laser wavelengths, see Figure 4.3. These cross sections are calculated with the help of the Johnson and Christy[61] permittivity values which are supposed to be more reliable than other data, but there exist quite some variations in literature,[101] especially for silver and the imaginary part of ε which determines the material absorption properties. This has in particular large consequences for the absorption cross sections at the position of the third harmonic near the absorption resonance of the silver, but can in general modify the cross sections quite a lot.[57, 83] As a result in real experiments[32] similar laser fluences compared to gold particles are found.

For a verification of these experiments in connection with the available setup and selected particles a colloidal suspension with a mean particle diameter of 73 nm and an aspect ratio of 1.08 was first irradiated with the second harmonic (λ_{Ex}=532 nm) of the Nd:YAG laser with pulse energies between 2 and 6 mJ. Before irradiation, a suitable particle concentration was obtained by diluting a volume of the original suspension 1:10. According to Figure 4.6, the particle size is promising for this first test approach since for these parameters the smallest amount of energy is required to initiate shape transformation and heat up the particles to the boiling point.

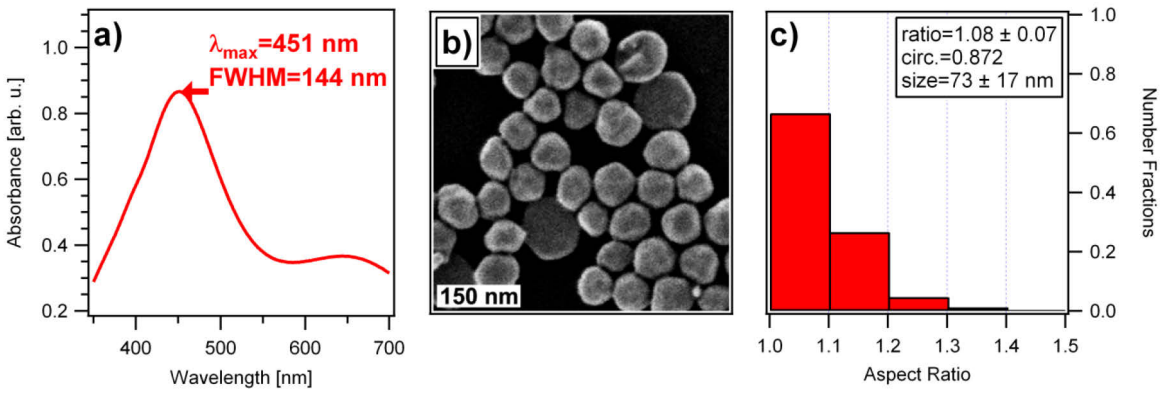

Figure 4.18: *UV/Vis spectrum of gold particles before the irradiation, (b) corresponding scanning electron micrograph, (c) distribution of the aspect ratios obtained by SEM images.*

The UV-Vis spectrum of the particle suspension before the irradiation is shown in Figure 4.18 (a) with the corresponding electron micrograph in (b) and the distribution of the aspect ratios in (c). The selected synthesis[102] is characterized by the abundance of both elongated particles and hexagonal nanoplates. In the presented SEM image in (b) the nanoplates are visible and appear in 2D larger than the spherical particles. According to Mie's theory[22] small spherical nanocrystals – either silver or gold – should exhibit a single localized surface plasmon band, whereas anisotropic particles should give rise to two or more bands depending on the shape of the particles. Larger particles can exhibit additional bands, corresponding to quadrupole and higher multipole plasmon excitations.[103, 104] The UV-Vis spectrum in (a) shows two resonance bands. For the spherical silver particles the slight deviation from the ideal spherical shape is not expected to lead to more resonances in the presented wavelength and size range. The distribution of aspect ratios in (c) is too narrow, particularly compared to gold particles. The first peak in the UV-Vis at around 451 nm can be attributed to the transversal plasmon mode of the nanoplates and simultaneously due to its relative intensity to the dipole plasmon band of the spherical nanoparticles which is red-shifted from the resonance position of 400 nm in water due to retardation. The second peak at the longest wavelength side, which should be very sensitive to the size and aspect ratio, is due to the longitudinal plasmon mode of the nanoplates.[105] Neither the accompanying longitudinal quadrupole mode nor the interband transition can be seen in the spectra since they are either masked by the broad dipole resonance or out of the measured wavelength range.[103, 104]

The results of the irradiation with the second harmonic are presented in Figure 4.19. Since the in-situ absorption spectra during the irradiation should not contain any information for the second harmonic, they have been relinquished on cost of the UV-Vis spectra after the irradiation in (a-c). For silver they promise a better spectral resolution, especially at small wavelengths. The laser-induced changes are comparable to the previous cases for gold. The dipole resonance of the spherical particles shifts to smaller wavelength while its width gets narrower with a decrease of the FWHM from 144 nm to around 116 nm. The longitudinal plasmon mode of the nanoplates completely disappears already for an energy of 2 mJ/pulse. No nanoplates are visible in the representative SEM images in (d-g), thus collaborating with the UV-Vis spectra. In the irradiation range, the resulting particles are still not completely transformed to spheres and in all cases surface corrugations and crystal faces are visible, although these features are quite reduced for the highest pulse energy. In another experiment not-presented here, the fragmentation started for particles of comparable size and shape at around 8 mJ/pulse with the shape transformation of the remaining particles still not completed. In the SEM image (d) for the lowest energy the particle melting appears to have occurred locally at the surface, reducing the surface roughness at these places. After

the particle re-cooling these regions appear as small round up-ticks on the particles, whereas the remaining surface still shows corrugations. For higher energies both these hills disappear and the surface looks overall smoother with some crystal faces particularly for large particles still visible. The statistical data in (g-i) indicate a very small size reduction and a smaller distribution of aspect ratios after the irradiation, but this data is not considering the features on the surface.

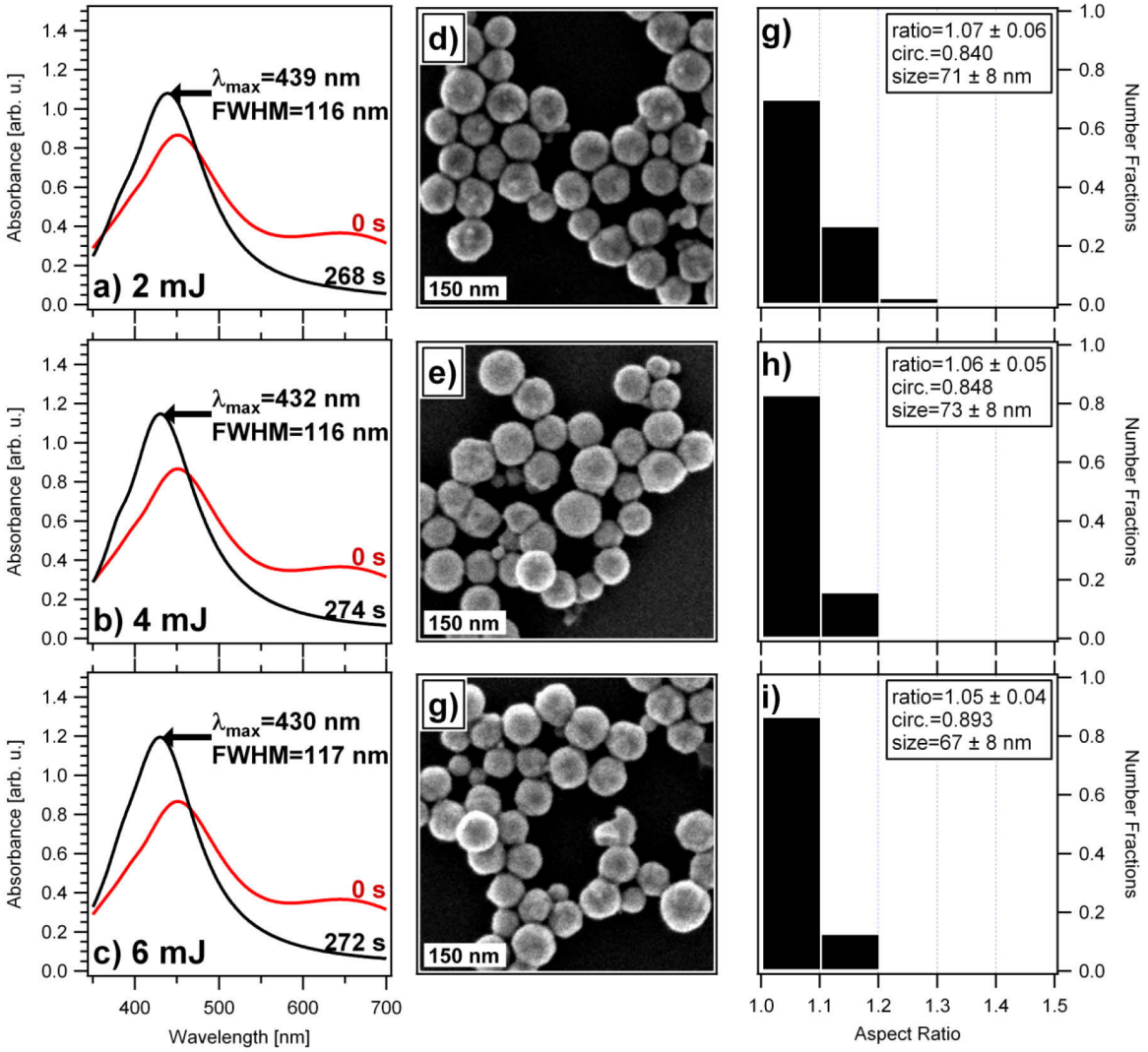

Figure 4.19: *(a-c) UV-Vis spectra of particle suspensions before and after irradiation with energies 2,4 and 6 mJ/pulse for the second harmonic (λ_{Ex}=532 nm), (d-f) corresponding SEM and (g-i) extracted aspect ratio distributions*

In conjunction with the selected silver particles, the second harmonic of the Nd:YAG laser does not provide the right instrument to initiate the complete shape transformation and smoothening of the particle surfaces. In a very narrow range of energies between 6 and 8 mJ/pulse in particular for small particles the irradiation results are encouraging, but not as good as for gold. The results are worse for the larger ones, although particles smaller and larger than 90 nm should need more energy as indicated by Figure 4.6. In literature[30, 57, 71, 83] silver particles for the irradiation with the second harmonic are either produced by

reduction with citrate or sodium borohydride which results in a broad distribution of sizes and shapes or in really small particles, respectively. However, these kinds of particles are not particularly suited for single object investigations on sphere-on-plane systems, whereas the selected particles which originate from the reduction with ascorbic acid and have a protecting polymer shell around were already successfully used for this purpose, see Chapter 8. The purpose of these irradiation investigations was to improve these particles in order to get a more defined optical response and have a comparison to already performed experiments, as presented for gold in Chapter 7. For the second harmonic and silver this can obviously not be acquired in the same way.

In a second approach a comparable silver suspensions with a mean particle of 80 nm and aspect ratio of 1.09 was irradiated with the third harmonic and pulse energies of 4, 5 and 6 mJ. For this wavelength the required energy for particle heating to the boiling point continuously increases with particle size as indicated by Figure 4.6, but is quite lower in the whole particle range compared to the second harmonic. The results for this irradiation are summarized in Figure 4.20. The absorption spectra before and during the irradiation with different energies are displayed in (a-d). The total absorbance is determined by the particle concentration, whereas an aliquot from the original suspension was diluted 1:10 for each irradiation. The absorption spectra in (d) show a profound absorption on the blue side below 400 nm which does not appear in the previous measurements. This could indicate an aggregation of the original suspension, a contamination in the suspension or also be a problem of the spectrometer in the optical setup. During the irradiation the positions of the sphere dipole resonance are stable at 399 nm for all energies with the maximum intensity weakly decreasing. With this spectrometer from Ocean Optics the longitudinal plasmon mode of the nanoplates is apparently not seen, but the decrease in intensity above 560 nm is most probably caused by their disappearance and consequently no nanoplates are seen in the corresponding SEM micrographs (f-h). For the irradiation with 4 mJ/pulse the same condensed droplets reappear on the particle surfaces in the SEM image (f) which have already been described for gold in Figure 4.8 and are associated to the same origin. At around 6 mJ/pulse fragmentation starts already to occur, clearly seen from the bimodal size distribution. In the statistic plot (l) very small particles have not been considered and the size increase from a mean diameter of 75 nm from the previous irradiations to 82 nm is surprising, but is most probably related to the difference in the absorption spectra in (d). The best results are obtained for an irradiation energy of 5 mJ/pulse, but the particle surface is still not as good as obtained for gold with some crystal faces still visible. However, the transformation starts at lower energies what is favorable to avoid side processes. The particle surfaces look marginally better compared to the irradiation with the second harmonic. Also the statistic data in (j-l) indicate a small improvement for the third harmonic.

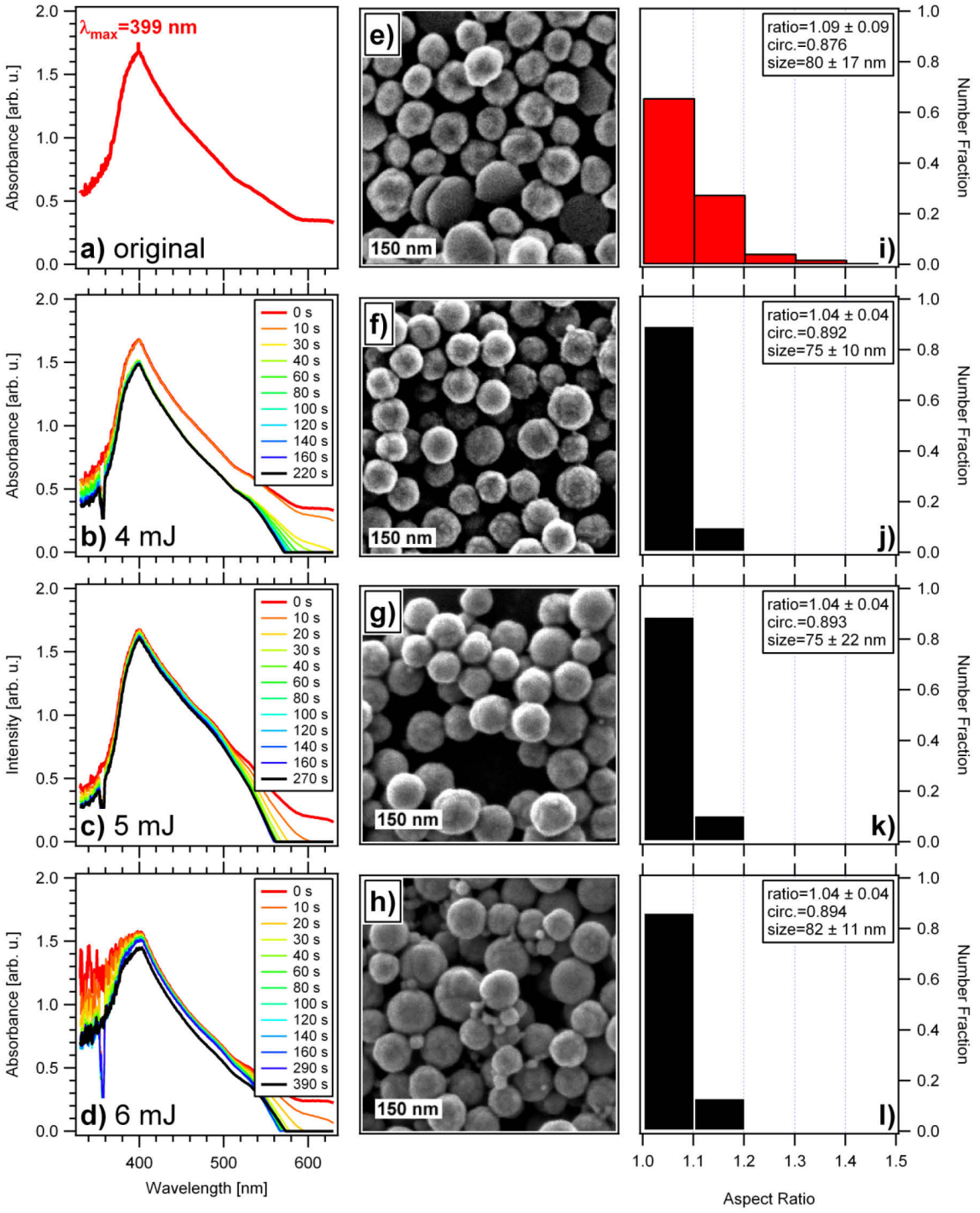

Figure 4.20: *(a-d) in-situ absorption spectra show the laser induced transformations for pulse energies of 4, 5 and 6 mJ with time for the third harmonic (λ_{Ex}=355 nm), (e-h) show the corresponding SEM images and (i-l) the extracted statistical data and the aspect ratio distribution*

4.3.3 Application: The Focus of Light – Field Distribution Measurements by Nanoparticles

Optical microscopy has been an indispensable tool in many scientific disciplines and in many applications a smaller two dimensional focal spot size improves the performance of the whole optical system. In the case of confocal microscopy[106] it is also important to have

knowledge about the third dimensions of the focal field distribution. A highly concentrated and well-matched field is necessary for coupling to small quantum systems[107] and for applying light forces to microscopic particles.[108, 109] The spatial engineering of the focal intensities has been successfully demonstrated for example in stimulation emission depletion microscopy[110, 111] for providing spatial resolution far beyond the diffraction limit.

For optical systems using high numerical apertures (NA) polarization effects in the focal plane emerge that go beyond the description by paraxial approximations or scalar theories in general, because they arise due to the vector character of the electric field. For such systems Richards and Wolf[112] established a vectorial diffraction theory and found two closely related consequences. First, the polarized beam is asymmetrically deformed and second, the effective numerical aperture is reduced. The asymmetry was described in detail by Stamnes[113] and can be overcome by using radially or azimuthally polarized input fields which best fit the symmetry of the focusing system.[114, 115] In the focus a strong longitudinal field component with narrow intensity distribution parallel to the optical axis is formed. The positions of these fields are presented in the ray-tracing picture in Figure 4.21.

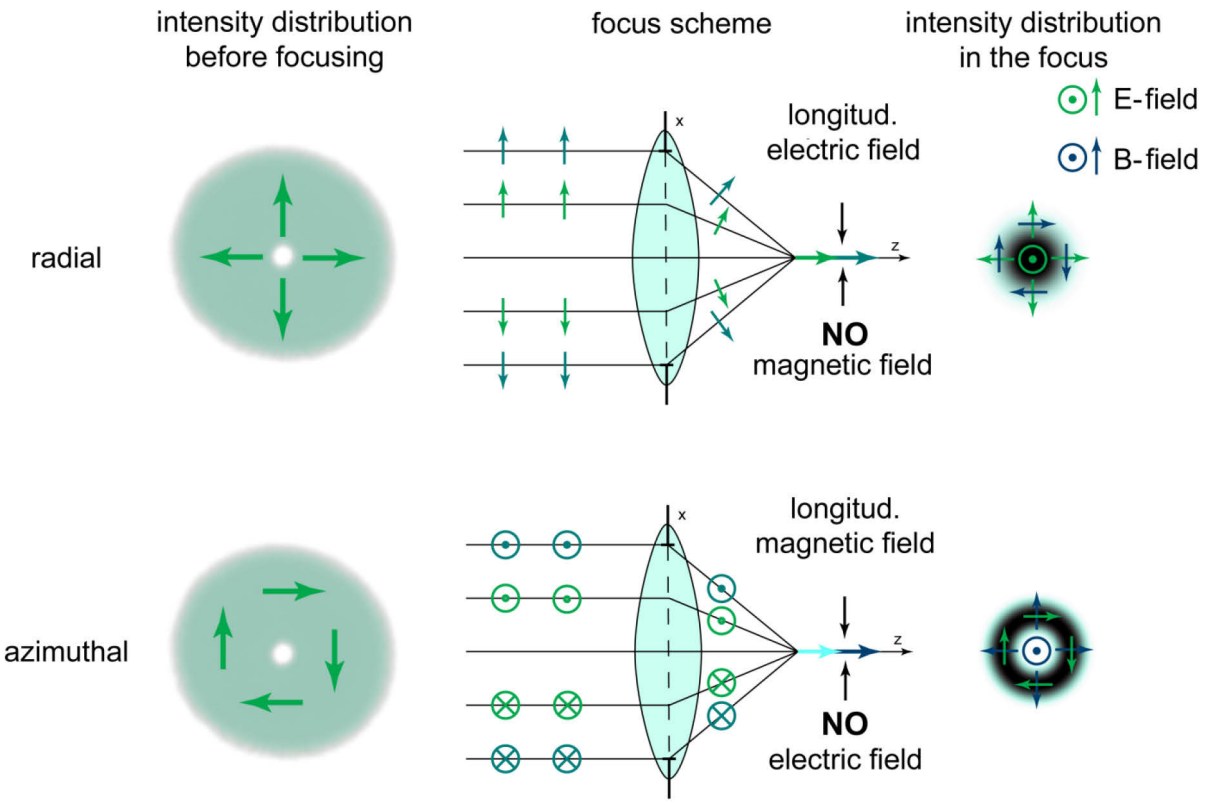

Figure 4.21: *ray-tracing model for focusing a radial and azimuthal polarized incoming beam. [figure by courtesy of [in printed version available]]*

Furthermore, the focal spot size for these polarized fields can be reduced compared to the case of linearly polarized input fields and when an annular aperture is inserted one finds that the spot size drastically decreases by a factor of 2 to 3. The theoretical field distributions

with complex polarization distributions are known for some time and can already be calculated very well by using the Debye approximation.[114] There also exist various methods to experimentally determine them, but most of them have various disadvantages. For example the widely used knife-edge method[116] depends on the thickness, the edge quality, the selected material, the field polarization and a lot of more factors, which makes the interpretation of the results difficult.

A more promising procedure that will be described in detail represents the raster scanning of an ideal point-like scatterer in the focal plane. For a reconstruction of all field components with their relative strength in the focus one has to rely on amorphous sphere-like nanoparticles which should be as small as possible. Of all materials, metallic particles in general have the largest scattering cross section relative to their geometric cross section and gold in particular has the advantage of its relative strong plasmon resonance in the visible and long-term optical and chemical stability. While the surface corrugation of these particles represent only a minor problem, the broad shape variety of particles in general remains the biggest obstacle to a successful application. Here the laser induced shapes transformation comes into play where gold particles from Figure 4.9 are first completely transferred to spheres and a single nearly ideal gold sphere then serves as probe to reconstruct the field distribution in the focus. Figure 4.22 shows the radiation patterns for two electric dipoles which are aligned transversal (a) and longitudinal (b) respectively to the focal plane. While the local field in the focus can excite both orientations in the probing nanoparticle, the relative proportion of each signal in the detection is limited by the characteristic angular range in the reflection (α) or transmission (β) direction. When the detected angles are modified the response from the system will be different for each dipole orientation and by detecting the response for all possible angles the field distribution in the focus can be reconstructed from the scattering response of the nanoparticle in the focal plane.

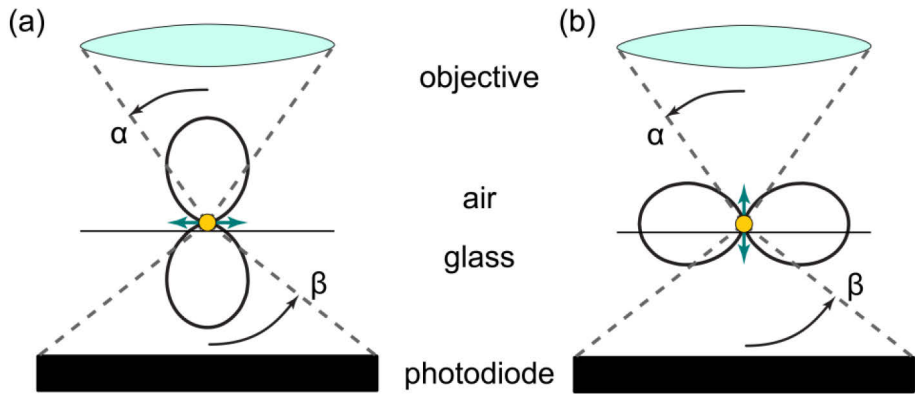

Figure 4.22: *Schematic of the collected angular range in transmission and reflection for a transversal emitting (a) and a longitudinal emitting dipole (b) [figure by courtesy of [in printed version available]]*

The coupling to the nanoparticle is most efficient when the TEM_{01}*-mode of a laser is used, also called doughnut mode.[117, 118] The use of this mode results in a radial symmetric focal spot as shown in Figure 4.21 which can interact with the nanoparticle with nearly every available field component. The whole setup is shown in Figure 4.23.

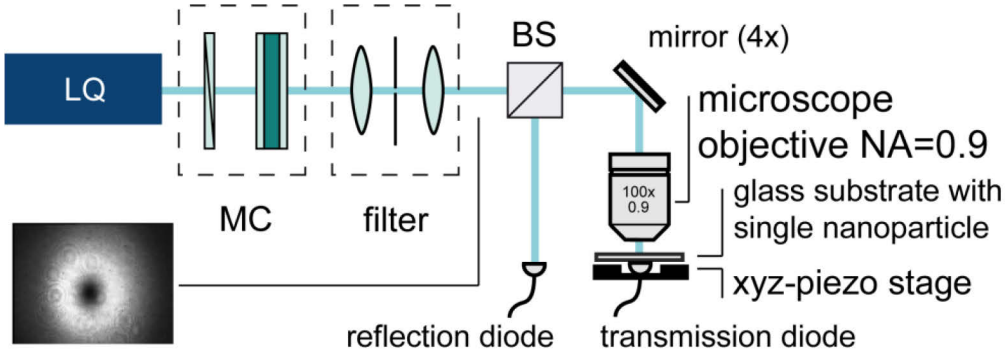

Figure 4.23: *Experimental setup to measure the focal intensity distribution by nanoparticles, LQ: in the visible tunable light source with Gaussian beam profile, MC: polarization mode converter, BS: beam splitter, four mirrors for polarization-insensitive deflection [figure by courtesy of [in printed version available]]*

Light with a Gaussian beam profile from a fully tunable laser source in the visible is converted by a polarization mode converter (MC) into a radial or azimuthal polarized beam. The created beam mode is purified by a Fourier filter and then directed through four mirrors to a microscope objective with a numerical aperture of 0.9. In the focal plane of the objective a single gold nanoparticle with a diameter of 80 nm on a glass substrate is stepwise scanned over the focus by a xyz-piezoelectric stage and the detected photons are counted at each step in the transmission and reflection by photo diodes.

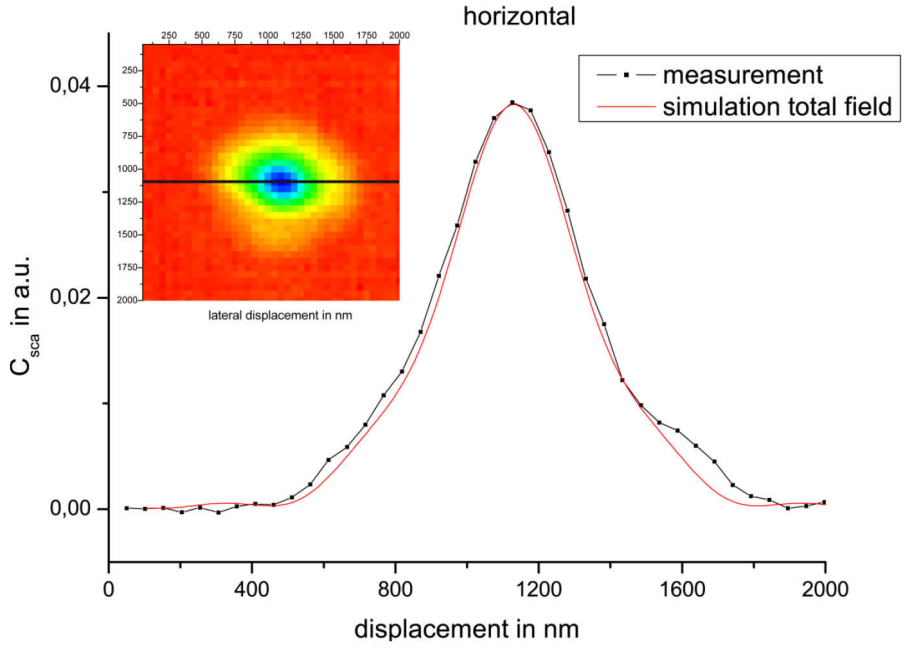

Figure 4.24: *Field intensity distribution for a 80 nm gold particle in transmission and reflection for radial polarized incident light (black) and comparison to the theoretical predicted total intensity (red) with normalization of the measurement to the theory [figure by courtesy of [in printed version available]]*

The so collected data results in the end in a two-dimensional map of the particle interaction with the field. Under consideration of the collected angular range this image correlates very well with the theoretical field distribution in the focus as shown for a wavelength of 525 nm in the horizontal direction in Figure 4.24. As this is working already very well the setup will be further improved and new measurements in the future are planned.

4.4 Summary and Outlook

On the basis of the theoretical estimations different mechanisms for particle size transformation and reduction were described and their influence to the experiments was estimated. The probability of the processes caused by electron ejection depended on the laser energy flow density, which in turn was a function of particle diameter and laser wavelength. For laser flows less than 10^{13} W/m^2 the particle heating, melting and evaporation mechanism was mostly responsible for reducing the particle sizes. The irradiation of a pulsed Nd:YAG laser at 532 nm provided a very efficient reproducible method to cause shape changes in gold particles. The required pulse energies for complete sphere transformation were in the diameter range between 40 and 170 nm with values around 3-4 mJ/pulse experimentally quite constant, whereas the selected model predicted an energy decrease for smaller sizes. The stability of gold particles with a diameter of 20 nm for laser energies up to 16 mJ/pulse was overall very surprising, especially in the light of the performed irradiations with larger particles. The energy easily exceeded all calculated thresholds without any emerging influence of fragmentation from whatever described mechanisms. The combination with light scattering techniques provided some interesting insights and gave an important starting point for further applications of these suspensions in this field.

The irradiation using the same wavelength for silver particles with the naphthalene sulfonic acid/formaldehyde copolymer in terms of surface smoothing was not as successful as the gold case, although experiments in literature with citrate or sodium borohydride reduced particles looked quite promising. The protecting polymer shell was most probably disturbing the surface melting while the shape transformation from the existing hexagonal nanoplates to spheres was completed at quite low energies of 2 mJ/pulse. The irradiation with a wavelength of 355 nm was more efficient and lower energies were required to initiate the shape transformation of all particles. However, on the surfaces crystal faces were still visible.

The created suspensions containing nearly ideal spheres from noble metals have a great potential for various applications, since they provide a much more defined optical response and a narrow resonance width. They can be used in solar cells to improve the conversion of light, act as a model resonator in a sphere-on-plane system, or used in dynamic light

scattering experiments to investigate for example the diffusion behavior in hydrogels. Another example of an application has already been presented. A spherical noble metal particle is used as a probe to determine the field distribution in a highly focused laser beam. This represents the current state of research in the optical field.

The final proof for excluding any fragmentation from the 20 nm gold particles at the high energies can only be verified by more experiments in the future. Here, detailed transmission electron microscopy images in combination with the dynamic light scattering measurements are planned to reproduce the results and get a better impression from the particles after the irradiation and their surfaces.

4.5 Bibliography

1. Kreibig, U.; Vollmer, M., *Optical Properties of Metal Clusters,*. Springer-Verlag: Berlin, 1995.

2. Kamat, P. V., Photophysical, photochemical and photocatalytic aspects of metal nanoparticles. *Journal of Physical Chemistry B* **2002,** *106* (32), 7729-7744.

3. Feldheim, D. L.; Foss, C. A. J., *Metal nanoparticles: Synthesis, Characterization, and Applications*. Marcel Dekker: New York, 2002.

4. Crooks, R. M.; Zhao, M. Q.; Sun, L.; Chechik, V.; Yeung, L. K., Dendrimer-encapsulated metal nanoparticles: Synthesis, characterization, and applications to catalysis. *Accounts Chem. Res.* **2001,** *34* (3), 181-190.

5. Valden, M.; Lai, X.; Goodman, D. W., Onset of catalytic activity of gold clusters on titania with the appearance of nonmetallic properties. *Science* **1998,** *281* (5383), 1647-1650.

6. Maier, S. A.; Brongersma, M. L.; Kik, P. G.; Meltzer, S.; Requicha, A. A. G.; Atwater, H. A., Plasmonics - A route to nanoscale optical devices. *Adv. Mater.* **2001,** *13* (19), 1501-1505.

7. Barnes, W. L.; Dereux, A.; Ebbesen, T. W., Surface plasmon subwavelength optics. *Nature* **2003,** *424* (6950), 824-830.

8. Chang, D. E.; Sorensen, A. S.; Demler, E. A.; Lukin, M. D., A single-photon transistor using nanoscale surface plasmons. *Nat. Phys.* **2007,** *3* (11), 807-812.

9. Nie, S. M.; Emory, S. R., Probing single molecules and single nanoparticles by surface-enhanced Raman scattering. *Science* **1997,** *275* (5303), 1102-1106.

10. Freeman, R. G.; Grabar, K. C.; Allison, K. J.; Bright, R. M.; Davis, J. A.; Guthrie, A. P.; Hommer, M. B.; Jackson, M. A.; Smith, P. C.; Walter, D. G.; Natan, M. J., Self-Assembled Metal Colloid Monolayers - An Approach to SERS Substrates. *Science* **1995,** *267* (5204), 1629-1632.

11. Otto, A.; Mrozek, I.; Grabhorn, H.; Akemann, W., Surface-enhanced raman-scattering. *J. Phys. Condens. Matter* **1992,** *4* (5), 1143-1212.

12. Zijlstra, P.; Chon, J. W. M.; Gu, M., Five-dimensional optical recording mediated by surface plasmons in gold nanorods. *Nature* **2009,** *459* (7245), 410-413.

13. Chon, J. W. M.; Bullen, C.; Zijlstra, P.; Gu, M., Spectral encoding on gold nanorods doped in a silica sol-gel matrix and its application to high-density optical data storage. *Adv. Funct. Mater.* **2007,** *17* (6), 875-880.

14. Bohren, C. F.; Huffman, D. R., *Absorption and scattering of light by small particles*. Wiley-VCH: New York, 1983.

15. Im, S. H.; Lee, Y. T.; Wiley, B.; Xia, Y. N., Large-scale synthesis of silver nanocubes: The role of HCl in promoting cube perfection and monodispersity. *Angew. Chem.-Int. Edit.* **2005,** *44* (14), 2154-2157.

16. Millstone, J. E.; Hurst, S. J.; Metraux, G. S.; Cutler, J. I.; Mirkin, C. A., Colloidal Gold and Silver Triangular Nanoprisms. *Small* **2009,** *5* (6), 646-664.

17. Lu, L.; Kobayashi, A.; Tawa, K.; Ozaki, Y., Silver nanoplates with special shapes: Controlled synthesis and their surface plasmon resonance and surface-enhanced Raman scattering properties. *Chem. Mat.* **2006,** *18* (20), 4894-4901.

18. Maillard, M.; Huang, P. R.; Brus, L., Silver nanodisk growth by surface plasmon enhanced photoreduction of adsorbed Ag+. *Nano Lett.* **2003,** *3* (11), 1611-1615.

19. Xiong, Y. J.; Washio, I.; Chen, J. Y.; Cai, H. G.; Li, Z. Y.; Xia, Y. N., Poly(vinyl pyrrolidone): A dual functional reductant and stabilizer for the facile synthesis of noble metal nanoplates in aqueous solutions. *Langmuir* **2006,** *22* (20), 8563-8570.

20. Jana, N. R.; Gearheart, L.; Murphy, C. J., Wet chemical synthesis of silver nanorods and nanowires of controllable aspect ratio. *Chem. Commun.* **2001,** (7), 617-618.

21. Yu, Y. Y.; Chang, S. S.; Lee, C. L.; Wang, C. R. C., Gold nanorods: Electrochemical synthesis and optical properties. *Journal of Physical Chemistry B* **1997,** *101* (34), 6661-6664.

22. Mie, G., Beiträge zur Optik trüber Medien, speziell kolloidaler Metallösungen. *Annalen der Physik, Vierte Folge* **1908,** *25* (3), 377-445.

23. Maxwell, J. C., A Dynamical Theory of the Electromagnetic Field. *Philosophical Transactions of the Royal Society of London* **1865,** *155*, 459-512.

24. Aravind, P. K.; Metiu, H., The effects of the interaction between resonances in the electromagnetic response of a sphere-plane structure - applications to surface enhanced spectroscopy. *Surface Science* **1983,** *124* (2-3), 506-528.

25. Okamoto, T.; Yamaguchi, I., Optical Absorption Study of the Surface Plasmon Resonance in Gold Nanoparticles Immobilized onto a Gold Substrate by Self-Assembly Technique. *Journal of Physical Chemistry B* **2003,** *107* (38), 10321-10324.

26. Raether, H., *Surface Plasmons on Smooth and Rough Surfaces and on Gratings (Springer Tracts in Modern Physics)*. Springer: Berlin, 1988.

27. Wang, H.; Halas, N. J., Mesoscopic Au "Meatball" particles. *Adv. Mater.* **2008,** *20* (4), 820-825.

28. Rodriguez-Fernandez, J.; Funston, A. M.; Perez-Juste, J.; Alvarez-Puebla, R. A.; Liz-Marzan, L. M.; Mulvaney, P., The effect of surface roughness on the plasmonic response of individual sub-micron gold spheres. *Phys. Chem. Chem. Phys.* **2009,** *11* (28), 5909-5914.

29. Eckstein, H.; Kreibig, U., Light-Induced Aggregation of Metal Clusters. *Z. Phys. D-Atoms Mol. Clusters* **1993,** *26* (1-4), 239-241.

30. Takami, A.; Yamada, H.; Nakano, K.; Koda, S., Size reduction of silver particles in aqueous solution by laser irradiation. *Jpn. J. Appl. Phys. Part 2 - Lett.* **1996,** *35* (6B), L781-L783.

31. Kurita, H.; Takami, A.; Koda, S., Size reduction of gold particles in aqueous solution by pulsed laser irradiation. *Appl. Phys. Lett.* **1998,** *72* (7), 789-791.

32. Takami, A.; Kurita, H.; Koda, S., Laser-induced size reduction of noble metal particles. *Journal of Physical Chemistry B* **1999,** *103* (8), 1226-1232.

33. Inasawa, S.; Sugiyama, M.; Noda, S.; Yamaguchi, Y., Spectroscopic study of laser-induced phase transition of gold nanoparticles on nanosecond time scales and longer. *Journal of Physical Chemistry B* **2006,** *110* (7), 3114-3119.

34. Inasawa, S.; Sugiyama, M.; Yamaguchi, Y., Laser-induced shape transformation of gold nanoparticles below the melting point: The effect of surface melting. *Journal of Physical Chemistry B* **2005,** *109* (8), 3104-3111.

35. Plech, A.; Kotaidis, V.; Gresillon, S.; Dahmen, C.; von Plessen, G., Laser-induced heating and melting of gold nanoparticles studied by time-resolved x-ray scattering. *Phys. Rev. B* **2004,** *70* (19).

36. Hartland, G. V.; Hu, M.; Sader, J. E., Softening of the symmetric breathing mode in gold particles by laser-induced heating. *Journal of Physical Chemistry B* **2003,** *107* (30), 7472-7478.

37. Yamada, K.; Tokumoto, Y.; Nagata, T.; Mafune, F., Mechanism of laser-induced size-reduction of gold nanoparticles as studied by nanosecond transient absorption spectroscopy. *Journal of Physical Chemistry B* **2006,** *110* (24), 11751-11756.

38. Yamada, K.; Miyajima, K.; Mafune, F., Thermionic emission of electrons from gold nanoparticles by nanosecond pulse-laser excitation of interband. *J. Phys. Chem. C* **2007,** *111* (30), 11246-11251.

39. Kamat, P. V.; Flumiani, M.; Hartland, G. V., Picosecond dynamics of silver nanoclusters. Photoejection of electrons and fragmentation. *Journal of Physical Chemistry B* **1998,** *102* (17), 3123-3128.

40. Grua, P.; Morreeuw, J. P.; Bercegol, H.; Jonusauskas, G.; Vallee, F., Electron kinetics and emission for metal nanoparticles exposed to intense laser pulses. *Phys. Rev. B* **2003,** *68* (3).

41. Giammanco, F.; Giorgetti, E.; Marsili, P.; Giusti, A., Experimental and Theoretical Analysis of Photofragmentation of Au Nanoparticles by Picosecond Laser Radiation. *J. Phys. Chem. C* **2010,** *114* (8), 3354-3363.

42. Heilweil, E. J.; Hochstrasser, R. M., Non-Linear Spectroscopy and Picosecond Transient Grating Study of Collodial Gold. *J. Chem. Phys.* **1985,** *82* (11), 4762-4770.

43. Inagaki, T.; Kagami, K.; Arakawa, E. T., Photo-Accoustic Study of Surface-Plasmons in Metals. *Applied Optics* **1982,** *21* (5), 949-954.

44. Sun, C. K.; Vallee, F.; Acioli, L. H.; Ippen, E. P.; Fujimoto, J. G., Femtosecond-Tunable Measurement of Electron Thermalization in Gold. *Phys. Rev. B* **1994,** *50* (20), 15337-15348.

45. Del Fatti, N.; Voisin, C.; Achermann, M.; Tzortzakis, S.; Christofilos, D.; Vallee, F., Nonequilibrium electron dynamics in noble metals. *Phys. Rev. B* **2000,** *61* (24), 16956-16966.

46. Hodak, J. H.; Martini, I.; Hartland, G. V., Spectroscopy and dynamics of nanometer-sized noble metal particles. *Journal of Physical Chemistry B* **1998,** *102* (36), 6958-6967.

47. Logunov, S. L.; Ahmadi, T. S.; ElSayed, M. A.; Khoury, J. T.; Whetten, R. L., Electron dynamics of passivated gold nanocrystals probed by subpicosecond transient absorption spectroscopy. *Journal of Physical Chemistry B* **1997,** *101* (19), 3713-3719.

48. Doremus, R. H., Optical Properties of Small Gold Particles. *J. Chem. Phys.* **1964,** *40* (8), 2389-2396.

49. Link, S.; El-Sayed, M. A., Size and temperature dependence of the plasmon absorption of colloidal gold nanoparticles. *Journal of Physical Chemistry B* **1999,** *103* (21), 4212-4217.

50. Ahmadi, T. S.; Logunov, S. L.; ElSayed, M. A., Picosecond dynamics of colloidal gold nanoparticles. *J. Phys. Chem.* **1996,** *100* (20), 8053-8056.

51. Hodak, J. H.; Henglein, A.; Hartland, G. V., Photophysics of nanometer sized metal particles: Electron-phonon coupling and coherent excitation of breathing vibrational modes. *Journal of Physical Chemistry B* **2000,** *104* (43), 9954-9965.

52. Link, S.; Burda, C.; Nikoobakht, B.; El-Sayed, M. A., Laser-induced shape changes of colloidal gold nanorods using femtosecond and nanosecond laser pulses. *Journal of Physical Chemistry B* **2000,** *104* (26), 6152-6163.

53. Barnes, S. C.; Singer, K. E., Field-Emission Retarding-Potential Device for Absolute Work Function Measurements. *Journal of Physics E-Scientific Instruments* **1977,** *10* (7), 737-740.

54. Dou, Y. S.; Zhigilei, L. V.; Winograd, N.; Garrison, B. J., Explosive boiling of water films adjacent to heated surfaces: A microscopic description. *J. Phys. Chem. A* **2001,** *105* (12), 2748-2755.

55. Plech, A.; Kotaidis, V.; Lorenc, M.; Wulff, M., Thermal dynamics in laser excited metal nanoparticles. *Chemical Physics Letters* **2005,** *401* (4-6), 565-569.

56. do Couto, P. C.; Cabral, B. J. C.; Canuto, S., Electron binding energies of water clusters: Implications for the electronic properties of liquid water. *Chemical Physics Letters* **2006,** *429* (1-3), 129-135.

57. Pyatenko, A.; Yamaguchi, M.; Suzuki, M., Mechanisms of Size Reduction of Colloidal Silver and Gold Nanoparticles Irradiated by Nd:YAG Laser. *J. Phys. Chem. C* **2009,** *113* (21), 9078-9085.

58. Davey, W. P., Precision measurements of the lattice constants of twelve common metals. *Phys. Rev.* **1925,** *25* (6), 753-761.

59. Anisimov, S. I.; Kapeliov.Bl; Perelman, T. L., Electron-emission from surface of metals induced by ultrashort laser pulses. *Zhurnal Eksperimentalnoi Teor. Fiz.* **1974,** *66* (2), 776-781.

60. Mätzler, C. *Mie Matlab Code*, 2009.

61. Johnson, P. B.; Christy, R. W., Optical Constants of Noble-Metals. *Phys. Rev. B* **1972,** *6* (12), 4370-4379.

62. Hale, G. M.; Querry, M. R., Optical Constants of Water in 200 nm to 200 µm Wavelength Region. *Applied Optics* **1973,** *12* (3), 555-563.

63. Groeneveld, R. H. M.; Sprik, R.; Lagendijk, A., Effect of a Nonthermal Electron-Distribution on the Electron-Phonon Energy Relaxation Process in Noble-Metals. *Phys. Rev. B* **1992,** *45* (9), 5079-5082.

64. Lide, D. R., *CRC Handbook of Chemistry and Physics, 90th Edition (Internet Version 2010)*. CRC Press/Taylor and Francis: Boca Raton, Fl., 2010.

65. Lin, Z.; Zhigilei, L. V.; Celli, V., Electron-phonon coupling and electron heat capacity of metals under conditions of strong electron-phonon nonequilibrium. *Phys. Rev. B* **2008,** *77* (7), 075133.

66. Nickalls, R. W. D., A New Approach to Solving the Cubic: Cardan's Solution Revealed. *The Mathematical Gazette* **1993,** *77* (480), 354-359.

67. Naher, U.; Bjornholm, S.; Frauendorf, S.; Garcias, F.; Guet, C., Fission of metal clusters. *Phys. Rep.-Rev. Sec. Phys. Lett.* **1997,** *285* (6), 245-320.

68. Saunders, W. A., Metal-Cluster Fission and the Liquid-Drop Model. *Phys. Rev. A* **1992,** *46* (11), 7028-7041.

69. Crowell, R. A.; Lian, R.; Shkrob, I. A.; Qian, J.; Oulianov, D. A.; Pommeret, S., Light-induced temperature jump causes power-dependent ultrafast kinetics of electrons generated in multiphoton ionization of liquid water. *J. Phys. Chem. A* **2004,** *108* (42), 9105-9114.

70. Link, S.; Burda, C.; Nikoobakht, B.; El-Sayed, M. A., How long does it take to melt a gold nanorod? A femtosecond pump-probe absorption spectroscopic study. *Chemical Physics Letters* **1999,** *315* (1-2), 12-18.

71. Pyatenko, A.; Yamaguchi, M.; Suzuki, M., Synthesis of spherical silver nanoparticles with controllable sizes in aqueous solutions. *J. Phys. Chem. C* **2007,** *111* (22), 7910-7917.

72. Green, D. W.; Perry, R. H., *Perry's Chemical Engineers' Handbook*. 8th ed.; McGraw-Hill: New York, 2008.

73. Buffat, P.; Borel, J. P., Size Effect on Melting Temperature of Gold Particles. *Phys. Rev. A* **1976,** *13* (6), 2287-2298.

74. Lai, S. L.; Guo, J. Y.; Petrova, V.; Ramanath, G.; Allen, L. H., Size-dependent melting properties of small tin particles: Nanocalorimetric measurements. *Phys. Rev. Lett.* **1996,** *77* (1), 99-102.

75. Lereah, Y.; Deutscher, G.; Cheyssac, P.; Kofman, R., A direct Observation of Low-Dimensional Effects on Melting of Small Lead Particles. *Europhysics Letters* **1990,** *12* (8), 709-713.

76. Peters, K. F.; Chung, Y. W.; Cohen, J. B., Surface melting on small particles. *Appl. Phys. Lett.* **1997,** *71* (16), 2391-2393.

77. Peters, K. F.; Cohen, J. B.; Chung, Y. W., Melting of Pb nanocrystals. *Phys. Rev. B* **1998,** *57* (21), 13430-13438.

78. Mohamed, M. B.; Wang, Z. L.; El-Sayed, M. A., Temperature-dependent size-controlled nucleation and growth of gold nanoclusters. *J. Phys. Chem. A* **1999,** *103* (49), 10255-10259.

79. Wang, Y. T.; Dellago, C., Structural and morphological transitions in gold nanorods: A computer simulation study. *Journal of Physical Chemistry B* **2003,** *107* (35), 9214-9219.

80. Kofman, R.; Cheyssac, P.; Aouaj, A.; Lereah, Y.; Deutscher, G.; Bendavid, T.; Penisson, J. M.; Bourret, A., Surface Melting Enhanced by Curvature Effects. *Surface Science* **1994,** *303* (1-2), 231-246.

81. Link, S.; Wang, Z. L.; El-Sayed, M. A., How does a gold nanorod melt? *Journal of Physical Chemistry B* **2000,** *104* (33), 7867-7870.

82. Wang, Z. L.; Mohamed, M. B.; Link, S.; El-Sayed, M. A., Crystallographic facets and shapes of gold nanorods of different aspect ratios. *Surface Science* **1999,** *440* (1-2), L809-L814.

83. Pyatenko, A.; Yamaguchi, M.; Suzuki, M., Laser photolysis of silver colloid prepared by citric acid reduction method. *Journal of Physical Chemistry B* **2005,** *109* (46), 21608-21611.

84. Alvarez, M. M.; Khoury, J. T.; Schaaff, T. G.; Shafigullin, M. N.; Vezmar, I.; Whetten, R. L., Optical absorption spectra of nanocrystal gold molecules. *Journal of Physical Chemistry B* **1997,** *101* (19), 3706-3712.

85. Link, S.; Burda, C.; Nikoobakht, B.; El-Sayed, M. A., How long does it take to melt a gold nanorod?: A femtosecond pump-probe absorption spectroscopic study. *Chemical Physics Letters* **1999,** *315* (1-2), 12-18.

86. Link, S.; Burda, C.; Mohamed, M. B.; Nikoobakht, B.; El-Sayed, M. A., Laser photothermal melting and fragmentation of gold nanorods: Energy and laser pulse-width dependence. *J. Phys. Chem. A* **1999,** *103* (9), 1165-1170.

87. Link, S.; El-Sayed, M. A., Spectroscopic determination of the melting energy of a gold nanorod. *J. Chem. Phys.* **2001,** *114* (5), 2362-2368.

88. Mafune, F.; Kohno, J.; Takeda, Y.; Kondow, T., Dissociation and aggregation of gold nanoparticles under laser irradiation. *Journal of Physical Chemistry B* **2001,** *105* (38), 9050-9056.

89. v. d. Veen, J. F., *Phase transitions in surface films 2*. Plenum Press: New York, 1991; p 518.

90. Kern, K., *Phase transitions in surface films 2*. Plenum Press: New York, 1991; p 518.

91. Atkins, P. W.; De Paula, J., *Atkins' Physical Chemistry*. 8th ed. ed.; Oxford University Press: Oxford, 2006.

92. Inasawa, S.; Sugiyama, M.; Yamaguchi, Y., Bimodal size distribution of gold nanoparticles under picosecond laser pulses. *Journal of Physical Chemistry B* **2005,** *109* (19), 9404-9410.

93. Hu, M.; Hartland, G. V., Heat dissipation for Au particles in aqueous solution: Relaxation time versus size. *Journal of Physical Chemistry B* **2002,** *106* (28), 7029-7033.

94. Grand, J.; Adam, P. M.; Grimault, A. S.; Vial, A.; De la Chapelle, M. L.; Bijeon, J. L.; Kostcheev, S.; Royer, P., Optical extinction Spectroscopy of oblate, prolate and ellipsoid shaped gold nanoparticles: Experiments and theory. *Plasmonics* **2006,** *1* (2-4), 135-140.

95. Williams, G.; Watts, D. C., Non-Symmetrical Dielectric Relaxation Behaviour Arising from a simple Empirical Decay Function. *Transactions of the Faraday Society* **1970,** *66* (565P), 80-85.

96. Provencher, S. W., A Constrained Regularization Method for Inverting Data Represented by Linear Algebraic or Integral-Equations. *Computer Physics Communications* **1982,** *27* (3), 213-227.

97. Provencher, S. W., CONTIN - A General Purpose Constrained Regularizaton Program for Inverting Noisy Linear Algebraic and Integral-Equations. *Computer Physics Communications* **1982,** *27* (3), 229-242.

98. Bigot, J. Y.; Merle, J. C.; Cregut, O.; Daunois, A., Electron Dynamics in Copper Metallic Nanoparticles Probed with Femtosecond Optical Pulses. *Phys. Rev. Lett.* **1995,** *75* (25), 4702-4705.

99. Turkevich, T.; Stevenson, P. C.; Hillier, J., A study of the nucleation and growth processes in the synthesis of colloidal gold. *Discussions Faraday* **1951,** *11* (55-75).

100. Grimm, A.; Nowak, C.; Hoffmann, J.; Schartl, W., Electrophoretic Mobility of Gold Nanoparticles in Thermoresponsive Hydrogels. *Macromolecules* **2009,** *42* (16), 6231-6238.

101. Lynch, D. W.; Huttner, W. R., *Handbook of Optical Constants of Solids*. Academic Press Inc.: 1985; p 275-367.

102. Suber, L.; Sondi, I.; Matijevic, E.; Goia, D. V., Preparation and the mechanisms of formation of silver particles of different morphologies in homogeneous solutions. *J. Colloid Interface Sci.* **2005,** *288* (2), 489-495.

103. Jin, R.; Cao, Y.; Mirkin, C. A.; Kelly, K. L.; Schatz, G. C.; Zheng, J. G., Photoinduced Conversion of Silver Nanospheres to Nanoprisms. *Science* **2001,** *294* (5548), 1901-1903.

104. An, J.; Tang, B.; Ning, X.; Zhou, J.; Zhao, B.; Xu, W.; Corredor, C.; Lombardi, J. R., Photoinduced Shape Evolution:From Triangular to Hexagonal Silver Nanoplates. *J. Phys. Chem. C* **2007,** *111* (49), 18055-18059.

105. Chen, S.; Carroll, D. L., Silver Nanoplates: Size Control in Two Dimensions and Formation Mechanisms. *Journal of Physical Chemistry B* **2004,** *108* (18), 5500-5506.

106. Wilson, T., *Confocal Microscopy*. Academic Press: London, 1990.

107. van Enk, S. J.; Kimble, H. J., Single atom in free space as a quantum aperture. *Phys. Rev. A* **2000,** *61* (5), 051802.

108. Grier, D. G., A revolution in optical manipulation. *Nature* **2003,** *424* (6950), 810-816.

109. Neto, P. A. M.; Nussenzveig, H. M., Theory of optical tweezers. *Europhysics Letters* **2000,** *50* (5), 702-708.

110. Hell, S. W., Far-Field Optical Nanoscopy. *Science* **2007,** *316* (5828), 1153-1158.

111. Hell, S. W.; Wichmann, J., Breaking the diffraction resolution limit by stimulated emission: stimulated-emission-depletion fluorescence microscopy. *Optics Letters* **1994,** *19* (11), 780-782.

112. Richards, B.; Wolf, E., Electromagnetic Diffraction in Optical Systems - 2. Structure of the Image FIeld in an Aplanatic System. *Proceedings of the Royal Society of London Series a-Mathematical and Physical Sciences* **1959,** *253* (1274), 358-379.

113. Stamnes, J. J., *Waves in Focal Regions*. Adam Hilger: Bristol, 1986.

114. Quabis, S.; Dorn, R.; Eberler, M.; Glockl, O.; Leuchs, G., The focus of light - theoretical calculation and experimental tomographic reconstruction. *Applied Physics B-Lasers and Optics* **2001,** *72* (1), 109-113.

115. Dorn, R.; Quabis, S.; Leuchs, G., Sharper focus for a radially polarized light beam. *Phys. Rev. Lett.* **2003,** *91* (23).

116. Arnaud, J. A.; Hubbard, W. M.; Mandevil.Gd; Claviere, B. D.; Franke, E. A.; Franke, J. M., Technique for Fast Measurement of Gaussian Laser Beam Parameters. *Applied Optics* **1971,** *10* (12), 2775-&.

117. Quabis, S.; Dorn, R.; Leuchs, G., Generation of a radially polarized doughnut mode of high quality. *Applied Physics B-Lasers and Optics* **2005,** *81* (5), 597-600.

118. Saleh, B. E. A.; Teich, M. C., *Fundamental of Photonics*. Wiley-Interscience: New York, 1991.

5 Plasmon Mediated Confocal Dark-Field Microscopy

5.1 Introduction

Optical plasmonic resonances of nanometer-sized metal particles are frequently accompanied by strong enhanced fields which are localized in volumes far smaller than the diffraction-limited foci that can be achieved by far-field illumination. Based on this field localization, several physical effects with significant potential for applications have been discussed such as surface enhanced spectroscopy,[1, 2] sensing[3] as well as enhanced light collection[4] and emission.[5]

For a detailed investigation of plasmonic resonances, single-object spectroscopy is mandatory since big variations between individual resonators are rather the rule than an exception. The power of optical single-particle spectroscopy has been demonstrated by investigations on resonances on metal rods[6, 7] and on platelets with different simple geometrical contours.[8, 9] In these studies, a customized dark field optical microscope with evanescent illumination and a commercial dark field system was used. Metal surfaces as a support for plasmonic structures bear the advantage of direct electrical contact and the availability of a well-developed, simple means of surface chemical modifications based on thiols. In a sphere-on-plane geometry this self-assembling monolayers can act as molecular spacers and define the distance between a particle on top and the metal film. For investigations on the optical properties of this gap[10-13] with the large field enhancements, scattering spectroscopy on individual objects represents a central experimental technique. The presence of the metal surface, though, due to the presence of surface plasmons, significantly modifies the coupling between the local resonator and incident or outgoing plane waves in a way that standard dark field microscopy is quite inefficient for studying these objects. Similar plasmon-induced modifications have been discussed for the direction-dependent emission from dye molecules[14] and for their excitation efficiency for illumination from different directions[15] which strongly modifies the appearance of single dyes in fluorescence microscopy.[16] For individual scatterers, analogous direction dependences have been shown.[17]

In the following the role of the intermediate surface plasmon excitation for dark field microscopy on objects close to a metal surface is investigated. It is pointed out to which extent the intermediate excitation of surface plasmons can be used to obtain high quality dark field micrographs through a thin metal film.

5.2 Concept

In general, dark field microscopy relies on the selection of a limited angular spectrum illuminating the specimen. The specular reflection from this light is then blocked such that only scattered light reaches the detection path. An experimental realization of this concept is schematically depicted in Figure 5.1 (a). Two blocks B1 and B2 are placed in the excitation and detection path of the scanning confocal optical microscope, respectively.

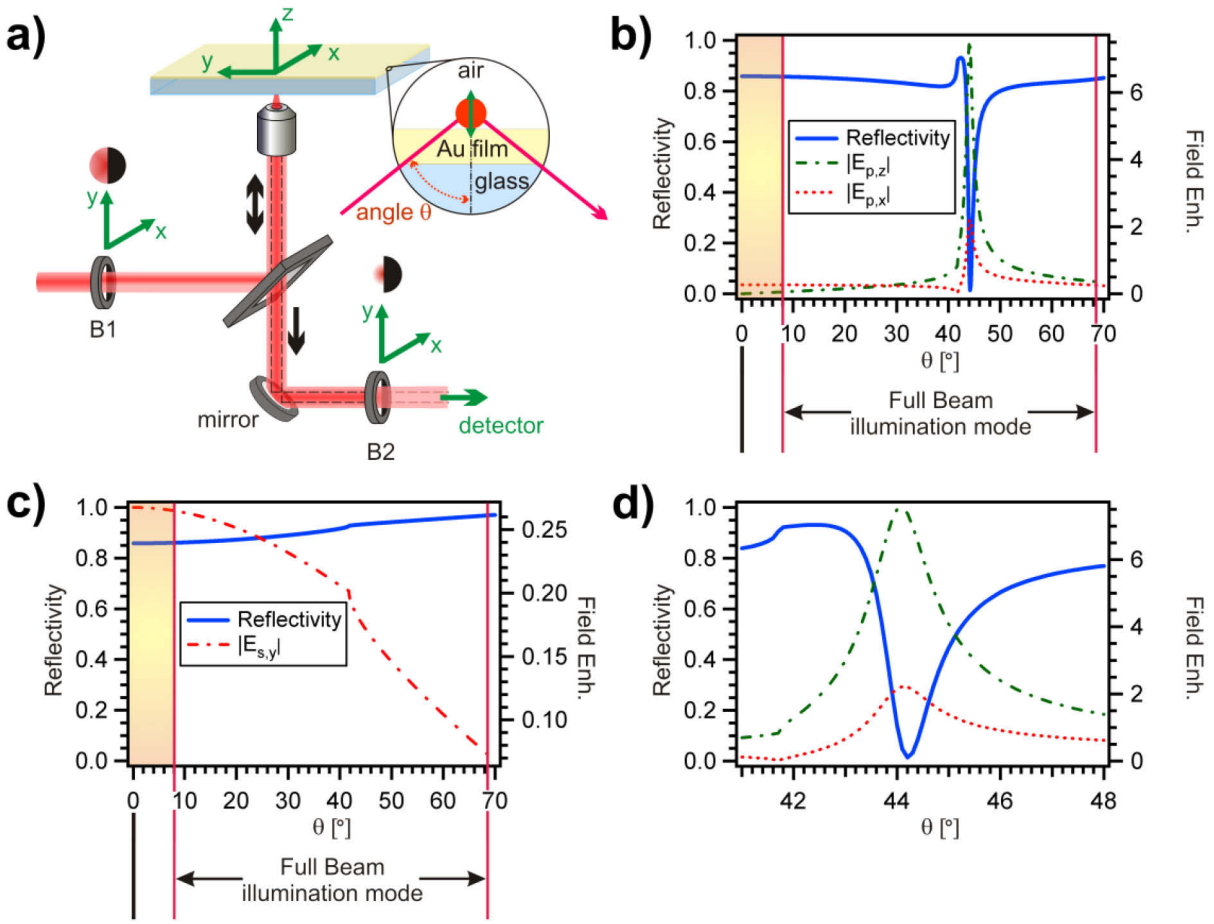

Figure 5.1: *(a) Schematic representation of a dark field microscope. (b) Reflectivity and field enhancement for plane wave illumination with a wavelength of 633 nm in p polarization (Dielectric constants are ε_{glass}=2.25901, ε_{gold} =-11.8321 + i·1.36442, ε_{air}=1, the thickness of the gold film is d_{Au}=50 nm. (c) Same as (b) for s polarization. (d) Magnified view on (b).*

In principle, the blocks may have any form in two dimensions as long as they are complementary in the sense that their superposition blocks the entire beam. Note that reflection at the surface corresponds to a point reflection of the beam profile about the optical axis such that blocking is achieved if the sum of B1 and the point reflected B2, seen along the beam propagation, covers the entire plane. Due to diffraction, some overlap is generally required for good blocking. Usually, rotationally symmetric blocks, i.e. a disc and an annulus are employed to keep the symmetry of the imaging system. As soon as objects

are to be investigated through a thin metal film, this geometry becomes unsuitable as will be explained in the following.

The type of sample that is to be investigated is also shown in Figure 5.1 (a). An oil immersion objective focuses the incident light on the surface of a microscope cover-slip which is covered by a gold film with a thickness of approximately 50 nm. Behind the film a polarizable object is placed whose scattering cross-section is to be studied. For the following discussion a polarizability only perpendicular to the sample surface is assumed. Excitation is due to a plane wave with amplitude $E_{B1,x}$ in the plane where B1 is placed. Only fields within the area A_{B1} which corresponds to rays collected by the objective are contributing. Two different linear polarizations of the exciting light with the electrical field vector being parallel and perpendicular to the y coordinate are considered, denoted in the following by the subscripts and respectively. The light field not blocked by B1 is focused by the objective. The polarizable unit emits radiation which is transformed to plane waves in the area A_{B2} which is defined as the analogue of A_{B1} in the detection path. These waves are partially removed by the block B2, the transmitted fraction is detected. For a derivation of expressions which allows for the modeling of this dark field signal three independent steps are taken: The calculation of the 3D–field distribution in the focus, the modeling of a dipole with wavelength-independent scattering cross-section and the collected radiation from a dipole in the focus. In the end these results are combined to yield the final equations used in the further discussion of this chapter.

5.2.1 Field Distribution in the Focus

The microscope objective is modeled as an aplanatic system[18] which transforms each “ray” of the parallel incident beam with the electrical field $\vec{E}_{Bl}$ in the block plane 1 (B1) to a source situated at the focal sphere of the system (immaterial sphere centered at the Gaussian focal point with Radius *R* equal to the focal length *f* of the microscope objective). The geometry under consideration is sketched in Figure 5.2. The optical system is illuminated by a homogenous linearly polarized plane wave along the optical axis. A coordinate system is chosen such that x is parallel to the electrical field vector of the incident wave and z anti-parallel to the lights propagation direction. The source at the focal sphere of the system has an electrical field $\vec{E}'_{FS}$ tangential to the focal sphere which may be decomposed in a p- and s-polarized component where the polarization direction refers to the plane of incidence of this particular “ray”. For illustration, such a ray is sketched in Figure 5.2 (b).

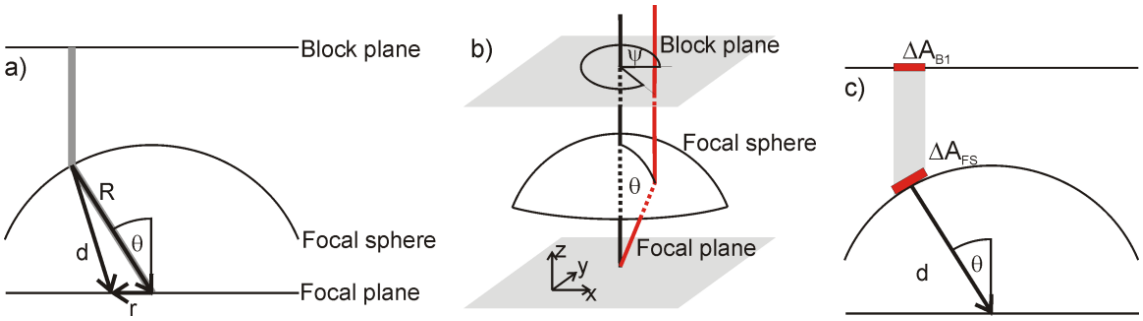

Figure 5.2: *Geometry under consideration, (a) 2D-sketch, (b) 3D-sketch illustrating the definition ψ, (c) Energy conservation of connected areas on the focal plane*

To determine $\vec{E}'_{FS}$, one needs to rotate the incident field $\vec{E}_{B1}$ around the z-axis to a coordinate system where the plane of incidence coincides with the x-z plane in Figure 5.1 (a) or polarization, this rotation is expressed by the matrix **R**.

$$\begin{pmatrix} E^{p'}_{FS} \\ E^{s'}_{FS} \\ 0 \end{pmatrix} = \begin{pmatrix} \cos(\psi) & \sin(\psi) & 0 \\ -\sin(\psi) & \cos(\psi) & 0 \\ 0 & 0 & 1 \end{pmatrix} \cdot \begin{pmatrix} E^{x}_{B1} \\ E^{y}_{B1} \\ 0 \end{pmatrix} \sqrt{\cos(\theta)} \quad \Leftrightarrow \quad \vec{E}'_{FS} = \mathbf{R}\vec{E}_{B1} \cdot \sqrt{\cos(\theta)} \tag{5.1}$$

Identical energy flux through connected areas *A* on the focal plane and in B2 is guaranteed by multiplication with $\cos(\theta)^{1/2}$: $P \propto \left|\vec{E}_{FS}\right|^2 A_{FS} = \left|\vec{E}_{B1}\right|^2 A_{B1}$ (compare Figure 5.2 (c)). The dash indicates that fields are expressed in a rotated coordinate system that varies with the position in B1 that is considered. The angles ψ and θ are defined according to Figure 5.2 (b). These fields are propagated towards the focal region as spherical waves according to the Huygens-Fresnel principle.[18] In the absence of a multilayer system, the total field strength in the focus is obtained by summing contributions ΔA_{FS} from the entire focal sphere:

$$\vec{E}_{FP} = \sum \Delta A_{FS} \left[-\frac{ik}{2\pi} \vec{E}'_{FS} \right] \frac{e^{i\mathbf{kd}}}{d} \tag{5.2}$$

with the distance **d** as shown in Figure 5.2 and the wave vector **k** of the incident light. Close to the Gaussian focal point **kd** >> *1* and therefore one may approximate

$$\frac{e^{i\mathbf{k}(d)\mathbf{d}}}{d} = \frac{e^{i\mathbf{k}(d)(\mathbf{R}+\mathbf{r})}}{d} \approx \frac{e^{i\mathbf{k}(R)(\mathbf{R}+\mathbf{r})}}{d} = \frac{e^{i\mathbf{k}(R)(R)}}{d} e^{i\mathbf{k}(R)\mathbf{r}} \tag{5.3}$$

where the first (constant) overall phase factor may be neglected. Thus:

$$\vec{E}_{FP} = \sum \Delta A_{FS} \left[-\frac{ik}{2\pi} \vec{E}'_{FS} \right] \frac{e^{i\mathbf{kr}}}{d} = \sum \Delta A_{FS} \vec{E}'_{FP,C} \tag{5.4}$$

The index *C* indicates that those are contributions to the total field which remain to be summed up. When focusing through a multilayer system, each incident plane wave contribution $\vec{E}^{inc'}_{FP,C}$ will give rise to a local field $\vec{E}'_{FP,C}$ at the specified position which is

calculated by the transfer matrix algorithm[19] for the locally p and s polarized components. The connection between incident field amplitude and local field amplitude may be expressed as three "*enhancement factors*" which are combined in the matrix **A**.

$$\begin{pmatrix} E_{FP,C}^{x'} \\ E_{FP,C}^{y'} \\ E_{FP,C}^{z'} \end{pmatrix} = \begin{pmatrix} E_{p,x} & 0 & 0 \\ 0 & E_{s,y} & 0 \\ E_{p,z} & 0 & 0 \end{pmatrix} \begin{pmatrix} E_{FP,C}^{inc,p'} \\ E_{FP,C}^{inc,s'} \\ 0 \end{pmatrix} \qquad \vec{E}_{FP,C}^{'} = \mathbf{A}\vec{E}_{FP,C}^{inc'} \tag{5.5}$$

The components of the matrix represent local electrical fields at the position of the polarizable unit upon illumination with a plane wave with unit electrical field. $E_{p,x}$ and $E_{p,z}$ correspond to transverse-magnetic (p) polarization and denote Cartesian field components in a coordinate system where the plane of incidence equals the x-z-plane. $E_{s,y}$ is the corresponding field component for transverse-electric (s) polarization. For the summation all these contributions have to be transformed to the common coordinate system by the rotation matrix **R**.

$$\begin{pmatrix} E_{FP,C}^{x} \\ E_{FP,C}^{y} \\ E_{FP,C}^{z} \end{pmatrix} = \begin{pmatrix} \cos(\psi) & -\sin(\psi) & 0 \\ \sin(\psi) & \cos(\psi) & 0 \\ 0 & 0 & 1 \end{pmatrix} \begin{pmatrix} E_{FP,C}^{x'} \\ E_{FP,C}^{y'} \\ E_{FP,C}^{z'} \end{pmatrix} \qquad \vec{E}_{FP,C} = \mathbf{R}^{-1}\vec{E}_{FP,C}^{'} \tag{5.6}$$

The field is finally obtained by integration of all those contributions

$$\vec{E}_{FP} = \sum \Delta A_{FS} \left[-\frac{ik}{2\pi} \vec{E}_{FS} \right] \frac{e^{i\mathbf{kr}}}{d} = \frac{-ik}{2\pi d} \sum \Delta A_{FS} e^{i\mathbf{kr}} \mathbf{R}^{-1}\mathbf{A}\mathbf{R}\vec{E}_{B1} \sqrt{\cos(\theta)} \tag{5.7}$$

When summing over contributions from B1 with $\Delta A_{B1} = \Delta A_{FS} \cos(\theta)$ this results in

$$\vec{E}_{FP} = \frac{-ik}{2\pi d} \sum \Delta A_{B1} e^{i\mathbf{kr}} \mathbf{R}^{-1}\mathbf{A}\mathbf{R}\vec{E}_{B1} = \frac{-ikA_{B1}}{2\pi d} \sum \frac{\Delta A_{B1}}{A_{B1}} e^{i\mathbf{kr}} \mathbf{R}^{-1}\mathbf{A}\mathbf{R}\vec{E}_{B1} \cdot \frac{1}{\sqrt{\cos(\theta)}} \tag{5.8}$$

Here the illumination with a linearly polarized plane wave in B1 is considered, thus E_{B1}^{x} is the only non-vanishing component in the B1 plane. A block partly covering B1 is identified with a certain area in B1. It is modeled by setting the corresponding plane wave contributions to 0.

5.2.2 Source of the Scattering Signal

This field gives rise to an oscillating charge distribution, represented as a dipole $\vec{p}$:

$$\vec{p} = \begin{pmatrix} \alpha_{xx} & \alpha_{xy} & \alpha_{xz} \\ \alpha_{yx} & \alpha_{yy} & \alpha_{yz} \\ \alpha_{zx} & \alpha_{zy} & \alpha_{zz} \end{pmatrix} \begin{pmatrix} E_{FP}^{x} \\ E_{FP}^{y} \\ E_{FP}^{z} \end{pmatrix} \tag{5.9}$$

In order to compare dipoles with identical scattering cross-sections, the polarizability α will depend on wavelength. Since the radiated power *P* from a point dipole in free space is given as

$$P = \frac{ck^4}{3}\frac{|\vec{p}|^2}{4\pi\varepsilon_0} \tag{5.10}$$

with *p* the dipole moment, *c* the speed of light in vacuum and ε_0 the permittivity in vacuum, a z-polarized scatterer can be modeled with wavelength-independent scattering cross-section by introducing the wavelength-dependent polarizability

$$\alpha_{zz} = \frac{k_0^{\,2}}{k^2}\alpha_0 = \frac{\lambda^2}{\lambda_0^{\,2}}\alpha_0 \tag{5.11}$$

where a constant factor α_0/λ_0^2 may be chosen arbitrarily. Experimentally, this dipole represents the source of the scattered field which is finally detected.

5.2.3 Emitted Radiation

It is assumed that all intensity passing the block B2 in the detection path finally reaches the detector. Then, a calculation of the detectable power (photon rate) requires knowledge of the field components E_{B2}^x and E_{B2}^y in B2 due to this dipole *p.* The reciprocity theorem[20] states

$$\int dV\, \vec{E}_{FP} \cdot \vec{J}_{B2} = \int dV\, \vec{E}_{B2} \cdot \vec{J}_{FP} \tag{5.12}$$

for current distributions $\vec{J}_{B2}$ and $\vec{J}_{FP}$ in B2 in the focal plane which radiate the electrical fields $\vec{E}_{B2}$ and $\vec{E}_{FP}$. If the two currents are described to the point dipoles $\vec{p}_{FP}$ and $\vec{p}_{B2}$ the following equation is obtained:

$$\vec{E}^{\,p_{B2}}\left(\vec{r}_{FP}\right) \cdot \vec{p}_{FP} = \vec{E}^{\,p_{FP}}\left(\vec{r}_{B2}\right) \cdot \vec{p}_{B2} \tag{5.13}$$

Thus (assuming dipoles with unit strength) the problem of calculating the x-component of the field in B2 E_{B2}^x due to the radiating dipole $\vec{p}_{FP}$ in the focal plane is equivalent to the calculation of projection of the field on $\vec{p}_{FP}$ due to a dipole $\vec{p}_{B2}$ with identical strength situated at B2, when $\vec{p}_{B2}$ is chosen parallel to the x coordinate. This situation is sketched for a z-oriented dipole $\vec{p}_{FP}$ in Figure 5.3. For the y component, an analogous argument holds. (Note: the electrical fields right behind the focal sphere and in B1 are assumed to be identical)

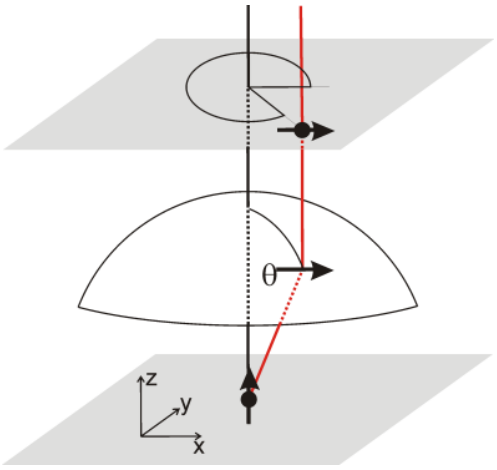

Figure 5.3: *Illustration of reciprocity*

Now the x-component of the electrical field $E_{B2}^{x}\left(\vec{r}_{B2}\right)$ in B2 is considered which is calculated as the z-component of the field due to the dipole $\vec{p}_{B2}\left(\vec{r}_{B2}\right)$ oriented parallel to the x axis. Its contribution is decomposed in a p- and an s-component, giving rise to plane wave contributions travelling towards the focal plane

$$\vec{E}^{s/p} = \vec{p}^{s/p} k^2 \frac{e^{ikd}}{d} \frac{1}{4\pi\varepsilon_0} \tag{5.14}$$

p and s denote the polarizations relative to the plane of incidence. By interaction with the multilayer system, this radiation gives rise to a local field at the dipole position. Therefore, the strategy to calculate this focal field $E_{FP,C}^{z}$ due to an incident local plane wave from the block plane as outlined in 5.2.1 can be applied again when this field is assumed to have the amplitude in x-direction:

$$\tilde{E}_{B2}^{x} = pk^2 \frac{1}{4\pi\varepsilon_0} \frac{1}{d\sqrt{\cos(\theta)}} \tag{5.15}$$

Here, the correction factor $1/\sqrt{\cos(\theta)}$ must be applied when transforming $\Delta A_{FS} \rightarrow \Delta A_{B2}$. The same steps yield after:

- transformation to a local coordinate system where the (x', z') plane equals the plane of incidence for this ray,
- calculation of the individual local fields for the p/s component by the transfer matrix algorithm,
- rotation back to the fixed coordinate system

$$\tilde{E}_{FP} = \mathbf{R^{-1}} \times \mathbf{A} \times \mathbf{R} \cdot \hat{e}_x \tilde{E}^x_{B2} = \left[R^{-1} A R \right](r_{B2}) \cdot \hat{e}_x \tilde{E}^x_{B2} = \left[R^{-1} A R \right](r_{B2}) \hat{e}_x p k^2 \frac{1}{4\pi\varepsilon_0} \frac{1}{d\sqrt{\cos(\theta)}} \tag{5.16}$$

Now this quantity equals the field component E^x_{B2} due to reciprocity and for an arbitrarily oriented dipole $\vec{p}$ the following equation is obtained

$$E^x_{B2} = \begin{pmatrix} p_x \\ p_y \\ p_z \end{pmatrix} \cdot \left[\begin{pmatrix} \left[R^{-1}AR\right]_{xx} & \left[R^{-1}AR\right]_{xy} & \left[R^{-1}AR\right]_{xz} \\ \left[R^{-1}AR\right]_{yx} & \left[R^{-1}AR\right]_{yy} & \left[R^{-1}AR\right]_{yz} \\ \left[R^{-1}AR\right]_{zx} & \left[R^{-1}AR\right]_{zy} & \left[R^{-1}AR\right]_{zz} \end{pmatrix} \begin{pmatrix} 1 \\ 0 \\ 0 \end{pmatrix} \right] \frac{k^2}{4\pi\varepsilon_0} \frac{1}{d\sqrt{\cos(\theta)}} \tag{5.17}$$

And in an analogous manner

$$E^y_{B2} = \begin{pmatrix} p_x \\ p_y \\ p_z \end{pmatrix} \cdot \left[\begin{pmatrix} \left[R^{-1}AR\right]_{xx} & \left[R^{-1}AR\right]_{xy} & \left[R^{-1}AR\right]_{xz} \\ \left[R^{-1}AR\right]_{yx} & \left[R^{-1}AR\right]_{yy} & \left[R^{-1}AR\right]_{yz} \\ \left[R^{-1}AR\right]_{zx} & \left[R^{-1}AR\right]_{zy} & \left[R^{-1}AR\right]_{zz} \end{pmatrix} \begin{pmatrix} 0 \\ 1 \\ 0 \end{pmatrix} \right] \frac{k^2}{4\pi\varepsilon_0} \frac{1}{d\sqrt{\cos(\theta)}} \tag{5.18}$$

If a pure z dipole is now assumed the following result is obtained with equations (5.11), (5.17) and (5.18), respectively:

$$\begin{pmatrix} p_x \\ p_y \\ p_z \end{pmatrix} = \begin{pmatrix} 0 \\ 0 \\ E^z_{FP} \left(\frac{\lambda}{\lambda_0} \right)^2 \alpha_0 \end{pmatrix} \tag{5.19}$$

$$E^x_{B2} = E^z_{FP} \left(\frac{\lambda}{\lambda_0} \right)^2 \alpha_0 \left[R^{-1} A R \right]_{zx} (r_{B2}) \, k^2 \frac{1}{4\pi\varepsilon_0} \frac{1}{d\sqrt{\cos(\theta)}} \tag{5.20}$$

$$E^y_{B2} = E^z_{FP} \left(\frac{\lambda}{\lambda_0} \right)^2 \alpha_0 \left[R^{-1} A R \right]_{zy} (r_{B2}) \, k^2 \frac{1}{4\pi\varepsilon_0} \frac{1}{d\sqrt{\cos(\theta)}} \tag{5.21}$$

The energy flux of this field is

$$\frac{dP}{dA_{B2}} = \frac{c}{n} \vec{E} \cdot \vec{D} = cn\varepsilon_0 \left| \vec{E} \right|^2 = \frac{cn}{\varepsilon_0} \left[\frac{\alpha_0 \lambda^2 k^2}{d 4\pi \lambda_0^2} \right]^2 \left[E^z_{FP}(r_{FP}) \right]^2 \left\{ \left[\left[R^{-1} A R \right]_{zx} (r_{B2}) \right]^2 + \left[\left[R^{-1} A R \right]_{zy} (r_{B2}) \right]^2 \right\} \cdot \frac{1}{\cos(\theta)} \tag{5.22}$$

with the dielectric displacement $\vec{D}$, the speed of light *c* and the refractive index *n*. The expression (5.22) factorizes into (i) a constant pre-factor, (ii) the modulus squared of the excitation field projected on the polarizable unit and (iii) a contribution that depends exclusively on r_{B2}. From this, the intensity is obtained by integrating over the non-covered part of B2

$$P = \frac{cn}{\varepsilon_0}\left[\frac{\alpha_0 \lambda^2 k^2}{d\,4\pi\lambda_0^2}\right]^2 A_{B2}\left[E_{FP}^{z}(r_{FP})\right]^2 \times \sum_{\Delta A_{B2}} \frac{\Delta A_{B2}}{A_{B2}}\left\{\left[T_{zx}(r_{B2})\right]^2 + \left[T_{zy}(r_{B2})\right]^2\right\} \qquad (5.23)$$

$$T_{zx} = \left[R^{-1}AR\right]_{zx} \cdot \frac{1}{\sqrt{\cos(\theta)}} \qquad T_{zy} = \left[R^{-1}AR\right]_{zy} \cdot \frac{1}{\sqrt{\cos(\theta)}}$$

where the local field $E_{FP,z}$ that drives the polarizable unit is given by

$$E_{FP,z} = \frac{-ikA_{B1}}{2\pi d}\sum_{\Delta A_{B1}} \frac{\Delta A_{B1}}{A_{B1}} e^{ikr} T_{zx}(r_{B1})\, E_{B1,x} \qquad (5.24)$$

for polarization and a corresponding expression with x replaced by y for polarization. Together with (5.8), these expressions form the base of the following discussion. The computer program code for actually doing the calculations was written by [in printed version available] in Igor program code. The values of the real and imaginary parts of the dielectric function were provided by Dr. Adriana Rueda who determined them experimentally for wavelengths between 500 and 850 nm by various reflection measurements during her dissertation.[21] The advantage of this approach is that they express in the best way the properties of gold films prepared with our methods. Figure 5.4 shows a summary of her measurements.

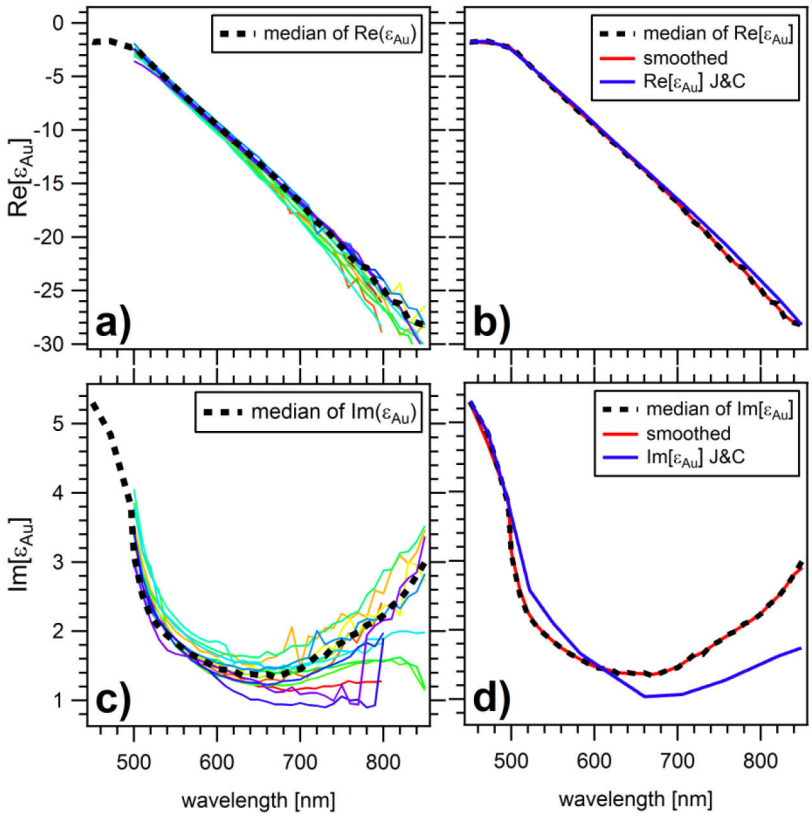

Figure 5.4: *The real and imaginary part of the dielectric function used in the calculations (red) and compared with the ones (blue) from Johnson and Christy*[22]

In (a) and (c) 13 different gold films were investigated and the extracted values averaged (black dashed curves). The imaginary parts show stronger variations than the real ones since all for the experiment important parameters like surface roughness, grain size and other inhomogeneity play a role here.[21] In (b) and (d) the experimental noise in both medians was then decreased by a binominal smoothing over one point. For values below 500 nm the literature based values from Johnson and Christy[22] were used. The red curves in the graphs on the right side are then the values used in the calculations. For comparison reasons the original dielectric values from Johnson and Christy are plotted in blue which show especially above 620 nm a lower damping than the measured ones.

The important information of the whole calculation lies in the field enhancement factors $E_{s,y}$, $E_{p,x}$ and $E_{p,z}$ of the matrix **A**. In Figure 5.1 (b-d) they are plotted as a function of the angle of incidence θ for an illumination with a red He-Ne laser line (633 nm). One can note that for s polarization the field at the back side of the metal film is quite weak. For p polarization, a strong field is seen in a narrow angular range, accompanied by a minimum in reflectivity. A maximum field enhancement factor of almost 8 is reached. This effect is well known as *surface plasmon excitation in Kretschmann-configuration*[23] and has important consequences for the signal obtained in dark field microscopy through a thin metal film. Obviously, the magnitude $E_{p,z}$ dominates the experimental signal. Different from standard microscopy where contributions everywhere in A_{B1} and A_{B2} are of similar weight, both excitation and emission are dominated by contributions in the very narrow angular range corresponding to intermediate surface plasmon excitation. As a consequence the standard way of utilizing circular symmetric complementary blocks with some overlap will either prevent efficient excitation or efficient emission and in turn produce only weak signals. A solution for this problem is the use of complementary linear blocks in the excitation and emission pathway that both allow for a significant coupling to propagating surface plasmons.

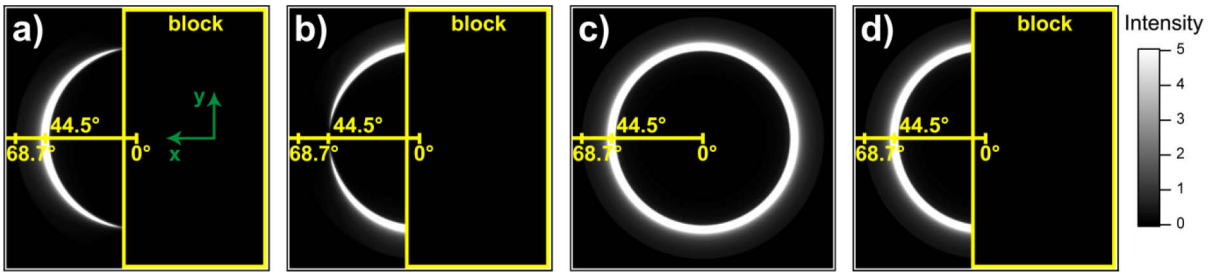

Figure 5.5: *(a) $|T_{zx}(r_{B1})|^2$, b) $|T_{zy}(r_{B1})|^2$ (c) Intensity in B2 (Term in curly brackets in equation (5.23)). (d) Same as (c) if a linear block is introduced. The scaling does not represent the full range of values which goes up to 78.*

In Figure 5.5 (a) and (b) the moduli squared of the quantities $T_{zx}(r_{B1})$ and $T_{zy}(r_{B1})$ are displayed, representing effective intensities which contribute to the excitation for ▯ and ▯▯ polarization, respectively. Only the radiation passing a block which is displaced by 0.5 mm from the optical axis as used in the experiment was plotted. In both cases, an efficient

excitation is expected. Figure 5.5 (c) shows the quantity $|T_{zx}(r_{B1})|^2+|T_{zy}(r_{B1})|^2$ corresponding to the unpolarized intensity in A_{B2} due to a z dipole in the focus. Figure 5.5 (d) finally shows the intensity that remains detectable if a second linear block is introduced in A_{B2}. In the next section it will be first shown that this experimental approach of "*surface plasmon-mediated dark field microscopy*" allows for a sensitive measurement of resonators through a thin gold film. The experimentally obtained patterns are compared with the theoretical prediction based on the simplified model of a point-like polarizable unit and the wavelength-dependence of the plasmon-mediated dark field signal is investigated and the implications for spectroscopy on this kind of system are discussed. To demonstrate the need of single object spectroscopy particle spectra are compared to an ensemble spectrum of the same sample. Then further optimizations follow to selectively detect contributions from $E_{p,z}$ and efficiently block the ones from $E_{p,x}$ and $E_{p,y}$. In the end theoretical predictions for a silver film are presented.

5.3 Experimental Validation and Comparison to Theory

First an experiment is presented which was designed to validate the expectation that efficient imaging is possible with the proposed plasmon-mediated dark field microscopy. A test sample was prepared by coating a microscope cover slip with a 50 nm gold film. The gold surface was decorated with polystyrene spheres with a diameter of 300 nm. In Figure 5.6 the resulting patterns for the two linear polarizations under investigation are displayed. In both cases, a clear signal is observed. For ⊥ polarization, a slightly elongated spot is seen with two "streaks".

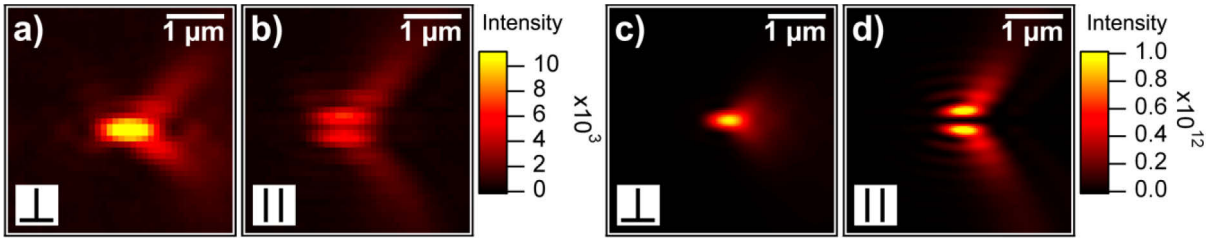

Figure 5.6 *(a-b) Measured scattering signals from a polystyrene sphere (d=300 nm) for incident light of λ = 633 nm polarized parallel (∥) and perpendicular (⊥) to the block edge, (c-d) calculated signal assuming a point-like dipole in z-direction.*

In ∥ polarization, a nodal plane is seen crossing the Gaussian focal point, indicating a dominant contribution of a z-polarized dipole[24] with similar "streaks". Note the similarity to the patterns that are obtained without B2 which have been discussed in detail and measured by near field microscopy[25]. The calculations for a point-like z-dipole are shown in Figure 5.6 (c) and (d). Taking into account the simplicity of the model, the shape of the patterns is reproduced quite well. The lateral extension of these patterns is around 1 µm for the main maximum; including the "streaks" a total size of the pattern of the order of 2 µm is

obtained. Only objects which are separated by at least this distance can be individually addressed in a straightforward manner.

The role of intermediate excitation of surface plasmons in the emission process can be nicely demonstrated by imaging the light intensity distribution in a plane which is an image of the objectives back focal plane and is placed behind B2. Directions of light rays emitted from the sample correspond to positions in this image plane. The recorded images are shown in Figure 5.7 where (a) shows the specular reflected light from a mirror in the focal plane if no blocks are present. The approximately homogenous beam profile from A_{B1} is reproduced in A_{B2}. In the image, the angles of incidence θ corresponding to the positions in A_{B2} are indicated: 0° corresponds to rays on the optical axis of the system. The angle of incidence corresponding to the outermost rays is determined by the numerical aperture of the microscope objective,[26] yielding 68° for the NA=1.4 objective used and a cover slip with a refractive index n_{glass} of 1.503. Figure 5.7 (b) shows the light intensity in A_{B2} if a polystyrene sphere is measured in plasmon-mediated dark field mode. A bright ring is observed at a position which corresponds to plasmon-mediated emission. Since the detection is unpolarized, this pattern corresponds to Figure 5.5 (d). Note that in addition to the plasmon-mediated light some experimental background intensity is seen which does not vanish if a clean part of the gold surface is investigated (Figure 5.7(c)).

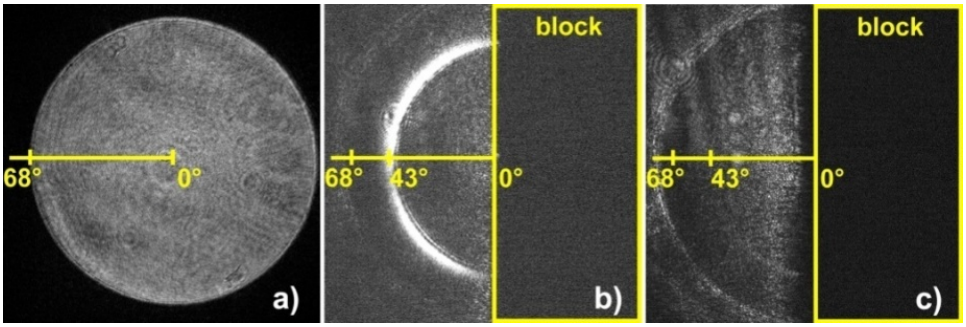

Figure 5.7: *Light intensity distribution in A_{B2}, recorded with a CCD camera. (a) Specular reflection from a mirror, no blocks. (b) Scattered light from a polystyrene sphere in dark field mode. (c) Light scattered by a 'clean' part of the gold film.*

Figure 5.8 shows dark-field micrographs of a gold film decorated with gold nanoparticles in a sphere-on-plane system. The images were obtained with differently shaped blocks B1 and B2, sketched in the inset. With two circularly symmetric blocks (disc of 5 mm, pinhole of 1 mm), no objects can be seen (a). Choosing two linear blocks, several objects with different strength are readily identified (b). Figure 5.8 (c) finally demonstrates that the experimental background may be reduced by adding an annulus to the linear block of 5 mm diameter in B1, thus efficiently reducing the background signal which dominates for these values of θ. This represents the direct experimental proof that the proper choice of block shapes allows

for a very efficient detection of scattering objects through intermediate surface plasmon excitation.

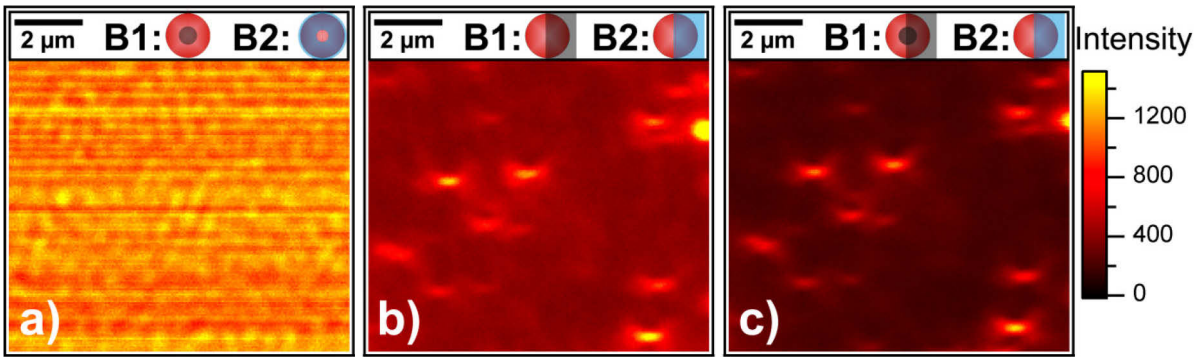

Figure 5.8: *Dark-field micrographs of 60 nm Au colloids on Au at 633 nm for different block shapes as shown in the insets. (a) Circular symmetric blocking. (b) Double-linear blocking. (c) Double-linear blocking with additional central block preventing light at low θ to pass B1.*

The diameter of the annular disc determines the possible θ values for the excitation. An increase of the disc diameter by 1 mm decreases the possible angular range by around 7° starting from the optical axis of the system or 0°.[26] Figure 5.7 shows the bright ring of the plasmon-mediated emission at around 43° and the excitation happens in the same range. For an optimal background reduction it would be preferable to excite and detect only angles around this ring.

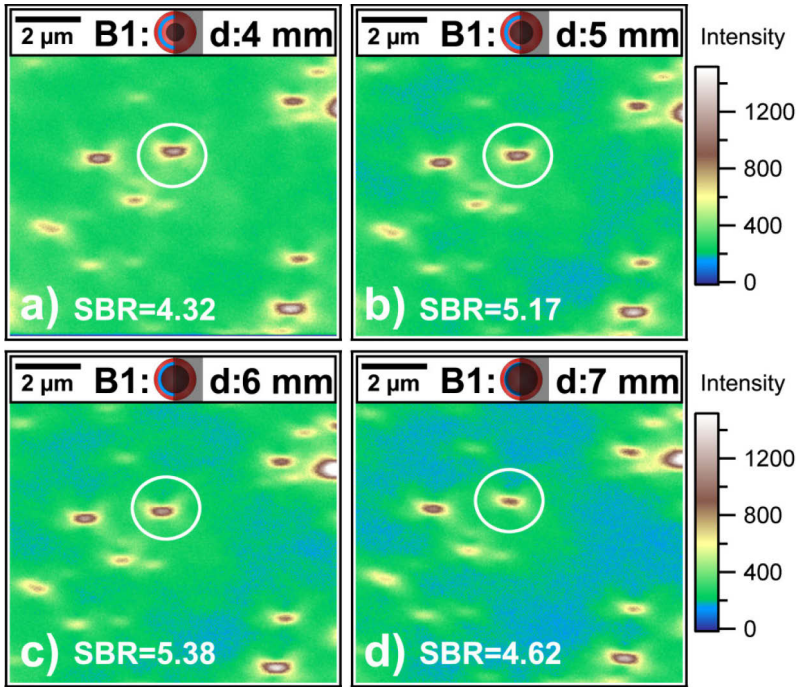

Figure 5.9: *Dark-field micrographs with different diameter of the annulus in the excitation and signal to background comparisons for the marked object in the circle. (a) SBR ratio improves from 2.19 to 4.32 by using a 4 mm annulus with possible θ values of 25° to 68°. (b) Further improvement of the SBR ratio to 5.17, the minimum θ value for illumination is 32°. (c) SBR ratio increases to 6.38 with a minimum possible θ angle of 39° and (d) a disc diameter of 7 mm and possible θ illumination range of 46°-68° obstruct in the excitation and the SBR ratio decreases to 4.62.*

Figure 5.9 shows the influence of an increasing beam diameter on the signal to background (SBR) ratio of the particle labeled with the white circle. It is the same section as in Figure 5.8 with a different color scale for better visibility. The blue ring in the inset shows the plasmon illumination and detection channel at around 43°. The disc diameter is continuously increased from 4 mm in (a) to 7 mm in (d). The SBR ratio for the tagged particle changes from 2.9 without any disc to a maximum value of 5.38 for a diameter of 6 mm. Since the signal originating from the particle is not modified, it is basically a direct consequence of the lower background noise originating from the metal film. In Figure 5.9 (c) the sample is illuminated in an angular range between 39° and 68° which is still below the critical angle of incidence for the intermediate excitation of surface plasmons. The situation changes when the diameter of the disc is increased to 7 mm in (d) and the minimum illumination angle is now 46°. The signal of the particle starts to decrease and hence the SBR ratio decreases.

Since the optical properties of gold vary strongly over the visible spectral region, the signal obtained in plasmon-mediated dark field microscopy will be wavelength dependent. Figure 5.10 displays calculated patterns as well as the enhancement factors $E_{p,x}(\theta)$ and $E_{p,z}(\theta)$ for four representative wavelengths.

At 450 nm in (a), gold is a good absorber and only a weak local electrical field with correspondingly weak patterns is seen. Note that the intensity scales are adjusted for optimum dynamic range for each wavelength. The patterns are very localized due to the short wavelength.

At 525 nm, some feature is seen in $R(\theta)$ that can be interpreted as a surface plasmon with accompanying field enhancement, reflected in maxima in $E_{p,x}$ and $E_{p,z}$. The enhancement is moderate but the resonance covers a broad angular range. At this wavelength, the strongest scattering signals are obtained. A further increase in wavelength to 633 nm leads to a sharp surface plasmon resonance. At resonance, the field increases significantly, nonetheless the scattering signal is getting weaker. Apparently, the increase in maximum field strength is overcompensated by the decrease in angular range where the enhancement occurs.

At 850 nm, the angular range where field enhancement occurs is reduced further while the amplification factor does not increase. As a consequence, the signal has further weakened significantly. Note that even when focusing in free space, the lateral extension of the focal spot scales with the wavelength λ, as a consequence, the maximum exciting field scales with λ^{-1} and the maximum scattering signal with λ^{-2}. This effect gives an additional contribution to the observed intensity reduction at increasing λ.

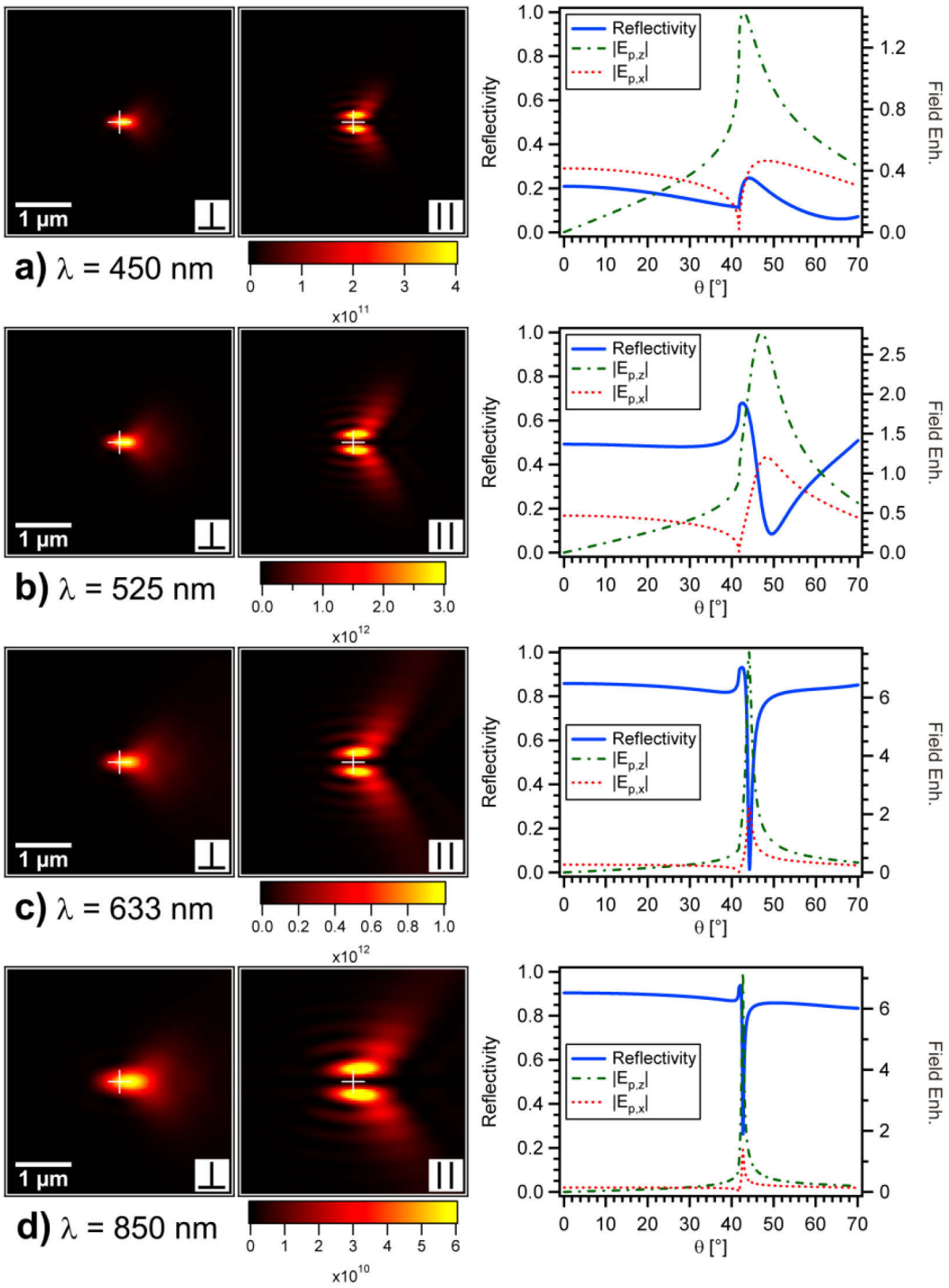

Figure 5.10: *Calculated patterns for a point like dipole in z-direction on a gold-film, field enhancement factors and reflectivity for four selected wavelengths and two polarization directions. The white cross indicates the Gaussian focal point.*

In Figure 5.11 (a) the maximum intensity in the calculated scattering patterns is displayed for an object with wavelength-independent scattering cross-section across the visible spectral range. This representation reproduces the maximum signal strength around 530 nm and the significant reduction for shorter and longer wavelengths. Figure 5.11 (a) can be interpreted as a transmission function of the entire optical system including the gold film. To recover

wavelength-dependent scattering cross-sections, it is necessary to normalize any measured signal by this transmission function.

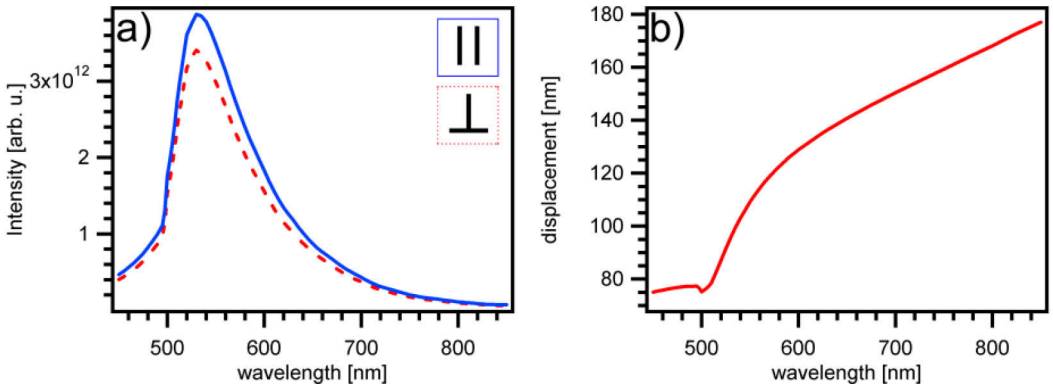

Figure 5.11: *(a) Maximum scattering intensity as a function of wavelength for a dipole in z-direction on a gold film. (b) Displacement of the object position from the Gaussian focal point for maximum intensity and polarization.*

A further important effect is seen in the patterns in Figure 5.10, which is a direct consequence of the block shapes that are not circular symmetric: maximum intensity is achieved if the scatterer is displaced from the Gaussian focal point. Figure 5.11 (b) shows this displacement for polarization across the visible range. The variations are not completely negligible but small enough to allow for spectroscopy in plasmon-mediated dark field mode across the visible range by adjusting the microscope to maximum intensity before recording a spectrum.

Figure 5.12 shows as an example scattering spectra from a gold particle, taken at different positions of a scattering pattern. Around the intensity maximum, the spectra do not vary much and show all identical features: Peaks at 760 nm, 610 nm and a shoulder around 520 nm. The peaks are assigned to resonances of the coupled system of the metal particle with the metal surface. At larger distance from the maximum, the relative strength of short-wavelength features decreases rapidly, as is directly intelligible due to the smaller focus for smaller wavelength.

Single object spectroscopy has some advantages over ensemble measurements. It can depict variations in the optical response of individual resonators, reveal structure-property relations by combining electron microscopy and avoids inhomogeneous broadening because there is no averaging other a large amount of different resonators. A combination of single object and ensemble spectroscopy of the same sample should also provide the final proof of the efficiency and correct functionality of the plasmon-mediated dark field method. Figure 5.13 (a) shows the scattering spectra for a representative selection of 10 objects out of 28 identified by electron microscopy as single particles.

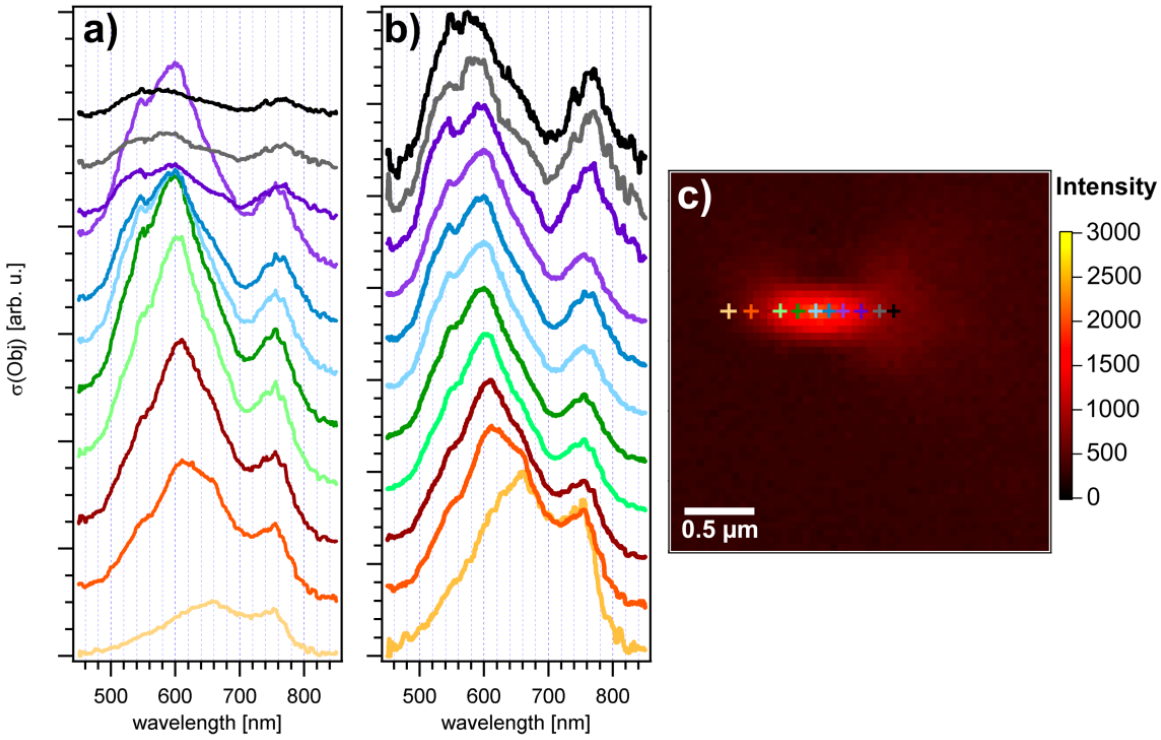

Figure 5.12: *(a-b) Spectra from a gold particle of 115 nm diameter on top of a 50 nm gold film and a cysteamine spacer layer (1 nm) in white light illumination, taken for different positions as absolute (a) and normalized values (b). In (c) positions where spectra are taken are indicated on top of a lateral intensity distribution obtained in scanning mode with white light illumination.*

The remaining part of the objects was identified as aggregates of more than one particle like dimers or trimers. Most of them possess two resonances at around 580 nm and 700 nm. Particles 10 and 15 show a deviation with only one resonance at 585 nm and 655 nm respectively. For particles fabricated by chemical reduction deviations from the theoretical optical response are rather the rule than an exception as will be seen in Chapter 7. Note that all single particle spectra are not corrected by the calculated transmission function in Figure 5.11, since this is only a theoretical function according to the calculation and the resonance in the experiment coincides not with its maximum. Figure 5.13 (b) shows the optical response for the ensemble obtained for the same sample by multi-wavelength surface plasmon spectroscopy[21] under the assumption of an effective film thickness of induced dipoles as particle layer. It is a characteristic for this method that different combinations of pairs for thickness d_f and dielectric function ε_f show the same precision of the applied fits to the measured reflectivity $R(\theta)$.[21] Thus only a set of possible combinations can be determined which is shown in Figure 5.13 (b). The effective thickness d_f varies between 5 and 10 nm. For smaller thicknesses the fit within the theoretical model gets problematic and that is the reason that the thickness is not reduced further. Within the selected thickness range two resonances at around 600 and 760 nm are visible which correspond to the results of the single particle experiment.

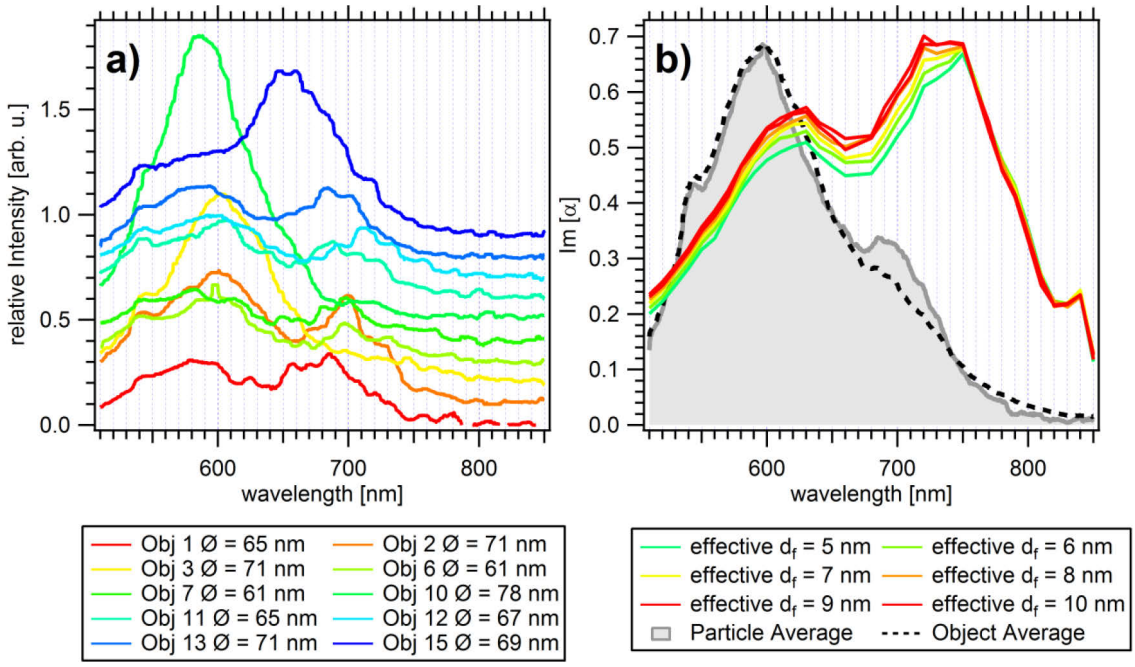

Figure 5.13: *(a) Plasmon mediated Dark field spectroscopy of single particles with SEM identification, (b) Surface plasmon spectroscopy of an ensemble from the same sample*

The gray curve shows the averaged response of the 10 single particles in (a) while the dotted black line shows it for all the 28 measured objects including the aggregates. The different height ratios of the resonances in the two experiments are a consequence of the wavelength dependent sensitivity of the plasmon mediated dark-field microscopy as shown in Figure 5.11. The mean value of the full width at half-maximum (FWHM) for the single particles adds up to 88 nm for the blue shifted resonance and 84 nm for the red shifted one. The ensemble in surface plasmon spectroscopy shows more than twice the width, since in this case inhomogeneous broadening has to be considered.

5.4 Optimization of Plasmon-Mediated Dark Field Microscopy

After the re-design of the confocal microscope to compensate for mechanical instability the modified setup provided the opportunity to place the linear block B1 between the beam splitter and the microscope objective. As a consequence of the point reflection of the beam profile at the surface the second block B2 in the detection was no longer required. This does not only save adjustment time for the block calibration, but also has the benefit that the remaining block B is automatically placed in the center of the illumination beam during the adjustment with an symmetric overlap on both sides. As a second optimization step a second polarizer was placed in the detection (D) with a polarization direction perpendicular to the existing one in the excitation (E). The changes are summarized in the schematic of Figure 5.14. This should allow for selective detection of z-dipoles or the direct interaction between a particle and the gold film while other contributions originating from different

sources like ordinary reflected light from angles of incidence where the metal film acts purely as a mirror are efficiently blocked.

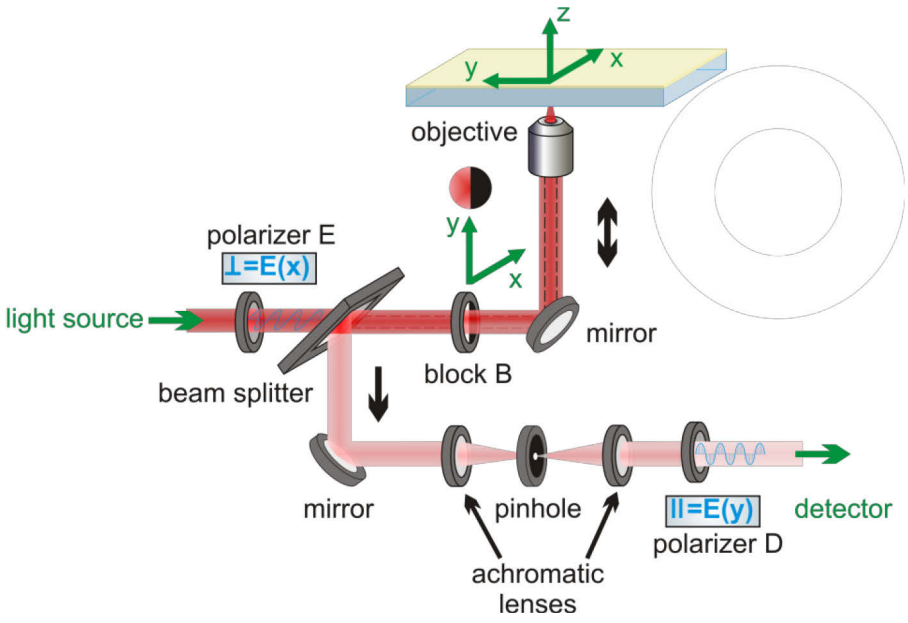

Figure 5.14: *Optimization of the setup: (1) by placing one block between the beam splitter and the microscope objective one block becomes redundant, (2) an additional polarizer in the detection with a perpendicular direction to the first one allows for the selective detection of z-dipoles*

For the theoretical modeling of the signal only point-like dipoles in the z-direction were considered with a signal dominated by contributions from $E_{p,z}$, but experimental accessible sphere-on-plane resonators do also possess degenerated resonances parallel to the plane (x,y-direction) and hence have an detectable incident field $E_{p,x}$.[27, 28] While the z-dipoles have a radial polarization and a uniform emission in all directions within a narrow angular range (Figure 5.15 (a)) these degenerated modes are consequently polarized parallel to the surface. Therefore, they can be blocked by a second polarizer in the detection (D) which is adjusted to a polarization direction perpendicular to the first one in the excitation (E). As seen in Figure 5.15 (b) most emission from the z-dipoles can still be detected, even with the linear block in the beam profile as shown in (c). The intensity distribution in the x-direction originates completely from $|T_{zx}(r_{B1})|^2$ and in y-direction completely from $|T_{zy}(r_{B1})|^2$, while it is an equal mixture of both in the diagonal direction between the two.

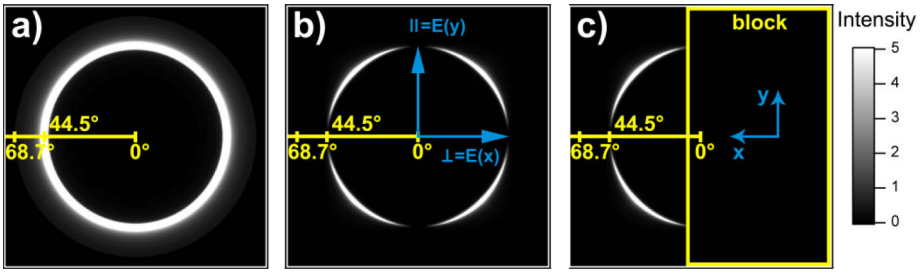

Figure 5.15: *(a) Intensity from $|T_{zx}(r_{B1})|^2+|T_{zy}(r_{B1})|^2$ corresponding to radial polarization, (b) Intensity with two polarizers as shown in Figure 5.14 without any block and (c) with the block B*

The improvement is validated in Figure 5.16. The position of the excitation polarizer determines the shape of the patterns. The signal to background (SBR) ratio improves independently from the patterns by a factor of 6-8 when the second polarizer is added. As expected both signal and background intensities are reduced, but the noise from the background is the dominant part in this process and leads to an efficient enhancement of the signal to background ratio.

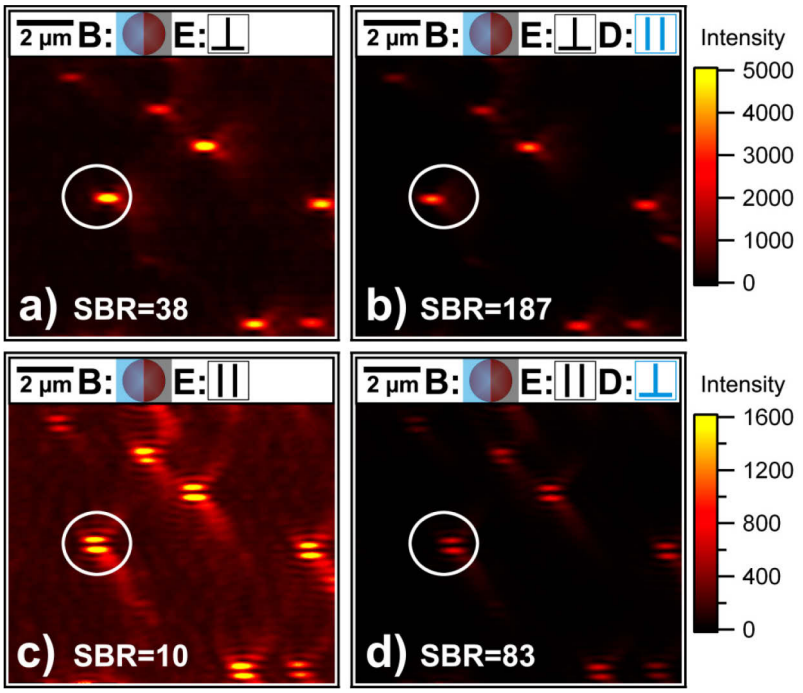

Figure 5.16: *(a) Dark-Field Micrograph with the polarizer in the excitation (E) parallel (∥) and (c) perpendicular (⊥) to the block edge. (b)+(d) Same area of interest with a second polarizer in the detection (D) perpendicular to the first one.*

The pattern shapes with the "streaks" in the vicinity are not changed by the presence of the second polarizer in the right and left pictures. By selecting a suitable combination of block and polarizer positions and by measuring at the minima of the patterns between the loops like in Figure 5.16 (d) it could be possible to estimate the contributions of the degenerated modes in the x- and y- direction to the total scattering response. For particles with large differences in resonance wavelengths for the different directions like for gold rods with an aspect ratio it could even be possible to image the individual scattering patterns in all directions when a suitable band-pass filter is placed in the detection.

5.5 Silver Sphere-On-Plane Systems

To be suitable as plasmonic material, a metal must have conduction band electrons capable of resonating with light at a suitable wavelength. Gold, silver and copper are the only metals which satisfy this condition in the visible range and show somehow the free electron behavior described by Drude.[29, 30] Particularly gold and silver plasmon absorptions are

unique because other elements are affected by two type of characteristics. The first one involves the position of the plasmon absorption which lies for most elements too high in energy for visible light, as for platinum. The second one is that the superposition of the plasmon absorption band with interband transitions produces a strong damping, as for lead and copper, although in the latter case the damping allows the observation of a well definite absorption.[31]

Gold is commonly used as it possesses highly stable optical and chemical properties and allows for facile surface modification due to the freely available thiol chemistry. However, relativistic effects cause a contraction of the 6sp hybridized valence band (inert-pair-effect) of the gold, decreasing the energy distance to the 5d band and shifting the corresponding wavelength of the plasma frequency to 496 nm (2.5 eV). These interband transitions also strongly influence the imaginary part of the gold's dielectric function and lead to additional absorption processes which worsen its plasmonic behavior at least in the blue part of the visible spectrum.

In contrast Silver is not affected by these relativistic effects in the same way as gold, but the main drawback is its chemical instability. Silver oxidizes rapidly when exposed to air, and the process is accelerated in aqueous solutions, making it difficult to get reliable optical signals. In terms of optical properties the metal has a plasma wavelength of 310 nm (4.0 eV) and shows nearly Drude-like behavior in the whole visible range. It also provides the sharpest SPR signal and is reported to have an enhanced sensitivity to thickness and refractive index variation in comparison to gold.[32, 33] Moreover, optical excitation of plasmon resonances in nano-sized silver particles is the most efficient mechanism by which light interacts with matter. A single silver nanoparticle interacts with light more efficiently than a particle of the same dimension composed of any known organic or inorganic chromophore. The light-interaction cross-section for silver can be about ten times that of the geometric cross-section, which indicates that the particles capture much more light than is physically incident on them.[34]

In a sphere-on-plane geometry silver should provide the largest enhancement factors of the electric field which is for example suitable for the amplification of the fluorescence behavior of chromophores. The obtained signals in the plasmon-mediated dark-field microscopy will be again wavelength dependent on the optical properties of the silver. For four representative wavelengths the calculated patterns are shown together with the enhancement factors $E_{p,x}(\theta)$ and $E_{p,z}(\theta)$ in Figure 5.17. For the calculation the experimental available data for the dielectric functions from Johnson and Christy[22] is used. At 300 nm (a) below the plasma frequency of silver where the material properties are in the transition from a conductor to an insulator the material is not reflecting the light and a surface

plasmon is not supported. Thus only a weak response of the electric fields and the dipole is seen with corresponding localized patterns. At 365 nm (b) this changes dramatically and the field enhancement is already as high as for the gold film and the resonance covers a broad angular range around the plasmon angle of 57°.

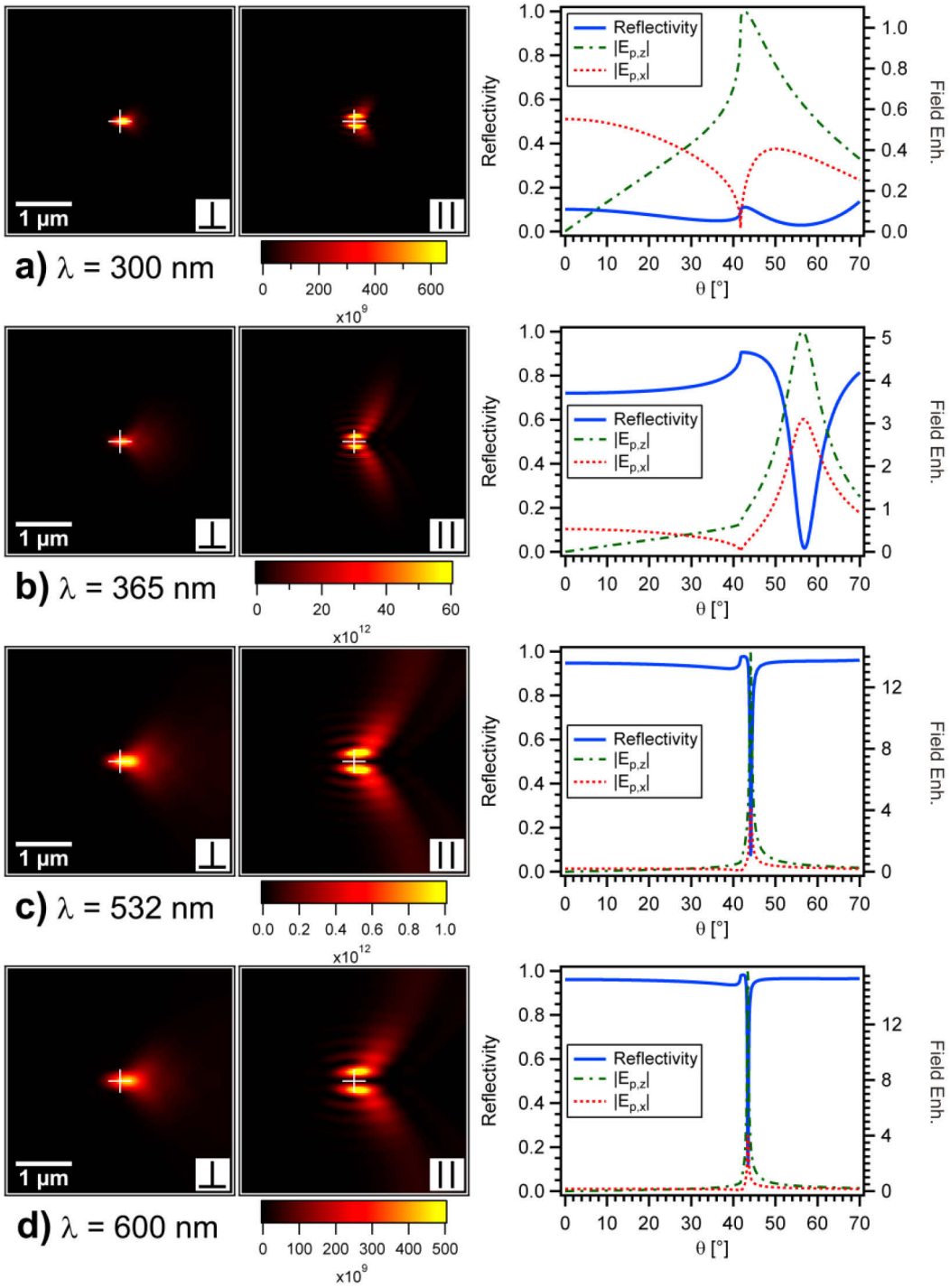

Figure 5.17: *Calculated patterns for a point like dipole in z-direction on a silver film, field enhancement factors and reflectivity for four selected wavelengths and two polarization directions. The white cross indicates the Gaussian focal point.*

Both factors make sure that the patterns display the strongest scattering intensity of all wavelengths which is 20 times higher compared to gold. The intensity of the pattern reaches

the maximum values for the gold already at 385 nm. For a wavelength of 532 nm, the light of a green diode, the situation resembles the gold case for 633 nm. The scattering patterns reveal the same intensity and shape, but the effect originates obviously from a narrower plasmon resonance at around 44° with an accompanying stronger field enhancement of 14.3. At a wavelength of 600 nm the signal is further weakened due to the compensating effect of a smaller angular emission range and an enhancement factor which is not increasing significantly.

In Figure 5.18 (a) and (b) the light distribution in the plasmon-mediated emission is displayed for a silver film and an excitation wavelength of 532 nm by plotting the moduli squared of the quantities $T_{zx}(r_{B1})$ and $T_{zy}(r_{B1})$, representing effective intensities which contribute to the excitation for the two polarization directions. In (c) the sum of the two factors is shown corresponding to the unpolarized intensity. Please note the different intensity scaling compared to the gold to compensate for the higher field enhancement.

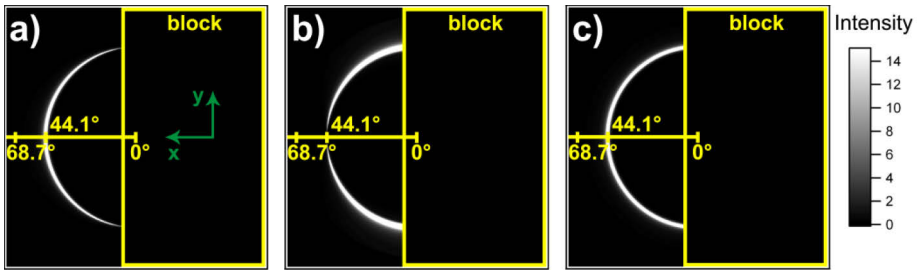

Figure 5.18: *(a) $|T_{zx}(r_{B1})|^2$, b) $|T_{zy}(r_{B1})|^2$ (c) Intensity of the sum. The scaling does not represent the full range of values which goes up to 270.*

The light is concentrated in a narrower angular range what was already seen from the calculation of the reflectivity. This figure will be useful in chapter 8. In Figure 5.19 (a) the transmission function for silver is shown which is normally needed to normalize any spectroscopic measurement.

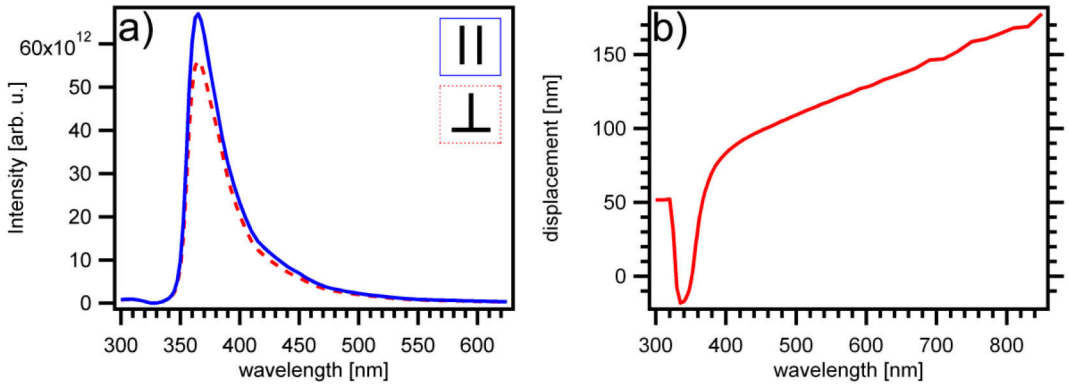

Figure 5.19: *(a) Maximum scattering intensity as a function of wavelength for a dipole in z-direction on a silver film. (b) Displacement of the object position from the Gaussian focal point for maximum intensity and polarization.*

The maximum intensity at a wavelength of 365 nm is 20 times higher compared to gold while the FWHM of 38 nm is more than half the value. In the visible range above 470 nm the enhancement is as strong as for gold at the best case. Figure 5.19 (b) shows the displacement from the Gaussian focal point between 300 and 850 nm for polarization. The noise above 680 nm is related to a lower wavelength resolution in the calculation. Around 340 nm the patterns shift strongly to the opposite direction compared to the trend, while the displacement in the visible range is comparable to gold and should allow for spectroscopic investigations.

5.6 Summary and Outlook

In summary, dark field microscopy through a thin metal film can be performed efficiently if a non-symmetric blocking scheme is used, which allows for the intermediate excitation of surface plasmons both for excitation and for detection. This concept was demonstrated by comparing lateral patters obtained experimentally with the theoretical prediction and by directly monitoring the emission pattern. The resulting signal depends on the wavelength with a maximum efficiency for gold around 530 nm and for silver around 365 nm. This effect, together with a wavelength-dependent lateral displacement between the Gaussian focal point and the maximum in the scattering pattern, should be considered for spectroscopy.

5.7 Bibliography

1. Lakowicz, J. R., Radiative Decay Engineering: Biophysical and Biomedical Applications. *Anal. Biochem.* **2001,** *298*, 1-24.

2. Otto, A.; Mrozek, I.; Grabhorn, H.; Akemann, W., Surface-enhanced raman-scattering. *J. Phys. Condens. Matter* **1992,** *4* (5), 1143-1212.

3. Willets, K. A.; Van Duyne, R. P., Localized Surface Plasmon Resonance Spectroscopy and Sensing. *Annu. Rev. Phys. Chem.* **2007,** *58*, 267-297.

4. Schaadt, D. M.; Feng, B.; Yu, E. T., Enhanced semiconductor optical absorption via surface plasmon excitation in metal nanoparticles. *Appl. Phys. Lett.* **2005,** *86* (6).

5. Joulain, K.; Mulet, J. P.; Marquier, F.; Carminati, R.; Greffet, J. J., Surface electromagnetic waves thermally excited: Radiative heat transfer, coherence properties and Casimir forces revisited in the near field. *Surface Science Reports* **2005,** *57* (3-4), 59-112.

6. Sönnichsen, C.; Geier, S.; Hecker, N. E.; von Plessen, G.; Feldmann, J.; Ditlbacher, H.; Lamprecht, B.; Krenn, J. R.; Aussenegg, F. R.; Chan, V. Z. H.; Spatz, J. P.; Moller, M., Spectroscopy of single metallic nanoparticles using total internal reflection microscopy. *Appl. Phys. Lett.* **2000,** *77* (19), 2949-2951.

7. Sönnichsen, C.; Franzl, T.; Wilk, T.; von Plessen, G.; Feldmann, J.; Wilson, O.; Mulvaney, P., Drastic reduction of plasmon damping in gold nanorods. *Phys. Rev. Lett.* **2002,** *88* (7).

8. Schultz, S.; Smith, D. R.; Mock, J. J.; Schultz, D. A., Single-target molecule detection with nonbleaching multicolor optical immunolabels. *Proceedings of the National Academy of Sciences of the United States of America* **2000,** *97* (3), 996-1001.

9. Mock, J. J.; Barbic, M.; Smith, D. R.; Schultz, D. A.; Schultz, S., Shape effects in plasmon resonance of individual colloidal silver nanoparticles. *J. Chem. Phys.* **2002,** *116* (15), 6755-6759.

10. Aravind, P. K.; Metiu, H., The effects of the interaction between resonances in the electromagnetic response of a sphere-plane structure - applications to surface enhanced spectroscopy. *Surface Science* **1983,** *124* (2-3), 506-528.

11. Xu, H.; Käll, M., Surface-Plasmon-Enhanced Optical Forces in Silver Nanoaggregates. *Phys. Rev. Lett.* **2002,** *89* (24), 246802.

12. Prodan, E.; Radloff, C.; Halas, N. J.; Nordlander, P., A hybridization model for the plasmon response of complex nanostructures. *Science* **2003,** *302* (5644), 419-422.

13. Okamoto, T.; Yamaguchi, I., Optical absorption study of the surface plasmon resonance in gold nanoparticles immobilized onto a gold substrate by self-assembly technique. *J. Phys. Chem. B* **2003,** *107* (38), 10321-10324.

14. Gerbshtein, Y. M.; Merkulov, I. A.; Mirlin, D. N., Transfer of Luminescence-center energy to surface plasmons. *Jetp Letters* **1975,** *22* (2), 35-36.

15. Knobloch, H.; Brunner, H.; Leitner, A.; Aussenegg, F.; Knoll, W., Probing the evancescent field of propagating plasmon surface-polaritons by fluorescence and raman spectroscopy. *J. Chem. Phys.* **1993,** *98* (12), 10093-10095.

16. Stefani, F. D.; Vasilev, K.; Bocchio, N.; Stoyanova, N.; Kreiter, M., Surface-plasmon-mediated single-molecule fluorescence through a thin metallic film. *Phys. Rev. Lett.* **2005,** *94* (2).

17. Hecht, B.; Bielefeldt, H.; Novotny, L.; Inouye, Y.; Pohl, D. W., Local excitation, scattering, and interference of surface plasmons. *Phys. Rev. Lett.* **1996,** *77* (9), 1889-1892.

18. Born, M.; Wolf, E., *Principles of Optics: Electromagnetic Theory of Propagation, Interference and Diffraction of Light*. 6 ed.; Cambridge University Press;: 1997.

19. Yeh, P., *Optical Waves in Layered Media*. John Wiley & Sons Inc: Hoboten, 1988.

20. Collin, R. E., *Field Theory of Guided Waves*. IEEE Press: New York, 1991.

21. Rueda, A. Optical resonances of sphere-on-plane geometries. Dissertation, Johannes Gutenberg Universität, Mainz, 2008.

22. Johnson, P. B.; Christy, R. W., Optical Constants of Noble-Metals. *Phys. Rev. B* **1972,** *6* (12), 4370-4379.

23. Kretschmann, E.; Raether, H., Radiative Decay of Non Radiative Surface Plasmons Excited by Light. *Zeitschrift für Naturforschung Part A* **1968,** *23* (12), 2135-2136.

24. Sick, B.; Hecht, B.; Novotny, L., Orientational imaging of single molecules by annular illumination. *Phys. Rev. Lett.* **2000,** *85* (21), 4482-4485.

25. Bouhelier, A.; Ignatovich, F.; Bruyant, A.; Huang, C.; Colas des Francs, G.; Weeber, J. C.; Dereux, A.; Wiederrecht, G. P.; Novotny, L., Surface plasmon interference excited by tightly focused laser beams. *Opt. Lett.* **2007,** *32* (17), 2535-2537.

26. Stefani, F. D. Confocal Microscopy applied to the Study of single entity Fluorescence and Light Scattering. Dissertation, Johannes Gutenberg Universität, Mainz, 2004.

27. Nordlander, P.; Le, F., Plasmonic structure and electromagnetic field enhancements in the metallic nanoparticle-film system. *Applied Physics B-Lasers and Optics* **2006,** *84* (1-2), 35-41.

28. Yang, S. C.; Kobori, H.; He, C. L.; Lin, M. H.; Chen, H. Y.; Li, C. C.; Kanehara, M.; Teranishi, T.; Gwo, S., Plasmon Hybridization in individual Gold Nanocrystal Dimers: Direct Observation of Bright and Dark Modes. *Nano Lett.* **2010,** *10* (2), 632-637.

29. Ashcroft, N.; Mermin, D., *Solid State Physics*. 1st ed.; Brooks Cole: 1976.

30. Kittel, C., *Introduction to Solid Sate Physics*. 8th Edition ed.; John Wiley & Sons: New York, 2005.

31. Xia, Y. N.; Halas, N. J., Shape-controlled synthesis and surface plasmonic properties of metallic nanostructures. *Mrs Bulletin* **2005,** *30* (5), 338-344.

32. Chah, S.; Hutter, E.; Roy, D.; Fendler, J. H.; Yi, J., The effect of substrate metal on 2-aminoethanethiol and nanoparticle enhanced surface plasmon resonance imaging. *Chem. Phys.* **2001,** *272* (1), 127-136.

33. Yuan, X. C.; Hong, B.; Tan, Y. G.; Zhang, D. W.; Irawan, R.; Tjin, S. C., Sensitivity-stability-optimized surface plasmon resonance sensing with double metal layers. *J. Opt. A-Pure Appl. Opt.* **2006,** *8* (11), 959-963.

34. Zhao, L. L.; Kelly, K. L.; Schatz, G. C., The extinction spectra of silver nanoparticle arrays: Influence of array structure on plasmon resonance wavelength and width. *Journal of Physical Chemistry B* **2003,** *107* (30), 7343-7350.

6 Individual Resonances of Polystyrene-Spheres on Gold Films

6.1 Introduction

Light scattering by small particles has been the topic of many studies, even before Maxwell's equations[1] were discovered. Gustav Mie[2] was the first one to provide an exact analytical solution to this problem by solving these equations for light interacting with a perfect sphere of arbitrary dimensions. Today there are several excellent textbooks on the subject[3-5] as this scattering problem is important for fundamental science in general and for a number of applications in particular in atmospheric or sensor optics. A related problem is the light scattering by spherical particles on or near a conductive plane surface. This geometry is relevant for certain manufacturing processes in which surfaces must be maintained in an uncontaminated condition[6] and in the design of optical scanning instruments for the use in the semiconductor industry. In spite of its simplicity a detailed investigation with respect to the involved plasmonic effects is not available. The interface breaks the symmetry of the whole system and can lead to a coupling of the Mie resonances to the surface plasmon modes.

An accurate theoretical framework to predict the light scattering by particles deposited on surfaces would be desirable. Unfortunately the solution to this problem is much more difficult than for isolated particles and the existing theoretical framework is tedious. Much of this research was initiated by Sommerfeld,[7, 8] who investigated the radiation from an oscillating point dipole in the presence of a finitely conducting plane. Weyl[9] was later able to develop the idea that Sommerfeld's results could be interpreted as a bundle of plane waves reflected and refracted from the surface at various angles of incidence. The additional problems caused by the surface are seen when the behavior of a free dipole is compared to the one near an interface.[10] Later Bobbert and Vlieger[11] extended Weyl's method to the problem of extended spheres and applied Mie theory along with the Debye-potential method. With the advent of high-performance computing a combination of the multipole expansion method and image theory were used to calculate the electromagnetic scattered fields.[12, 13] The analytical solutions are in most cases validated by calculating the angular distribution of the light in the sphere-plane system since this is less time-consuming than the wavelength response.

On the other side experiments in the field try to determine these field distributions[14, 15] or concentrate on the morphology dependent resonances of larger spheres.[16, 17] Jory *et al.*[18] compared the angular scattering profile of latex microspheres with 200 nm diameter on gold

with the one on glass. The excitation of surface plasmons along the interface occupied by the spheres resulted in an increase of the scattered intensity by a factor of 14. This enhancement can be used in the field of optical bio-sensing. Hillenbrand *et al.*[19] used a scattering scanning near-field optical microscope (SNOM) in the far-infrared to study the scattering of a metal coated tip in close proximity to a phonon-active SiC surface. The surface phonons are the infrared counterpart to the surface plasmons of noble metals in the visible. The observed signals exhibited a clear resonance indicating the excitation of surface phonons at the surface via the near-field of the illuminated tip or reduced sphere which was not in resonance. Such near-field properties are important for all processes that are sensitive to the local electric field, such as Raman scattering.[20] In this context the excitation of the surface plasmons via a conducting plane was extensively considered both experimentally[21, 22] and theoretically.[23-27] The interaction of the coupled system creates a special type of electromagnetic normal mode which is called gap resonance. The position of this resonance largely depends on the ratio of the sphere-film distance and the sphere radius. The question arises whether a dielectric sphere on a gold film can support a similar resonance in the visible as a gold sphere in vacuum.

In this chapter the wavelength dependent scattering response from polystyrene spheres with diameters between 200 and 500 nm on a gold film is studied to investigate the interaction of the sphere with the metal. In the context of plasmon-mediated dark-field, the comparable shape and size of the particles is exploited as a reference system to prove the reproducibility of the method and exclude spectroscopic influence from the signal-to-background (SBR) optimizations. The geometry of the reference system is comparable to a sphere-on-plane metal system, but it has the advantage that different dielectric particles with identical size act as some kind of unit scatterer with a comparable response for each particle. This can be exploited to demonstrate the reproducibility of plasmon mediated dark-field spectroscopy. For the metal counterparts with their variations in shape and size this is not achievable. The optical response of the characterized particles is finally correlated to their size as determined by scanning electron microscopy. An approach to combine scanning electron microscopy with atomic force microscopy is also presented.

6.2 Results and Discussion

6.2.1 Calculations of the Sphere-Metal-Interaction

The scattering problem of a single polystyrene sphere with a refractive index of 1.59 in vacuum can be solved by Mie[2] theory. Figure 6.1 shows the backscattered intensity for different diameters using a free available Mie program code.[3, 28] For spheres with diameters of 200 and 250 nm a broad fundamental (1) is seen which shifts with increasing size to the

red. This continues for the 300 nm spheres while a higher order resonance (2) appears on the far blue side of the spectrum. Increasing the diameter to 350 nm shifts the whole spectrum by 71 nm to the red. For spheres with a diameter of 400 nm a second shift of 71 nm is observed and even the next higher order resonance (3) appears on the blue side while the fundamental (1) disappears on the red side of the spectrum. This process continues for the spheres with 450 nm and 500 nm diameters with the whole spectrum moving to the red. Every resonances appearing on the blue side of the spectrum gets sharper and increases in maximum intensity.

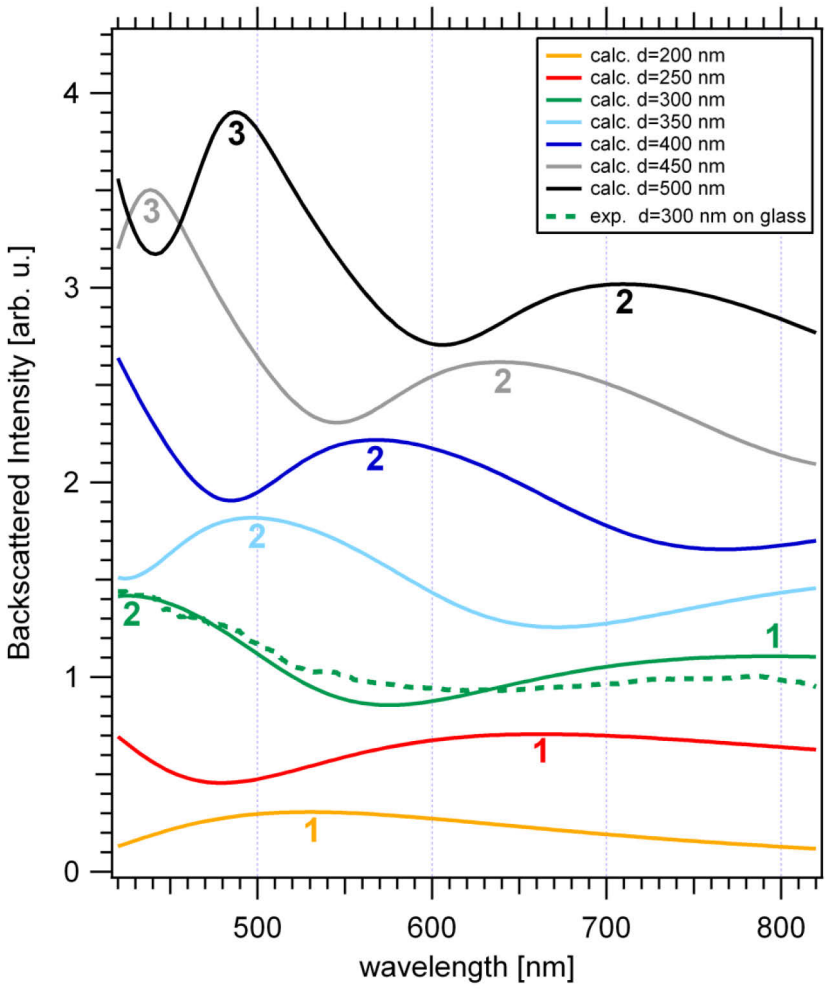

Figure 6.1: *Calculation of the back-scattered intensity using Mie's equation[3, 28] for spheres of different diameters with a homogenous environment of n=1 and a refractive index of polystyrene of n=1.59. The dashed line shows the measured response of single polystyrene beads with a diameter of 300 nm on glass. The numbers 1, 2, 3 represent the fundamental (1) and higher order Mie resonances (2, 3)*

As an experimental verification of the calculation the green dashed line shows a spectrum for a sphere with a diameter of 300 nm on glass, which was determined with the confocal microscope in plasmon-mediated dark-field mode. In the experiment the fundamental is red-shifted and the minimum to the higher order mode is weaker, but except of that the agreement to the calculation is good.

In the vicinity of a gold interface the field generated by the sphere is reflected and interacts again with the sphere. In a quasistatic approach, the coupled system can be described by the superposition of the sphere's original dipole and the field from an image dipole in the substrate[12, 29] as shown in Figure 6.2. Applicability of this static theory to the scattering problem is normally limited to the case where the size of the particle and its distance to the sample surface are much smaller than the wavelength of the illumination light, so that retardation can be neglected. In the presented case the quasistatic approach can normally not be applied and multipolar particle modes have to be considered. Still it allows for a qualitative impression of the interaction and for spheres with a diameter of 300 nm the approximation as point dipole in the previous Chapter 5 agreed well with the experimental results. In this quasistatic model the total field radiated to the far field can be attributed to the total dipole moment made up of the sphere and its image charge distribution. Under the described dark field illumination conditions charge oscillations in the nanoparticle are excited both lateral and normal to the substrate. At low frequencies (below the plasma frequency of the gold) the external field normal to the interface polarizes both the particle and substrate in the same direction such that the induced local field acting on the particle is along the applied field and against the restoring force as shown in the center panel in Figure 6.2. Thereby the resonance frequency of the particle is decreased.

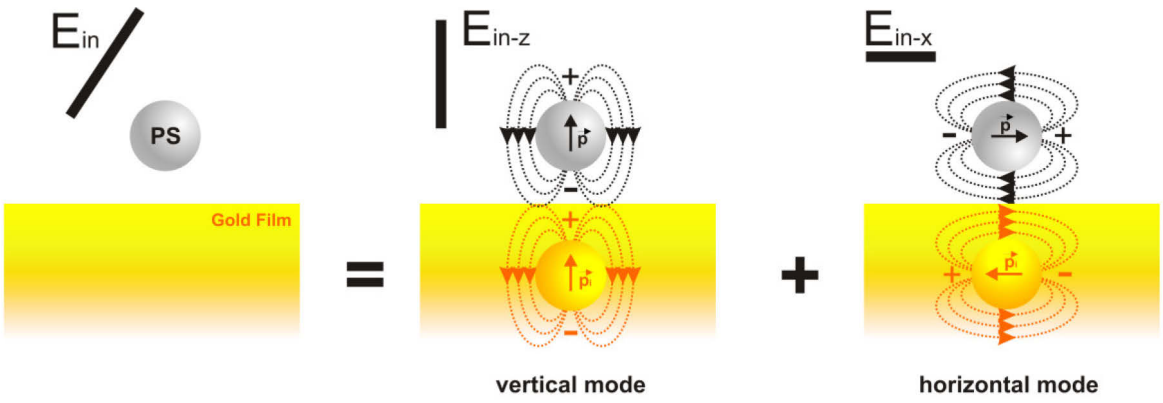

Figure 6.2: *Schematic representation of dipole-dipole interaction for the particle-gold system. The distance between the two was only selected for better visibility. The electric field (E_{in}) of the incident wave is also shown. Both the horizontal and vertical localized modes can be excited on the particle.*

The external field parallel to the interface polarizes the particle in the opposite direction to the substrate polarization. The induced local field acting on the particle is along the applied field and against the restoring force, again red-shifting the. Therefore the dipole resonance of a polystyrene sphere on gold should be further red-shifted from the Mie resonances as seen for the glass substrate.

Considering retardation effects, both the sphere and the substrate-induced field acting on the ample volume of the sphere is no longer homogenous in space and multipolar modes are excited in addition to the dipole mode. To account for these modes first a simulation using

the finite element method (FEM) with the software package JCMwave[30] was performed by [in printed version available]. The main principle of the technique is that the solution of partial differential equations is approximated by a sum of base functions that are only defined on small elements or patches in space, for example triangles in two dimensions (2D) or tetrahedrons in three dimensions (3D). For the original partial differential equations a variational formulation is derived and an ansatz consisting of these functions is inserted. The result is a system of linear equations which has to be inverted to find a solution. Figure 6.3 shows the results of this simulation for spheres of 300 and 400 nm diameters above an interface. The system is calculated in 2D with regards to the radial symmetry and excited through the gold film with an angle of incidence of the incoming light of 51.4°. The scattered light is then analyzed by a detector in the same half space as the excitation source.

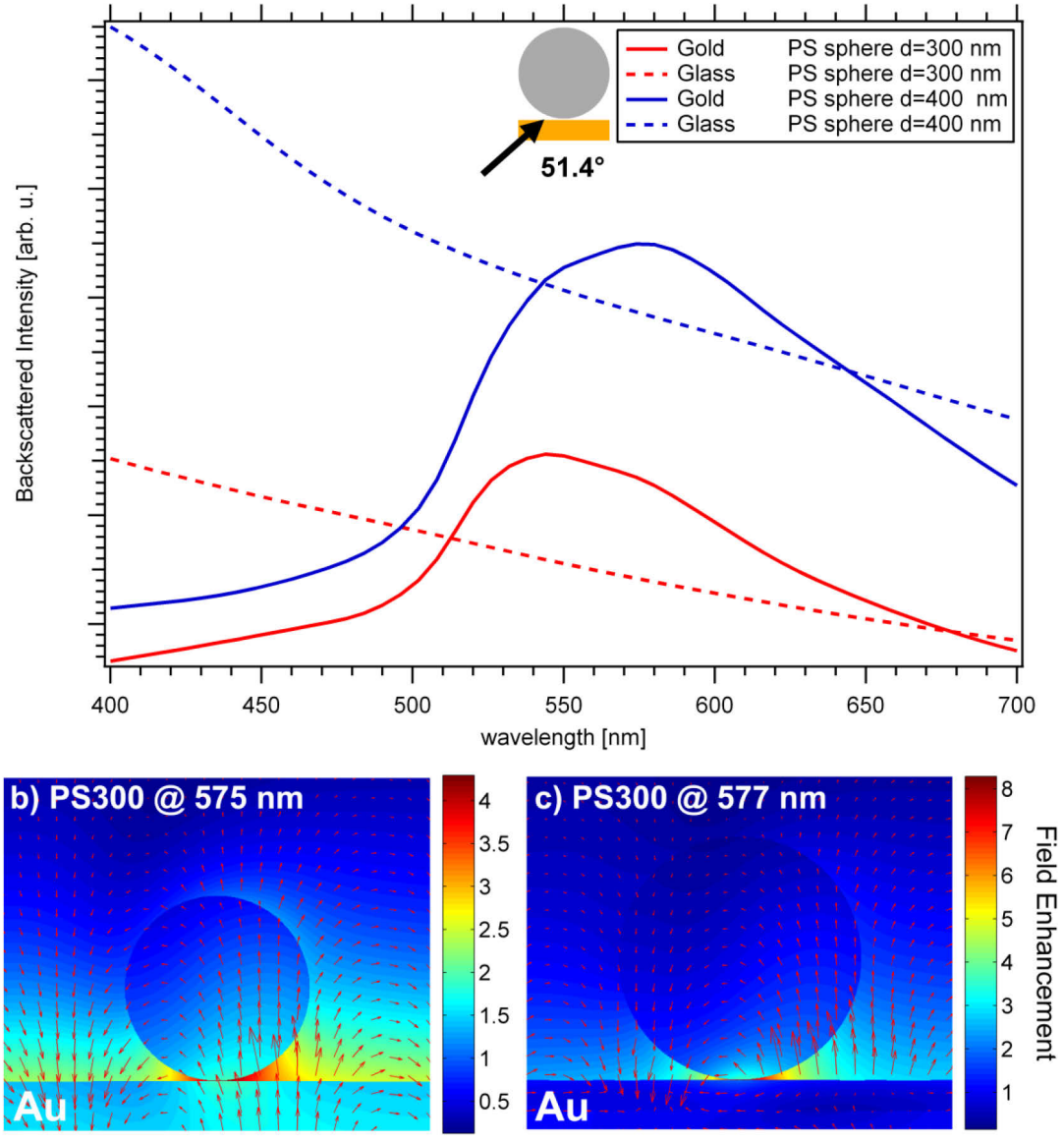

Figure 6.3: *(a) FEM simulated spectra of polystyrene spheres of 300 (red) and 400 nm (blue) diameters on glass and gold, (b) electric field distribution around a sphere of 300 nm above a gold film for an excitation wavelength of 575 nm and (c) the same for a sphere of 400 nm for an excitation wavelength of 577 nm. The light is incident in at an angle of 51.4° to the vertical.*

For both spheres on glass the scattering spectra look quite different from the Mie calculation and the experimental determination of Figure 6.1. No clear resonance is visible in the considered wavelength range. This is a direct consequence of the angular distribution of the scattered light where forward and back scattering dominates. In the simulation this light is not collected by the detector in the same half space as the incoming light and therefore no resonance is visible. When the incident light is normal to the glass surface, the response of the sphere glass system changes dramatically and is similar to Mie calculation as presented in Figure 6.4.

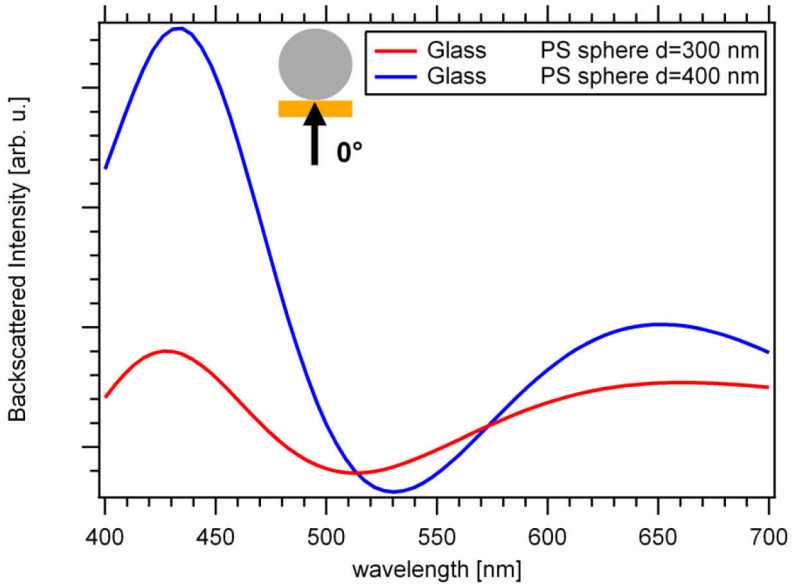

Figure 6.4: *FEM simulated spectra of polystyrene spheres of 300 (red) and 400 nm (blue) diameters on glass with incident light at 0° as indicated.*

The coupling of the sphere with the gold surface results in both cases in an asymmetrically broadened resonance which has a maximum at around 545 nm for the small sphere and at 575 nm for the larger sphere. Inspection of the electric field distribution around the asymmetric broadening provides some insight into the nature of the two resonant modes. As seen in the images of Figure 6.3 (b) and (c), the largest values of the field are located in the gap and the sphere do not show a dipolar like response. The field reverses its directions over a very short distance along the interface. This corresponds to the excitation of surface waves.

As a 2D description of a 3D-system is not very realistic and the editor of JCMwave does not allow to model an ideal sphere, the electromagnetic response of the system was studied a second time in 3D by using the finite integration technique[31] (FIT) implemented in Microwave Studio 2010.[32] The simulations, which were performed by [in printed version available] from the University of Mainz, have also the advantage that both the far and near field response can be calculated. Figure 6.5 shows both spectra for a 3D sphere of 300 nm

diameter on a gold film as well as the electric-field distribution for two selected wavelengths surrounding the sphere. The far-field spectrum up to a wavelength of 610 nm shows in principle the same features seen from the 2D model. For larger wavelengths an additional broad emission is seen which could not be detected in the previous case. The wave-like fine structure is most probably a related to the selected mesh size in the simulation. The near-field spectrum shows two pronounced resonances in the selected wavelength range at 560 nm and 660 nm, respectively and a feature at 800 nm. For a wavelength of 575 nm in (b) the electric field above the sample is dominated by a normal component with the excitation of surface plasmons. The largest fields are located in the gap between the sphere and film. The field distribution looks similar to Figure 6.3 (b). At 800 nm the sphere becomes more polarized along the surface, in accordance with the electric field parallel to the interface as illustrated in (c).

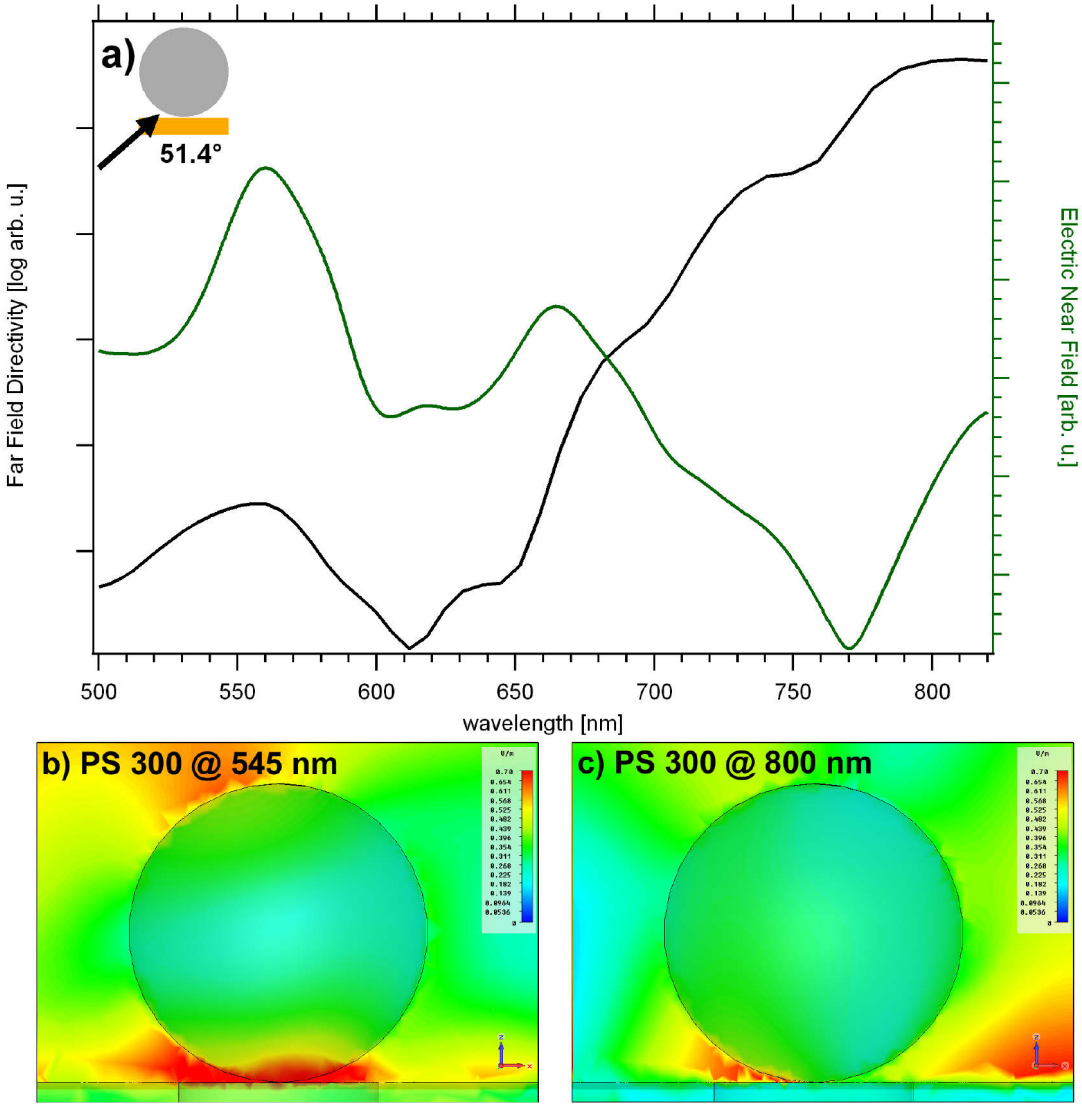

Figure 6.5: *FIT simulated spectra of the near- and far-field for a polystyrene sphere of 300 nm on gold, (b) electric field distribution around the sphere for an excitation wavelength of 575 nm and (c) for an excitation wavelength of 800 nm. The light is incident in at an angle of 51.4° to the vertical.*

6.2.2 Experimental Results

After these calculations and simulations of the dielectric-on-plane (DOP) resonances the theoretical investigations are compared to experimental results. The chapter is divided into the following sections. First scanning electron microscopy (SEM) combined with atomic force microscopy (AFM) is used for the 3D determination of the particle size. Second the geometry is exploited further as reference system to investigate the influence of the polarizer positions and the other described optimization procedures of Chapter 5 on the scattering patterns and scattering response of the spheres. As important prerequisite for the investigation of the gap resonance in metal sphere-on-plane (SOP) systems the modifications in the illumination and detection pathway should not induce a change in the spectral response of the particles. Finally spheres of different sizes are investigated to experimentally approach the dielectric-on-plane (DOP) resonances in the visible wavelength range.

6.2.2.1 Particle Identification and Size determination

The combination of local optical measurements with precise nanoscale imaging of the same nanostructure with scanning electron microscopy allows to relate specific spectroscopic data with nanoscale geometry. This enables quantitative comparison between experimental spectra and theoretical calculations of their electromagnetic modes. While this is already an important step toward a deeper understanding of the optical response from the gap in a metal sphere-on-plane system, SEM measurements offer only a two dimensional view of the sample with no information about the involved particle topography and height. Atomic force microscopy in combination with the two other methods provides the missing link to this third dimension and makes it possible to image small variations in particle shape in all dimensions. Since the polystyrene colloids in contrast to any chemically produced metal particle in this work are nearly perfect spheres, they can not only act as a model system to test the features of plasmon-mediated dark-field microscopy, but also to establish the whole identification procedure with all three microscopic methods by offering a validation of the results. The whole process was performed for two different samples while the remaining samples were only characterized by subsequent SEM measurements, because no deviations were seen. Figure 6.6 illustrates the whole approach. First all objects are measured in the confocal microscope at the position of the two scratches (a). The investigated particles are marked by circles and numbers. Afterwards the sample is taken to an atomic force microscope and the area of interest is identified by looking for the intersection of the two scratches with the integrated camera. The slow scan axis (y) should normally follow the bisecting line of the two scratches which is actually the same scan direction of the piezo-stage in the confocal microscope. In this way the distance between the two scratches can be measured right from the beginning of a scan and the sample position can be properly

adjusted. This approach to locate the area of interest was found after these measurements, which is the reason that the AFM micrograph in (b) is rotated clockwise by approximately 90° to achieve correspondence. The particles appear as individual bright spots in the confocal scattering image (a) and as tiny white dots in the AFM image (b).

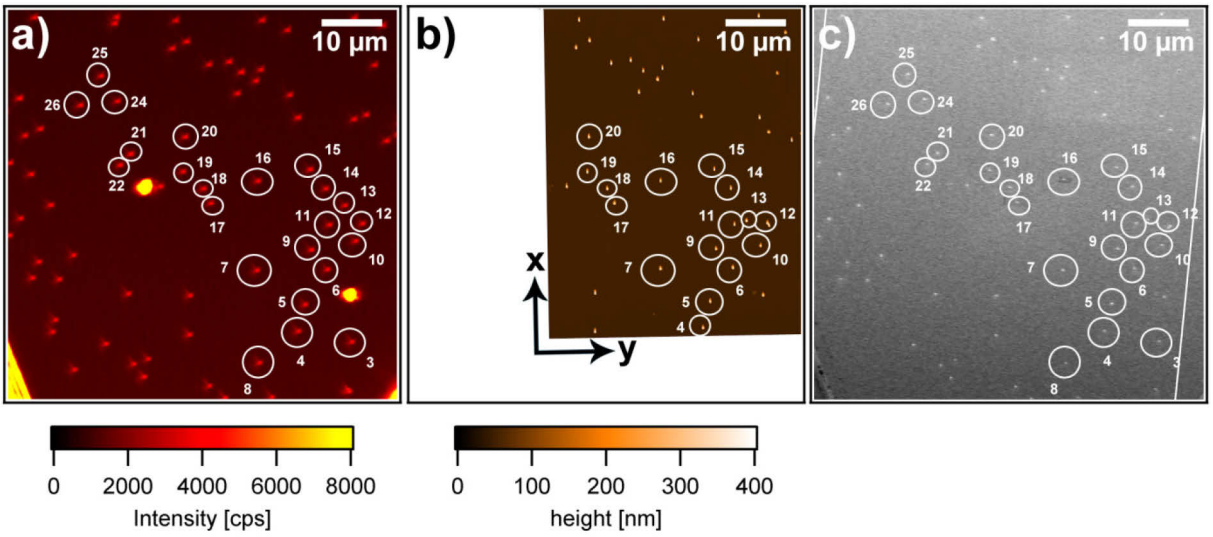

Figure 6.6: *(a) Scanning confocal scattering image with, (b) corresponding AFM and (c) scanning electron image*

The scratches are not seen in the image (b), but (a) and (b) show the same area as can be seen by the relative orientation of the particles to each other. At the end the region of interest is located again in the SEM with the help of the scratches, shown in the image (c). The particles appear likewise as bright white spots. From each identified particle a magnified image is taken to determine the size and shape. The two very intense large spots next to object 6 and 22 in the confocal image (a) are identified with the help of the AFM (b) and SEM micrographs (c) as defects in the gold film.

Figure 6.7 (a-c) shows objects 6 and 9 to 15 within an area of 21 x 21 µm. In this magnification the objects can already be identified as spheres in the SEM image (c) with object 12 consisting of two particles. In the presented case they have a diameter of around 360 nm. The image in (b) shows that the feedback parameters of the AFM were not adjusted properly and the tip was not tracing down the back side of the features in the applied tapping mode. Please remember the clockwise rotation of 90° in this image, which is the reason that the “tails” actually appear on the upper side of the colloidal spheres. As a result of this misadjustment object 12 corresponding to the dimer is not imaged correctly and particle 13 was displaced from an AFM scan by some micrometers. In a second image which is not presented here the setpoint voltage, gain and scan rate was optimized for a smaller section of (b).

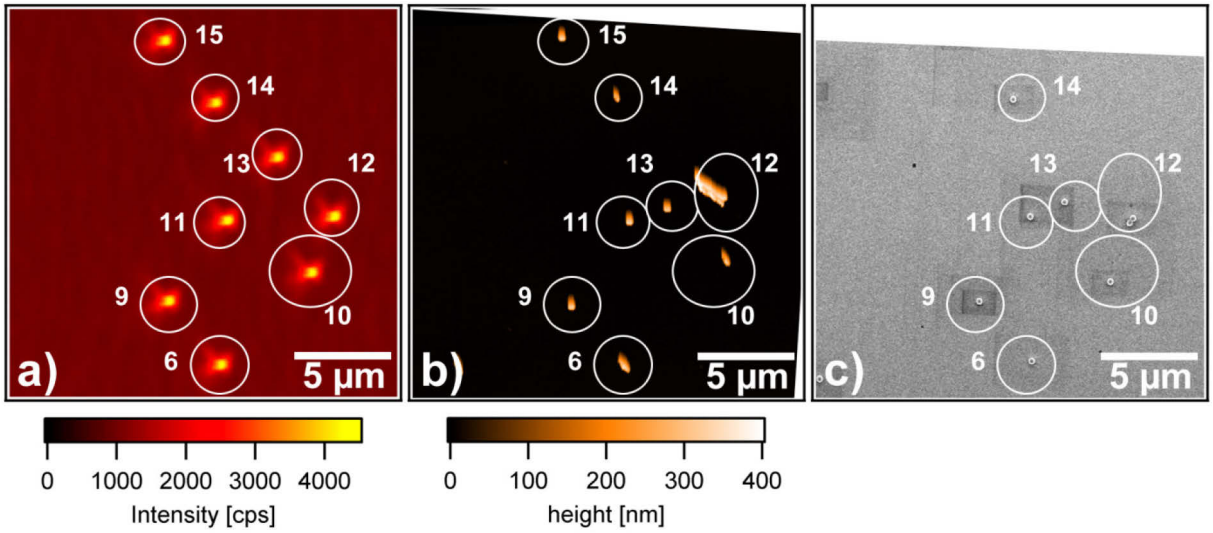

Figure 6.7: *(a) Scattering image of objects 9-15, (b) corresponding atomic force micrograph and (c) electron scanning micrograph with spheres visible*

The determined dimensions for the spheres in Figure 6.7 are summarized in Table 4.1. The x- and y-axis are the perpendicular lateral dimensions of the particles in the corresponding magnified SEM image. Their diameters are calculated as the average of the two axes, while the height is determined as the mean value obtained by the AFM images. The number in brackets indicates the number of considered values. The area of the particle covering the gold film is determined by counting the pixels representing the particle in the 8-bit gray scale SEM images and multiplying it with the pixel size in nanometers squared provided by the instrument. The volume is calculated for an ellipsoid with the three axes as determined by the measurements. The circularity is the proportion of the area and the perimeter (4π area/perimeter^2). For an ideal circle the factor would be 1.

Table 6.1: Determined dimensions of the presented colloidal spheres

Particle	x-axis [nm]	y-axis [nm]	Diameter [nm]	Height [nm]		Area [nm^2]	Volume [nm^3]	Circularity
Obj6	369	350	360	350	(1)	101208	23667974	0.899
Obj9	360	342	351	335	(2)	96595	21595936	0.896
Obj10	366	346	356	340	(2)	99657	22511041	0.899
Obj11	365	350	358	339	(2)	99551	22675623	0.894
Obj13	339	350	345	325	(2)	96419	20190623	0.888
Obj14	368	347	358	318	(1)	99747	21261947	0.895
Obj15	363	342	353	332	(1)	98095	21580894	0.900

For the given example the data shows that the selected polystyrene particles are not “ideal” spheres. This could already be seen from the SEM data, but AFM helps to confirm these results. The measured AFM height is always smaller than the lateral SEM dimensions of the colloidal particles. The spheres are oblate spheroids where the interaction with the interface is larger when they are lying on the “side”, but the differences between the two methods

can also be related to other problems. In Chapter 7 a further discussion will follow in which contamination effects from the SEM measurements play a major role.

For a closer inspection of the height determination itself the atomic force microscope was controlled with a calibration grid with a pitch size of 10 µm and a depth of 200 nm. A 20 x 20 µm section of this grid is shown in Figure 6.8 together with a cross section of the height profile. It shows the expected values and demonstrates the capability of the instrument to detect the smallest changes in height differences. The red arrow in (b) displays an exact distance of 200 nm. The maximum deviation from this reference value in the measurement is around 2% which is smaller than the experimental deviations between the two microscopic imaging methods in the example above.

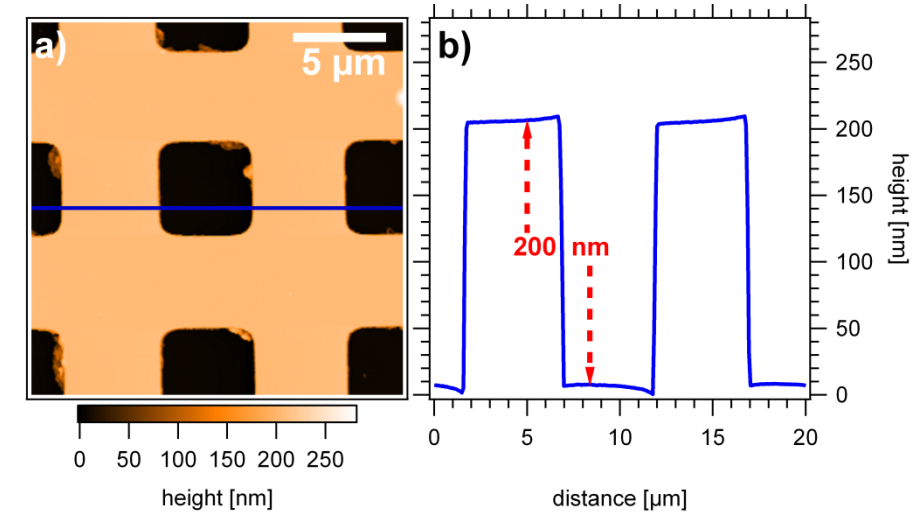

***Figure 6.8**: (a) AFM height image of the calibration grid, (b) height profile from the blue line in (a). The red arrows shows a height difference of exactly 200 nm*

6.2.2.2 Influence of Polarizer Directions and Optimization Methods

The scattering patterns in plasmon-mediated dark field of Figure 6.7 largely depend on the polarization direction of the excitation light relative to the block edge since the block introduces a symmetry breaking element. Patterns of polystyrene spheres with a diameter of 300 nm on gold were already presented relative to the polarizer direction in Figure 5.6 of Chapter 5.3 and their imaged shape could be calculated quite well with a simple model of a point dipole on a gold film. Figure 6.9 shows the scattering patterns for different sizes of polystyrene beads obtained for an excitation wavelength of 633 nm. Please note the different intensity scaling in each picture. For the smallest particles with a diameter of 200 nm and 300 nm the correspondence for both polarization directions is again very good and the particles show the typical patterns for dipoles excited normal (z-axis) to a metallic surface.[33, 34] For a polarization of the light perpendicular to the block edge (⊥-polarization) the particles appear as individual dots with two “streaks”, but they can be uniquely

identified as vertical dipoles when the polarization direction is changed parallel to the block edge (||-polarization).

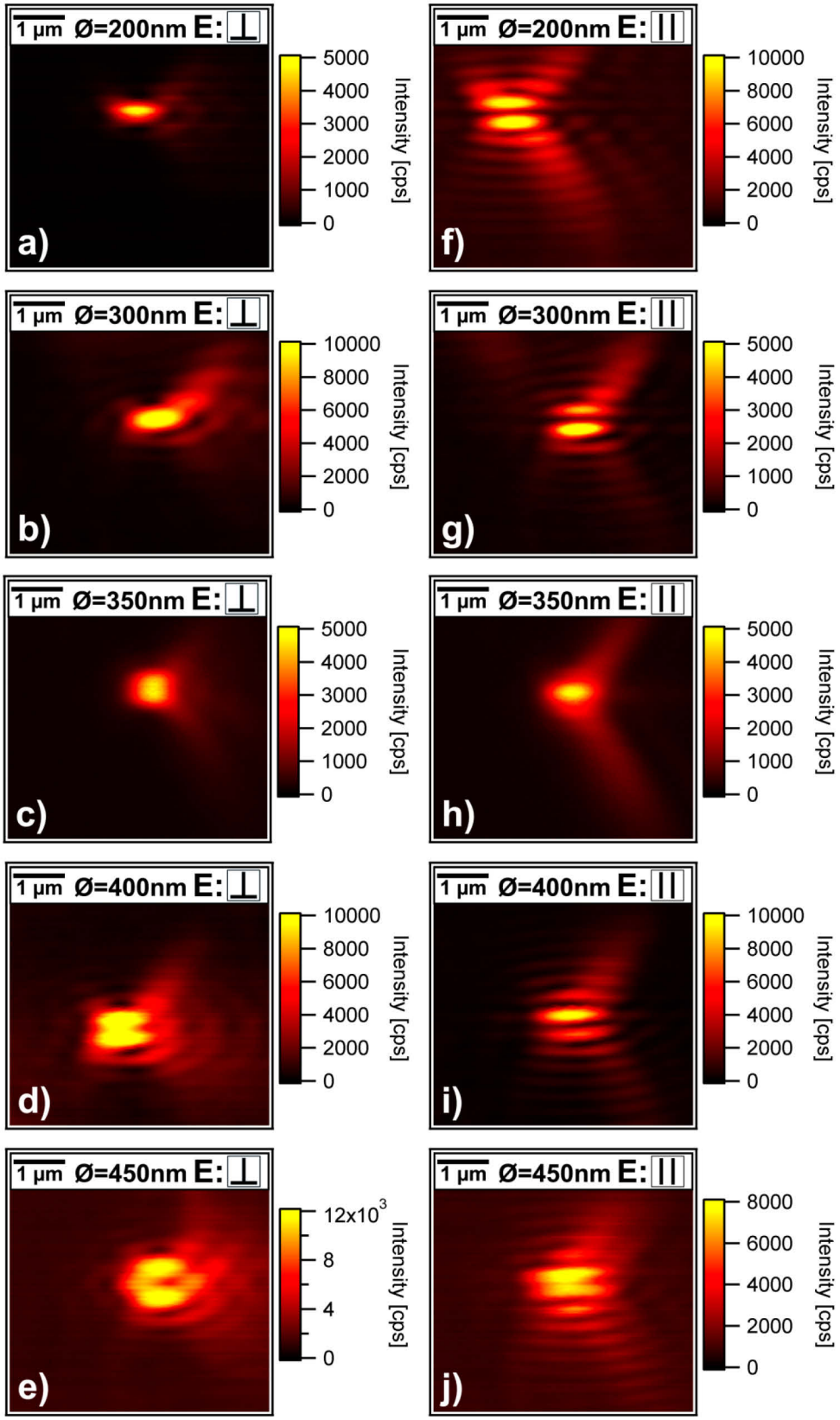

Figure 6.9: *(a-e) Measured scattering patterns from polystyrene spheres of different sizes (200-450 nm) for incident light of λ=633 nm polarized perpendicular ((⊥-polarization) and (f-j) parallel to the block edge (||-polarization).*

In || illumination mode they display the expected double-lobe like patterns of dipoles with a nodal plane in the center. For spheres with a diameter of 350 nm, deviations from this simple dipole-like response normal to the surface begin to emerge. The corresponding images look on first sight out of focus with the patterns in both polarizations directions nearly identical in shape and the nodal plane between the lobes for ||-polarization not observable. The excitation of higher order resonances in the spheres may start to play a role. For these resonances the charge distribution is different from this simple model. Alternatively different dipole modes inside the particle may be more efficiently excited with increasing diameter. While a spherical particle in a homogenous environment has three degenerate dipolar resonances, the reduced symmetry of the system induced by the presence of the metal film as indicated by Figure 6.2 results in a splitting of these modes into two distinct resonances, corresponding to the sphere dipole oscillating parallel and perpendicular to the substrate.[35, 36] For the gold film the vertical mode of the electric field is considerably stronger than the in plane component. As a result only the dipole moment normal to the surface is usually observed. For larger spheres the magnitude of the modes parallel to the substrate could get more important due to larger particle dimensions[37] and couple to the interface. Both modifications of the scattering response modify the scattering patterns. As the diameter is further increased to 400 nm the images for the two polarization directions seem to be misplaced. For ||-polarization a slightly elongated spot is seen with intense “streaks” on both sides while for ⊥-polarization a nodal plane with the two lobes could be suspected. For spheres of 450 nm or larger a situation is reached where both patterns look out of focus. For ⊥-polarization the minimum between the two intense lobes is more pronounced than the one for the spheres with 400 nm and two additional maxima perpendicular to the first ones can be suspected.

The addition of a second polarizer in the detection pathway as described in Chapter 5.4 allows an efficient detection of the z-dipoles normal to the surface. For spheres of 400 nm diameter Figure 6.10 shows the change in the pattern shape versus the polarizer position sketched in the inset on top of each image. The signal to background-ratio (SBR) of the tagged particle inside the white circle is given on the right side while its related scattering pattern is magnified in the inset on the bottom right. Please note that the color scheme is changed for better visibility, while the intensity scaling is the same as indicated by the corresponding color scale. The left side shows the patterns for excitation light with ⊥-polarization and the right side for light with ||-polarization. In the images (a) and (b) there is no polarizer in the detection pathway and the patterns look the same as described in Figure 6.9 for particles of the same size. The SBR of the marked particle reaches in both cases a magnitude of around 50. By adding the second polarizer in (c-f) two separate parts of the presented patterns can be distinguished depending on the polarization direction of the light

seen by the detector. This is especially noticeable for the left side of the scheme and ⊥-polarization for the excitation light. The sum of the patterns in (c) and (e) results in the pattern (a). In the applied scattering geometry with the oil immersion objective, illuminating angles of incidence between approximately 9° and 68° the linear polarized excitation light in both polarization directions can be decomposed into s-polarized and p-polarized waves which allows for the excitation of both described modes parallel and perpendicular to the substrate.[35] For ⊥-polarization the patterns can be imaged separately by turning the polarization direction in the detection pathway, indicating that these modes can be separated.

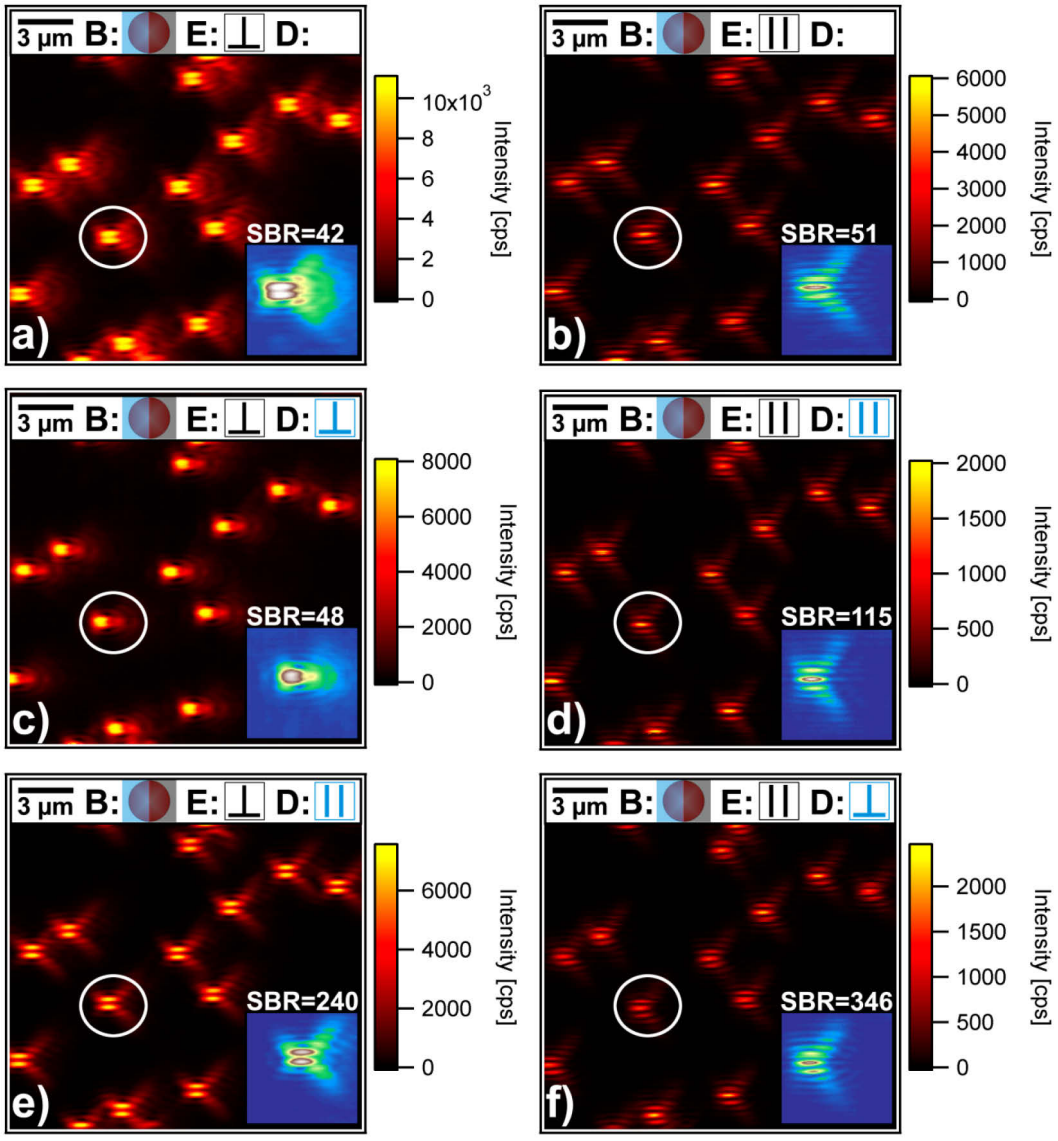

Figure 6.10: *Scattering patterns of polystyrene beads with a diameter of 400 nm for different polarizer directions in the excitation (E) and detection (D) relative to the block edge for incident light of λ=633 nm. The SBR value shows the signal-to-background ratio for the tagged object. The inset shows its scattering pattern in a different color scheme for better visibility.*

For ||-polarization of the excitation light the pattern shape is independent on the detection polarizer. The images (b), (d) and (f) show the same features. In contrast to the metal

sphere-on-plane case of Figure 5.10 the patterns in images (e) and (f) appear to be influenced by the polarizer position in the detection and not in the illumination. The SBR reaches with numbers of 240 and 346 respectively the highest values when the polarizer directions in excitation and detection are perpendicular to each other.

The Mie calculation from Figure 6.1 (symmetry breaking element of the conducting plane is not considered and a homogenous environment is assumed) shows that light of 633 nm can excite a considerable amount of higher order resonances in spheres which are larger than 350 nm. This agrees with the observation of Figure 6.9 where a deviation of the calculated dipole patterns occurred for spheres larger than 350 nm. Therefore higher order modes should not be forgotten in this interpretation. In addition the metal film in the coupled system can be polarized and allows for the excitation of surface plasmons.

When assuming a Mie-like response of the whole system, scattering spectra of large spheres on gold films should show two separated resonances under white light illumination. In Figure 6.11 the spectral response of polystyrene beads with a diameter of 400 nm is displayed for different polarizer positions in excitation and detection.

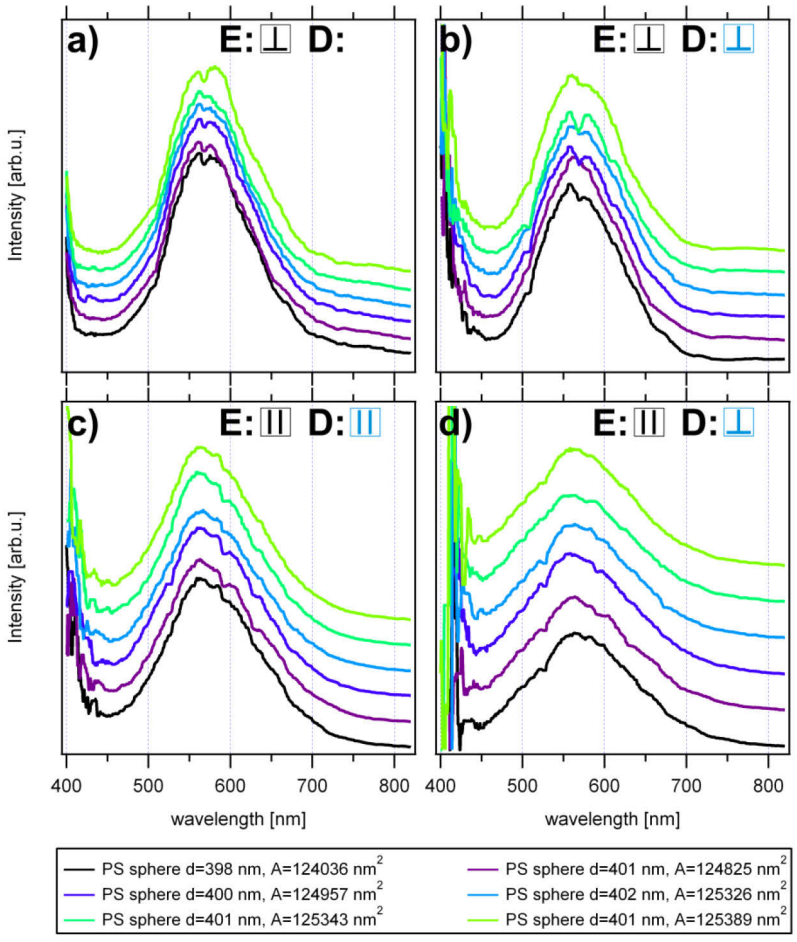

Figure 6.11: *Scattering patterns of polystyrene beads with a diameter of 400 nm for different polarizer directions in the excitation (E) and detection (D) relative to the block edge.*

The experimental scattering spectra show the same resonances as the calculated spectra of Figure 6.1 with one resonance at 570 nm and another noisy one at around 400 nm. At this wavelength the gold is a good absorber and the illuminating white light possesses only low intensity. Between 600 and 700 nm additional features with small shoulders are seen. The similarity of the scattering response is obvious. The different polarizer positions in (a) to (d) do not influence the spectra. The varying signal intensities for the different polarizer positions are explained by the strength of the incident illumination light which depends on these positions. While the scattering patterns can be easily distinguished by the polarizer directions, the same cannot be done for the spectral response of the gold-sphere system. As the polarizers separate the horizontal and vertical modes this is an indication that a charge distribution is involved which is not described by Figure 6.2. The fine-structure in the spectra most probably originates from experimental artifacts, but may also be related to the influence of the gold. Please note that these features are occasionally seen in regular dark-field mode even when no metal film is present. The source of these modifications is not well-understood; one hypothetical explanation is related to the position of the multimode fiber of the spectrometer and the focusing lens in relation to the incoming collimated beam.

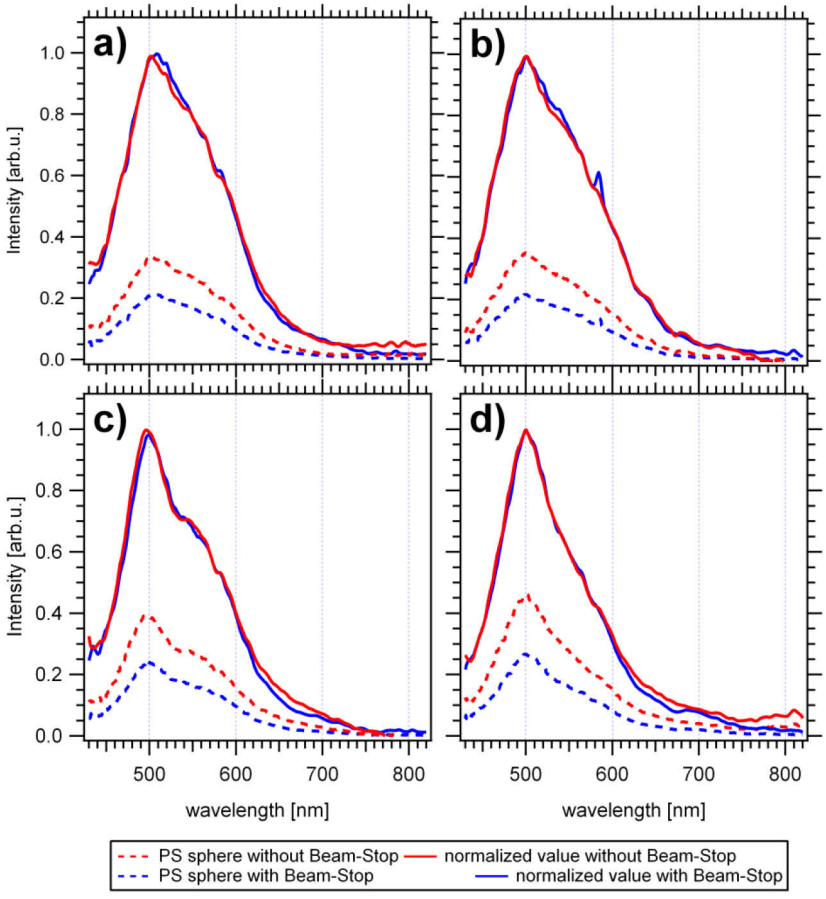

Figure 6.12: *Scattering spectra of four different polystyrene beads with a diameter of 480 nm with and without an annulus in the illumination*

In Chapter 5.3 an additional method was presented to improve the particle to background ratio by adding an annulus to the linear block in the illumination pathway. This resulted in an efficient reduction of the background scattering of the gold film which dominates the signal for small angles of incident light. Figure 6.12 compares the scattering spectra of polystyrene spheres of 480 nm diameter on gold if a disc of 5 mm diameter is present in the illumination pathway in front of the polarizer or not. In the examples (a-d) the total intensity of the scattering response is decreased when the disc is added, while the spectral profile is not depending on it. Therefore the disc seems to have no effect on the spectral response of the spheres. The resonance around 500 nm can be attributed to the Mie resonance with the difference that the resonance position is red-shifted, the resonance width is larger and additional features are visible on the red side of the resonance. In the selected wavelength range the higher order Mie resonance on the blue side of the spectrum is not visible.

The reproducibility of the new dark-field mode and the whole procedure has been successfully demonstrated with the identical response of different particles with the same size and shape. The two described optimization steps provide an efficient way to improve the signal-to-background ratio for particles on a metal film without influencing their spectroscopic detectable scattering profiles. While this is an important implication for the investigations of metal sphere-on-plane resonators the signals obtained in plasmon-mediated dark field microscopy are still wavelength dependent with the optical properties of the gold in the visible spectral region. The calculated transmission function of the entire optical system including the gold film from Figure 5.11 shows a strong maximum for 535 nm. Below 496 nm (above the plasma frequency) gold does not behave metal-like, but is a good absorber. Above 535 nm the method becomes inefficient with increasing wavelength as indicated by the calculated transmission function. To incorporate this wavelength-dependent scattering response into measurements it is normally necessary to normalize any measured signal by this theoretical function or a similar one derived from experiments.

6.2.2.3 Dielectric-on-Plane Resonances (DOP)

The Mie calculations show that a variation of the sphere diameter changes the resonance peak wavelength of the particle with new resonances appearing on the blue side for increasing size. For a certain sphere size a strong coupling of the Mie resonances to the gold film is expected which modifies then the scattering profile of the system. For a sphere of 300 nm and 400 nm the simulations predict a resonance around 545 and 575 nm, respectively. Therefore this dielectric-on-plane (DOP) resonance is size-dependent.

In Figure 6.13 the response of the particle gold system is presented for a sample with a polydisperse size distribution of particles. The single spectra are arranged by an off-set from bottom to top for increasing particle size. The sphere diameter and the covered area on the

surface are presented on the right side of the corresponding spectrum. The smallest particle with a diameter of 198 nm shows a resonance at 533 nm with a shoulder on the red side at 585 nm. While the first resonance disappears for increasing diameter the second one shifts to 610 nm for the largest particle. For a particle diameter of around 283 nm a new resonance appears on the blue side at 465 nm. The resonance increases in strength and shifts to 497 nm for the largest particle. As these two resonances are not explained by Mie, they should be closely related to the interaction with the gold film and therefore confirm the simulations. On the far red side of the scattering spectrums around 770 nm another weak resonance is seen in most cases which is also visible on the red side of the calculated far field spectrum in Figure 6.5. The different intensities in the experiment and the simulation are explained by the characteristic of the used optics like the oil immersion microscope objective and the wavelength dependent intensity of the white light source, which is not taken into account by the simulation.

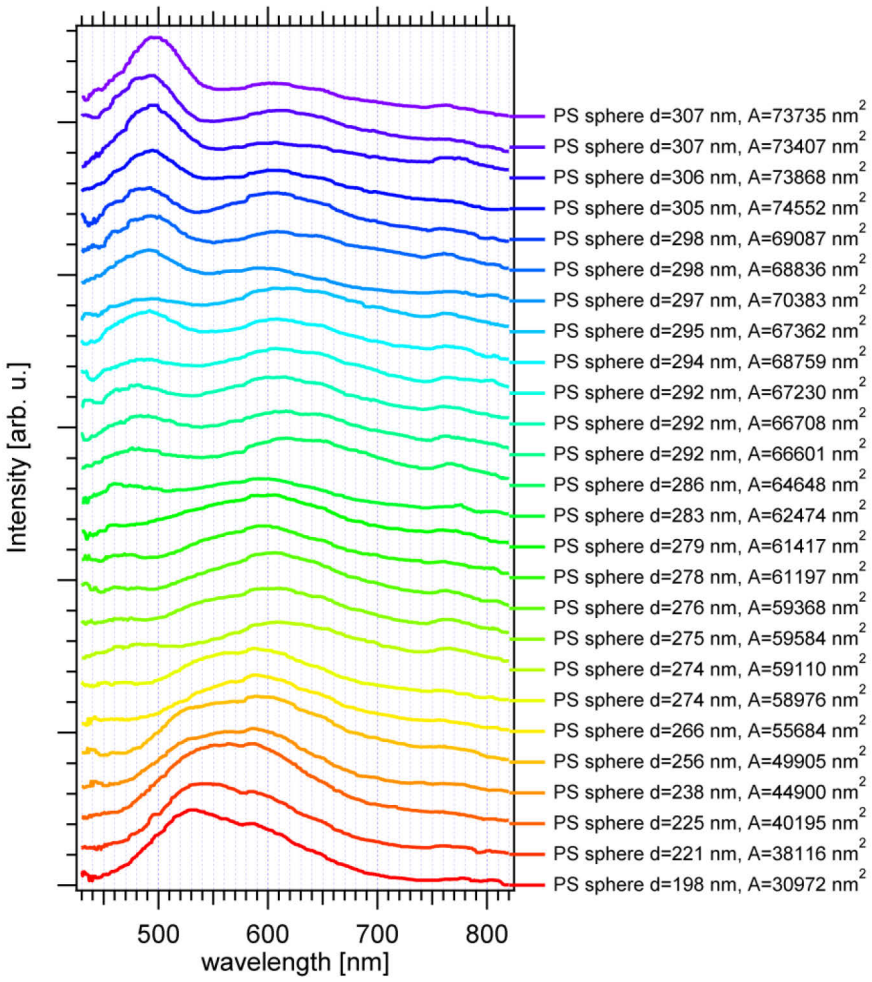

Figure 6.13: *Scattering spectra for one sample of polystyrene beads with different diameters determined by SEM*

For comparable particle size the spectra look quite reproducible demonstrating the efficiency of the whole procedure and method. The two described resonance at around

480 nm and 600 nm are called in the following the dielectric-on-plane (DOP) resonances. To track the course of these resonances and determine the range where these interactions happen, different samples with particle sizes between 200 and 500 nm were characterized. All the estimated resonance positions and particle sizes are presented in the correlation plot of Figure 6.14. For comparison, the three characterized Mie resonances of Figure 6.1 for a single polystyrene sphere in vacuum are added in gray. As described in Figure 6.13 the second DOP resonance (green) starts to appear for particles with a diameter of 280 nm or larger and shifts with increasing particle size to 590 nm for particles with a diameter of 500 nm. The first DOP resonance (red) is visible in the whole size range starting for the smallest particles at 570 nm and ending at 650 nm for the largest ones. The wavelength distance between the two is accordingly decreasing for larger particles.

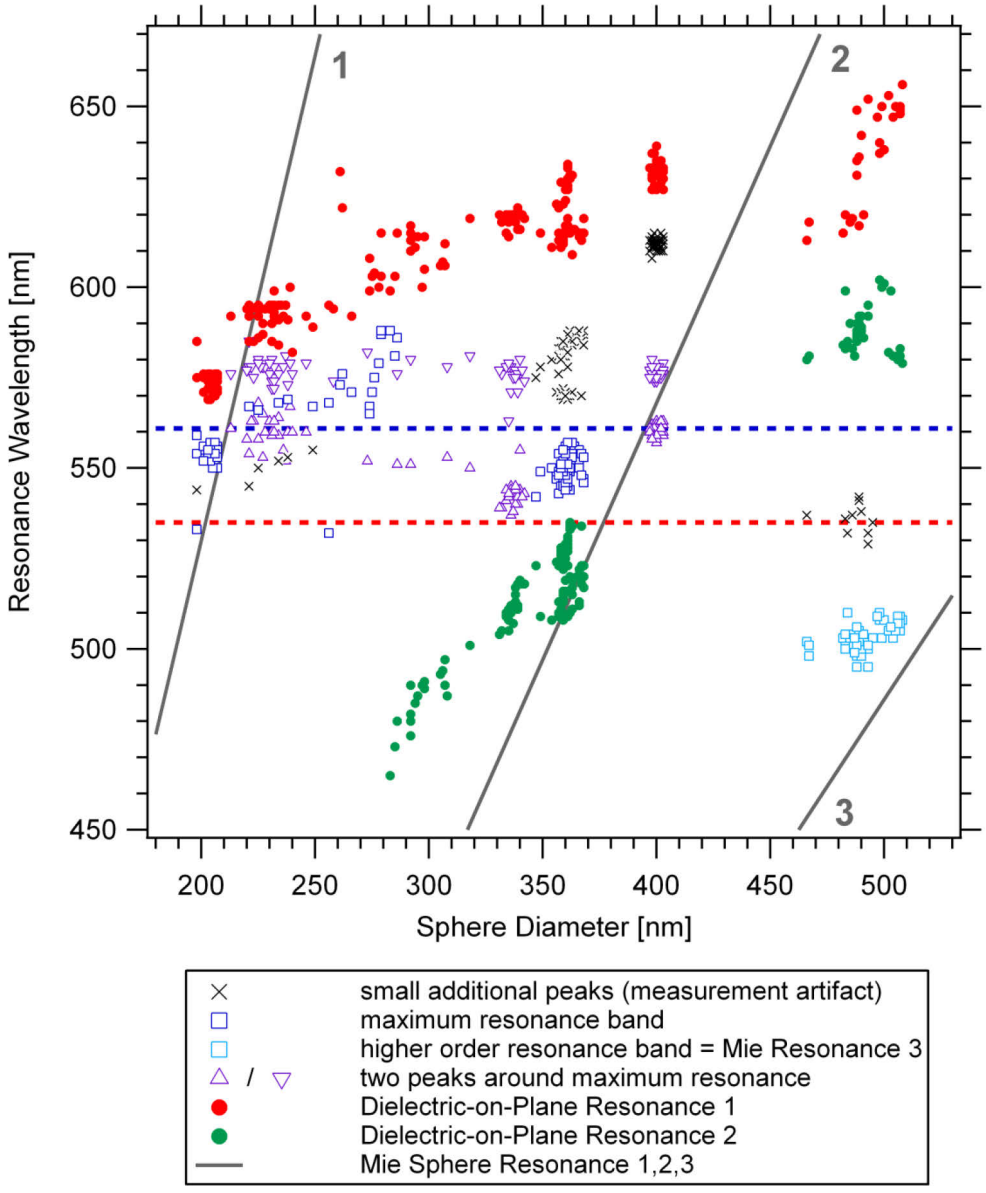

Figure 6.14: *Correlation plot of the resonance wavelength positions versus the sphere diameter for all characterized samples*

In a wavelength band of 530 and 590 nm all particles up to a size of 400 nm show a large resonance band (blue squares) which is sometimes split into two smaller peaks around the maximum position (purple triangles). This is either a consequence of the described fiber artifacts or an intrinsic property of the particle gold system. However, small peaks in the spectra, which are most probably related to noise, are depicted as black crosses. The mean value for these resonances dominating the spectral response is 561 nm which is shown in the figure as horizontal blue dashed line. Since it is dominating the spectral profile of all particles up to a diameter of 400 nm and cannot be explained by Mie theory this feature could be related to a real transmission function of the optical system in contrast to the calculated one with a maximum at 535 nm displayed as red horizontal dashed line. The spectra of the simulations in Figure 6.3 and Figure 6.5 show here high intensities for both calculated sizes. At this wavelength the sensitivity of the sphere-gold system is the highest because the excitation light penetrates the gold film nearly undisturbed. The particles act as an effective mirror (backscattering) and the mirrored light is detected again through the gold film. In the literature colloidal particles are also known to be used as colloidal lenses.[38]

The total spectral profile for particle sizes between 200 and 370 nm is quite different from the calculated Mie resonances with the interaction to the gold film as their origin. The spectra seem to be determined by more factors than just a red-shift of existing Mie modes. Therefore, a similar phenomenon as described by Hillenbrand[19] could play a role here in the visible. For particles larger than 400 nm the response is more Mie-like as shown in Figure 6.1. The position for the 400 nm spheres is perfectly predicted by Mie, only its width is smaller. This could also indicate that this is already the next mode from the blue side (Mie: 390 nm) which is red-shifted and exhibits by chance the same position as the lower mode (Mie: 570 nm). For the particles of 500 nm the next higher Mie mode appears on the blue side. The resonance width is comparable between the measurement and the calculation.

6.3 Summary and Outlook

Polystyrene beads on gold are a suitable reference system to proof the power of plasmon-mediated dark field microscopy with high sensitivity through metal films and reproducible results for different particles with identical shape. The optimizations of the signal-to-background ratio improved the method further while no influence on the spectroscopic profile of the investigated objects could be seen. The confocal measurements were successfully combined with scanning electron and atomic force microscopy to determine all dimensions of the investigated particles. The heights determined by AFM were checked with a calibration grid, but showed in the combination with SEM systematic lower values. The measured scattering patterns started to show deviations from the calculated ones for

spheres larger than 350 nm in diameter. These deviations can be effectively separated as a sum of two patterns by a suitable combination of polarizer positions. For a polarization direction of the illumination light perpendicular to the block edge (⊥-polarization) this effect is best to be seen. By changing the particle size the range of most effective coupling to the gold film could be determined for particle sizes between 200 and 370 nm. Two resonances not explained by a Mie calculation appeared through the whole range and shifted to the red with increasing diameter. They are assigned to effective coupling of the sphere and the gold film and are called dielectric-on-plane resonances. Above diameters of 400 nm the response of the system was dominated by Mie scattering with small deviations for large wavelengths corresponding to these resonances. From the large resonance band dominating the response for all particles at the same position the maximum of an experimental transmission function could be determined which was red-shifted by 30 nm from the calculated function.

The modifications of the scattering response in the coupling regime cannot be explained by a dipole approximation and a red shift of existing Mie-Resonances. For a full understanding more simulations are required to reproduce the spectra and image the near fields and the charge distributions in spheres of different sizes at different illumination angles. The calculation of the transmission function should also be adapted to compensate for the second polarizer and more realistic particles to explain the shift in the maximum of the transmission function. Light scattering experiments with smaller particles than 200 nm will reveal if the interaction to the gold film stops somewhere. For really small dimensions where the sphere is no longer resonant in the detected wavelength range the plasmonic counterpart to Hillenbrand's phonon-active surface[19] could be tested. Finally experiments with larger particles of sizes between 380-400 nm and 400-480 nm should bring some light into this somehow special situation in the Mie regime.

6.4 Bibliography

1. Maxwell, J. C., A Dynamical Theory of the Electromagnetic Field. *Philosophical Transactions of the Royal Society of London* **1865,** *155*, 459-512.

2. Mie, G., Beiträge zur Optik trüber Medien, speziell kolloidaler Metallösungen. *Annalen der Physik, Vierte Folge* **1908,** *25* (3), 377-445.

3. Bohren, C. F.; Huffman, D. R., *Absorption and scattering of light by small particles*. Wiley-VCH: New York, 1983.

4. van de Hulst, H. C., *Light Scattering by Small Particles*. Dover Publications Dover, New York, 1981.

5. Kerker, M., *The scattering of light, and other electromagnetic radiation*. Academic Press: New York, 1969.

6. Lilienfeld, P., Optical detection of particle contamination on surfaces - a review. *Aerosol Sci. Technol.* **1986,** *5* (2), 145-165.

7. Sommerfeld, A., The broadening of the waves and the wireless telegraph. *Ann. Phys.-Berlin* **1909,** *28* (4), 665-736.

8. Sommerfeld, A., The dispersion of waves in wireless telegraphy. *Ann. Phys.-Berlin* **1926,** *81* (25), 1135-1153.

9. Weyl, H., Expansion of electro magnetic waves on an even conductor. *Ann. Phys.-Berlin* **1919,** *60* (21), 481-500.

10. Chance, R. R.; Prock, A.; Silbey, R., Comments on Classical Theory of Energy-Transfer. *Journal of Chemical Physics* **1975,** *62* (6), 2245-2253.

11. Bobbert, P. A.; Vlieger, J., Light scattering by a sphere on a substrate. *Physica A: Statistical and Theoretical Physics* **1986,** *137* (1-2), 209-242.

12. Johnson, B. R., Light scattering from a spherical particle on a conducting plane 1. normal incidence. *J. Opt. Soc. Am. A-Opt. Image Sci. Vis.* **1992,** *9* (8), 1341-1351.

13. Videen, G., Light Scattering from a sphere behind a surface. *J. Opt. Soc. Am. A-Opt. Image Sci. Vis.* **1993,** *10* (1), 110-117.

14. Nahm, K. B.; Wolfe, W. L., Light Scattering Models for spheres on a conducting plane - comparison with experiment. *Appl. Optics* **1987,** *26* (15), 2995-2999.

15. Weber, D. C.; Hirleman, E. D., Light scattering signatures of individual spheres on optically smooth conducting surfaces. *Appl. Optics* **1988,** *27* (19), 4019-4026.

16. Hill, S. C.; Benner, R. E.; Rushforth, C. K.; Conwell, P. R., Structural resonances observed in the fluorescence emission from small spheres on substrates. *Appl. Optics* **1984,** *23* (11), 1680-1683.

17. Johnson, B. R., Morphology-dependent resonances of a dielectric sphere on a conducting plane. *J. Opt. Soc. Am. A-Opt. Image Sci. Vis.* **1994,** *11* (7), 2055-2064.

18. Jory, M. J.; Cann, P. S.; Sambles, J. R.; Perkins, E. A., Surface-plasmon-enhanced light scattering from microscopic spheres. *Appl. Phys. Lett.* **2003,** *83* (15), 3006-3008.

19. Hillenbrand, R.; Taubner, T.; Keilmann, F., Phonon-enhanced light-matter interaction at the nanometre scale. *Nature* **2002,** *418* (6894), 159-162.

20. Moskovits, M.; Jeong, D. H., Engineering nanostructures for giant optical fields. *Chemical Physics Letters* **2004,** *397* (1-3), 91-95.

21. Okamoto, T.; Yamaguchi, I., Optical Absorption Study of the Surface Plasmon Resonance in Gold Nanoparticles Immobilized onto a Gold Substrate by Self-Assembly Technique. *Journal of Physical Chemistry B* **2003,** *107* (38), 10321-10324.

22. Tsuboi, K.; Abe, S.; Fukuba, S.; Shimojo, M.; Tanaka, M.; Furuya, K.; Fujita, K.; Kajikawa, K., Second-harmonic spectroscopy of surface immobilized gold nanospheres above a gold surface supported by self-assembled monolayers. *Journal of Chemical Physics* **2006,** *125*, 174703-1-174703-8.

23. Aravind, P. K.; Metiu, H., The effects of the interaction between resonances in the electromagnetic response of a sphere-plane structure - applications to surface enhanced spectroscopy. *Surface Science* **1983,** *124* (2-3), 506-528.

24. Nordlander, P.; Le, F., Plasmonic structure and electromagnetic field enhancements in the metallic nanoparticle-film system. *Applied Physics B-Lasers and Optics* **2006,** *84* (1-2), 35-41.

25. Rendell, R. W.; Scalapino, D. J., Surface-Plasmons confined by Microstructures on Tunnel-Junctions. *Phys. Rev. B* **1981,** *24* (6), 3276-3294.

26. Ruppin, R., Surface-Modes and Optical-Absorption of a Small Sphere Above a Substrate. *Surface Science* **1983,** *127* (1), 108-118.

27. Wind, M. M.; Vlieger, J.; Bedeaux, D., The Polarizability of a Truncated Sphere on a Substrate I. *Physica A: Statistical and Theoretical Physics* **1987,** *141* (1), 33-57.

28. Mätzler, C. *Mie Matlab Code*, 2009.

29. Jackson, J. D., *Klassische Elektrodynamik*. 2nd ed.; de Gruyter: Berlin, 1982.

30. Pomplun, J.; Burger, S.; Zschiedrich, L.; Schmidt, F., Adaptive finite element method for simulation of optical nano structures. *Phys. Status Solidi B-Basic Solid State Phys.* **2007,** *244* (10), 3419-3434.

31. Weiland, T., Discretization Method for Solution of Maxwells Equation for 6-Component Fields. *Aeu-International Journal of Electronics and Communications* **1977,** *31* (3), 116-120.

32. CST *Microwave Studio 2010*, Computer Simulation Technology AG: Darmstadt, 2010.

33. Sick, B.; Hecht, B.; Novotny, L., Orientational imaging of single molecules by annular illumination. *Phys. Rev. Lett.* **2000,** *85* (21), 4482-4485.

34. Bouhelier, A.; Ignatovich, F.; Bruyant, A.; Huang, C.; Colas des Francs, G.; Weeber, J. C.; Dereux, A.; Wiederrecht, G. P.; Novotny, L., Surface plasmon interference excited by tightly focused laser beams. *Opt. Lett.* **2007,** *32* (17), 2535-2537.

35. Videen, G., Light scattering from a particle on or near a perfectly conducting surface. *Opt. Commun.* **1995,** *115* (1-2), 1-7.

36. Zhang, J. Z.; Noguez, C., Plasmonic Optical Properties and Applications of Metal Nanostructures. *Plasmonics* **2008,** *3* (4), 127-150.

37. Renger, J.; Grafstrom, S.; Eng, L. M.; Hillenbrand, R., Resonant light scattering by near-field-induced phonon polaritons. *Phys. Rev. B* **2005,** *71* (7).

38. Schwartz, J. J.; Stavrakis, S.; Quake, S. R., Colloidal lenses allow high-temperature single-molecule imaging and improve fluorophore photostability. *Nat. Nanotechnol.* **2010,** *5* (2), 127-132.

7 Individual Plasmonic Gap Resonances

7.1 Introduction

The resonance wavelength of metallic nanoparticles is highly dependent on the environment around the particles.[1, 2] An increase of the refractive index of the ambient medium causes a red-shift in the resonance wavelength. These effects can be exploited in sensor applications,[3-6] but the achievable shifts are normally not significant strong. On the other hand it is well known that the aggregation of metallic nanoparticles causes large red-shifts in the resonance wavelength. The close approach of the particles has been used in a number of applications, for example with the universal plasmon ruler[7-9] which has been used to measure the distance between two metal nanoparticles in biological systems and in optoelectronics where the near coupling of the nanoparticles transports light.[10, 11]

Metal particles placed next to a metal surface provide a conceptually orthogonal approach and exhibit the same unique optical properties as particle dimers or clusters. However, this so called sphere-on-plane (SOP) system has the advantage that it can be easily fabricated with defined spacing and in a way that it resembles theoretical models used for its description which facilitates the basic understanding of the underlying effects. In the sub-wavelength quasi-static regime the calculations[12-15] predict that the field that acts on the particle is no longer homogenous and that due to the interaction multipoles have to be considered. Therefore the coupled system becomes resonant at wavelengths which are highly red-shifted from that of the isolated sphere. Within these approximations the response of the system is a function of the materials, of the sphere radius and of the distance from the plane. On these small length-scales, the system behaves scale invariant[16] and the resonance position depends only on the ratio of the film-sphere distance to the sphere radius. The theory predicts also a large electromagnetic field in this nanogap at resonance condition, an effect that led to the term "*gap resonance*".[12] This large field which is localized in a volume of a few cubic nanometers plays an important role in many physical effects involving the emission and collection of light, for example in scanning tunneling microscopy (STM),[17] scanning near field optical microscopy (SNOM)[18] and surface enhanced raman scattering (SERS).[19] The large shifts are interesting for biological as well as chemical sensing[20-22] while the large field can be used as optical tweezers.[23] Apart from the obvious potentials in various applications the appearance of such high field enhancements in small volumes is also interesting from a fundamental point of view as it raises the questions of the applicability of the macroscopic description of the dielectric response of matter at the nanoscale.[24]

The first experimental indications for a special kind of interaction between a submicroscopic metal sphere placed at nanometer distances to a metal substrate were found in tunnel junction experiments.[25, 26] The tunnel junctions were seen to emit light when a voltage was applied across the junction. After the invention of scanning near field optical microscopes the role of the tip in the rate of the light emission from the tunnel junctions was investigated in more detail.[17] Independently from these experiments the large enhancements of the gap modes play a central role in surface enhanced Raman scattering spectroscopy[27-30] and are responsible for the large enhancements in Raman cross sections of up to 10^{14}.[29, 31, 32] In the light of these effects different authors systematically investigated the gap resonances using different types of systems. Holland and Hall decorated LiF covered silver films with silver island films.[33] Kume *et al.*[34-36] investigated silver particles embedded in a SiO_2 matrix, deposited on an aluminum substrate. Later on organic spacer layers like alkanethiols were used between the sphere and the plane to design better defined geometries.[20, 37-39] The standard method to study the optical response of the SOP systems was absorption spectroscopy.[38, 39] Okamoto *et al.*[38] could clearly show the gap resonances in the extinction spectrum and investigated the effect of the sphere diameter on the resonance wavelength. Tsuboi *et al.*[39] used different kinds of organic spacers to change the distance to the film while Le[40] varied the thickness of the supporting gold layer. The importance of the dielectric environment in the gap was shown in Raman scattering experiments.[41, 42] The most quantitative analysis for a gold sphere-on-plane system was performed by Rueda *et al.*[43] who varied all three central parameters and investigated the system by surface plasmon spectroscopy. In their experiments the influence of the dielectric function of spacer and surrounding medium on the resonance wavelength was found to be roughly equal in spite of the considerably smaller volume of the spacer. To their surprise the gap distance was in agreement with an estimate from the molecular structure. There was no evidence of geometrical imperfections or modifications to Maxwell's equations for continuous media on the sub-nanometer scale.

Although these systems have been studied in detail the consistency between theory and experiment remained always on a qualitative level. Estimates of the field enhancement are based on an ideal geometry where the nanoparticle is modeled as an ideal sphere surrounded by a homogenous medium on a perfectly flat plane. Models in which the experimentally necessary spacer layer has been included require numerical calculations,[44, 45] but here the small dimensions of the gap in relation to the large dimensions of the sphere are problematic in the models. The group around Nordlander developed a different concept in close analogy to the hybridization of atomic orbitals in molecules to understand the sphere-on-plane interaction.[46, 47] They described the gap resonance as a hybridized mode

due to the interacting resonance of a sphere and the continuum of surface excitations on the plane.

All described experiments in the past suffered from a number of imperfections. The available metal particles from chemical reduction have a broad variety of shapes, but hardly resemble ideal spheres. Their surface topography plays an additional part in their optical response. The surface corrugations on the nanoscale induce a very significant red-shift in the localized surface plasmon resonance and lead to broadening and damping of the higher modes.[48, 49] None of these particles provide sufficient control over the dimensions of the active gap and the systems strongly deviate from the model. The use of absorption spectroscopy or surface plasmon spectroscopy depends on the measurements of ensembles. However any ensemble contains a distribution of particle sizes and shapes, making it difficult to obtain detailed correspondence between the nanoparticle structure and its optical response as a sphere-on-plane resonator. To reveal the intrinsic optical response of the system it is necessary to study single particles. Single particle spectroscopy removes any inhomogeneous contributions from the measurements which could conceal subtle features in the spectra and prevent the accurate determination of the resonance line widths. Since most of the theoretical work considered a single particle above a film, experimental studies on single particles near conducting surfaces immediately allow further on the direct comparison between the experiment and the theory.

In the following experiments investigations on single objects are combined for the first time with sphere-on-plane systems of ideal gold spheres. The spheres are generated by the irradiation of chemical reduced gold particle suspensions with the second harmonic (λ_{Ex}=532 nm) of a Nd:YAG laser. The produced particles have all the same defined shape and possess a low surface roughness combined with a narrow size distribution. The line-width of the localized surface plasmon (LSP) resonance is dramatically decreased after the irradiation. Sphere-on-plane systems of unirradiated and irradiated gold particles separated from an evaporated gold surface by 2-aminoethanethiol are then investigated by plasmon mediated dark field microscopy on a single object basis. The influence of film roughness is considered by using two further samples of irradiated spheres with smooth template stripped gold surfaces. The optical response of the single resonators is correlated with the gold particle shape and size in all three dimensions by a combination of atomic force microscopy and scanning electron microscopy. The resonance position and width of the resonators is compared to theoretical calculations in the quasistatic regime. In the end the results for all different samples are compared to estimate the influence of the different variations.

7.2 Results and Discussion

In the calculations using the quasistatic approximation the metallic nanoparticle is modeled as an ideal sphere surrounded by a homogenous medium at a given distance to a perfect flat metal plane (Ambient Colloid Model, ACM), for a schematic see Figure 7.1 (a). In realistic experiments a spacer layer is required to assemble the particles in a defined distance to the metallic film. The spacer layer has a different refractive index than the surrounding medium. The metal film is not an ideal flat plane and shows considerable surface roughness due to the evaporation procedure. The available metal particles on top which are generally produced by chemical reduction of their corresponding metal salts are facetted and possess many different crystal shapes. A more realistic sample architecture which considers these modifications is shown in Figure 7.1 (b).

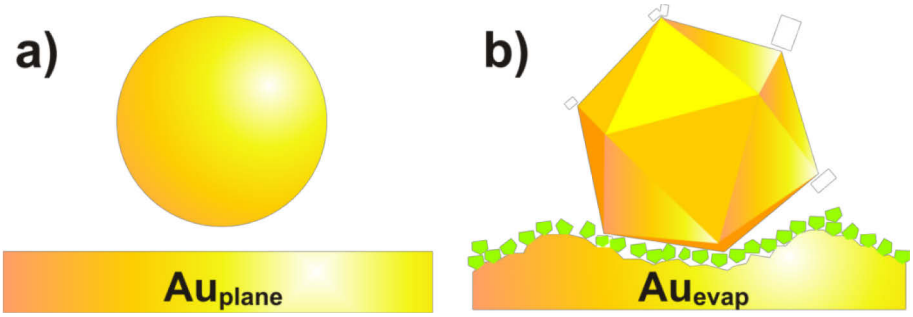

Figure 7.1: *(a) Ambient colloid model used for analytical calculations, (b) realistic sample architecture*

As an example according to Buffat *et al.*[50] an icosahedron is selected as gold particle. The spacer layer is sketched as an assembly of small particles (green) while the surface topography was taken from an atomic force microscope imaging a typical evaporated gold film. The two effects lead to an irregular shaped area between the particle and the film and increase the contact area compared to the model. The surface roughness of realistic particles will further intensify this effect. Calculations on rectangular particles coupled to a metallic film show that larger contact areas red-shift the gap resonances which can be compensated by considering a larger gap distance.[45]

The following strategy is pursued to achieve a better correspondence of the experimental and theoretical model and improve the understanding of the involved effects: First the gold particles on top are systematically modified to understand their influence on the gap resonance in a SOP system. As seen from Chapter 4 the laser induced shape transformation of gold particle suspensions is very helpful for this purpose as this procedure quantitatively transforms all particles of different shapes and crystal faces to ideal spheres and simultaneously reduces their surface corrugation. For a comparison all samples in this chapter were simultaneously prepared from one gold particle suspension. Second the

influence of the metal film topography is evaluated by modifying the surface roughness of the films using different preparation procedures as described in Chapter 3.1.6 and 3.1.7.

7.2.1 Variation of Particle Shape and Film Roughness

For particle modification one part of a gold suspension produced by the reduction of chloroauric acid with citrate is irradiated with the second harmonic (λ_{Ex}=532 nm) of a Nd:YAG Laser using a pulse energy of 3 mJ. Before the irradiation the gold particles have a mean diameter of 80 nm and a mean aspect ratio of 1.24. The procedure is repeated three times with 7 ml of this suspension in order to increase the available volume for the following sample preparation. The remaining portion of the suspension acts as reference where the optical response of two sphere-on-plane samples assembled with irradiated and un-irradiated particles on evaporated gold films is compared under the same experimental conditions. The progress of each irradiation is monitored with a white light and a spectrometer perpendicular to the laser beam and the laser induced changes are shown for each repetition in Figure 7.2 (a).

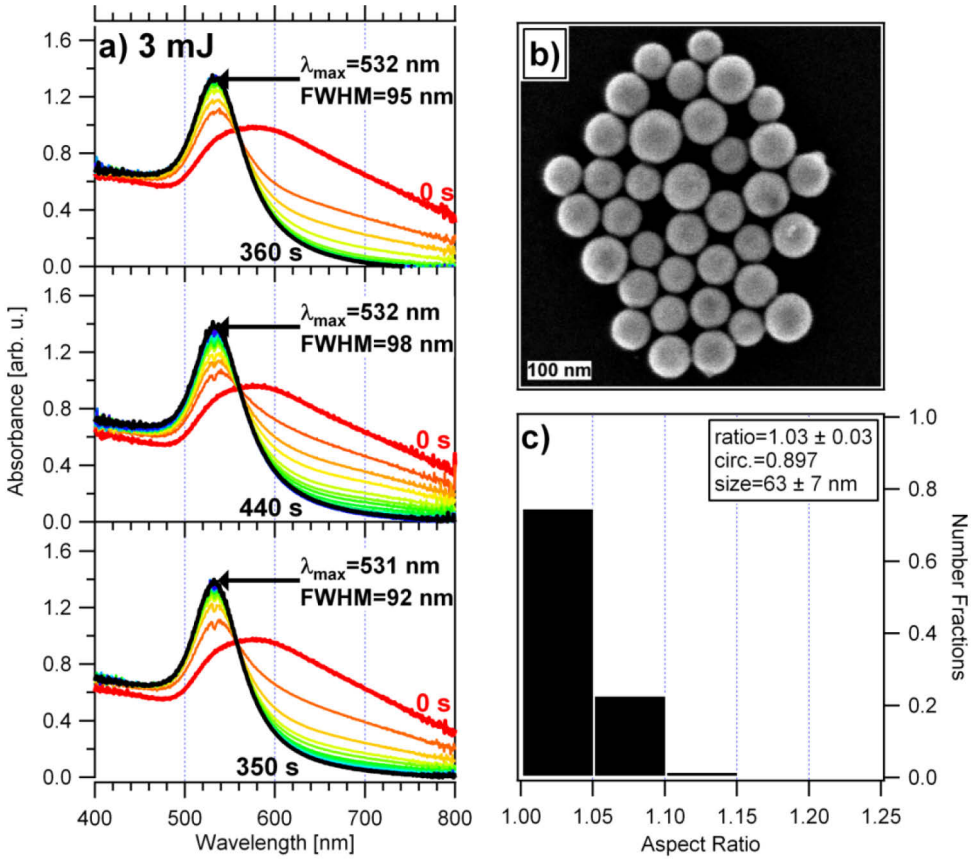

Figure 7.2: *(a) Three procedures of the laser irradiation, (b) representative SEM images of the final particles and (c) extracted statistical data from SEM measurements with distribution of aspect ratios*

The experimental details with the setup are described in Chapter 3.2.1. The result demonstrates the excellent reproducibility of this method. The red and black curves show

the initial and the final absorption of the colloidal suspensions respectively. During the irradiation the resonance position changes from 583 nm to around 532 with the maximum intensity increasing and the full width at half maximum (FWHM) decreasing from 220 nm to an average of 95 nm. The different colored curves in between show the progress with time where each curve represents a time difference of 15 s. The total irradiation time is adjusted in real time to achieve maximal consistency between the different processes. A representative image of the particles after the three suspensions were merged is shown in Figure 7.2 (b). After the irradiation they have an average diameter of 63 nm and exhibit a narrow distribution of aspect ratios with an average value of 1.03, shown in (c).

The modification of the particles is accompanied by the usage of different produced metal films. Gold surfaces prepared by thermal evaporation suffer normally from a number of imperfections. These variations in the nanoscale roughness modify the gap area and should influence the optical response of a SOP system. For an evaluation gold films were simultaneously evaporated on glass slides and silicon wafers. The samples with the evaporated gold on the glass slides were directly used to assemble SOP-systems with irradiated and unirradiated particles and are called the "*evaporated gold*" samples while the ones on the silicon wafers were treated by additional steps in order to prepare "*template stripped gold*" (TSG) surfaces.[51] This procedure takes advantage of the poor adhesion between gold and silicon. In the first step cleaned glass slides are glued on the evaporated gold surface of the silicon wafers by an epoxy glue. The interface between the gold and the silicon is then "stripped" free by application of mechanical pressure. In this way the natural smoothness of the polished silicon wafers surface is transferred on the metal interface to produce very smooth gold surfaces. This TSG surfaces are subsequently used to assemble additional SOP systems with irradiated particles. When the spacer layer is neglected these samples come the closest to the ambient colloid model of Figure 7.1.

The surfaces of the different prepared gold films are first investigated by atomic force microscopy (AFM) to evaluate the different film topographies and roughness values. The AFM images in Figure 7.3 (a-c) with a z-range of 6.5 nm show the usual topography of an evaporated gold interface. The surface is polycrystalline with a grain diameter of around 30 nm. These structural features are quantified by large root mean square (rms) roughness values of about 0.9 nm measured over a micrometer range. In contrast the template stripped gold surface in (d-f) displayed with the same z-range exhibits large terraces which are nearly atomically flat and are separated by granular areas. Therefore, the rms roughness of TSG is with a value of around 0.35 nm by a factor of 2.5 lower when the same micrometer range is considered. For TSG in general a surface roughness of 0.2 nm is accessible.[52] The larger values here are most probably a consequence of the used thin cover glasses where less surface pressure can be applied during the gluing process, but the differences between

the two substrates should still be large enough to evaluate the influence of the substrate on the optical response of a SOP system.

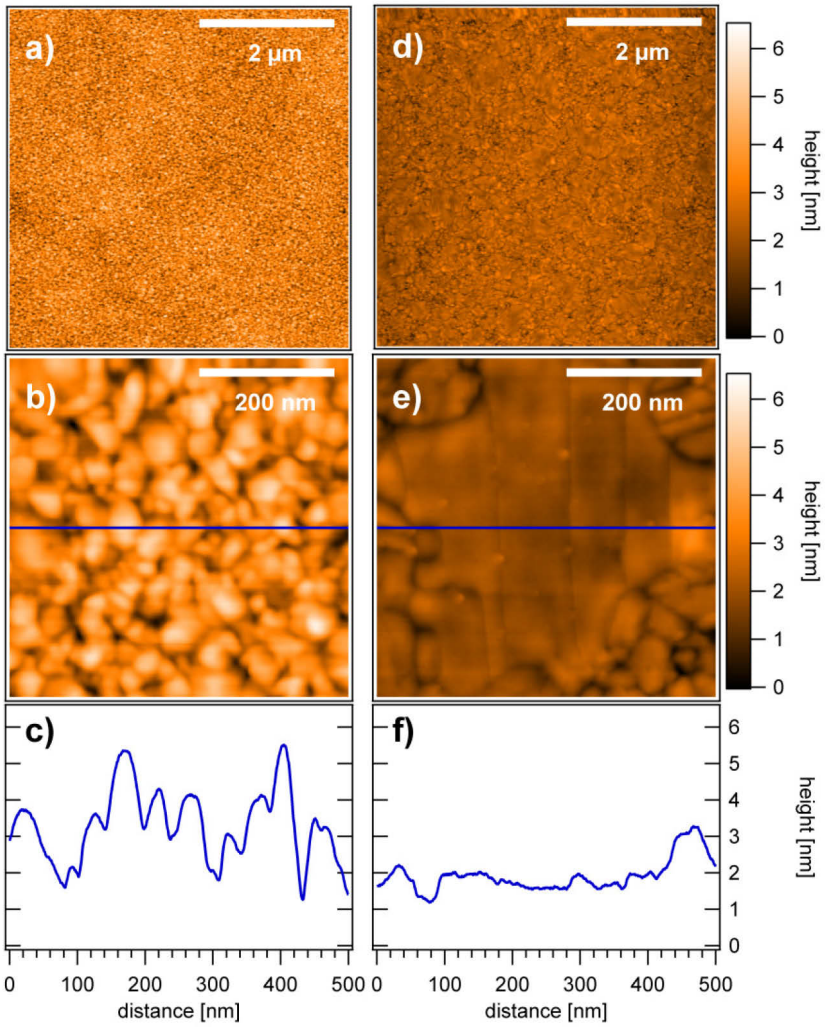

Figure 7.3: *(a-b) Evaporated gold film with a root mean square roughness of 0.759 nm (25 µm²) and 0.898 nm (0.25 µm²) respectively, (c) height profile of blue line from the evaporated gold surface (d-e) TSG with a root mean square roughness of 0.372 nm (25 µm²) and 0.354 nm (0.25 µm²) respectively, (f) height profile from the template stripped gold surface*

7.2.2 Particle Identification with Size Determination

For single object investigations on systems with a shape and size dependent response particle identification is mandatory. To establish a correlation between the physical and optical properties of the particles in three dimensions optical dark-field spectroscopy is combined with atomic force and electron microscopy. Figure 7.4 illustrates the identification of the same area with the three microscopic methods for the sample with the non-irradiated particle on the evaporated gold surface. First all objects are measured in the confocal microscope at the position of the two scratches (b). The scratches are visible on the left and right side of the presented scattering image and serve as an orientation mark to achieve correspondence between all microscopic methods. Then the AFM measurements follow

where the sample is first oriented in a way that the slow scan axis (y) is aligned parallel to the bisecting line of the two scratches. Then different micrographs of the different area of interests with various scan sizes are performed. After these measurements the same method is repeated to find the particles in the SEM. The scratches on the surface are seen in all images and fit excellent together when their position and distance is compared. The particles appear as individual bright spots in the confocal scattering image and as tiny white dots in the SEM and AFM micrographs. All of the analyzed particles reside inside the two white squares and are tagged by circles and numbers. The vertical and horizontal straight scratches in the center of the images (a) and (d) which are not visible in the scattering image were caused by the AFM cantilever during the measurements. This can be seen in one of the first AFM images (c) where they are not appearing.

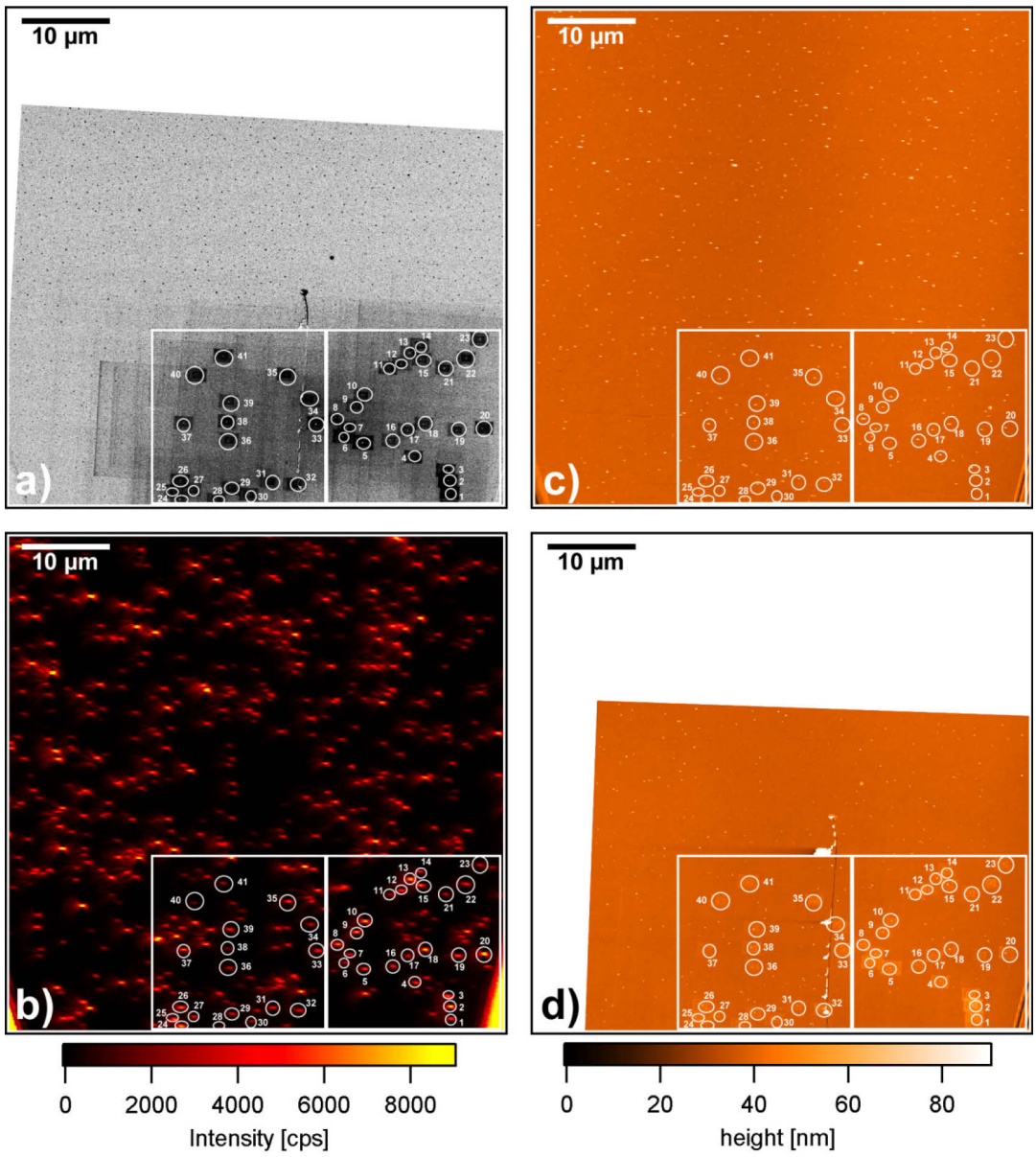

Figure 7.4: *(a) Scanning-electron micrograph, (b) corresponding scattering image, (c-d) atomic force micrograph of the same area of interest before and after SEM measurement; the white squares are the areas where the particles were measured with the investigated particles labeled with numbers and circles*

Figure 7.5 (a-c) shows the area of the right square with a size of 20 x 20 µm^2 seen by electron microscopy, scanning dark-field microscopy and atomic force microscopy. There is an excellent one-to-one correspondence between the white objects in the electron (a) and atomic force micrographs (c) and the bright spots in the scattering image of the confocal microscope (b). The objects are identified as surface immobilized gold particles by increasing the magnification in the electron microscope. The tagged objects were characterized by scattering spectra with the confocal microscope in dark-field mode.

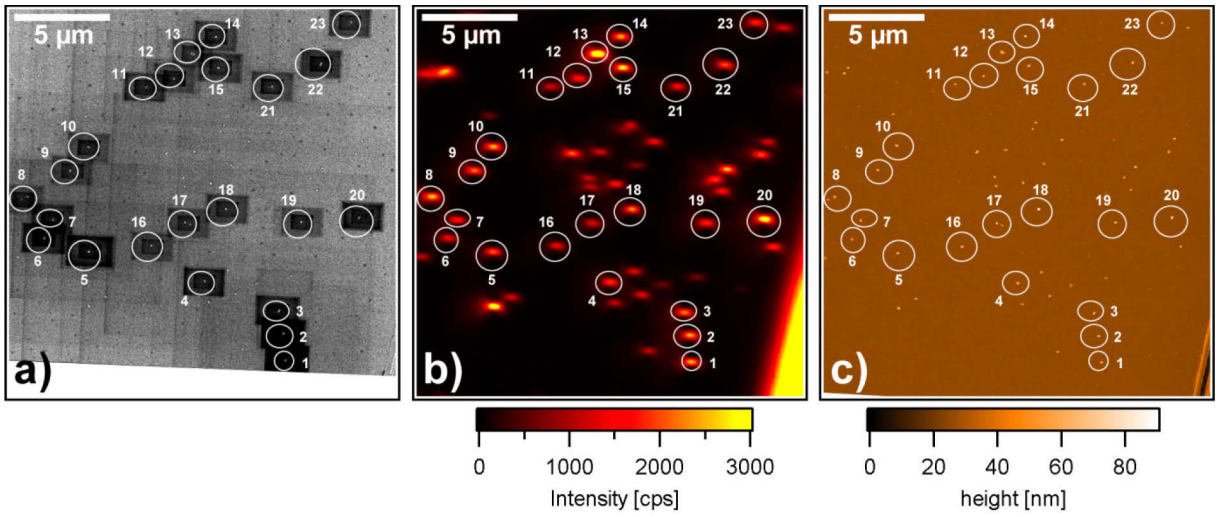

Figure 7.5: *(a) Scanning electron micrographs of the area under investigation, (b) corresponding scattering and (c) atomic force image*

A magnified image of the area inside the left white square is presented in Figure 7.6. Here the additional scratches of the AFM cantilever inside the area of interest are also visible in the SEM and AFM micrographs.

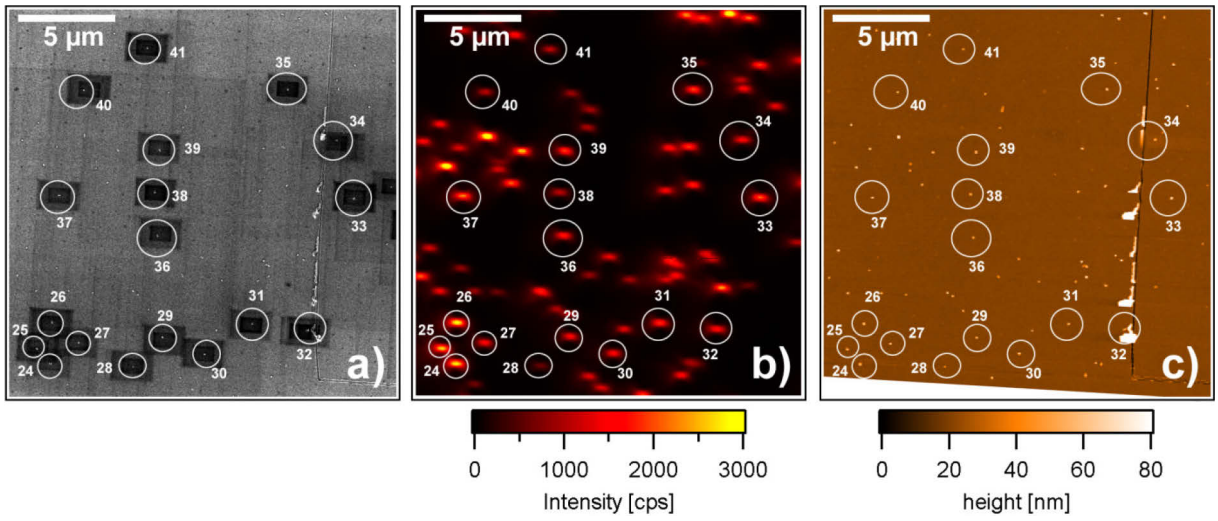

Figure 7.6: *(a) Scanning-electron micrograph of the left white square, (b) corresponding scattering image and (c) corresponding AFM image*

The scattering spectra of particle 32 was taken, but is not listed later since it was not possible to determine the height beyond doubt with the scratch in the way. The dark rectangular areas around the tagged particles in the scanning electron micrographs are contamination residues from higher magnification images.

In the early stages of particle analysis on samples with non-irradiated particles, the best available SEM image with the best contrast, resolution and largest magnification was used to determine the lateral particle dimensions, because with their arbitrary shapes no reference system was available which defined the “right” values. After the same analysis was performed for the irradiated gold spheres a systematic difference between the height from the AFM measurements and the lateral dimensions determined by SEM became evident, although the spheres were otherwise perfect round and there should be no preferential direction during the irradiation with laser light. A closer look of the SEM pictures themselves revealed a systematic increase of up to 5 nm in the lateral dimensions of the particles in a sequence of recorded micrographs for the same object. An increase of the size on this scale was never anticipated. The thiol spacer layer with the amino head group seems to affect the SEM measurements in a way that large amounts of carbon are deposited at places of high electron doses.

In Figure 7.7 the situation for the evaporated gold sample with non-irradiated gold particles is summarized. (a) and (d) show atomic force micrographs before and after the SEM measurement with the corresponding height profile of the blue horizontal line in (b) and (e). The first and last electron micrograph of particle 14 crossed by the blue line is presented in (c) and (f), respectively. The contamination for two different magnifications of first 200.000 x and then 361.000 x is visible in the AFM image (d) as lighter rectangles in two different sizes. In the height profile (e) which crosses particle 14 in (d) the different sections can be clearly separated by their respective height which increases with measurement progress and magnification. The borders of the rectangles where the turning points of the raster-scanning electron beam are located show an even higher contamination with local walls on both sides as the exposure time at these places is larger. The height difference from a point with no or less contamination to a place right next to the base of the particle is 2.5 nm. The difference in particle height from this position at the base to the maximum height of the particle is 3.3 nm compared to the result before the SEM measurement, see profile (b). All generated contamination carpets have an average height of around 3 nm above the surface. The influence of the contamination on the particle cross section itself is again demonstrated for particle 14 with the first SEM image in (c) and last one in (f). Under assumption of the blue particle-background boundary the two in-plane axes for this ellipsoid increase 5 and 6 nm respectively with the covered area of the particle increasing from around 4136 to 4728 nm^2.

For all investigated particles the analysis was therefore repeated and the first suitable SEM image was then used to determine the lateral dimensions.

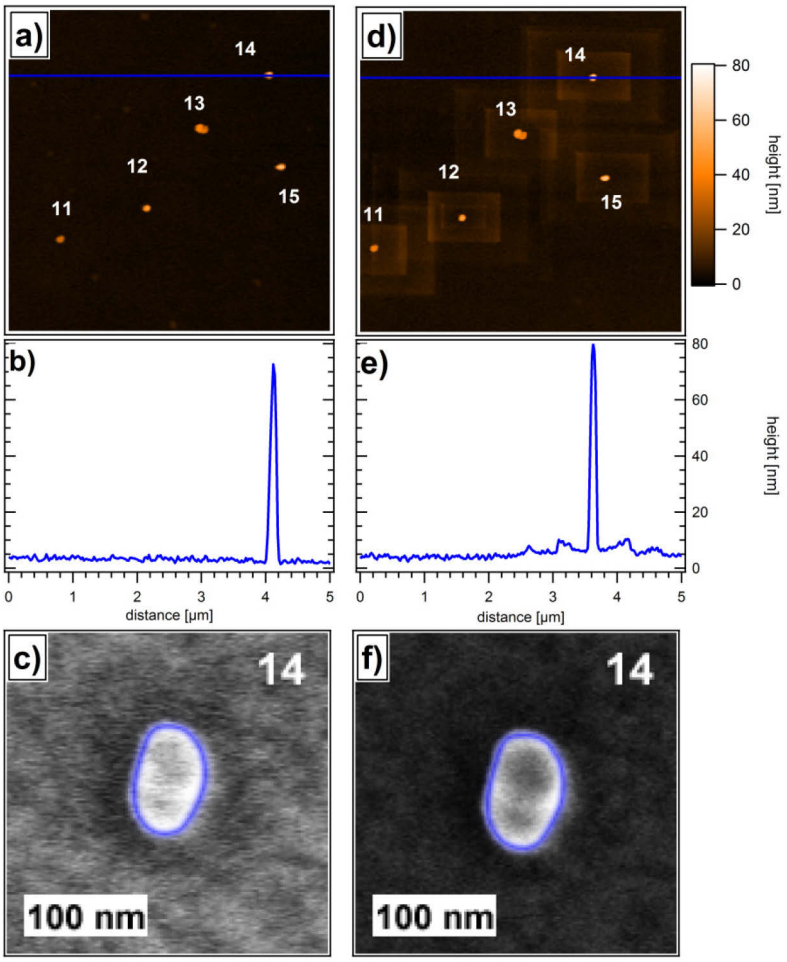

Figure 7.7 *(a) AFM image before SEM contamination and after (d). The areas of contaminated squares have an average height of 3 nm. In (b) and (e) the height profiles of particle 14 in (a) and (d) are shown. In (c) and (f) two electron micrographs for the first and sixth pictures after different magnifications and scanning techniques are shown. The blue border is the assumed boundary of the particle. The two axes in the first image were measured as 90 nm and 57 nm and in the last image as 95 nm and 63 nm.*

7.2.3 Calculation of the Gap Resonance

The optical properties of the different assembled SOP systems is compared to the calculated response using the quasistatic model from Wind *et al.*[15] for a homogenous dielectric environment and disregarding the spacer. The calculation of this ambient colloid model is based on bulk dielectric functions using gold values from Johnson and Christy,[53] although non-local effects[54, 55] and surface states[56] are expected to play a role on the involved length scales which are typically in the range of 0.5 to 3 nm. Another key problem for the calculation is the ambiguity on the choice of the gap distance and the surrounding dielectric function. At least in ensemble experiments using surface plasmon spectroscopy the determined gap distance was in agreement with an estimation from the molecular structure of the spacer layer and no evidence of geometrical imperfections or modifications to

Maxwell's theory on the sub-nanometer scale could be seen.[43] Other authors could also qualitatively reproduce the predicted trend from absorption spectra by systematic changing the sphere radius[38] or the gap distance through the spacer.[39] Nevertheless the ambiguity in the choice of spacer thickness and spacer dielectric function which are needed to calculate the problem quantitatively remains and ensemble measurements have the drawback of inhomogeneous contributions with averaging over a lot of different particles.

For spheres with diameters of 50 nm and 80 nm the solution of the Wind equation are shown in Figure 7.8 (a). The permittivity of the homogenous environment was selected as ε=1.7 with a distance of 0.9 nm from the gold film which is a reasonable choice for the used spacer.[57] The behavior of the system can be modeled by a Lorentz resonator. For the selected sizes the imaginary part of its polarizability shows two principal resonances. The strong resonances in the red which exhibits a large shift with increasing sphere diameter can be attributed to the gap resonance or described in other words to a plasmonic mode oscillating perpendicular to the substrate surface.

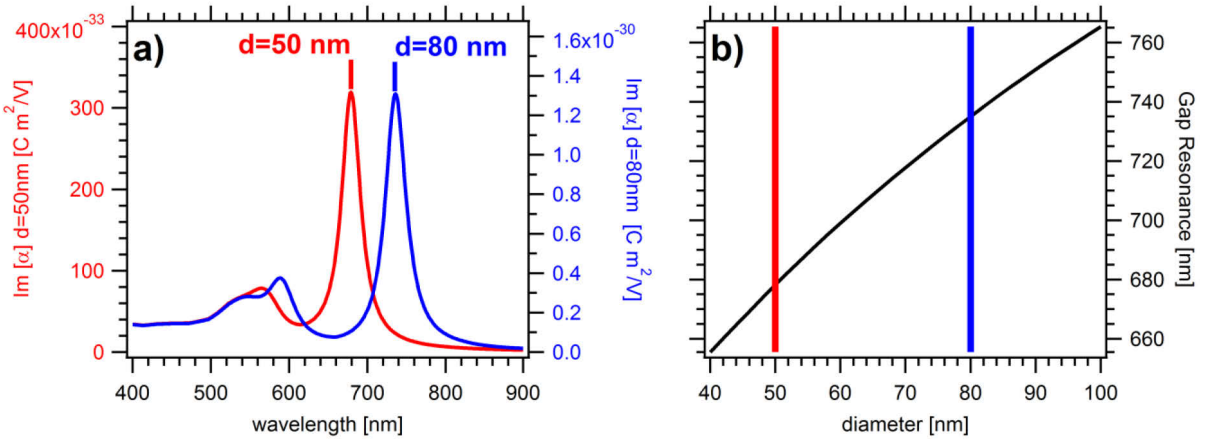

Figure 7.8: *(a) Calculation with Wind's equation[15] for a sphere with d=50 nm (red) and d=80 nm (blue) with a homogenous environment of ε=1.7 in a distance of 0.9 nm from the gold film. The ε values for gold are from Johnson and Christy.[53],(b) position of the gap resonance with increasing sphere diameter using the same values.*

In this quasistatic approximation the position of this mode depends only on the dielectric function of the material, the sphere diameter and the distance between sphere and film. The second resonance on the blue side which is nearly independent from the sphere size in the examples is either a contribution from the sphere alone[43] or a weak plasmonic interaction with the film oscillating parallel to the interface.[58, 59] For ratios of the gap distance to the sphere diameter which are smaller than 0.01 this parallel mode shows a small red-shift and for even smaller ratios new higher order resonances appear at this position.[60] Their appearance is already indicated by the third peak around 590 nm next to the sphere resonance in the example of the larger sphere. In Figure 7.8 (b) the gap resonance is plotted

as function of sphere diameter between 40 and 100 nm. For a diameter of 50 nm and 80 nm the gap mode has its position at around 680 nm and 735 nm, respectively.

7.2.4 Comparison of the Different Experimental Samples

The experimental determination of the gap resonance on a single particle base has the big advantage that it allows for a direct comparison to the theory and eliminates all effects from inhomogeneous broadening which is involved with every ensemble measurement. The measurements were done with two polarizers in a crossed configuration as described in Chapter 5.4. This mode efficiently excites and detects only the gap resonance and is shortly described in Figure 7.9.

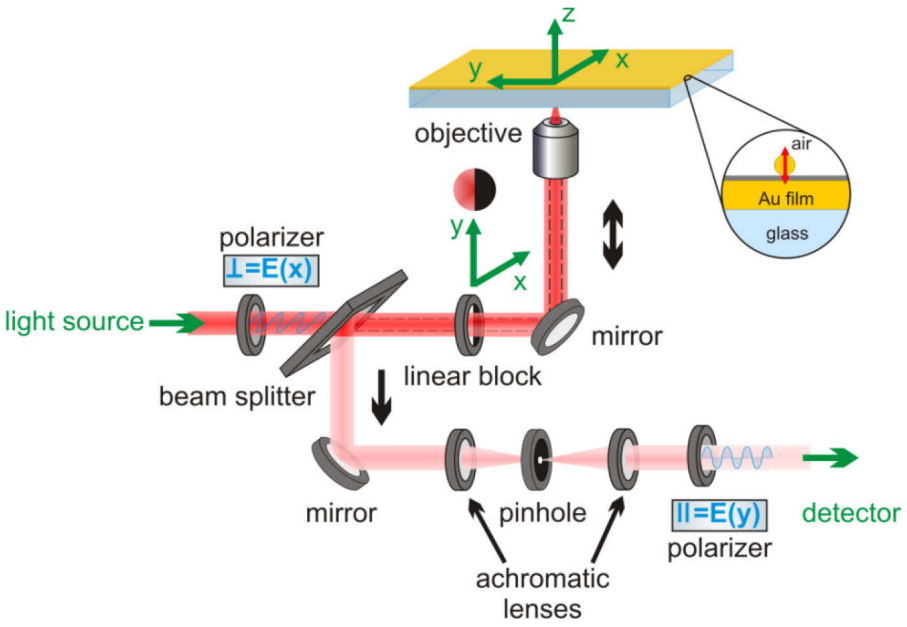

Figure 7.9: *Schematic representation of a dark field microscope with two perpendicular polarizers in the excitation and detection pathway*

First the sample with the evaporated gold film and the unirradiated particles is investigated because this system is used by various authors[38, 39, 43] as model system and already gives even in ensemble experiments a good qualitative agreement with calculations using the quasistatic approximation. The experimental response for a representative selection of 6 particles out of totally 34 is presented in Figure 7.10. Spectra for all other particles can be found in Appendix 10.2. The dashed red line on the bottom of the graph is an example for the scattering of the uncovered gold film in the vicinity of particle 41. For all other particles the scattering response of the gold surface looks nearly identical. The resonators in the graph are arranged by increasing volume which is calculated for this system as the area determined by SEM multiplied with the maximum height from AFM. Detailed information obtained by the combination of the two microscopic methods is presented for each particle in the following Table 7.1 and in Appendix 10.2.

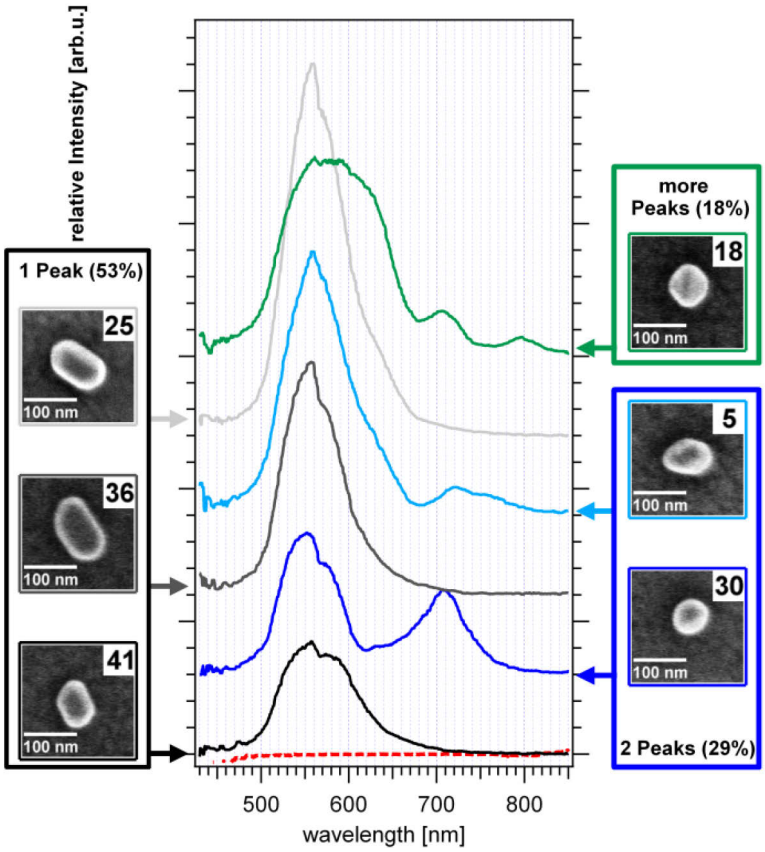

Figure 7.10: *Scattering response for a selection of non-irradiated original particles on the evaporated gold surface plotted by increasing particle volume from bottom to top*

The numbers in brackets indicate how many values were determined by AFM and considered for the average height. The circularity is the proportion of the area and the perimeter (4π area/perimeter^2) and gives an indication of the two dimensional roundness of the considered particle from the SEM images. For an ideal circle the factor would be exactly 1.

Table 7.1: determined dimensions of the presented colloidal particles on evaporated gold

Particle	x-axis [nm]	y-axis [nm]	Height [nm]	2Area [nm^2]	Volume [nm^3]	Circularity
18	80	70	67 (5)	4320	290995	0.905
25	112	70	42 (4)	6660	282451	0.836
5	92	66	58 (2)	4800	279600	0.855
36	122	71	48 (6)	7372	247761	0.808
30	70	60	62 (4)	3364	209998	0.891
41	85	60	36 (3)	4504	161513	0.851

The measured response of the presented particles is quite different from the calculated one in Figure 7.8 (a). Three different groups of resonators can be distinguished. The largest group with 53% of all particles shows only one resonance which is either caused by the particle resonance alone or an interaction of the horizontal mode of the particle with the film as described before. In the following this resonance is called particle resonance in contrast to

the vertical mode which is called gap-resonance. The second group with 29% shows the two resonances expected from the calculation for an ideal sphere-on-plane resonator. The third group with 18% shows more than these two resonances. From the spectra no correlation to the shape and size of the particles can be derived which would explain this behavior. For example particle 30 with a sphere-on-plane like response seems to have the same shape as particle 18 which exhibits 3 resonances. Another case is particle 41. It shows only one resonance at around 550 nm while resembling in shape and size particle 5 which has two resonances. Obviously there are more factors influencing the gap resonance in experimental accessible sample architectures than just the distance and the particle diameter. These variations may originate from nanometer-sized differences in the gap area between the metallic structures, which are not directly accessible by the microscopic methods. It is surprising that ensemble measurements[38, 39] give such a good agreement of the resonance position in spite of the observed strong variations in the optical behavior of single resonators. The sphere resonance takes values within the measured ensemble from 550 to 580 nm while the full width at half-maximum (FWHM) ranges from 69 to 158 nm with an average of 88 nm. Its intensity increases with particle size and in 68% of all cases a shoulder on the right side of the resonance is seen which is predicted from the calculated response of the larger sphere in Figure 7.8 (a). The gap resonance on the red-side of the spectrum which is observed for only 10 particles (29%) emerges at positions between 651 and 740 nm and shows no correlation to the determined diameter or volume. The FWHM for the gap response ranges from 69 to 114 nm with a mean value of 75 nm which is significantly more than theoretically predicted (22 nm). In single particle experiments as stated inhomogeneous broadening can be excluded and therefore, a significant deviation from the expected theoretical response of a perfect SOP system is observed. In literature different values for the dielectric function of gold can be found, for example in the book of Palik[61] significantly higher damping factors are quoted. This higher damping leads to larger resonance widths than that found by using the dielectric function stated by Johnson and Christy,[53] but even these values cannot completely explain the described behavior. Measurements of the dielectric function are necessarily performed on non-perfect samples and therefore can be regarded as an upper limit for damping.[52] Therefore, the data from Johnson and Christy is considered to be the better choice for the theoretical model.

The replacement of the irregular shaped particles from chemical reduction with the laser irradiated spheres on the evaporated gold substrate improves the reproducibility of the scattering response for each resonator tremendously. For this sample all characterized particles behave as predicted by the theoretical response from the Wind calculation above and show the two resonances. A selection of 6 out of 43 particles is presented in Figure 7.11 with increasing volume from bottom to top. For these nearly ideal spheres the volume is

calculated for an ellipsoid with three different axes as determined by AFM and SEM measurements.

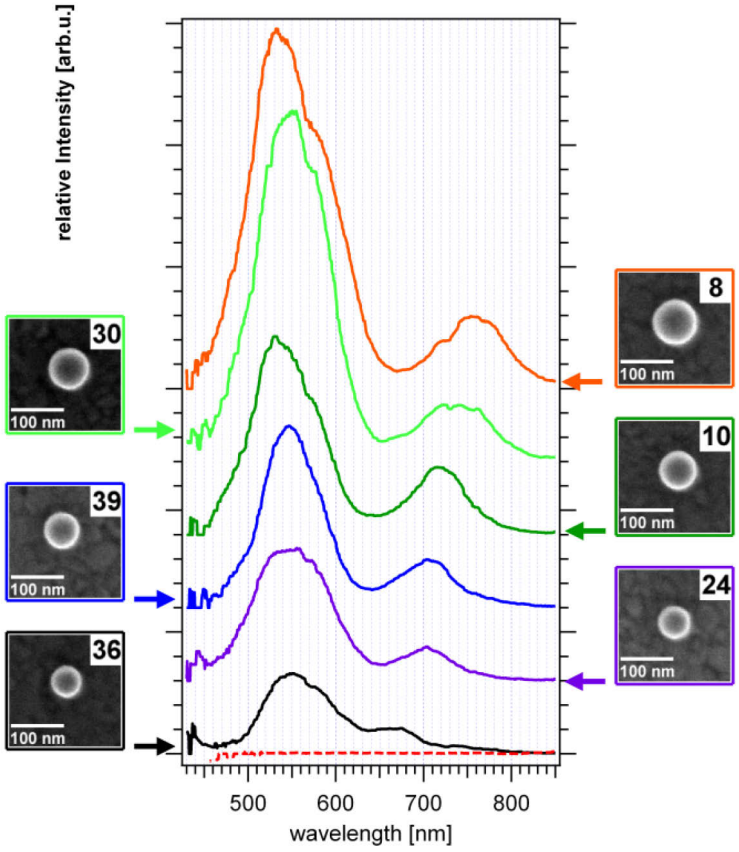

Figure 7.11: *Scattering response for a selection of irradiated particles on the evaporated gold surface plotted by increasing particle volume from bottom to top*

The height from AFM for all investigated particles is in average 2 nm lower than the lateral particle dimensions obtained by SEM. As the particles are getting larger in the SEM due to all the effects involved with contamination they can be thought to be nearly spherical. An exemplary scattering spectrum of the clean metal film next to a position of particle 36 is given by the red dashed line and shows the same features as before. All details for the particles from the figure are summarized in Table 7.2 in the same way as before with all particles presented in Appendix 10.3.

Table 7.2: determined dimensions of the presented gold spheres on evaporated gold

Particle	x-axis [nm]	y-axis [nm]	Height [nm]	Area [nm^2]	Volume [nm^3]	Circularity
8	84	84	80 (11)	5748	296535	0.904
30	74	73	72 (7)	4516	203893	0.906
10	71	70	66 (11)	4064	172839	0.895
39	66	64	64 (6)	3504	142101	0.908
24	62	60	57 (9)	3044	110467	0.918
36	56	54	51 (11)	2476	81156	0.899

The resonance corresponding to the sphere interaction remains unchanged after the particle modification and still holds positions between 550 and 570 nm. The average FWHM has a value of 95 nm while the shoulder from the emerging higher order mode on the right side of the resonance can be seen in 91% of all cases. The gap resonance on the red side of the spectrum which is according to the theory highly sensitive to the particle size reproducibly shifts to longer wavelength when the particle size is increased. The full width at half-maximum (FWHM) ranges from 58 to 100 nm with an average value of 77 nm. In spite of the improved sample geometry these values are still much higher than the theoretically predicted ones (22 nm).[38] For both resonances the maximum intensity increases with particle volume. Their different proportions in theory and experiment are related to the wavelength-dependent response in plasmon mediated dark field microscopy which decreases its efficiency with increasing wavelength. For further details see Chapter 5.3.

After the particle modification the reduction of surface roughness by replacing the evaporated gold with the template stripped gold film does not improve the scattering response of the SOP system as becomes evident from Figure 7.12.

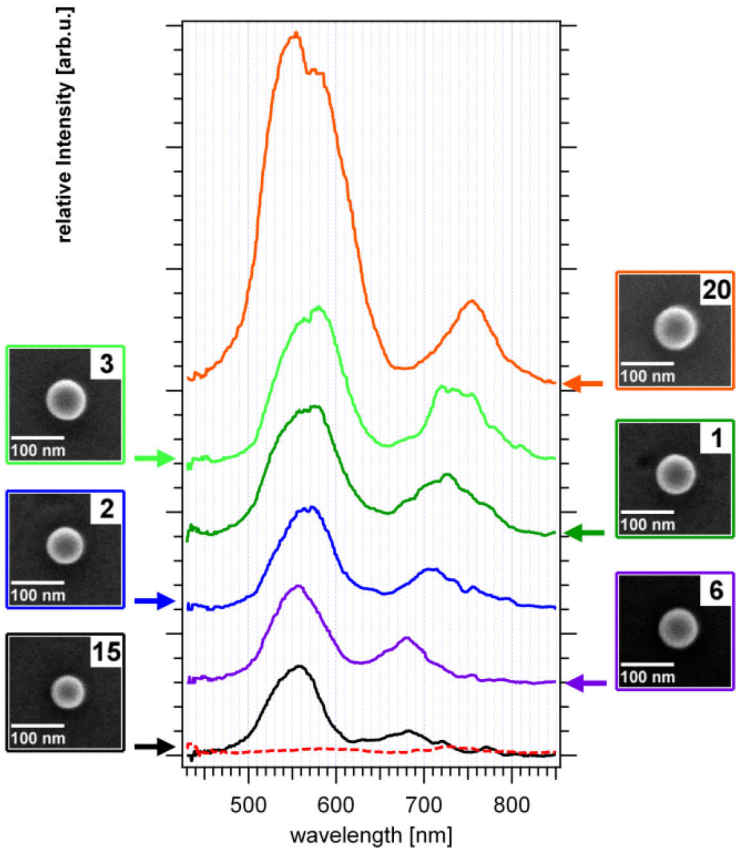

Figure 7.12: *Scattering response for a selection of irradiated particles on the template stripped gold surface plotted by increasing particle volume from bottom to top*

In the presented case the cleaned glass slides are glued on the gold film with an EPO-TEK 377 epoxy glue. The selection of 6 out of 21 particles is arranged from bottom to top according

to an increase in particle volume which is again calculated for an ellipsoid with three different axes. The spectra show the same features as before and agree with the Wind calculation, although in 38% of all cases additional weak sharp peaks red-shifted from the gap resonance are visible. This can be seen from the scattering response of particles 15, 6 and 2 and is also noticeable in the related reference spectrum of the metal film next to particle 15, displayed on the bottom as red dashed line. The overall scattering intensity from the film is also stronger than before. Therefore this spectral modification is rather related to the TSG surface itself than to the smaller surface roughness or the gap resonance. Table 7.3 shows the particle details for the presented SOP resonators. Details for all other particles are found in Appendix 10.4.

Table 7.3: determined dimensions of the presented gold spheres on template stripped gold

Particle	x-axis [nm]	y-axis [nm]	Height [nm]		Area [nm^2]	Volume [nm^3]	Circularity
20	76	73	74	(28)	4527	215582	0.901
3	71	70	69	(28)	3940	179879	0.911
1	66	65	63	(18)	3412	142372	0.904
2	61	61	58	(18)	2912	112682	0.913
6	56	55	53	(20)	2426	85025	0.912
15	51	50	50	(19)	2042	66230	0.896

The behavior of the gap resonance with particle size is again reproducible. The FWHM varies between 47 and 95 nm and has an average value of 65 nm. This is the lowest value for all investigated samples, but is still significantly more than theoretically predicted. For the position of the sphere resonance on the blue side of the spectrum no difference can be seen to the previous samples. The FWHM values are between 70 and 120 nm with a mean value of 95 nm. The shoulder of the higher order mode seen from the calculation is visible in 86% of all cases. As the TSG surface with the irradiated particles resembles more than all the other systems the theoretical model, the intensity from the investigated scattering patterns in a representative confocal dark-field image is plotted in Figure 7.13 as a function of the determined height. The values for the intensity is extracted from the image in (a) by fitting a two dimensional Gaussian function to each investigated pattern and using the maximum as the reference value. The AFM height is favored above the other dimensions, firstly because it is not influenced by contamination and secondly because it is determined with some statistics as indicated by the values in the brackets of Table 7.3. The black dashed line in plot (b) acts as guide to the eye, but gives already a very good agreement to the experimental data. This supports the argument from Chapter 5.5 that an efficient way of selectively detecting z-dipoles in a sphere-on-plane geometry was found where the response should increase when the particle height gets larger.

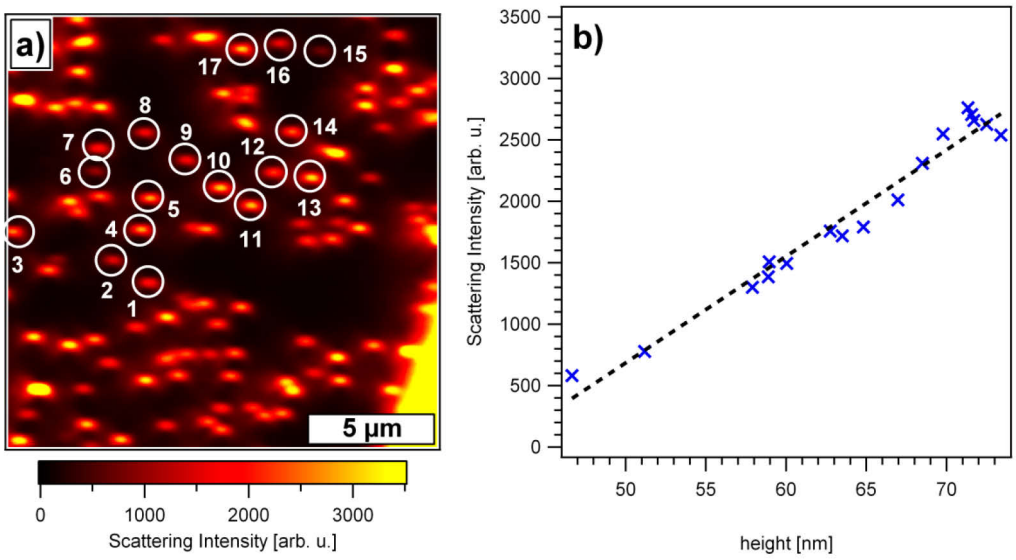

Figure 7.13: *(a) Intensity patterns in a confocal dark field image used in plot (b) to correlate the scattering intensity and the particle height. The particles tagged with circles and numbers were characterized by both methods.*

For all samples both the illumination and detection occur through all layers of the system which include, for the evaporated gold surfaces, only the glass slide and the gold film. For the TSG surfaces an additional layer is introduced by the epoxy glue during the preparation which leads to additional scattering and has direct consequences for the scattering response of the whole sample. This layer also establishes a wavelength dependency in the scattering response of the whole film. For a further evaluation of the glue layer influence on the scattering response of a SOP system, a second TSG sample was prepared under the same conditions and with the same particles, but this time the glass substrates were glued to the gold with an EPO-TEK 353ND-4 epoxy. A comparison of two confocal dark field micrographs for this new system and the already presented TSG system is presented in (a) and (b) of Figure 7.14 respectively.

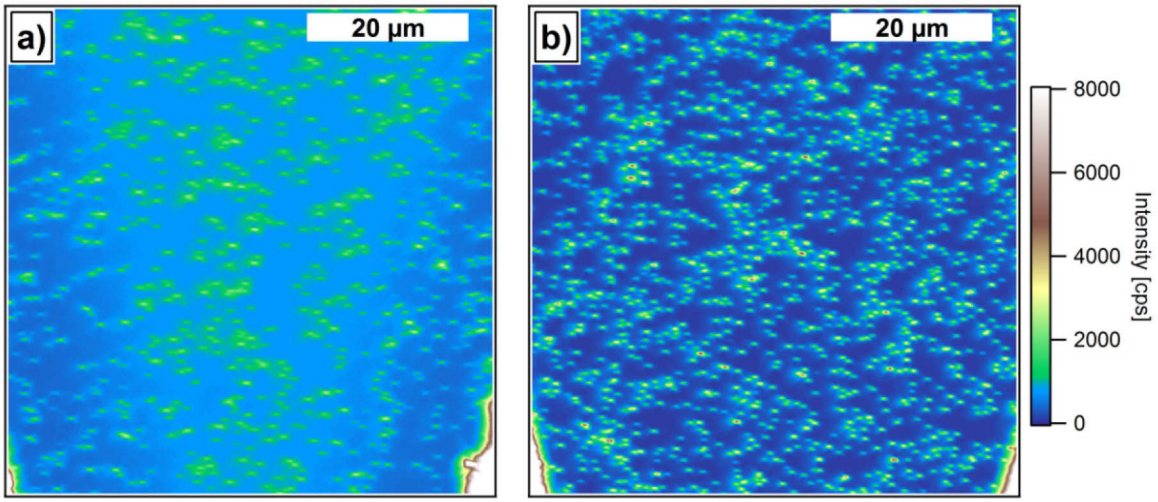

Figure 7.14: *(a) Confocal overview image with scratches for a template stripped gold surface glued to the glass with Epotek 353 ND, (b) Confocal image with a template stripped gold surface with Epotek 377 as glue.*

Both images show a large area of 60 x 60 µm with the scratches on the left and right side of the images. A different color scale is selected for a better visibility of the glue layer influence. The used EPO-TEK 353ND-4 in (a) is a two component high temperature epoxy glue which is specially designed for the use in semiconductor, hybrid, fiber optic, and medical applications. Due to its high stability against different solvents it is frequently used in our group to prepare template stripped gold surfaces on microscopic glass slides. For optical experiments through the glue layer the adhesive has some serious disadvantages. Before curing it has a refractive index n_D^{20} of 1.5694 which is very different from the Menzel glass slides with n_D^{20}=1.5230 and for wavelengths below 550 nm the spectral transmission is only around 50%. After curing the glue layer is clearly visible in amber color at the backside of the gold film. The viscosity of the two component mixture is very high which complicates the TSG processing when thin cover slides are involved. In the confocal micrograph (a) the background scattering is accordingly not uniform over the whole area and the scattering patterns in the center are out of focus. The glue layer in the image is either not uniformly thick or it is so thick that it can be compressed by the cannula which is used for scratching the surface for the identification procedure. The scattering intensity from the particles in relation to the background is also not very high when compared to image (b) of the previous sample where the EPO-TEK 377 glue was used. The EPO-TEK 377 focuses on the same range of applications, but has a different refractive index n_D^{20} of 1.5195 which is closer to the one from the glass slides. Furthermore its pot viscosity is merely a fraction of the one for the EPO-TEK 353ND-4 and therefore allows for a thinner glue layer between the gold film and the glass interface when thin cover slips are required. After the epoxy hardening the glue layer is not visible at the backside of the gold film and also the corresponding dark field image in (b) reveal no inhomogeneity. The scattering from the background is constant and all scattering patterns are in focus. The intensity to background ratio is by a factor of around 4 higher compared to (a). The spectroscopic response of this EPO-TEK 353ND-4 layer is also strongly wavelength dependent.

In Figure 7.15 a representative selection of 4 out of 36 measured particles taken within the visible area of Figure 7.14 (a) are presented. All other spectra and particle information obtained by SEM and AFM are found in Appendix 10.5. The blue dashed line shows the scattering efficiency of the particle presented top right while the scattering efficiency of the metal film in the vicinity is shown as red dashed line. The relative intensity of the particle alone which is displayed throughout this chapter results by subtraction of the red spectra from the blue ones. Please note that all spectra are scaled to the same value. The scattering response from the metal film alone is large compared to all previous background spectra and strongly depends on the illumination wavelength and the measurement position on the sample. In some cases the scattering below 460 nm increases tremendously for both the

particle and the film, in all cases a lot of noise on the far blue side is seen. This effect originates accordingly from the glue layer and is not an optical property of the sphere-on-plane resonators. The stronger interaction of the illumination light with this layer creates an additional fine structure in the background adjusted response of the resonators compared to Figure 7.12 where the EPO-TEK 377 glue was used, but does not modify the position or the intensity of the gap resonance itself. Both agree with the previous cases where spherical gold particles were used. This can be observed by correlating all characteristic parameters obtained from the scattering spectra, atomic force microscopy and electron microscopy.

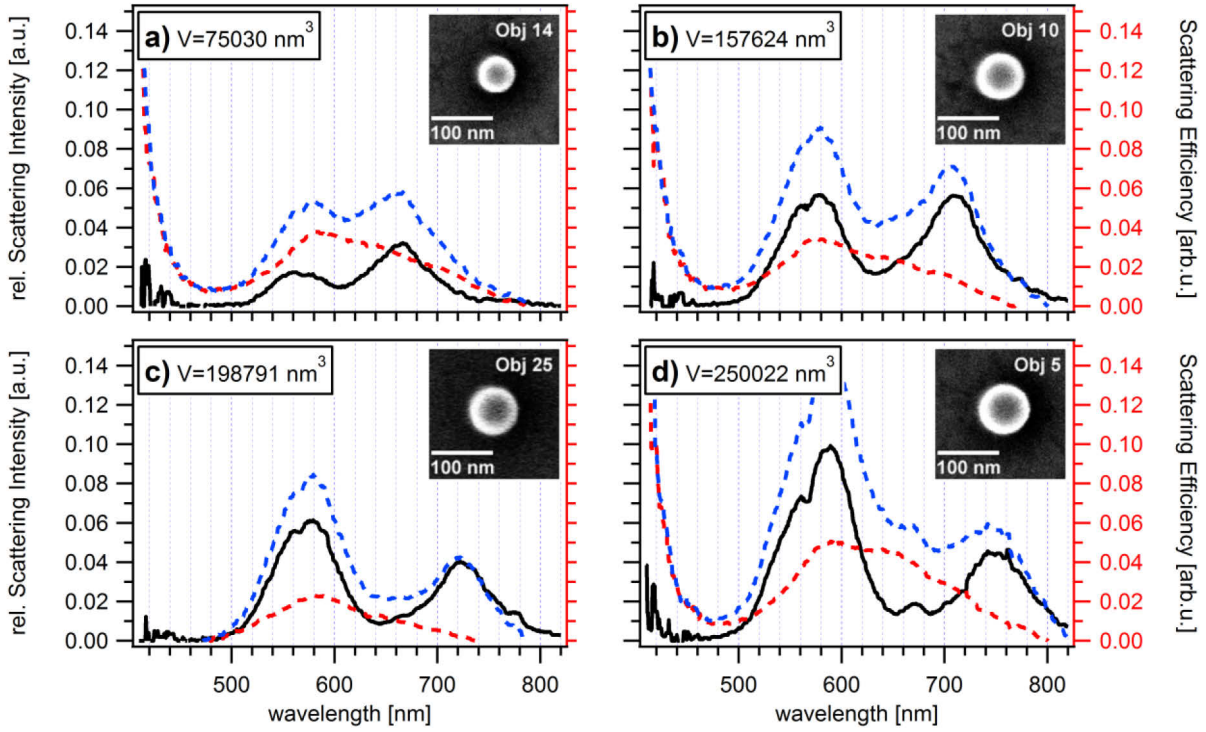

Figure 7.15: *(a-d) Scattering efficiencies (blue dashed line) for different particles with inreasing volume compared to the scattering of an uncovered position next to it (red dashed line). The black solid lines show the reponse without the background response.*

In Figure 7.16 the position of the gap resonance is plotted as function of the particle volume (a, c, e) and the particle height (b, d, f) for all samples with the different prepared gold films and spherical laser-irradiated particles. Plots for all other possible combinations involving the scattering maximum intensity, the FWHM and the signal to background ratio of the resonance are shown for each sample in the appendix. The gap resonance red-shifts with the particle volume and height respectively, but is not dependent on the surface roughness or the different film preparations. For the same particle sizes different resonance positions are obtained for all samples which points to additional factors, e. g. the nanostructure in the gap region influencing the plasmonic resonance, but this is again not accessible by our microscopic methods. In an ensemble experiments these individual differences would be averaged out and all samples would confirm the theoretically predicted trend. In the plots of

the single resonators the experimental data is also compared to the theory by using again Wind's equation.[15] The ambiguity in the choice of the gap distance and the surrounding dielectric function is solved by adjusting the gap distances in the calculation with values between 0.8, 0.9 and 1.0 nm while the dielectric function of the surrounding is kept constant with ε=1.7.

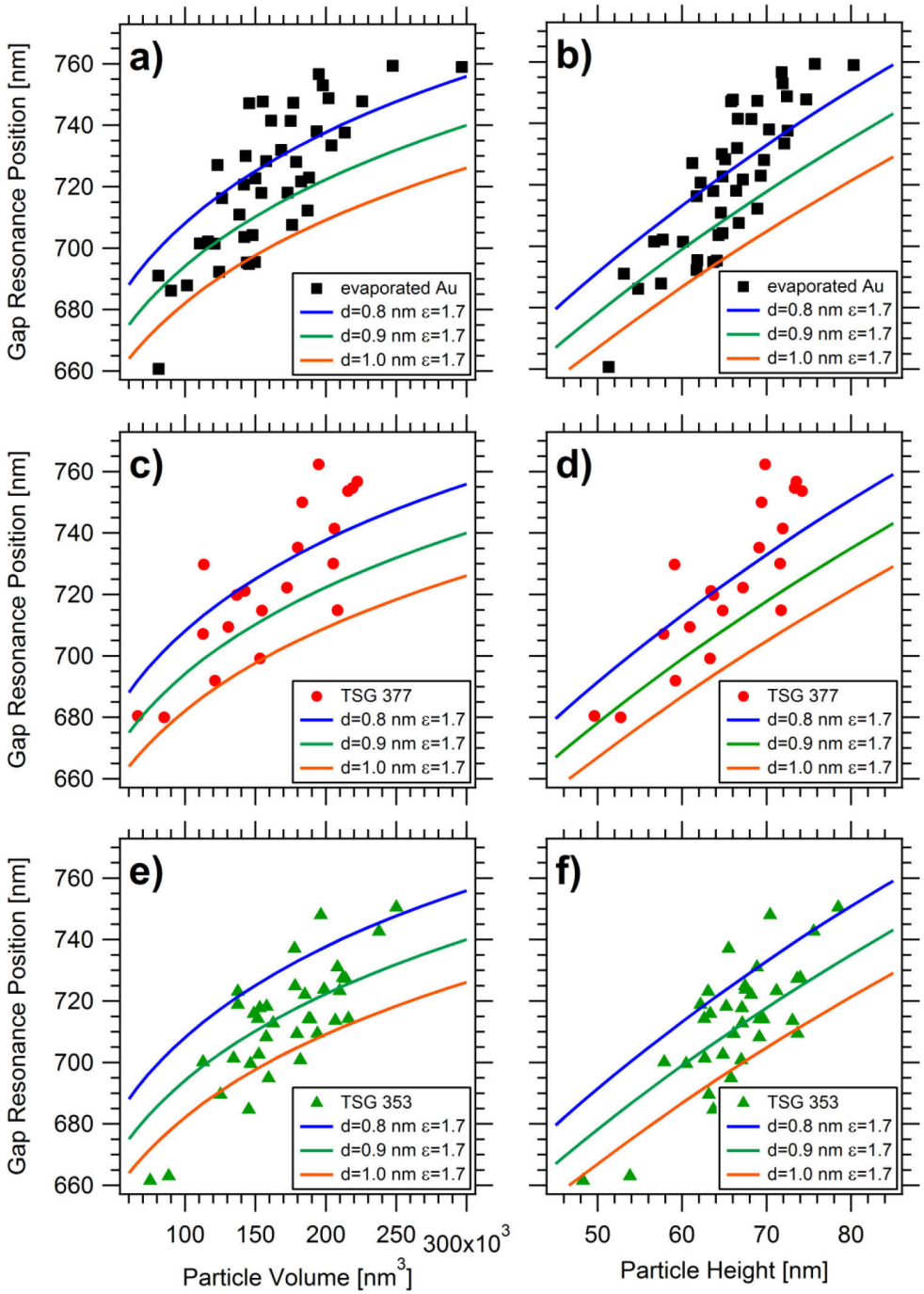

Figure 7.16: *(a) Position of the gap resonance in nanometer versus the particle volume and (b) versus the particle height for the evaporated gold film with irradiated particles, (c-d) the same plots for spherical particles with the template stripped gold film using EPO-TEK 377 as glue and (e-f) using EPO-TEK 353ND-4*

The opposite approach of changing the dielectric function and keeping the gap distance constant would have the same effect. The results of the calculation for the different set of

parameters are given by the three colored curves in each plot and already show a very good agreement to the resonance positions of almost all SOP resonators. For particle sizes larger than 70 nm or volumes larger than 180.000 nm^3 retardation effects emerge and the experimental data starts to red-shift from the calculated curves which only take the dipole interaction into consideration. The distribution of resonance positions for the sample with the TSG 353 surface is slightly blue-shifted compared to the other two surfaces as shown in Figure 7.17.

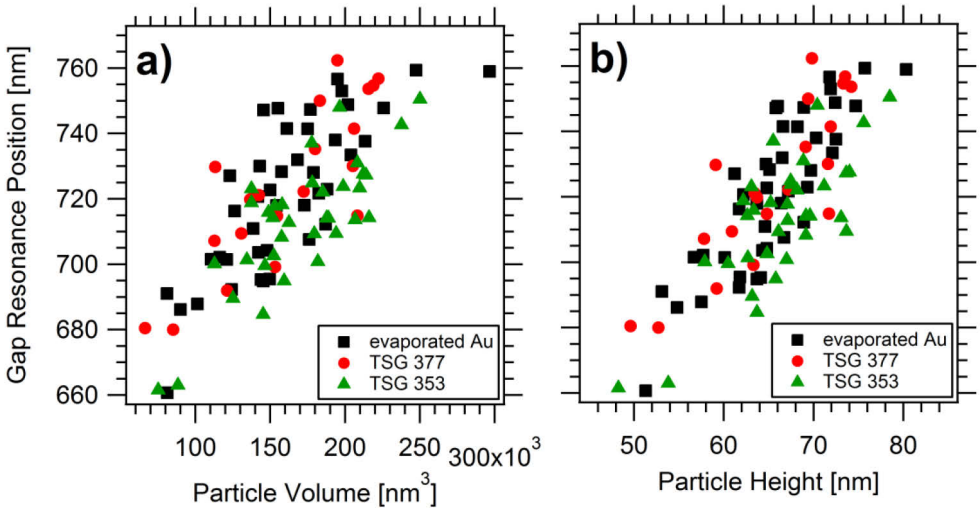

Figure 7.17: *Positions of the gap resonances for all samples as a function of particle volume (a) and particle height (b)*

The origin of this shift is unclear, but with respect to the strong glue layer interaction it is most probably an experimental artifact. In principle a smoother surface should reduce the active contact area and blue-shift the resonance,[45] but this should also be visible for the TSG 377 surface which shows less glue interaction and allows for a better detection.

In summary to all experiments in which the particles as well as the surface roughness were modified the particle modification showed the greatest impact on the scattering response of SOP resonators while a change from the reduction in metal film roughness could not be seen. The evaporated gold film with the chemically reduced gold particles represents the system of choice in various ensemble measurements[38, 39, 43] where it showed close experimental agreement to the same calculation. After the single particle measurements this is truly surprising as only a small portion is acting in the predicted way and strong spectral variations between the resonators are revealed. These results demonstrate the power of single particle spectroscopy and identification. The shape transformation of the particles by laser irradiation has a big impact on the response of the SOP resonators and lead to a much more defined system. In contrast the changes induced by the TSG surfaces and the surface roughness reduction are small. For the nanometer-size dimensions of the active gap area the differences between evaporated and template stripped gold surfaces should also nearly

disappear as seen in the AFM micrographs of Figure 7.18 where 100 x 100 nm small sections of the TSG and evaporated gold films are imaged.

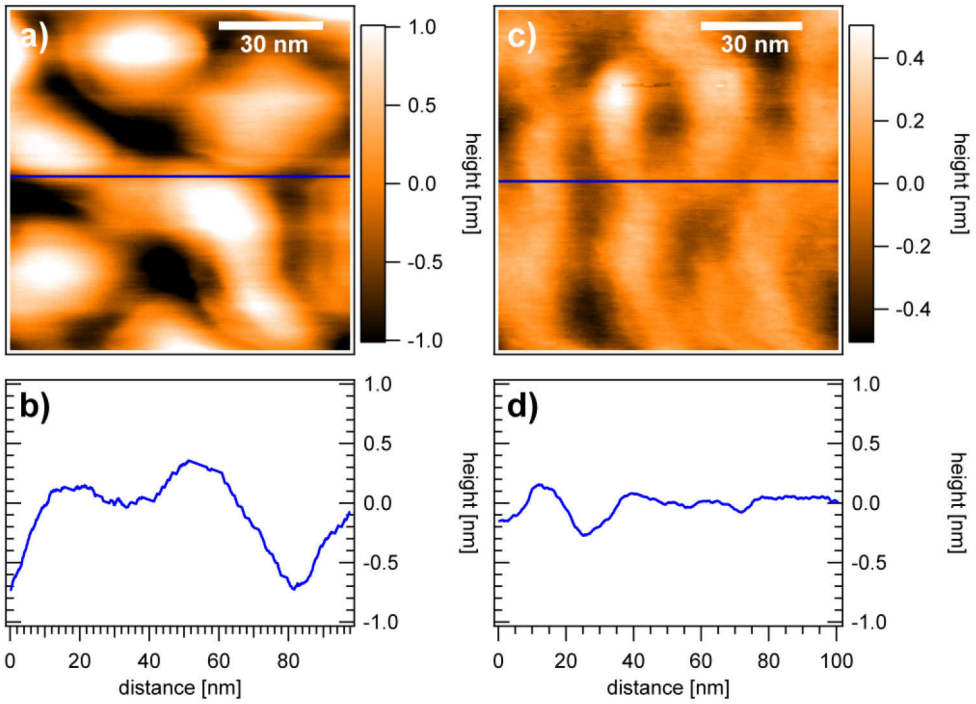

Figure 7.18: *(a-b) Evaporated gold film with a root mean square roughness of 0.576 nm (0.01 µm^2) and related height profile, (c-d) template stripped gold film with a root mean square roughness of 0.153 nm (0.01 µm^2) and the related height profile*

On a scale of 5 nm the differences between the two substrates in terms of the rms roughness values diminish for most particles, lying on a crystalline terrace or directly on a grain, independently from the large structural differences for the films on the large scale. Therefore the impact of the substrate on the optical response is expected to be small when the films are not too different.

7.3 Summary and Outlook

On a single object basis different architectures were investigated to estimate both the influence of particle shape and film roughness on the gap resonance in a sphere-on-plane system. The optical response of irregularly shaped gold particles produced by chemical reduction was compared to the resonances of gold spheres created by a laser induced transformation process. The film roughness was modified by using evaporated gold surfaces and template stripped gold surfaces. The gap was created by a monolayer of an amino thiol which acted as spacer layer between film and particle. Plasmon mediated dark field microscopy provided an efficient method to detect even weak spectral variations of the individual sphere-on-plane resonators. The optical experiments were combined with scanning electron microscopy and atomic force microscopy to determine the related particle

shape and size in all dimensions. For all samples with spherical gold particles a defined response could be independently seen from the film roughness which showed a resonance from the interaction in the gap and the sphere alone. In some cases a higher order peak on the red-side of the sphere resonance emerged. The position of the gap resonance agreed with theoretical calculations using Wind's equation while the full-width at half maximum values for all resonances were significantly broader than theoretically predicted. Despite the defined system geometry with the combination of spherical gold particles and flat films the results point to more factors influencing the gap resonance than just the distance to the film and the particle size like nanoscale fluctuations in the shape of the active gap region. For the sample with the chemically reduced particles of various shapes the single particle experiments found at least three different classes of resonators which differed strongly from the ideal case and showed strong spectral variations in number and position of the optical resonances with no correlation to the shape. Only a small proportion of all investigated particles showed the expected behavior with two resonances. It is surprising that ensemble measurements reveal such a good agreement with theory in spite of these strong variations.

The spherical gold particles are quite valuable for investigations on the gap resonance and allow with their defined response a much closer look on the experimental data. Since they are also useful in other applications and already have a narrow localized surface plasmon resonance, new experiments should focus on the surface roughness on the atomic scale and the degree of their crystallinity by using transmission electron microscopy. The combination with confocal dark field microscopy and the investigation on particle dimers should clarify how the gap resonance is depending on the shape of the active area. This should also allow for the first time for very defined particle dimer systems, which are suitable for other applications like SERS. The template stripped gold process on thin cover slides should be improved to further reduce the film roughness and the interaction of light in the glue layer. Dark field microscopy from both sides of a sphere-on-plane sample should reveal the influence of the glue layer on the optical response of a sphere-on-plane resonator. Future challenges should also resolve the origins of the resonance broadening in the single particle experiment and improve the understanding of the spacer layer. For this purpose more versatile type of molecules are already available on the basis of polyphenylene dendrimers which exhibit shape persistency and establish the necessary affinity to gold by various peripheral functional groups.

7.4 Bibliography

1. Bohren, C. F.; Huffman, D. R., *Absorption and scattering of light by small particles*. Wiley-VCH: New York, 1983.

2. Kreibig, U.; Vollmer, M., *Optical Properties of Metal Clusters,*. Springer-Verlag: Berlin, 1995.

3. Meriaudeau, F.; Wig, A.; Passian, A.; Downey, T.; Buncick, M.; Ferrell, T. L., Gold island fiber optic sensor for refractive index sensing. *Sensors and Actuators B-Chemical* **2000,** *69* (1-2), 51-57.

4. Nam, J. M.; Thaxton, C. S.; Mirkin, C. A., Nanoparticle-based bio-bar codes for the ultrasensitive detection of proteins. *Science* **2003,** *301* (5641), 1884-1886.

5. Okamoto, T.; Yamaguchi, I.; Kobayashi, T., Local plasmon sensor with gold colloid monolayers deposited upon glass substrates. *Opt. Lett.* **2000,** *25* (6), 372-374.

6. Willets, K. A.; Van Duyne, R. P., Localized Surface Plasmon Resonance Spectroscopy and Sensing. *Annu. Rev. Phys. Chem.* **2007,** *58*, 267-297.

7. Jain, P. K.; Huang, W. Y.; El-Sayed, M. A., On the universal scaling behavior of the distance decay of plasmon coupling in metal nanoparticle pairs: A plasmon ruler equation. *Nano Lett.* **2007,** *7*, 2080-2088.

8. Reinhard, B. M.; Siu, M.; Agarwal, H.; Alivisatos, A. P.; Liphardt, J., Calibration of dynamic molecular rule based on plasmon coupling between gold nanoparticles. *Nano Lett.* **2005,** *5* (11), 2246-2252.

9. Sönnichsen, C.; Reinhard, B. M.; Liphardt, J.; Alivisatos, A. P., A Molecular Ruler Based on Plasmon Coupling of Single Gold and Silver Nanoparticles. *Nature Biotechnology* **2005,** *23* (6), 741-745.

10. Krenn, J. R.; Dereux, A.; Weeber, J. C.; Bourillot, E.; Lacroute, Y.; Goudonnet, J. P.; Schider, G.; Gotschy, W.; Leitner, A.; Aussenegg, F. R.; Girard, C., Squeezing the optical near-field zone by plasmon coupling of metallic nanoparticles. *Physical Review Letters* **1999,** *82* (12), 2590-2593.

11. Quinten, M.; Leitner, A.; Krenn, J. R.; Aussenegg, F. R., Electromagnetic energy transport via linear chains of silver nanoparticles. *Opt. Lett.* **1998,** *23* (17), 1331-1333.

12. Aravind, P. K.; Metiu, H., The effects of the interaction between resonances in the electromagnetic response of a sphere-plane structure - applications to surface enhanced spectroscopy. *Surface Science* **1983,** *124* (2-3), 506-528.

13. Rendell, R. W.; Scalapino, D. J., Surface-Plasmons confined by Microstructures on Tunnel-Junctions. *Phys. Rev. B* **1981,** *24* (6), 3276-3294.

14. Ruppin, R., Surface-Modes and Optical-Absorption of a Small Sphere Above a Substrate. *Surface Science* **1983,** *127* (1), 108-118.

15. Wind, M. M.; Vlieger, J.; Bedeaux, D., The Polarizability of a Truncated Sphere on a Substrate I. *Physica A: Statistical and Theoretical Physics* **1987,** *141* (1), 33-57.

16. Nordlander, P.; Le, F., Plasmonic structure and electromagnetic field enhancements in the metallic nanoparticle-film system. *Applied Physics B-Lasers and Optics* **2006,** *84* (1-2), 35-41.

17. Johansson, P.; Monreal, R.; Apell, P., Theory for Light-Emission from a Scanning Tunneling Microscope. *Phys. Rev. B* **1990,** *42* (14), 9210-9213.

18. Fischer, U. C.; Pohl, D. W., Observation of Single-Particle Plasmonics by Near-Field Optical Microscopy. *Physical Review Letters* **1989,** *62* (4), 458-461.

19. Abe, H.; Manzel, K.; Schulze, W.; Moskovits, M.; Dilella, D. P., Surface-Enhanced Raman-Spectroscopy of CO Adsorbed on Colloidal Silver Particles. *J. Chem. Phys.* **1981,** *74* (2), 792-797.

20. Hutter, E.; Cha, S.; Liu, J. F.; Park, J.; Yi, J.; Fendler, J. H.; Roy, D., Role of substrate metal in gold nanoparticle enhanced surface plasmon resonance imaging. *Journal of Physical Chemistry B* **2001,** *105* (1), 8-12.

21. Lyon, L. A.; Pena, D. J.; Natan, M. J., Surface plasmon resonance of Au colloid-modified Au films: Particle size dependence. *Journal of Physical Chemistry B* **1999,** *103* (28), 5826-5831.

22. Tsuboi, K.; Fukuba, S.; Naraoka, R.; Fujita, K.; Kajikawa, K., Multichannel biosensing platform of surface-immobilized gold nanospheres for linear and nonlinear optical imaging. *Applied Optics* **2007,** *46* (20), 4486-4490.

23. Xu, H. X.; Kall, M., Surface-plasmon-enhanced optical forces in silver nanoaggregates. *Physical Review Letters* **2002,** *89* (24).

24. Zuloaga, J.; Prodan, E.; Nordlander, P., Quantum Description of the Plasmon Resonances of a Nanoparticle Dimer. *Nano Letters* **2009,** *9* (2), 887-891.

25. Hansma, P. K.; Broida, H. P., Light-Emission from Gold Particles Excited by Electron-Tunneling. *Applied Physics Letters* **1978,** *32* (9), 545-547.

26. Lambe, J.; McCarthy, S. L., Light-Emission from Inelastic Electron-Tunneling. *Physical Review Letters* **1976,** *37* (14), 923-925.

27. Moskovits, M.; Jeong, D. H., Engineering nanostructures for giant optical fields. *Chemical Physics Letters* **2004,** *397* (1-3), 91-95.

28. Pettinger, B.; Krischer, K.; Ertl, G., Giant Raman-Scattering Cross-Section for an Adsorbed Dye at Ag Colloids Associated with Low EM Field Enhancement. *Chemical Physics Letters* **1988,** *151* (1-2), 151-155.

29. Xu, H. X.; Bjerneld, E. J.; Kall, M.; Borjesson, L., Spectroscopy of single hemoglobin molecules by surface enhanced Raman scattering. *Physical Review Letters* **1999,** *83* (21), 4357-4360.

30. Hill, R. T.; Mock, J. J.; Urzhumov, Y.; Sebba, D. S.; Oldenburg, S. J.; Chen, S.-Y.; Lazarides, A. A.; Chilkoti, A.; Smith, D. R., Leveraging Nanoscale Plasmonic Modes to Achieve Reproducible Enhancement of Light. *Nano Letters* **2010,** *10* (10), 4150-4154.

31. Kneipp, K.; Wang, Y.; Kneipp, H.; Perelman, L. T.; Itzkan, I.; Dasari, R.; Feld, M. S., Single molecule detection using surface-enhanced Raman scattering (SERS). *Physical Review Letters* **1997,** *78* (9), 1667-1670.

32. Nie, S. M.; Emory, S. R., Probing single molecules and single nanoparticles by surface-enhanced Raman scattering. *Science* **1997,** *275* (5303), 1102-1106.

33. Holland, W. R.; Hall, D. G., Frequency-Shifts of an Electric-Dipole Resonance Near a Conducting Surface. *Physical Review Letters* **1984,** *52* (12), 1041-1044.

34. Kume, T.; Hayashi, S.; Yamamoto, K., A new method of surface plasmon excitation using metallic fine particles. *Materials Science and Engineering a-Structural Materials Properties Microstructure and Processing* **1996,** *217*, 171-175.

35. Kume, T.; Hayashi, S.; Yamamoto, K., Light emission from surface plasmon polaritons mediated by metallic fine particles. *Phys. Rev. B* **1997,** *55* (7), 4774-4782.

36. Kume, T.; Nakagawa, N.; Hayashi, S.; Yamamoto, K., Ineraction between Localized and Propagating Surface Plasmons - Ag Fine Particles on Al Surface. *Solid State Communications* **1995,** *93* (2), 171-175.

37. Hutter, E.; Fendler, J. H.; Roy, D., Surface plasmon resonance studies of gold and silver nanoparticles linked to gold and silver substrates by 2-aminoethanethiol and 1,6-hexanedithiol. *Journal of Physical Chemistry B* **2001,** *105* (45), 11159-11168.

38. Okamoto, T.; Yamaguchi, I., Optical absorption study of the surface plasmon resonance in gold nanoparticles immobilized onto a gold substrate by self-assembly technique. *J. Phys. Chem. B* **2003,** *107* (38), 10321-10324.

39. Tsuboi, K.; Abe, S.; Fukuba, S.; Shimojo, M.; Tanaka, M.; Furuya, K.; Fujita, K.; Kajikawa, K., Second-harmonic spectroscopy of surface immobilized gold nanospheres above a gold surface supported by self-assembled monolayers. *J. Chem. Phys.* **2006,** *125* (17).

40. Le, F.; Lwin, N. Z.; Steele, J. M.; Kall, M.; Halas, N. J.; Nordlander, P., Plasmons in the metallic nanoparticle - Film system as a tunable impurity problem. *Nano Letters* **2005,** *5* (10), 2009-2013.

41. Futamata, M.; Maruyama, F.; Ishikawa, M., Adsorbed sites of individual molecules on Ag nanoparticles in single molecule sensitivity-surface-enhanced Raman scattering. *Journal of Physical Chemistry B* **2004,** *108* (35), 13119-13127.

42. Futamata, M.; Maruyama, Y.; Ishikawa, M., Critical importance of the junction in touching Ag particles for single molecule sensitivity in SERS. *Journal of Molecular Structure* **2005,** *735*, 75-84.

43. Rueda, A.; Stemmler, M.; Bauer, R.; Mullen, K.; Fogel, Y.; Kreiter, M., Optical resonances of gold nanoparticles on a gold surface: quantitative correlation of geometry and resonance wavelength. *New Journal of Physics* **2008**, 113001 (22 pp.).

44. Leveque, G.; Martin, O. J. F., Tunable composite nanoparticle for plasmonics. *Optics Letters* **2006,** *31* (18), 2750-2752.

45. Leveque, G.; Martin, O. J. F., Optical interactions in a plasmonic particle coupled to a metallic film. *Optics Express* **2006,** *14* (21), 9971-9981.

46. Nordlander, P.; Prodan, E., Plasmon hybridization in nanoparticles near metallic surfaces. *Nano Letters* **2004,** *4* (11), 2209-2213.

47. Prodan, E.; Radloff, C.; Halas, N. J.; Nordlander, P., A hybridization model for the plasmon response of complex nanostructures. *Science* **2003,** *302* (5644), 419-422.

48. Rodriguez-Fernandez, J.; Funston, A. M.; Perez-Juste, J.; Alvarez-Puebla, R. A.; Liz-Marzan, L. M.; Mulvaney, P., The effect of surface roughness on the plasmonic response of individual sub-micron gold spheres. *Phys. Chem. Chem. Phys.* **2009,** *11* (28), 5909-5914.

49. Wang, H.; Halas, N. J., Mesoscopic Au "Meatball" particles. *Adv. Mater.* **2008,** *20* (4), 820-825.

50. Buffat, P. A.; Flueli, M.; Spycher, R.; Stadelmann, P.; Borel, J. P., Crystallographic Structure of Small Gold Particles Studied by High-Resolution Electron Microscopy *Faraday Discussions* **1991,** *92* (92), 173-187.

51. Butt, H. J.; Wang, D. N.; Hansma, P. K.; Kuhlbrandt, W., Effect of surface roughness of carbon support films on high-resolution electron diffraction of two-dimensional protein crystals. *Ultramicroscopy* **1991,** *36* (4), 307-318.

52. Rueda, A.; Vogel, N.; Kreiter, M., Characterization of gold films by surface plasmon spectroscopy: Large errors and small consequences. *Surface Science* **2009,** *603* (3), 491-497.

53. Johnson, P. B.; Christy, R. W., Optical Constants of Noble-Metals. *Phys. Rev. B* **1972,** *6* (12), 4370-4379.

54. Barnes, W. L., Fluorescence near interfaces: the role of photonic mode density. *J. Mod. Opt.* **1998,** *45* (4), 661-699.

55. Fuchs, R.; Claro, F., Multipolar Response of Small Metallic Spheres - Nonlocal Theory. *Phys. Rev. B* **1987,** *35* (8), 3722-3727.

56. Kolb, D. M., *Spectroelectrochemistry: Theory and Practice*. Plenum: New York, 1988.

57. Rueda, A. Optical resonances of sphere-on-plane geometries. Dissertation, Johannes Gutenberg Universität, Mainz, 2008.

58. Hayashi, S., Spectroscopy of gap modes in metal particle-surface systems. *Near-Field Optics and Surface Plasmon Polaritons* **2001,** *81*, 71-95.

59. Hu, M.; Ghoshal, A.; Marquez, M.; Kik, P. G., Single Particle Spectroscopy Study of Metal-Film-Induced Tuning of Silver Nanoparticle Plasmon Resonances. *Journal of Physical Chemistry C* **2010,** *114* (16), 7509-7514.

60. Romero, I.; Aizpurua, J.; Bryant, G. W.; de Abajo, F. J. G., Plasmons in nearly touching metallic nanoparticles: singular response in the limit of touching dimers. *Optics Express* **2006,** *14* (21), 9988-9999.

61. Lynch, D. W.; Huttner, W. R., *Handbook of Optical Constants of Solids*. Academic Press Inc.: 1985; p 275-367.

8 Fluorescence Enhancement from Individual Plasmonic Gap Resonances

8.1 Introduction

The excitation and emission rate of electronic transitions in organic dyes near nanoscopically structured metallic objects can be greatly enhanced compared to the dye alone. These enhancement effects are exploited in surface enhanced Raman scattering.[1, 2] They can be used in sensor applications,[3, 4] to increase the electro-luminescence of light emitting diodes[5, 6] or to promote the conversion of light to electric current in solar cells.[7]

Fluorescence enhancement was first observed for several dyes adsorbed directly onto silver-island films.[8, 9] The maximum luminescence yield was obtained when the dye absorption maximum coincided with the particle plasmon resonance absorption maximum, which could be shifted by varying the island film average mass thickness. Wokaun[10] provided a comprehensive overview on early work in the field. Two physical processes are assumed to be involved: First, the excitation rate of the chromophore is determined by the electrical field at its position. This field can be greatly enhanced by metal particles compared to the incident field. Second, the emission rate of the dye is also influenced by the metal. This leads to further effects - new decay channels are generated, which may not lead to detectable photons, but to energy dissipation in the metal. In addition, the rate of emitted photons can be greatly increased.[11] The latter effect is by reciprocity closely connected to the local field enhancement.[12] As long as the enhancement factor remains moderate, the intrinsic excitation and emission spectrum of the dye remains unchanged. Then, the fluorescence of the coupled dye-metal system can be modeled by taking into account the excitation field enhancement and by convoluting the emission spectrum of the free dye with the wavelength dependent enhancement of the emission due to the metal. In spite of good understanding of the involved processes, even for this weak-coupling regime, only limited experimental progress was made for quite a time. The reason was that samples with controlled metal structures and dye positions have not been available. To date, quantitative experiments as reported for a single particle interacting with a single dye[13, 14] remain the exception rather than the rule.

Nanometer-sized gaps provide very large electromagnetic field enhancements. Double spheres[15, 16] and sphere-on-plane geometries[17-19] possess such gaps with dimensions down to the sub-nanometer level. At the same time their resonance wavelength can be easily tuned, e.g. by changing the sphere diameter to match the molecules excitation and emission wavelength. As a consequence they are simple and highly efficient structures for

fluorescence enhancement measurements. Quantitative experiments on these gap resonances are of great interest since they promise maximum enhancement factors. For small gaps of less than 3 nm, physical effects beyond the weak-coupling regime are expected, representing the main motivation for the work presented in this chapter.

Already at moderate coupling the total decay rate of the excited electronic state can become comparable to the internal relaxation rate. The excited electrons in a vibrational level of the excited electronic state may then return to the ground state radiatively and not undergo thermal relaxation to a lower-energy vibrational level of the excited state from which they can make transitions to the ground state. This mechanism is called "*hot luminescence*".[9] For very strong local field enhancements, which are achievable with very small dye/metal separations, several additional physical effects should be taken into account. The local field effects may be strong enough to shift the transition frequency of the dye by a considerable amount.[12] Similarly, the dye may shift the plasmon resonance. The latter effect has been observed for dye ensembles on single plasmonic resonators.[20-22] Ultimately, coupling of single dyes to single plasmonic resonators may lead to a "*strong coupling regime*".[23] Here, a quantum-electrodynamic description is required showing energy oscillations between the plasmon and the dye accompanied by a line splitting. On small length scales the description of the metal response as bulk dielectric breaks down. For sub-nanometer gaps between metal crystallites with a diameter of 2.5 nm, significant deviations from the calculation based on the bulk material response was shown.[24, 25] Larger spheres with dielectric material in the gap are expected to show these deviations for gaps in the range of a few nanometers (Nordlander, personal communication): Instead of a full quantum treatment, corrections to the bulk metal response may be approximately described in the framework of a nonlocal (*k*-dependent) dielectric function $\varepsilon(\omega,k)$.[26] In addition, surface states play a role.[27] Finally at some stage, the modeling of the chromophores as a point dipole must be replaced by a full quantum treatment for small dye/metal separations.[28] Truly quantitative experiments in these regimes require the defined placement of dyes relative to the enhancing metal structure.

In the following experiments, a silver "sphere-on-plane" (SOP) geometry is introduced which appears promising for this purpose. A perylene diimide loaded polyphenylene dendrimer in generation 2 (PDI-G2) serves both as a spacer and chromophore bearing unit (Figure 8.1 (a)). The dendrimer in the shell with only phenyl-phenyl linkages accounts for an outstanding rigidity and consequently exhibits strong shape persistency[29] while being optical inactive.[30] The 16 peripheral dithiolane rings establish the necessary affinity for binding to the silver substrate and the silver particles on top. The chromophore in the core can be accordingly placed with nanometer precision in the gap between the metallic structures. The selected perylene dye itself stands out in terms of photostability and fluorescence quantum yield.[31, 32]

On a single object basis, the fluorescence from these structures is investigated and correlated with both plasmonic resonances obtained by dark-field microscopy and particle shape obtained by scanning electron microscopy. A reproducible enhancement is found as well as several spectral features, which appear to be unique for the presented system. Although, these observations cannot be uniquely assigned to any described mechanism in the strong-coupling regime, the presented system provides several promising starting points for further experimental and theoretical investigations and can be regarded as an important step toward full quantitative experiments.

8.2 Results and Discussion

The investigated sphere-on-plane system with the perylene dye in the gap is presented in Figure 8.1. A monolayer of the PDI-G2 as depicted in (a) covers the silver film and serves as a spacer for additional silver particles. (b) illustrates the spacer region with the dendrimers shown as elliptical particles. In (c) a to-scale sketch is shown assuming a spacer layer with a thickness of 2.5 nm and a silver sphere with a radius of 40 nm. Details on the preparation of silver sphere-on-plane resonators, using the PDI-G2 as spacer layer, are given in the experimental section 3.1.9.

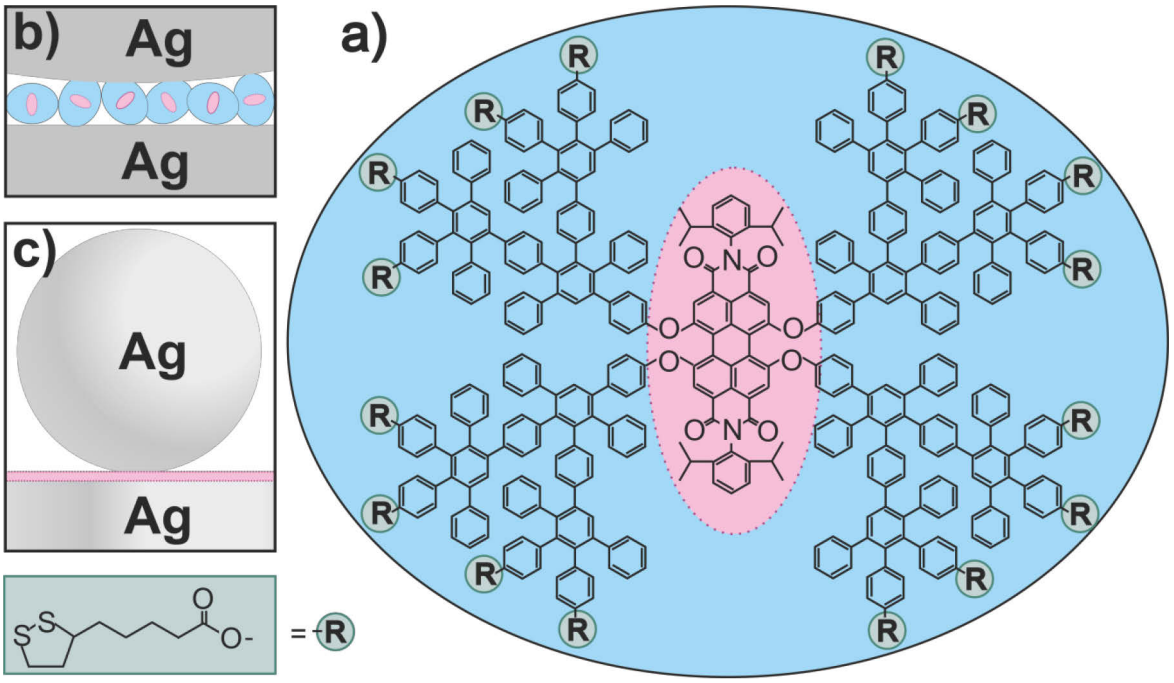

***Figure 8.1**: (a) Dendrimer PDI-G2, (b) sketch of the gap region, (c) geometry of the sphere-on-plane-system with a 3 nm spacer and 80 nm sphere (to-scale)*

In Figure 8.2 (a) the fluorescence of PDI-G2 in a THF solution is displayed for different excitation wavelengths between 400 and 700 nm. The diagonal line results from scattering of the illumination light. In (b) the emission spectrum for an excitation of 405 nm is

displayed. This spectrum is used in the following discussion as comparison for the single object spectra in the sphere on plane system depicted in Figure 8.1.

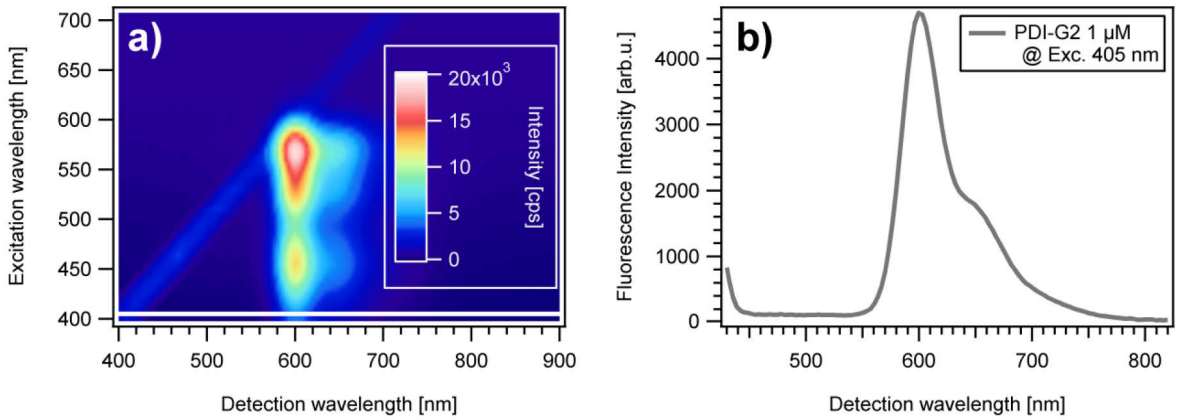

Figure 8.2: *(a) Fluorescence as a function of excitation and emission wavelength for a 1 µM solution of PDI-G2 in THF, (b) emission spectra for an excitation at 405 nm*

8.2.1 Particle Identification with Size Determination

The identification procedure, described in the experimental section 3.2.3, is illustrated with the help of Figure 8.3.

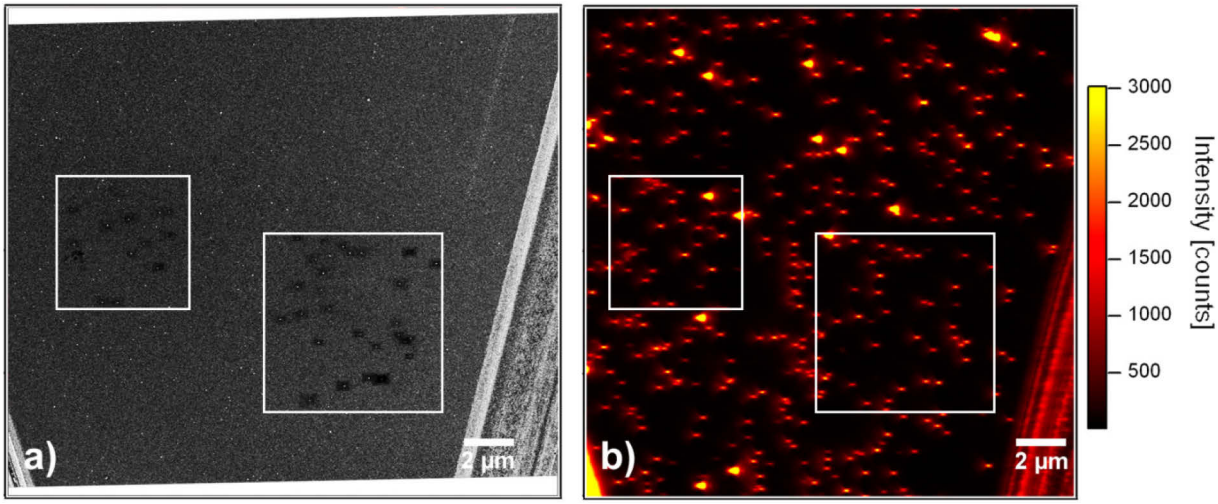

Figure 8.3*: (a) Scanning-electron micrograph, (b) corresponding scattering image; the white squares are the areas where the particles were measured*

First, all objects are measured in the confocal microscope at the position of the two scratches (b), then the sample is taken to the SEM and the area of interest is identified by looking for the intersection of the two scratches (a). The scratches on the surface are seen in both images and fit perfectly together when comparing their position, distance and opening angle. The particles appear as individual bright spots in the confocal scattering image and as tiny white dots in the SEM. All analyzed particles reside inside the two white squares.

Figure 8.4 shows the area of the right square with a size of 25 x 25 µm^2 seen by electron microscopy, scanning confocal fluorescence microscopy and scanning dark-field microscopy. Note the excellent one-to-one correspondence between the objects in all microscopic methods seen by electron microscopy (a) and the bright spots in fluorescence (b) and scattering mode (c) of the confocal microscope. These objects are identified as surface bound silver particles by increasing the magnification in the electron microscope. Areas without particles show only very little fluorescence.

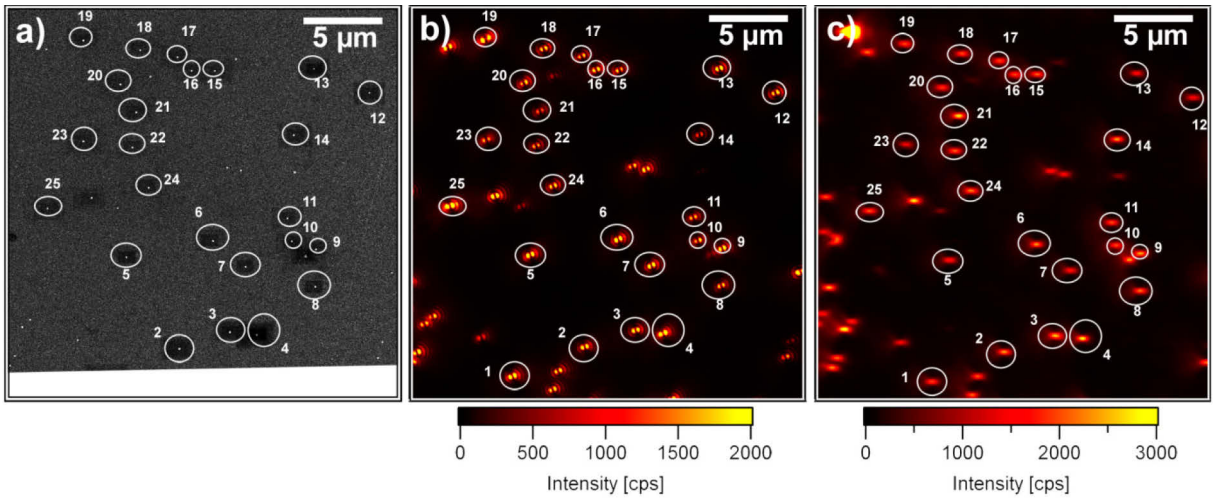

Figure 8.4: *(a) Scanning electron micrographs of the right square under investigation, (b-c) corresponding fluorescence and scattering images*

This indicates that all dye molecules are very close to the surface since they are almost perfectly quenched if not decorated by a particle. A surface bound silver particle on top leads to an effective "*de-quenchi*ng" of the dye and visible radiation is emitted. All particles show a signal which verifies that dye molecules are located under each of them. In (c) the unusual bright spot in the top left, showing no fluorescence in (b), is a depression in the silver film. A magnified image of it is shown in Figure 8.5 (b) together with images of the left square in all microscopic methods. The particles in the fluorescence images show the typical patterns for dipoles excited normal (z-axis) to a metallic surface.[33] This response is expected for the vertical resonance of the SOP-system, which is accompanied by a large field-enhancement in the gap.[17-19] The scattering in (c) can be assigned to z-dipoles as well. They appear as individual dots in the particular imaging mode used here, but can be uniquely identified as vertical dipoles since upon illumination with the appropriate polarization they display similar double-lobe patterns as seen in the fluorescence images. This was already demonstrated for a gold sphere-on-plane system in Chapter 5.3 for a polarization direction of the excitation light parallel to the block.

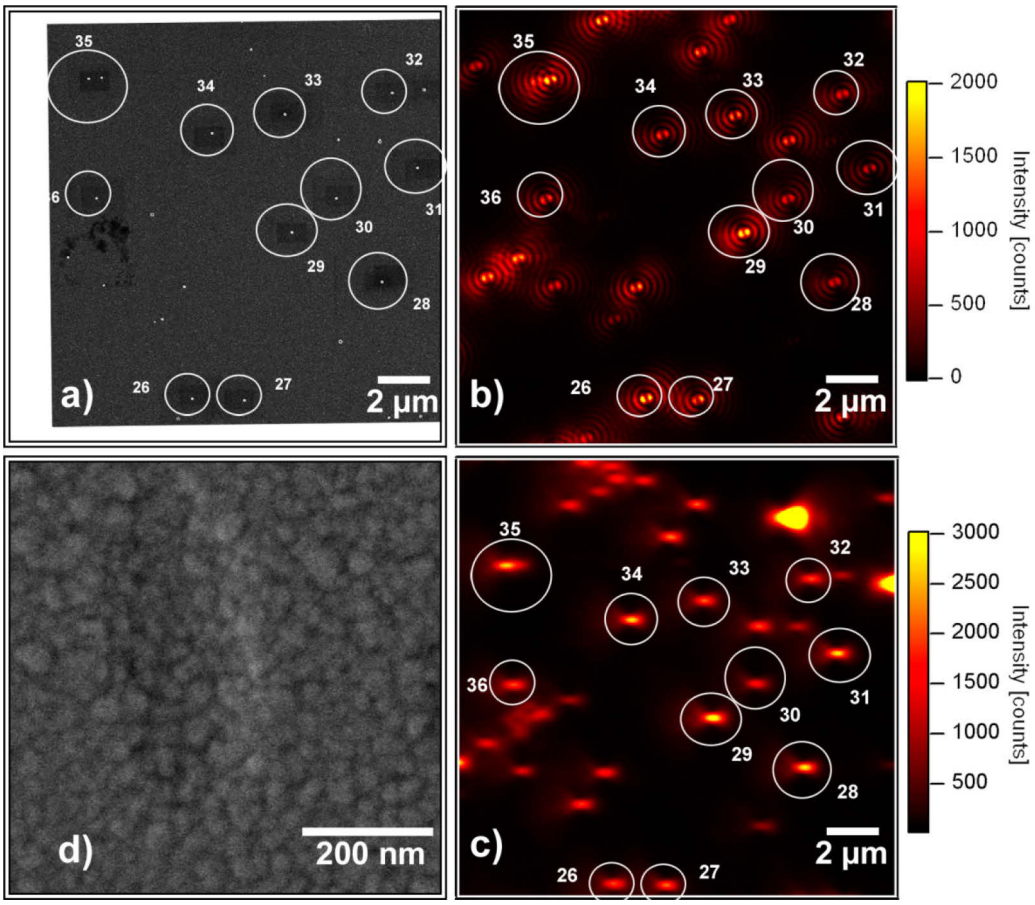

Figure 8.5: *(a) Scanning-electron micrograph of the left white square, (b) corresponding fluorescence image and (c) corresponding scattering image, (d) depression in the silver film*

An additional example for a silver particle on top of a silver film is shown for the object with the number 28 in Figure 8.6. In the presented case the excitation wavelength is 633 nm. Under consideration of the calculated patterns in Chapter 5.5 the shape of the patterns is reproduced very well.

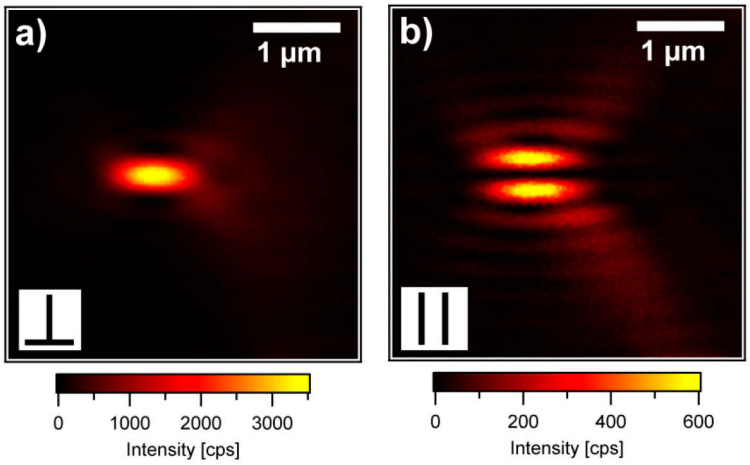

Figure 8.6: *Dark-field scattering signals from silver particle 28 (d=82 nm) for incident light of λ = 633 nm polarized perpendicular (a) and parallel (b) to the block edge.*

8.2.2 Scattering and Fluorescence Spectroscopy

In order to quantify the optical response of the SOP resonators, fluorescence and scattering spectra for the 36 tagged particles were recorded. For the scattering measurements the confocal microscope was used in a dark-field configuration as sketched in Figure 8.7. By placing two polarizers perpendicular to each other in the excitation (to the block edge) and detection pathway (to block edge) the z-dipoles of the sphere-on-plane resonators can be selectively detected as was theoretically demonstrated in Chapter 5.5. For the fluorescence measurements the block is removed and the polarizer in the detection pathway is replaced by the fluorescence filters.

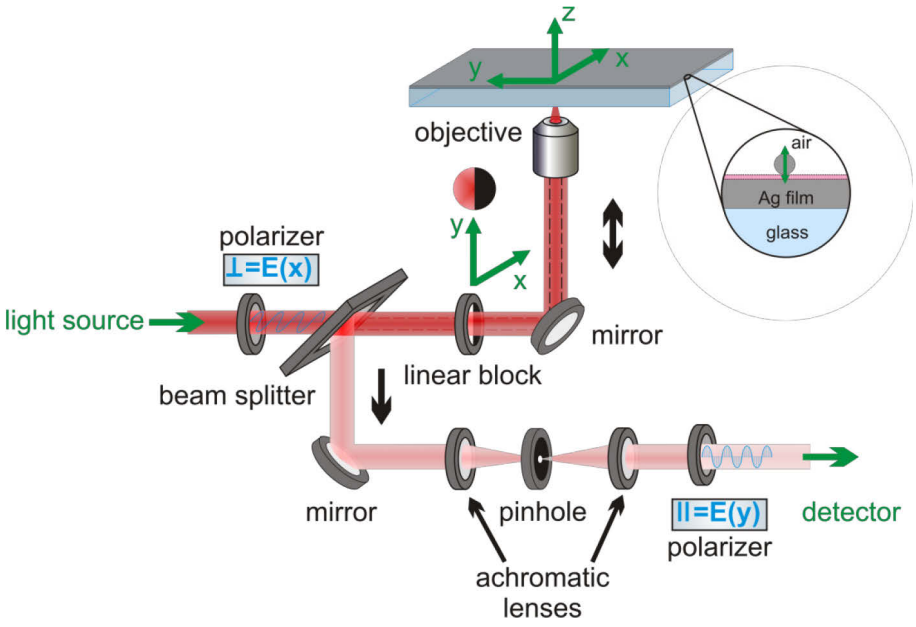

Figure 8.7: *Schematic representation of a dark field microscope with two perpendicular polarizers in the excitation and detection pathway*

A representative selection of fluorescence (red) and scattering spectra (black) obtained in such a way are presented in Figure 8.8 together with the emission spectrum of the dye in solution for comparison (gray) and a magnified electron micrograph. Please note that all individual particles are presented in Appendix 10.6 and are taken into account for the following discussion. The fluorescence signal of an uncovered position in the vicinity is displayed as a reference (blue). The sharp maximum at a wavelength of 532 nm originates from the illumination light. The scattering intensities are all scaled to the same value while the fluorescence intensities are scaled for optimum visibility. One can distinguish two classes of resonators by visual inspection of the scattering spectra. First, the ones showing two pronounced resonances at around 450 nm and around 600 nm, respectively, separated by a clear minimum. Around 50% of all particles (17 of 36) exhibit this behavior. In Figure 8.8 these resonators are represented by (a-c). Second, the other group of particles (19 of 36) with a different scattering response which are depicted in Figure 8.8 (e-f). In (d) an

ambiguous case is illustrated. It shows two clear peaks, but the long-wavelength peak at 530 nm is far blue-shifted relative to all SOP-like resonators which is the reason not to assign it to the first group.

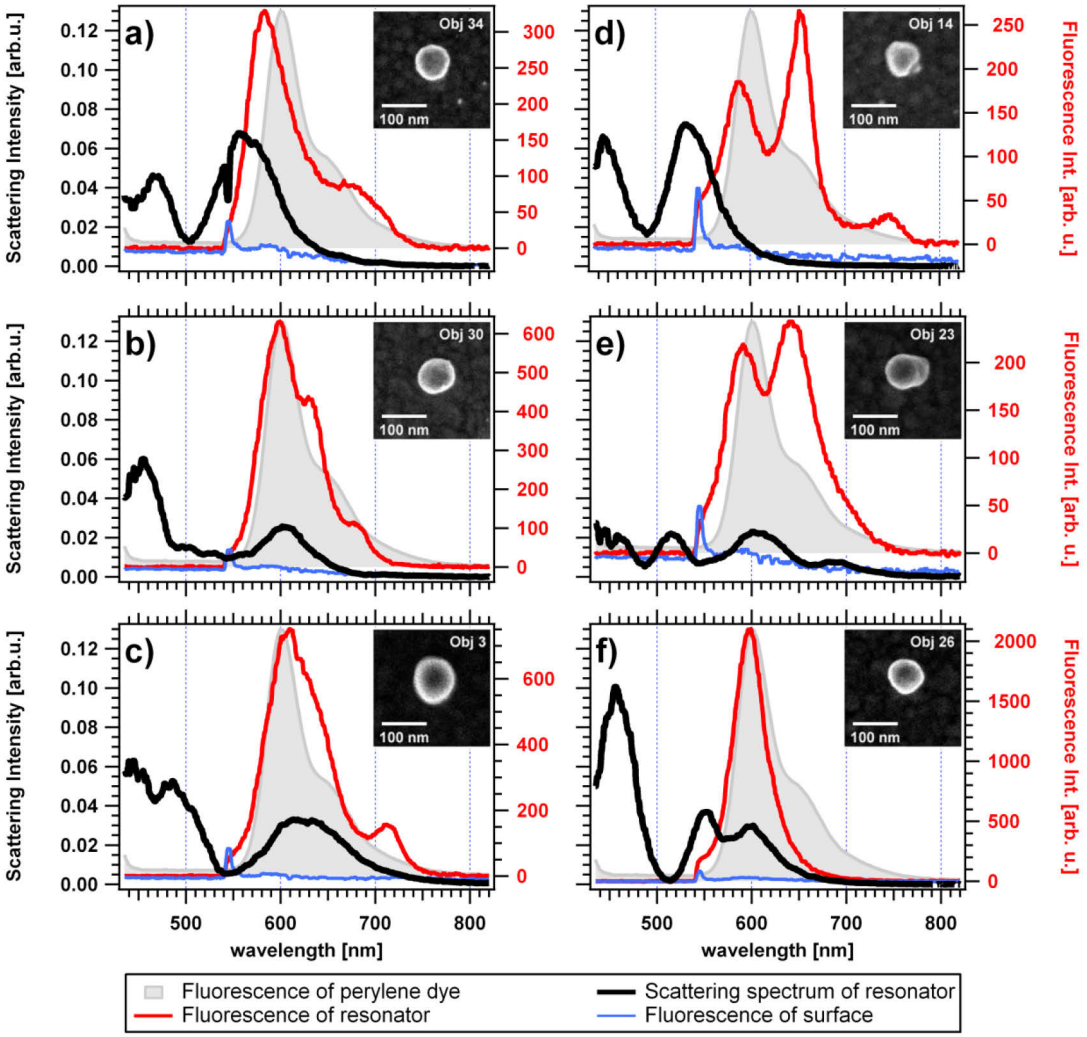

Figure 8.8: *Fluorescence spectra of particle positions, compared to the background fluorescence signal, the emission spectrum from the dye in solution at an excitation wavelength of 405 nm is shown in gray. The black curves are all scaled to the same maximum value and show the scattering signal of the particles which are presented top right.*

8.2.3 Scattering and Comparison to the Calculated Gap Resonance

A calculation for a silver SOP system with a homogenous dielectric environment using the quasistatic model from Wind *et al.*[34] is displayed in Figure 8.9. The imaginary part of the polarizability displays a peak at 580 nm and some additional peaks at wavelengths below 450 nm. They may be attributed to a fundamental (longer wavelength) and higher order resonances. Experimentally, the fundamental resonance is clearly seen in Figure 8.8 (a-c). The variations in peak wavelength from 560 nm to 640 nm are representative for all investigated particles. The different proportions of the fundamental and higher order peaks

in theory and experiment are related to the wavelength-dependent response in plasmon-mediated dark field microscopy which decreases its efficiency with increasing wavelength.

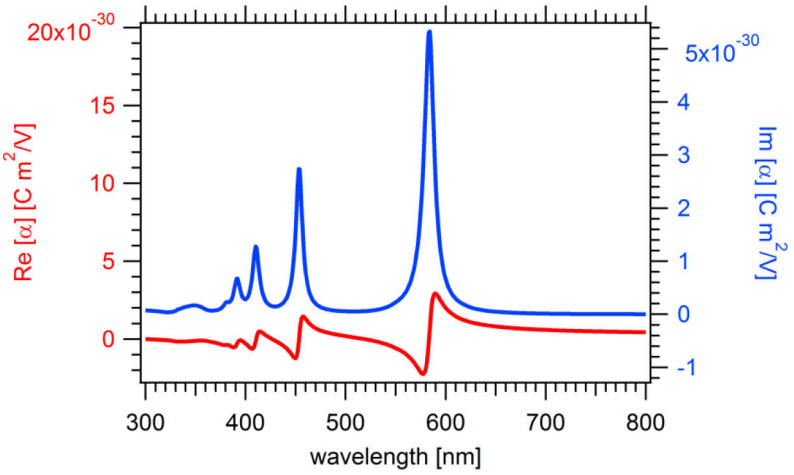

Figure 8.9: *Calculation with Wind's equation[34] for a sphere with r=40 nm in a distance of 2.5 nm to the film and a homogenous environment of ε=2.25. The ε values for silver are from Johnson and Christy.[35]*

The full width at half-maximum (FWHM) for the fundamental resonance ranges from 57 to 98 nm in the experiments and is significantly larger than predicted from the calculation (15 nm). Since inhomogeneous broadening can be excluded for single-particle experiments, a significant deviation of the presented system is observed from the response expected for a perfect SOP system. While one can only speculate about the physical mechanisms it can be noted that this increased resonance width points to a lower quality factor of the resonance and therefore may result in much lower local field enhancements than suggested by calculations. In the literature different values for the dielectric function of silver can be found. For example, in the book of Palik[36] significantly higher damping factors are quoted as can be seen in Figure 8.10 (b).

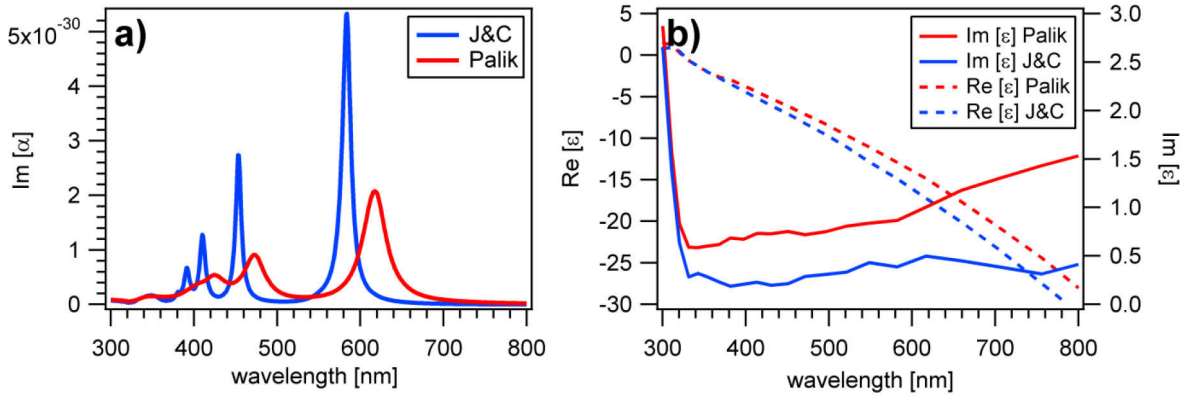

Figure 8.10*: (a) Polarizability for different dielectric functions stated by Johnson and Christy[35] and Palik[36], (b) real and imaginary part of the literature values*

A comparison of the calculation for the imaginary parts using these two different dielectric functions is presented in Figure 8.10 (a). The higher damping leads to a calculated resonance

width of 35 nm, which is more than double of that found for the dielectric function stated by Johnson and Christy, but is still below the determined experimental values. Measurements of the dielectric function are necessarily performed on non-perfect samples and therefore can be regarded as an upper limit for damping.[37] Therefore the data from Johnson and Christy is selected as the better choice.

The features seen experimentally below 500 nm are tentatively assigned to the higher-order peaks predicted by theory. Their positions show strong variations, but again they are much broader than predicted with the same consequences as for the fundamental. Please note that they do not contribute to the fluorescence enhancement since they occur at a wavelength far away from the emission of the particular dye studied here. The calculation clearly demonstrates that the first group of resonators in Figure 8.8 (a-c) exhibit a behavior which is expected for a silver sphere on-plane system. Therefore, they are grouped into the category “SOP-like resonators”. The individuals in Figure 8.8 (e-f) clearly exhibit a different behavior and show more resonances at different wavelength positions with no apparent correlation to the particle shape. They are consequently grouped into the category “non-SOP like resonators”. The observed variations may originate from different shapes of the gap between the metallic structures, which is not accessible by our methods and underline together with the large variation in peak wavelength for the “SOP-like” scatterers the importance of a single object-analysis.

8.2.4 Fluorescence and Modification of the Excitation Wavelength

The fluorescence spectra differ from the emission spectrum of the chromophore in solution. Of particular interest is the appearance of photons at wavelengths below 560 nm where the free chromophore does not emit at all. This emission is not only reproducible for different individuals, but also for different excitation wavelengths and different samples. In Figure 8.11 this is shown for a second sample which was completely characterized and illuminated with excitation wavelengths of 514 nm and 532 nm. The spectra are very similar for the two different wavelengths and the dye does not show significant bleaching after two images and spectra with an integration time of 30 s.

This modification of the fluorescence emission spectra by coupling to plasmonic resonances is assigned to *hot luminescence* from higher vibrational levels of the electronic excited state.[9] Since higher vibrational levels are excited with excitation light of shorter wavelength this feature is better visible for an excitation with 514 nm. It suggests that the PDI-G2 emission is enhanced to such an extent that the electromagnetic decay rate is at least of the same order as the vibronic relaxation, which occurs on the picosecond timescale.

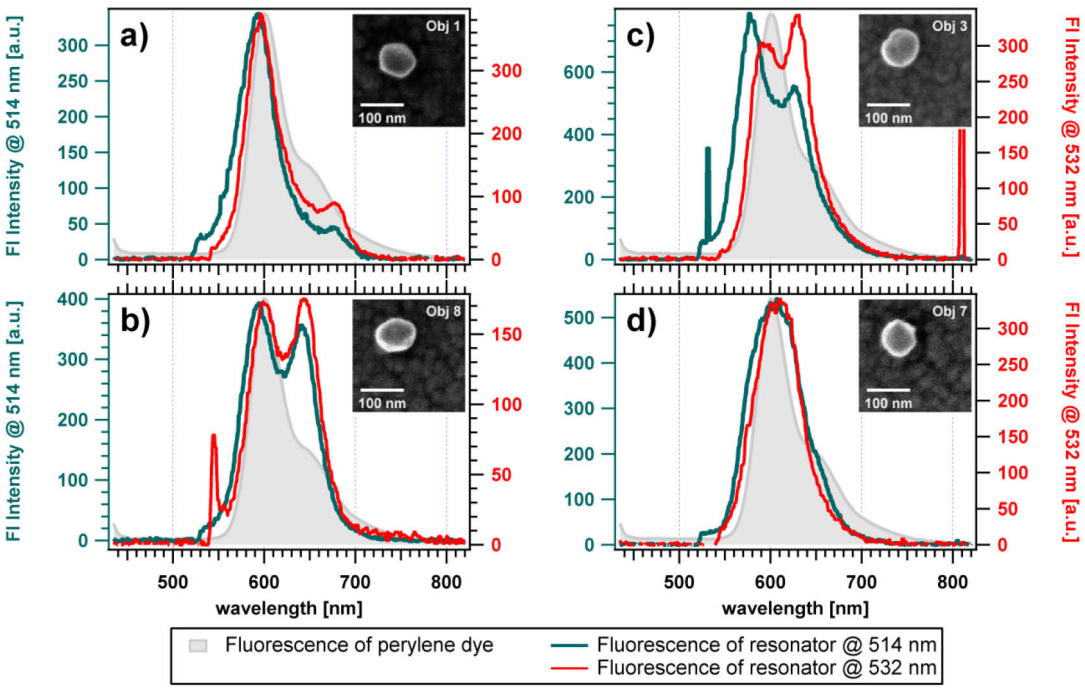

Figure 8.11: *Reproducibility of the spectra for two different excitation wavelengths, fluorescence emission for an excitation with 514 nm in green and an excitation with 532 nm in red.*

On the red side above 700 nm the emission spectra in Figure 8.8 and Figure 8.11 show in most cases less fluorescence than the free dye. This is true for 30 of all 40 characterized particles and is most probably due to the absence of a plasmonic resonance at this wavelength region. In some cases also additional fluorescence peaks appear on the right side of the spectrum. This observation cannot be explained in terms of *hot fluorescence* which manifests itself in a blue-shifted emission. This is a first hint for additional effects which have to be taken into account. For the SOP-like samples in Figure 8.8 (a-c) the fluorescence emission peak maximum shifts along with the scattering resonance from 593 nm to 609 nm. This can be experimentally understood in terms of a wavelength dependent enhancement of the dye fluorescence by the plasmonic resonance, assuming that the scattering spectrum roughly represents the wavelength dependent enhancement factor.[38, 39] For the non-SOP-like resonators in Figure 8.8 (d-f) the fluorescence signals show strong spectral variations. Both the strongest and the weakest fluorescing individuals are found in this class of resonators. The wavelength positions at maximum fluorescence vary from 588 nm up to 650 nm.

8.2.5 Estimation of the Fluorescence Enhancement Factor

An enhancement factor is first calculated by comparing the intensity from molecules on the clean film with molecules enhanced by a SOP resonator bearing in mind the different involved areas of the particle and the focal spot. The focal area A_{Foc} is larger than the area A_{Part} covered by the particle what can be derived from the microscope images and is

displayed in Figure 8.12 (a) in a to-scale cartoon. For the approximation it is further assumed that the complete fraction of dyes which are under the projection of the particle on the surface is enhanced. This is certainly a conservative estimate since the gap area A_{gap} is smaller, see Figure 8.12 (b) and (c).

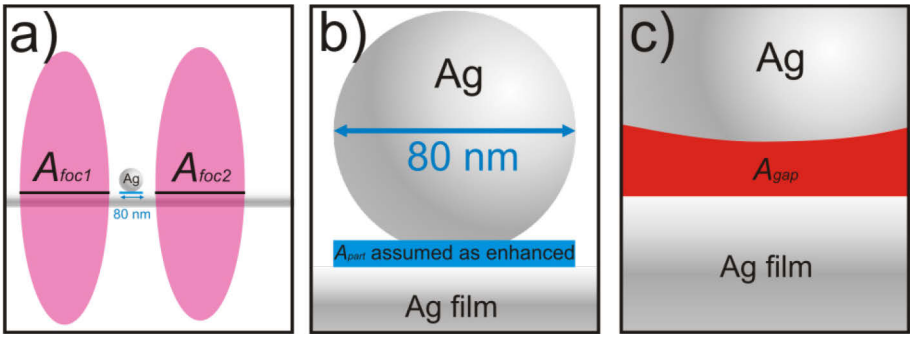

Figure 8.12:*(a) Focal area from the fluorescence image patterns, (b) area assumed to be enhanced, (c) gap area*

The enhancement factor is determined from the measured intensities of the characterized particles in the following way:

$$I_{Bg} = I_0 \cdot A_{Foc} \tag{8.1}$$

$$I_{Part} = I_0 \cdot EF \cdot A_{Part} + I_0 \cdot \left(A_{Foc} - A_{Part}\right) \approx I_0 \cdot EF \cdot A_{Part} \tag{8.2}$$

where I_0 is the intensity of the non-decorated dye. The intensity I_{Part} is obtained from the maximum fluorescence signal of a silver particle and the background intensity I_{Bg} from an uncovered part of the surface. Dividing equations (8.1) and (8.2) yields the enhancement factor EF:

$$EF = \frac{A_{Foc}}{A_{Part}} \cdot \frac{I_{Part}}{I_{Bg}} \tag{8.3}$$

A_{Part} is obtained by SEM and is typically around 5000 nm^2. A_{Foc} represents the size of the focal area for the laser beam at the silver interface. It is estimated from the confocal fluorescence images as the area where the intensity exceeds half the maximum intensity of the pattern, see Figure 8.13 as example. Here an average value of 73548 nm^2 is obtained. The average background signal I_{Bg} is estimated from the reference fluorescence spectra for all particles as 10. In some spectra this value is reached, other reference spectra show significantly less fluorescence below the detection limit of the spectrometer. If the former is assigned to enhancements due to some random roughness on the silver surface, this implies an even lower “true” background and a correspondingly stronger enhancement factor. The values for I_{Part} are obtained from the maximum fluorescence signal in the emission spectra and varied from 200 to 2000. By taking into account all these values an average

enhancement factor of around 1100 is estimated for the particle covered dye in comparison to the strongly quenched dye on the silver surface.

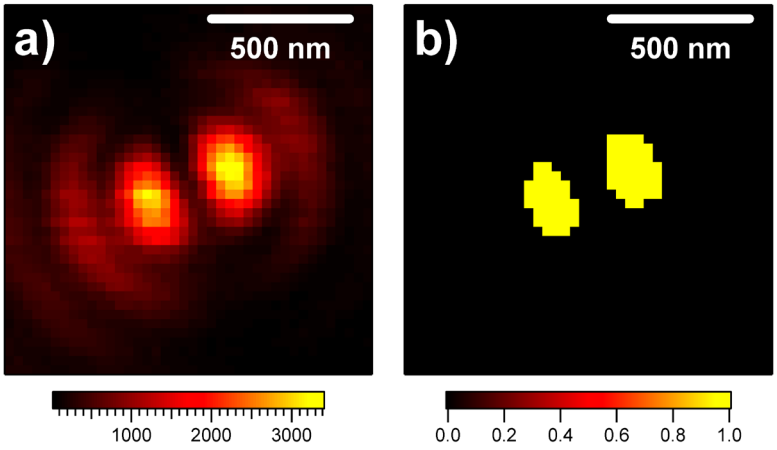

Figure 8.13: *a) Fluorescence pattern at 532 nm wavelength excitation, b) intensity pattern which exceeds half the maximum intensity and was assumed as the size of the focal area* A_{Foc}.

Another important reference is the brightness of the unquenched chromophore on a pure glass substrate which is completely independent from the quenching efficiency of the metal film. Here the single molecule fluorescence of the PDI-G2 is analyzed by diluting a solution of PDI-G2 from 1 µM to 0.1 pM and spin coating an aliquot of each solution on a cleaned cover glass. The images can be seen in Figure 8.14 (a-d).

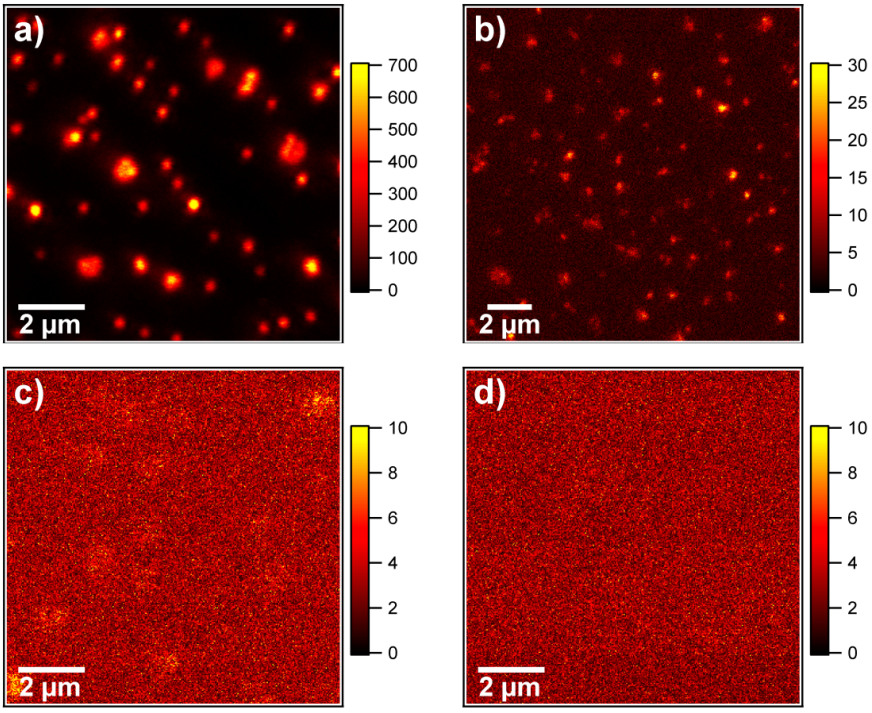

Figure 8.14: *(a) Fluorescence of a 0.1 µM solution of PDI-G2 spin-coated on glass, (b) diluted to 1.0 nM, (c) diluted to 10 pM and (d) diluted to 0.1 pM, in this case no fluorescence is seen at all. Please note the different scaling.*

In (a) for the 0.1 µM solution aggregates of the dye show a very high fluorescence intensity while in (d) for the 0.1 pM solution no fluorescence is detected. This image can act as a control that no additional impurities were added during the dilution process. In (b) for a concentration of 1 nM the typical local bleaching of single molecules along the horizontal scan direction is seen in some examples. The patterns also experience the asymmetric shape of single molecules and are in great contrast to what is expected for light focused through the silver film, because the longitudinal component of the electric field on glass is considerably weaker than the in plane component. The average sum of the intensity for a single molecule corrected by the background is around 2100. The figure in (c) nearly no fluorescence from the dye is observed.

The ratio of the intensities for a dye coupled to metal and the free dye is subsequently estimated by a comparison of the single molecule fluorescence on glass with the average fluorescence intensity in the sphere-on-plane systems:

$$\frac{I_{SOP}}{I_{SM,F}} = \frac{n \cdot I_{SM,E}}{I_{SM,F}} \tag{8.4}$$

I_{SOP} is the average sum of the focal intensity for all molecules inside the calculated active area from the previous calculation under the particles, but corrected by the background signal. An average value of the measured ensemble of 555300 is estimated. *n* is the number of dye molecules in this active area, estimated as 250 dendrimers for molecules with a diameter of 5 nm while $I_{SM,E}$ is the contribution to the whole enhanced fluorescence of a single dye molecule under the particles. $I_{SM,F}$ is the average sum of the intensity patterns for the single molecules of the dendrimer on glass and determined on different sites in Figure 8.14 (b). Dividing by the number of dye molecules n and defining the ratio of $I_{SM,E}$ and $I_{SM,F}$ as the total enhancement factor Γ_E the following equation is obtained:

$$\Gamma_E = \frac{I_{SM,E}}{I_{SM,F}} = \frac{1}{n} \cdot \frac{I_{SOP}}{I_{SM,F}} \approx 1.06 \tag{8.5}$$

This factor leads to the conclusion that the enhancement in the gap is so strong that the quenching of the metal at the rest of the film is fully compensated and that the single molecule fluorescence in a sphere-on-plane system is as effective as on glass. This is only a very rough estimation and there are significant errors involved, but at least the dimensions should be correct.

8.2.6 Additional Features and Data Correlation

In Figure 8.15 all emission spectra for the 36 individuals are summarized in one graph. The SOP-like resonators are displayed in dotted lines, the non-SOP-like with solid lines. There are clear emission lines at wavelengths found which differ from resonator to resonator.

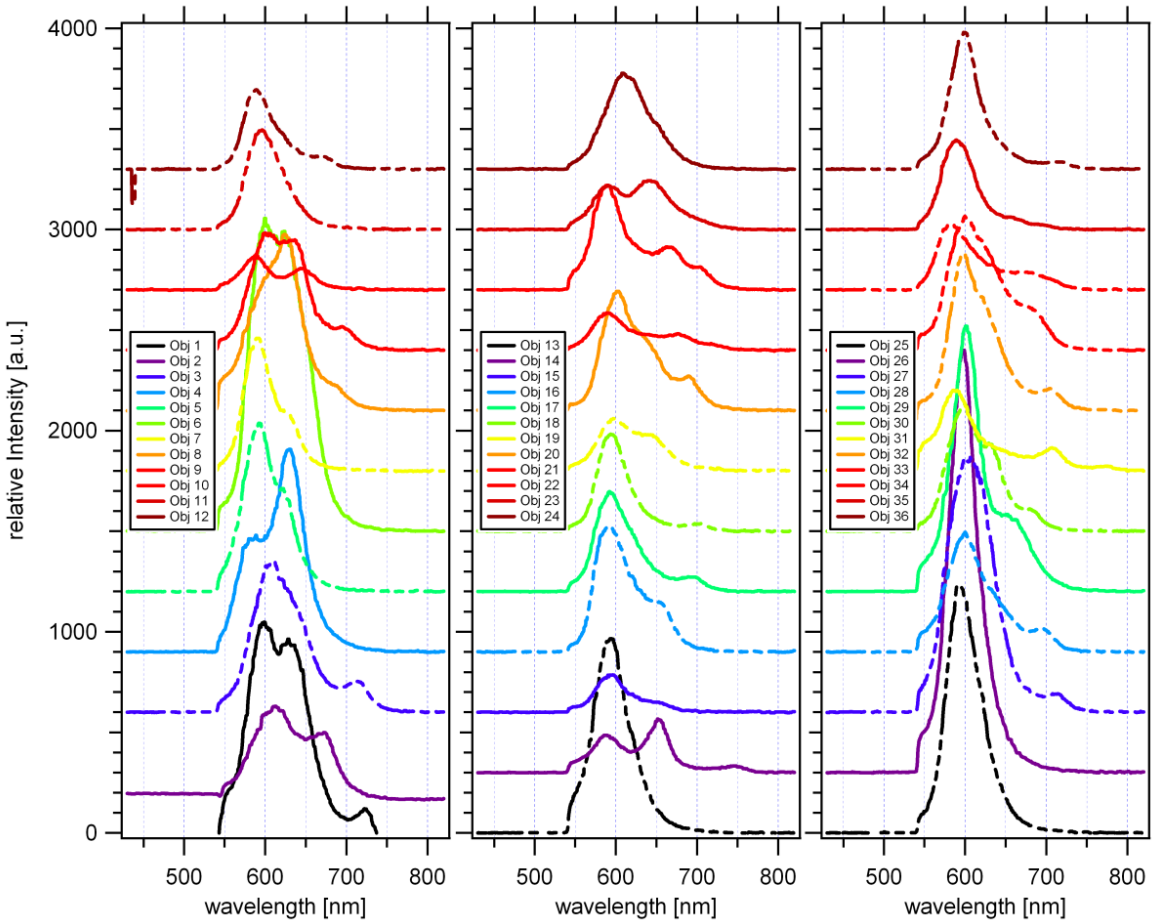

Figure 8.15: *Fluorescence emission spectra of all particles. The SOP-like resonators are displayed in dotted lines, the non-SOP-likes with solid lines.*

This behavior differs from the enhancement of individual transitions at a few well-defined wavelengths as observed by Ringler *et al.*.[39] There, the enhancement could be described in terms of a constant emission spectrum of the dye and a resonator-specific enhancement. Here, the exclusive emission from the gap is seen where the perturbation of the dye by the nearby silver is so strong that the found lines occur at different wavelengths for each resonator. This remarkable feature cannot be uniquely assigned to a specific physical effect, but strong coupling as discussed in the context of surface enhanced Raman scattering (SERS)[21, 22] as well as strong spectral shifts due to a high local density of states (LDOS)[12] may play a role here. For these non-SOP-like resonators, an average enhancement factor around 1000 is calculated taking again the quenched dye as the reference. Light-induced fragmentation of the chromophores in the gap cannot be excluded at these high field enhancements, although the accelerated emission is known to balance this effect and lead

to enhanced stability. Finally one has to rely on experimental evidence that the system is stable and that the spectral variations are not due to photoproducts. It was estimated that approximately 250 chromophores reside inside the gap and contribute to the signal. Assuming the different spectra were due to photofragments all molecules in one resonator should undergo the same photoreaction. At the same time the photoreactions in different resonators would be different. Furthermore, the stability of individual resonators was studied under typical experimental conditions as was shown in Figure 8.11. No changes were seen for the intensities and integration times used in the experiment.

In spite of strong individual variations the ensemble of investigated resonators shows some effects which are in agreement with the predictions of "classical" fluorescence enhancement. They can be observed by correlating characteristic parameters that are obtained from the scattering and fluorescence spectra and electron microscopy. The maximum fluorescence intensity, the wavelength where the maximum is seen, the maximum scattering intensity, the related wavelength and the particle area are considered. Plots of all 10 possible combinations of these 5 parameters are shown again in Appendix 10.6. In many cases no clear trend is seen. Figure 8.16 shows four combinations where a trend can be derived.

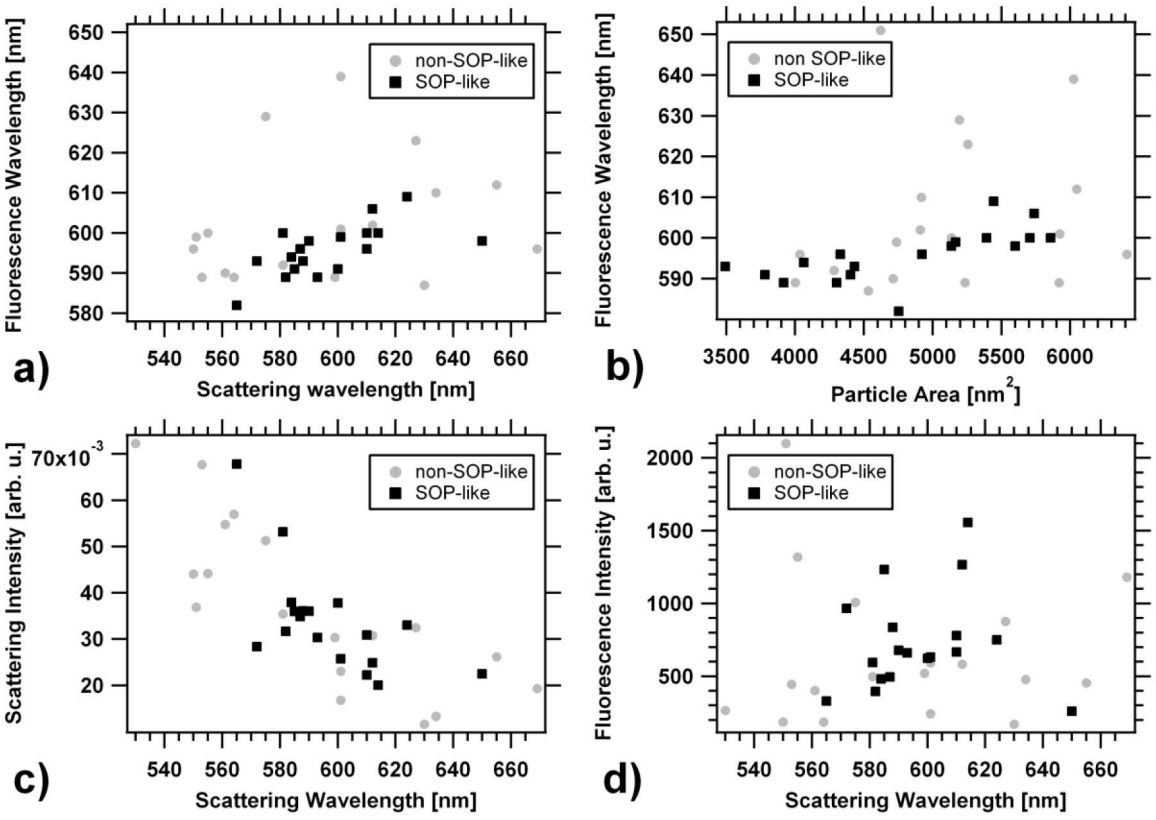

Figure 8.16: *Correlation plots. (a) Fluorescence wavelength versus scattering wavelength, (b) fluorescence wavelength versus particle area, (c) scattering intensity versus scattering wavelength, (d) fluorescence intensity versus scattering wavelength. The two classes SOP-like and non-SOP-like resonators are marked with different symbols.*

In (a) the wavelength of the scattering maximum correlates with the wavelength of the fluorescence maximum. This is expected for plasmonic resonators with a wavelength dependent emission enhancement which roughly coincides with the scattering spectrum. In spite of some scatter the correlation for the SOP-like resonators is obvious. Such behavior could already be inferred from Figure 8.8 (a-c), where the wavelength of maximum fluorescence emission follows the scattering maximum. For the non-SOP-like resonators, strong individual differences are seen indicating that a description in terms of a one-to-one correspondence between the scattering spectrum and the enhancement spectrum is too simplified. The variation between the individuals can be partly assigned to the different sizes of the silver particles (area from 3500 to 6400 nm^2). This becomes evident from a weak correlation between the particle size and the wavelengths of maximum fluorescence and scattering as seen in Figure 8.16 (b). A considerable scattering in the data, in particular for the non-SOP cases, points to additional factors, e. g. the nanostructure in the gap region influencing the plasmonic resonance. In (c) a decrease in the scattering intensity with increasing wavelength is seen. This is a consequence of the wavelength dependent sensitivity of the dark-field microscopy using the intermediate excitation of surface plasmons in the film for enhancement. In (d) an efficient enhancement of the fluorescence is visible for scattering wavelengths between 600 and 620 nm, which correspond to the emission of the free PDI-G2 in solution. From these correlations one can get some impression of the information an ensemble experiment would provide. Here, the strong individual differences would be averaged out and only comparably weak trends would be visible.

8.3 Summary and Outlook

A well-defined silver sphere-on-plane system has been presented where a perylene diimide dye could be placed in a defined position between a silver sphere and a silver plane due to the rigidity and shape persistency of the dendrimer shell. The selected geometry allowed the study of the fluorescence behavior of the dye in the resulting gap on a single object basis. The fluorescence was quenched on the metallic film while a strong signal was observed for each particle position. The fluorescence emission profile was modified and showed a significant emission on the blue side, which was assigned to *hot luminescence*. The maximum fluorescence emission peak shifted along with the scattering maximum of the plasmonic resonance. From the scattering response, two classes of resonators could be distinguished. SOP-like resonators could be identified, roughly agreeing with theoretical calculations assuming a perfect geometry. About half of all investigated objects were non-SOP-like and differed strongly from the ideal case. For the SOP-like resonators a fundamental and higher order peaks in the scattering response could be seen. Their positions agreed with theory while their full-width at half maximum was significantly broader than predicted. Strong

modifications of the dye emission spectrum were observed which seemed to involve physical mechanisms beyond a simple wavelength-dependent enhancement factor.

In future research it would be desirable to resolve the origins of the resonance broadening and the geometrical reasons why a particular resonator behaves as “non-SOP-like”. Furthermore, experiments on the dye lifetimes in the gap should be performed to investigate the origins of the fluorescence profile modifications.

8.4 Bibliography

1. Kneipp, K.; Moskovits, M.; Kneipp, H., *Surface-Enhanced Raman Scattering: Physics and Applications*. 1st ed.; Springer: Berlin, 2006; Vol. 103.

2. Xu, H. X.; Wang, X. H.; Persson, M. P.; Xu, H. Q.; Kall, M.; Johansson, P., Unified treatment of fluorescence and Raman scattering processes near metal surfaces. *Phys. Rev. Lett.* **2004,** *93* (24), 243002/1-243002/4.

3. Aslan, K.; Gryczynski, I.; Malicka, J.; Matveeva, E.; Lakowicz, J. R.; Geddes, C. D., Metal-enhanced fluorescence: an emerging tool in biotechnology. *Curr. Opin. Biotechnol.* **2005,** *16* (1), 55-62.

4. Lakowicz, J. R., Radiative decay engineering: Biophysical and biomedical applications. *Anal. Biochem.* **2001,** *298* (1), 1-24.

5. Fedutik, Y.; Temnov, V. V.; Schops, O.; Woggon, U.; Artemyev, M. V., Exciton-plasmon-photon conversion in plasmonic nanostructures. *Phys. Rev. Lett.* **2007,** *99* (13), 136802/1-136802/4.

6. Koller, D. M.; Hohenau, A.; Ditlbacher, H.; Galler, N.; Aussenegg, F. R.; Leitner, A.; Krenn, J. R.; Eder, S.; Sax, S.; List, E. J. W., Surface plasmon coupled electroluminescent emission. *Appl. Phys. Lett.* **2008,** *92* (10), 103304/1-103304/2.

7. Hayashi, S.; Kozaru, K.; Yamamoto, K., Enhancement of Photoelectric Conversion Efficiency by Surface-Plasmon Excitation - A Test with an Organic Solar-Cell. *Solid State Commun.* **1991,** *79* (9), 763-767.

8. Glass, M.; Liao, P. F.; Bergman, J. G.; Olson, D. H., Interaction of metal particles with adsorbed dye molecules: absorption and luminescence. *Optics Letters* **1980,** *5* (9), 367-370.

9. Ritchie, G.; Burstein, E., Luminescence of dye molecules adsorbed at a Ag surface. *Phys. Rev. B* **1981,** *24* (8), 4843-4846.

10. Wokaun, A., Surface Enhancement of Optical Fields Mechanism and Applications. *Molecular Physics* **1985,** *56* (1), 1-33.

11. Wokaun, A.; Lutz, H. P.; King, A. P.; Wild, U. P.; Ernst, R. R., Energy Transfer in Surface Enhanced Luminscence. *Journal of Chemical Physics* **1983,** *79* (1), 509-514.

12. Barnes, W. L., Fluorescence near interfaces: the role of photonic mode density. *J. Mod. Opt.* **1998,** *45* (4), 661-699.

13. Anger, P.; Bharadwaj, P.; Novotny, L., Enhancement and quenching of single-molecule fluorescence. *Phys. Rev. Lett.* **2006,** *96* (11), 113002/1-113002/4.

14. Kuhn, S.; Hakanson, U.; Rogobete, L.; Sandoghdar, V., Enhancement of single-molecule fluorescence using a gold nanoparticle as an optical nanoantenna. *Phys. Rev. Lett.* **2006,** *97* (1), 017402/1-017402/4.

15. Rogobete, L.; Kaminski, F.; Agio, M.; Sandoghdar, V., Design of plasmonic nanoantennae for enhancing spontaneous emission. *Optics Letters* **2007,** *32* (12), 1623-1625.

16. Romero, I.; Aizpurua, J.; Bryant, G. W.; de Abajo, F. J. G., Plasmons in nearly touching metallic nanoparticles: singular response in the limit of touching dimers. *Opt. Express* **2006,** *14* (21), 9988-9999.

17. Aravind, P. K.; Metiu, H., The Effects of the Interaction between Resonances in the Electromagnetic Response of a Sphere-On-Plane Structure - Applications to Surface Enhances Spectroscopy. *Surface Science* **1983,** *124* (2-3), 506-528.

18. Nordlander, P.; Le, F., Plasmonic structure and electromagnetic field enhancements in the metallic nanoparticle-film system. *Applied Physics B-Lasers and Optics* **2006,** *84* (1-2), 35-41.

19. Nordlander, P.; Prodan, E., Plasmon hybridization in nanoparticles near metallic surfaces. *Nano Letters* **2004,** *4* (11), 2209-2213.

20. Zhao, J.; Sherry, L. J.; Schatz, G. C.; Van Duyne, R. P., Molecular Plasmonics: Chromophore-Plasmon Coupling and Single-Particle Nanosensors. *IEEE J. Sel. Top. Quantum Electron.* **2008,** *14* (6), 1418-1429.

21. Futamata, M., Single molecule sensitivity in SERS: importance of junction of adjacent Ag nanoparticles. *Faraday Discuss.* **2006,** (132), 45-61.

22. Futamata, M.; Maruyama, Y.; Ishikawa, M., Critical importance of the junction in touching Ag particles for single molecule sensitivity in SERS. *Journal of Molecular Structure* **2005,** *735*, 75-84.

23. Trügler, A.; Hohenester, U., Strong coupling between a metallic nanoparticle and a single molecule. *Phys. Rev. B, Condens, Matter Mater. Phys.* **2008,** *77* (11), 115403/1-115403/6.

24. Zuloaga, J.; Prodan, E.; Nordlander, P., Quantum Description of the Plasmon Resonances of a Nanoparticle Dimer. *Nano Letters* **2009,** *9* (2), 887-891.

25.

35. Johnson, P. B.; Christy, R. W., Optical Constants of Noble-Metals. *Phys. Rev. B* **1972,** *6* (12), 4370-4379.

36. Lynch, D. W.; Huttner, W. R., *Handbook of Optical Constants of Solids*. Academic Press Inc.: 1985; p 275-367.

37. Rueda, A.; Vogel, N.; Kreiter, M., Characterization of gold films by surface plasmon spectroscopy: Large errors and small consequences. *Surface Science* **2009,** *603* (3), 491-497.

38. Le Ru, E. C.; Etchegoin, P. G.; Grand, J.; Felidj, N.; Aubard, J.; Levi, G., Mechanisms of spectral profile modification in surface-enhanced fluorescence. *J. Phys. Chem. C* **2007,** *111* (44), 16076-16079.

39. Ringler, M.; Schwemer, A.; Wunderlich, M.; Nichtl, A.; Kurzinger, K.; Klar, T. A.; Feldmann, J., Shaping emission spectra of fluorescent molecules with single plasmonic nanoresonators. *Phys. Rev. Lett.* **2008,** *100* (20), 203002/1-203002/4.

9 Concluding Remarks

In this thesis the gap modes in a system of a metal particle placed very near to a metal surface were investigated. These modes are strongly localized to a nanometer sized region between the particle and the surface and play an important role in various optical effects. In spite of its simplicity this sphere-on-plane geometry is among the most efficient structures to provide very strong field enhancements and can be well described by theoretical models. Numerous studies in the past demonstrated the qualitative agreement of these theories in ensemble measurements. In the quasistatic limit the resonance position only depended on the material, the environment, the film-sphere distance and the sphere radius itself. As reference systems evaporated gold films with metal particles produced by chemical reduction were used while the spacer layer was commonly created by alkanethiols.

As a small contribution towards a better quantitative understanding of these electromagnetic resonances, an efficient plasmon mediated dark-field mode for scanning confocal microscopy through a thin metal film was presented. It can be utilized to investigate sphere-on-plane resonators on a single object basis, but in general it is also suitable for obtaining high-contrast images of other metal film supported samples. Since the optical resonances of the selected system are size and shape dependent, a combination with atomic force and scanning electron microscopy was successfully established to characterize the optical investigated particles in three dimensions. This approach can also be extended to samples where no gold film is desired by scratching the glass substrates themselves, or by evaporating an adequate London finder grid or transmission electron microscopy (TEM) grid on the glass surface as relative coordinate system for the identification procedure.

The performance of plasmon mediated dark field spectroscopy was proven for a test system of polystyrene beads on a gold film, where particles of identical size showed the expected identical response. By placing two polarizers perpendicular to one another in the excitation and detection pathways, the horizontal and vertical mode of the coupled system could be separated. In addition a systematic study for particle diameters between 200 and 500 nm showed a size-dependent coupling of the Mie particle resonances with the surface plasmons on the metal film.

In the second part the established techniques were used to conduct a systematic study of gold sphere-on-plane systems in which the response of gold particles, produced by chemical reduction of chlorauric acid, were compared to the one of ideal spheres of the same suspension. The spheres were generated by the additional irradiation of the nanoparticle suspension with a picosecond Nd:YAG laser. A detailed description of the involved processes during the laser interaction with the metal particles has been given and the progress of the

shape transformation proceeded via surface melting at a reduced melting temperature. The advantages of single particle spectroscopy to reveal the inherent optical response of the system has been impressively demonstrated for these systems. The conventional architecture with the chemical reduced particles on an evaporated gold film, which qualitatively agreed very well with electromagnetic calculations in previous ensemble experiments, showed strong variations between individual resonators. Only one third of all resonators exhibited the predicted behavior with two resonances, but with no correlation to the size or the shape. The other resonators either showed only one resonance near the particle plasmon, or more resonances on the red side of the spectrum. However, for the new assembled structures with the ideal spherical gold particles on top, the behavior changed dramatically and all particles showed a response which agreed with theoretical predictions. A variation of the film roughness did not influence the response of the samples at all. Despite the defined system geometries with the combination of spherical gold particles and ultra-smooth surfaces, the line width of the resonances was significantly broader than predicted. This pointed to a lower quality factor of the resonances, which should result in a much lower local field enhancement than suggested. The considerable scattering in the data for the resonance position, even for the defined samples, pointed also to additional factors influencing the gap region, such as the shape of the gap region. The advantages of the spherical particles will have a great impact on newly designed experiments, where particle dimers are investigated optically and the gap is imaged with TEM.

Finally, the large fields in the gaps themselves were probed by placing a polyphenylene dendrimer with a chromophore core as rigid molecule in a defined way in the gap of a silver sphere-on-plane system. The presented system provided several promising starting points for further experimental and theoretical investigations and could be regarded as an important step toward full quantitative experiments. The fluorescence emission profile was modified and showed a significant emission on the blue side. The maximum fluorescence emission peak shifted with the scattering maximum of the scattering response. For the silver systems the scattering response showed that only about half of all investigated particles exhibited an optical response, which agreed with theoretical calculations. The results indicated again the influence of more factors which affect the gap resonances. While the positions of the sphere-on-plane like resonators agreed with the theory, their line widths were again significantly broader.

10 Appendix

10.1 Dynamic Light Scattering Measurements for Gold Particles with a Diameter of 20 nm

In Figure 10.1 the intensity correlation plots of all performed light scattering experiment in the high energy range are summarized. The plots for the energies with 12, 16 and 22 mJ/pulse are presented and discussed in the main part of the work.

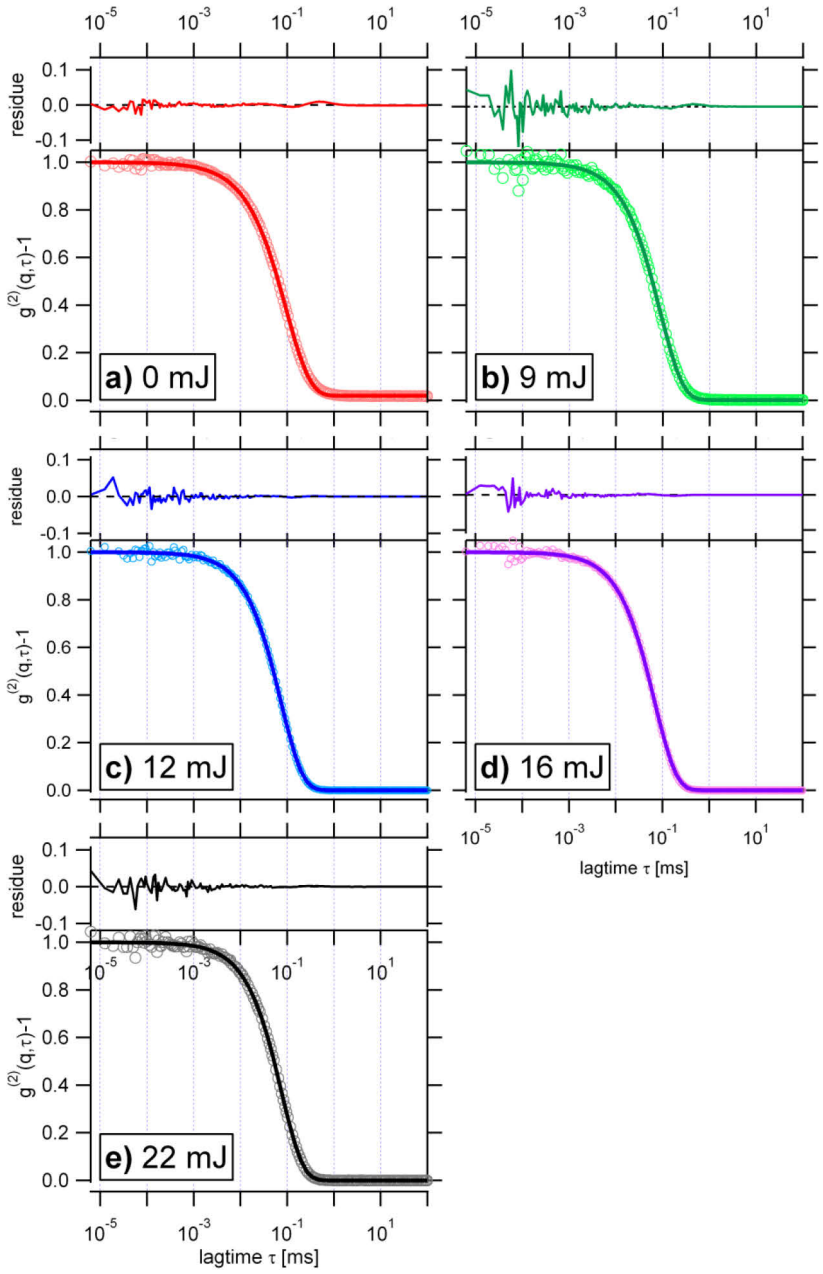

Figure 10.1: *Normalized intensity time autocorrelation function $g^{(2)}(q,\tau)$ for the unirradiated suspension and the irradiated one together with the fits obtained by the KWW analysis method and the residues.*

10.2 SOP: Evaporated Gold with Unirradiated Particles

In Figure 10.2 the scattering spectra (black) of 34 measured individuals are displayed with the respective scattering spectra of the gold film (red) in the vicinity at an uncovered position.

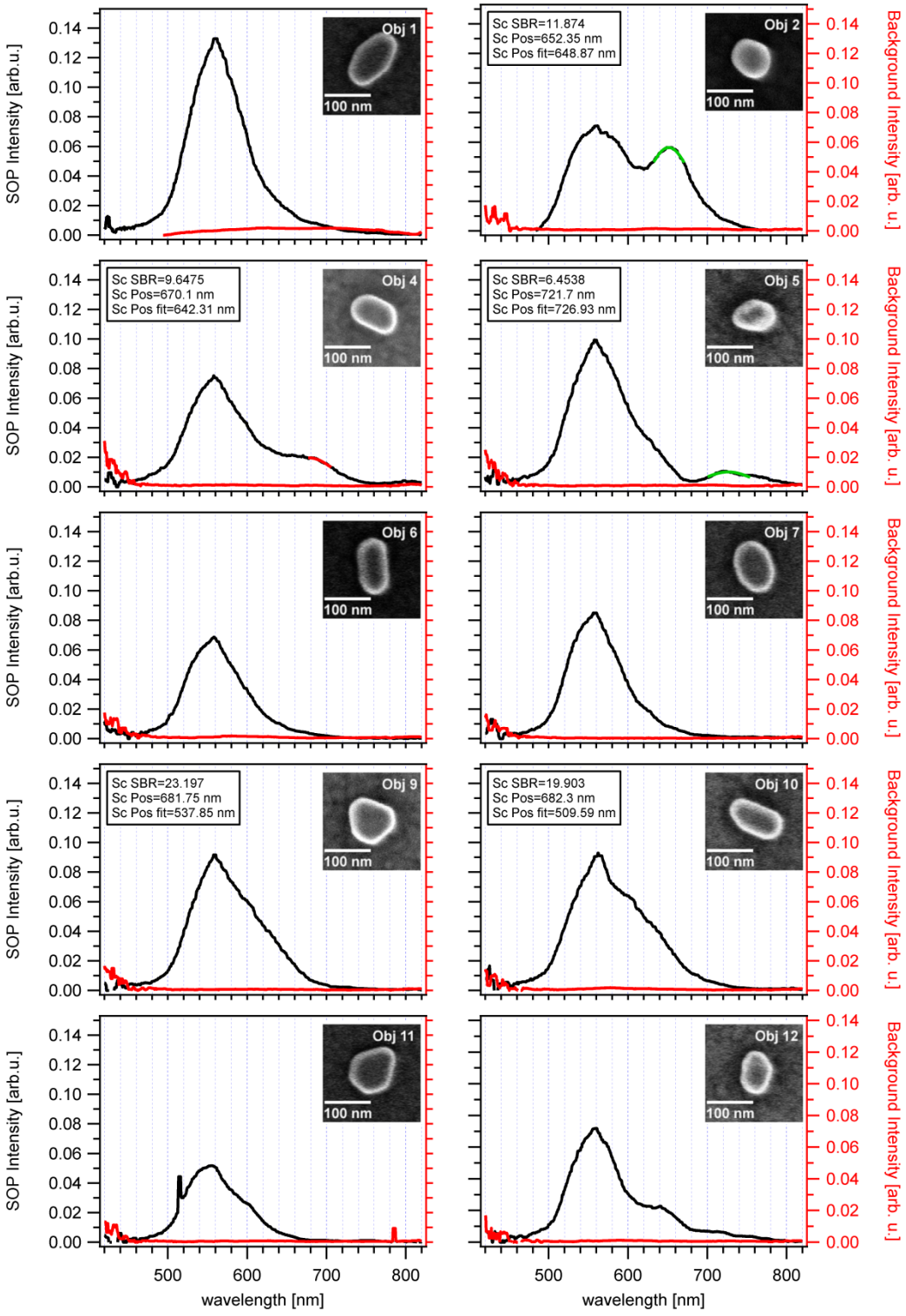

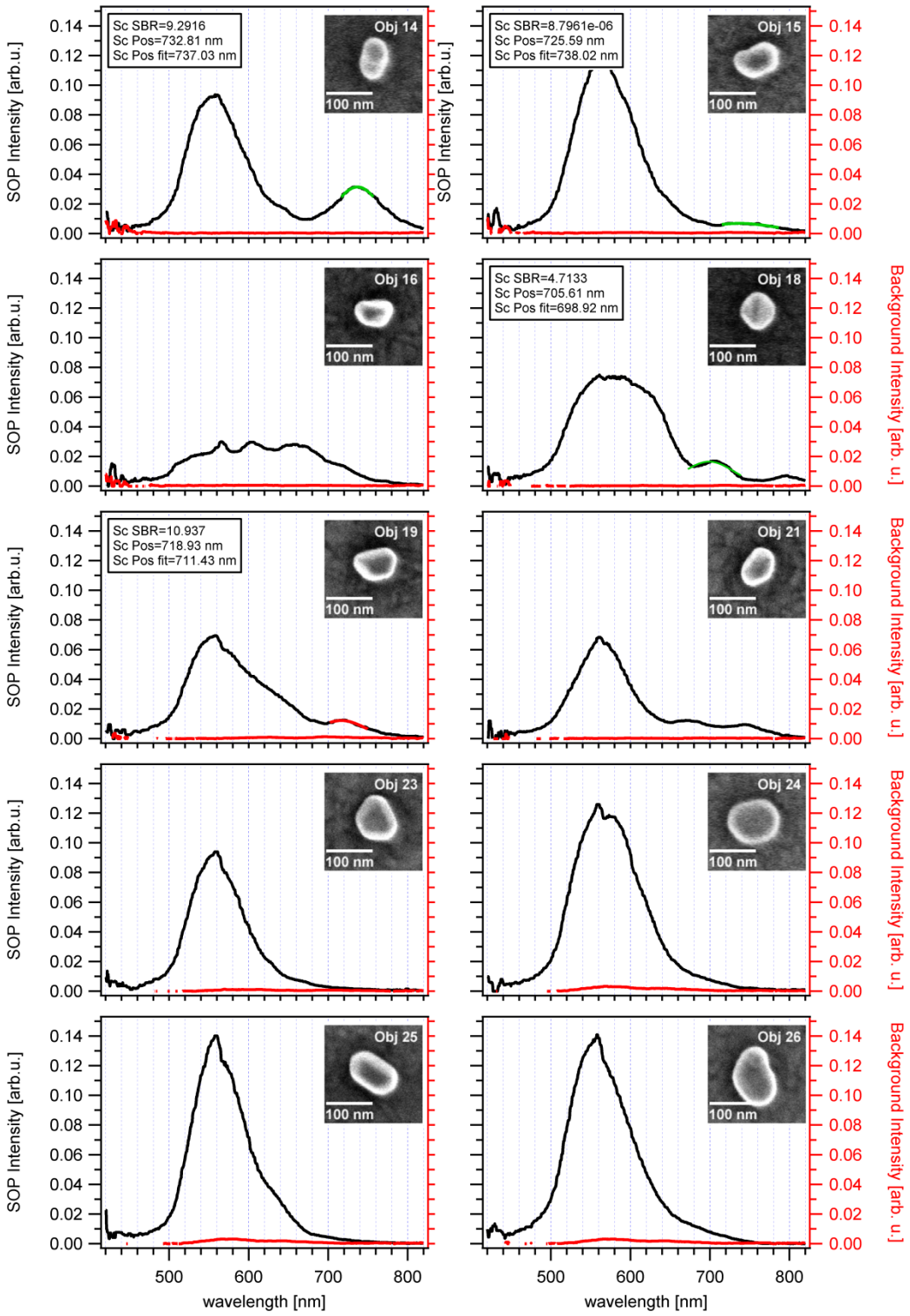
Sc SBR=9.2916
Sc Pos=732.81 nm
Sc Pos fit=737.03 nm
Obj 14
Sc SBR=8.7961e-06
Sc Pos=725.59 nm
Sc Pos fit=738.02 nm
Obj 15
Obj 16
Sc SBR=4.7133
Sc Pos=705.61 nm
Sc Pos fit=698.92 nm
Obj 18
Sc SBR=10.937
Sc Pos=718.93 nm
Sc Pos fit=711.43 nm
Obj 19
Obj 21
Obj 23
Obj 24
Obj 25
Obj 26
100 nm
SOP Intensity [arb.u.]
Background Intensity [arb. u.]
wavelength [nm]
0.00
0.02
0.04
0.06
0.08
0.10
0.12
0.14
500
600
700
800

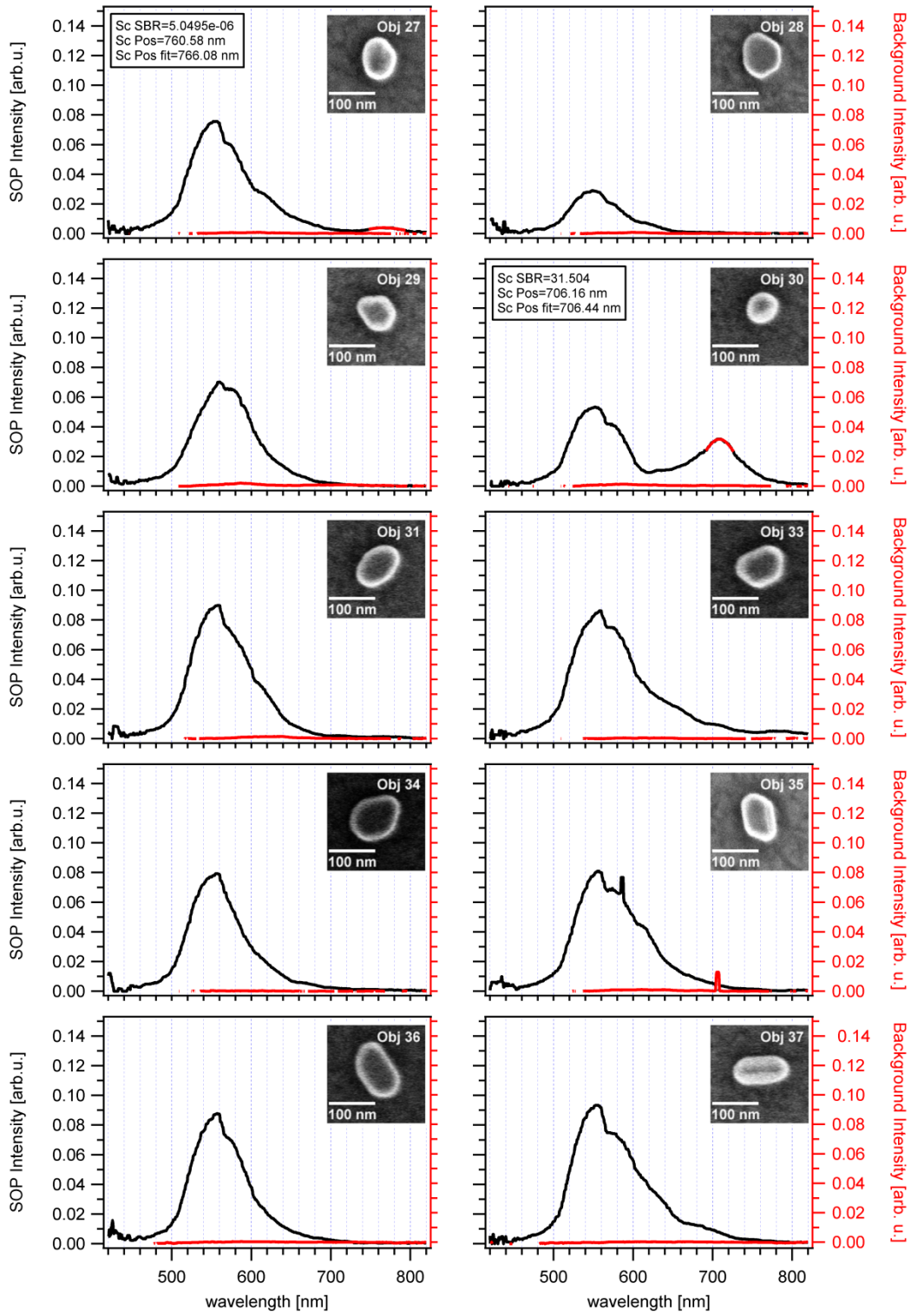
Sc SBR=5.0495e-06
Sc Pos=760.58 nm
Sc Pos fit=766.08 nm
Obj 27
Obj 28
Sc SBR=31.504
Sc Pos=706.16 nm
Sc Pos fit=706.44 nm
Obj 29
Obj 30
Obj 31
Obj 33
Obj 34
Obj 35
Obj 36
Obj 37
100 nm
SOP Intensity [arb.u.]
Background Intensity [arb. u.]
wavelength [nm]
0.00
0.02
0.04
0.06
0.08
0.10
0.12
0.14
500
600
700
800

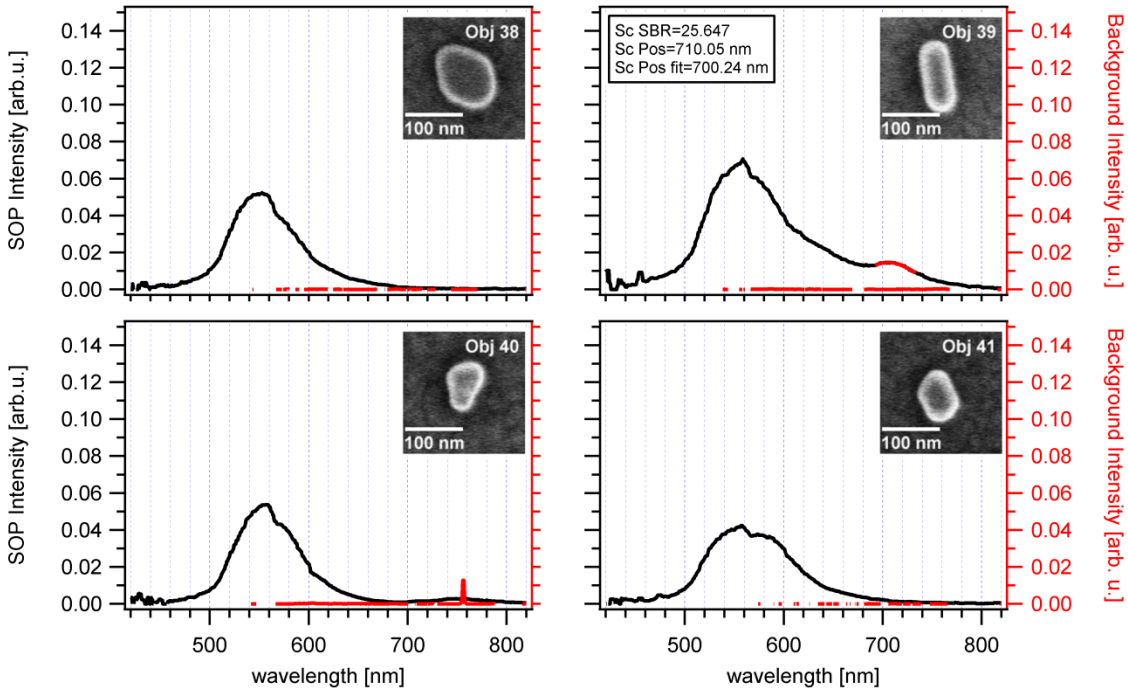

Figure 10.2: *Scattering spectra from particle positions (black), compared to the background scattering signal (black) of the film for the untreated particles on evaporated gold. The curves are all scaled to the same maximum value and show the scattering signal of the particles which are presented top right.*

Since the optical properties of the gold film vary strongly through the visible spectral region, the scattering signal obtained in the plasmon-mediated dark field microscopy is wavelength dependent. The particles show a great variation in their response and it is surprising that ensemble measurement show such a close correlation to theoretical calculations. Since the number of particles which showed a sphere-on-plane like response is so small no correlation plots were performed for this sample. All particle details obtained by the combined effort of atomic force and electron microscopy are presented in the following Table 10.1.

Table 10.1: determined dimensions of the presented colloidal particles on evaporated gold

Particle	x-axis [nm]	y-axis [nm]	Height [nm]	Area [nm^2]	Volume [nm^3]	Circularity
Obj1	128	74	40 (2)	7824	314525	0.795
Obj2	70	55	60 (2)	3264	195187	0.858
Obj4	104	66	50 (2)	5888	293311	0.847
Obj5	92	66	58 (2)	4800	279600	0.855
Obj6	114	54	36 (4)	5316	192359	0.762
Obj7	112	79	33 (4)	7220	240011	0.860
Obj9	103	90	36 (5)	7692	277897	0.876
Obj10	121	62	43 (5)	6660	285597	0.775
Obj11	105	89	29 (5)	7168	211277	0.861
Obj12	92	63	49 (5)	4796	232774	0.865
Obj14	90	57	72 (6)	4136	299033	0.841
Obj15	95	66	58 (6)	5580	321389	0.855
Obj16	82	56	56 (2)	3828	213296	0.854

Particle	x-axis [nm]	y-axis [nm]	Height [nm]	Area [nm^2]	Volume [nm^3]	Circularity
Obj18	80	70	67 (5)	4320	290995	0.905
Obj19	92	66	50 (4)	5020	249778	0.863
Obj21	85	59	53 (5)	4084	217779	0.849
Obj23	96	86	36 (5)	6464	233124	0.871
Obj24	110	95	39 (5)	8600	331461	0.888
Obj25	112	70	42 (4)	6660	282451	0.836
Obj26	130	86	46 (5)	8944	411317	0.843
Obj27	90	68	50 (5)	5032	250121	0.881
Obj28	98	80	24 (5)	6180	146899	0.874
Obj29	84	70	41 (4)	4708	192722	0.875
Obj30	70	60	62 (4)	3364	209998	0.891
Obj31	104	71	40 (3)	6084	242468	0.870
Obj33	104	78	48 (4)	6652	315970	0.885
Obj34	112	88	32 (4)	7780	248260	0.863
Obj35	106	70	39 (3)	6212	243862	0.851
Obj36	112	71	34 (6)	7372	247761	0.807
Obj37	118	62	48 (6)	6052	290405	0.776
Obj38	124	96	35 (7)	9140	317067	0.857
Obj39	125	52	49 (3)	6140	303091	0.731
Obj40	89	58	43 (3)	4068	174083	0.812
Obj41	85	60	36 (3)	4504	161513	0.851

The numbers in the brackets of the height indicate how many values were determined for the mean value. The volume for these particles is calculated as the particle area determined by SEM multiplied with the maximum height determined by AFM. The circularity is the proportion of the area and the perimeter (4π area/perimeter^2) and gives an indication of the two dimensional roundness of the considered particle from the SEM images. For an ideal circle the factor would be exactly 1.

10.3 SOP: Evaporated Gold with Irradiated Particles

In Figure 10.3 all measured scattering spectra of the laser-irradiated particles on the evaporated gold substrates are shown. The scattering response of a resonator is shown in black, while the background signal of the gold film is displayed in red. For the first 7 particles a problem arose with the normalization to the Xenon light source. Both the objective and the reference spectra in the source data go to infinity below 500 nm and show a fine-structure above 750 nm with more intensity than the rest of the investigated particles. This leads to additional noise in the scattering response of the resonators. It is not a physical response, but rather a technical problem.

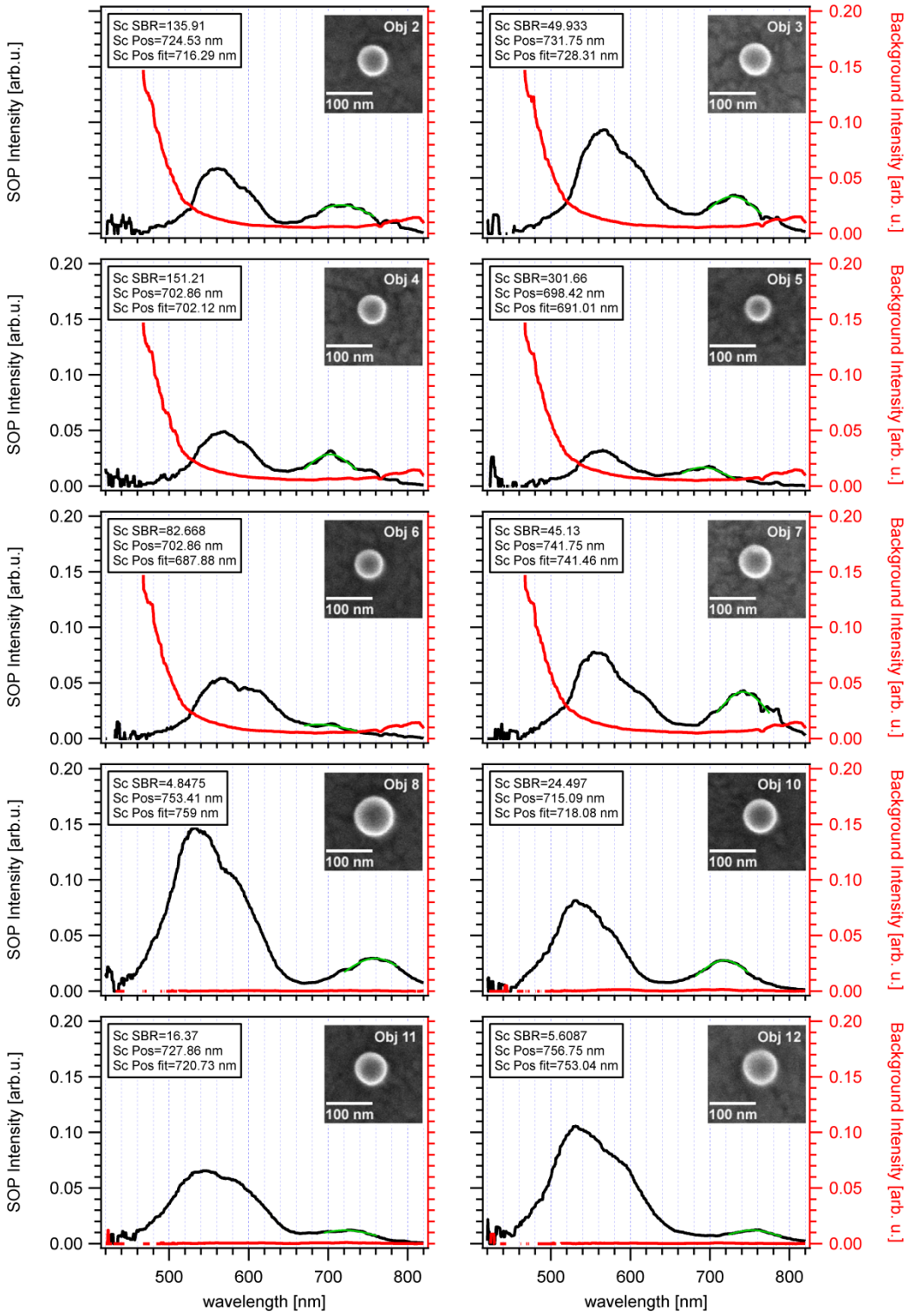
Sc SBR=135.91
Sc Pos=724.53 nm
Sc Pos fit=716.29 nm
Obj 2
Sc SBR=49.933
Sc Pos=731.75 nm
Sc Pos fit=728.31 nm
Obj 3
Sc SBR=151.21
Sc Pos=702.86 nm
Sc Pos fit=702.12 nm
Obj 4
Sc SBR=301.66
Sc Pos=698.42 nm
Sc Pos fit=691.01 nm
Obj 5
Sc SBR=82.668
Sc Pos=702.86 nm
Sc Pos fit=687.88 nm
Obj 6
Sc SBR=45.13
Sc Pos=741.75 nm
Sc Pos fit=741.46 nm
Obj 7
Sc SBR=4.8475
Sc Pos=753.41 nm
Sc Pos fit=759 nm
Obj 8
Sc SBR=24.497
Sc Pos=715.09 nm
Sc Pos fit=718.08 nm
Obj 10
Sc SBR=16.37
Sc Pos=727.86 nm
Sc Pos fit=720.73 nm
Obj 11
Sc SBR=5.6087
Sc Pos=756.75 nm
Sc Pos fit=753.04 nm
Obj 12
100 nm
SOP Intensity [arb.u.]
Background Intensity [arb. u.]
0.00
0.05
0.10
0.15
0.20
500
600
700
800
wavelength [nm]

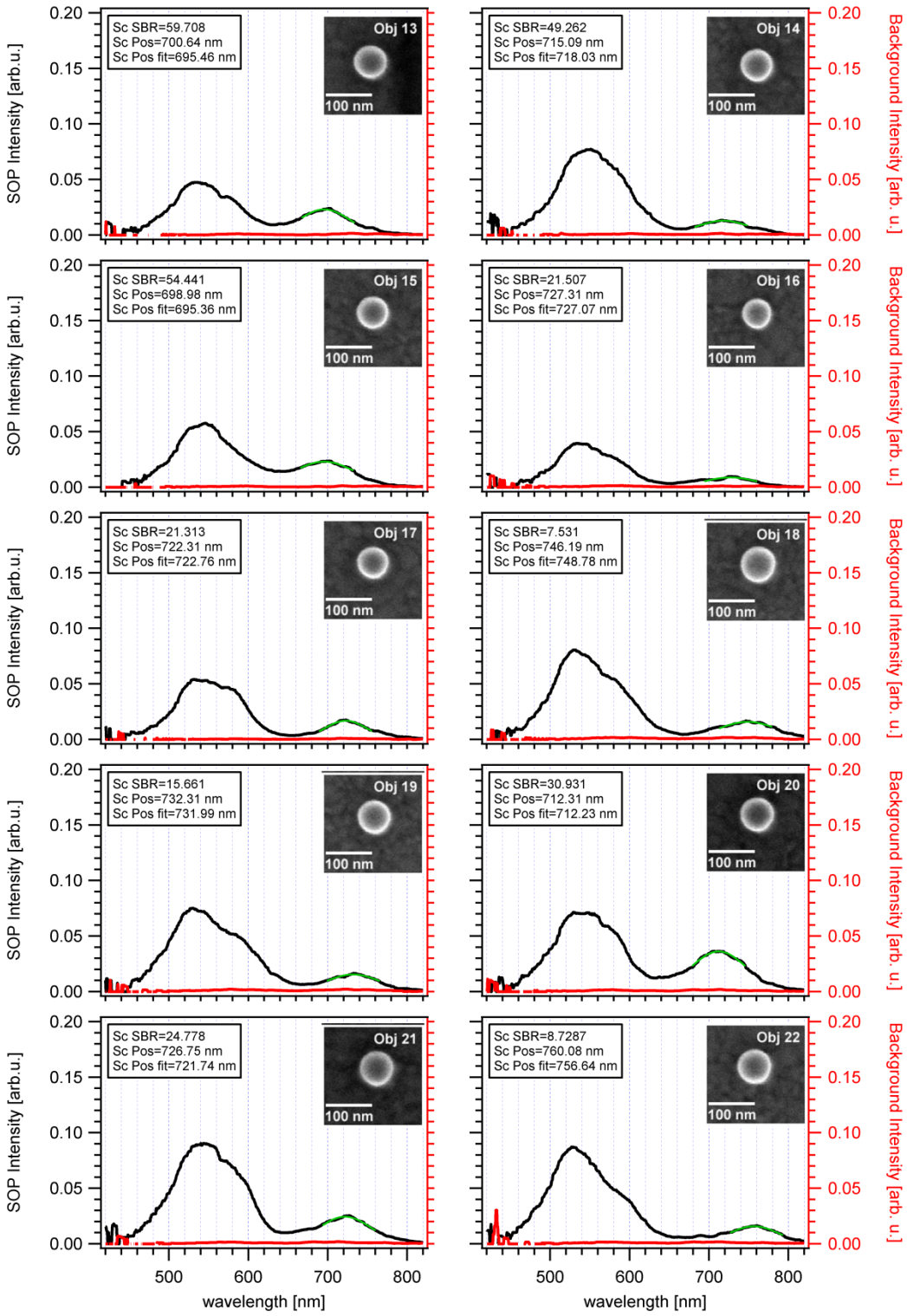
Sc SBR=59.708
Sc Pos=700.64 nm
Sc Pos fit=695.46 nm
Obj 13
100 nm
Sc SBR=49.262
Sc Pos=715.09 nm
Sc Pos fit=718.03 nm
Obj 14
100 nm
Sc SBR=54.441
Sc Pos=698.98 nm
Sc Pos fit=695.36 nm
Obj 15
100 nm
Sc SBR=21.507
Sc Pos=727.31 nm
Sc Pos fit=727.07 nm
Obj 16
100 nm
Sc SBR=21.313
Sc Pos=722.31 nm
Sc Pos fit=722.76 nm
Obj 17
100 nm
Sc SBR=7.531
Sc Pos=746.19 nm
Sc Pos fit=748.78 nm
Obj 18
100 nm
Sc SBR=15.661
Sc Pos=732.31 nm
Sc Pos fit=731.99 nm
Obj 19
100 nm
Sc SBR=30.931
Sc Pos=712.31 nm
Sc Pos fit=712.23 nm
Obj 20
100 nm
Sc SBR=24.778
Sc Pos=726.75 nm
Sc Pos fit=721.74 nm
Obj 21
100 nm
Sc SBR=8.7287
Sc Pos=760.08 nm
Sc Pos fit=756.64 nm
Obj 22
100 nm
SOP Intensity [arb.u.]
Background Intensity [arb. u.]
0.00
0.05
0.10
0.15
0.20
500
600
700
800
wavelength [nm]

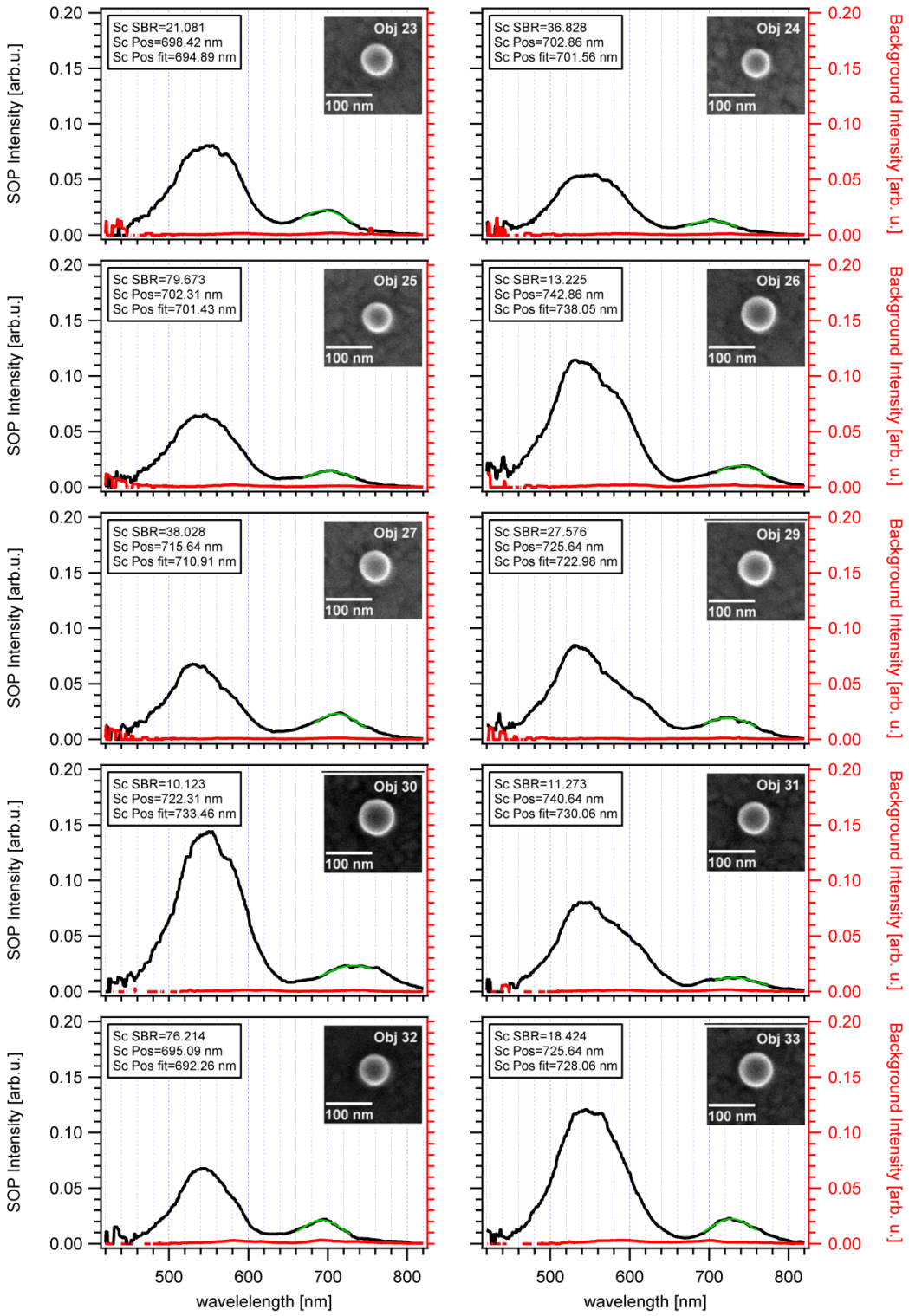
Sc SBR=21.081
Sc Pos=698.42 nm
Sc Pos fit=694.89 nm
Obj 23
Sc SBR=36.828
Sc Pos=702.86 nm
Sc Pos fit=701.56 nm
Obj 24
Sc SBR=79.673
Sc Pos=702.31 nm
Sc Pos fit=701.43 nm
Obj 25
Sc SBR=13.225
Sc Pos=742.86 nm
Sc Pos fit=738.05 nm
Obj 26
Sc SBR=38.028
Sc Pos=715.64 nm
Sc Pos fit=710.91 nm
Obj 27
Sc SBR=27.576
Sc Pos=725.64 nm
Sc Pos fit=722.98 nm
Obj 29
Sc SBR=10.123
Sc Pos=722.31 nm
Sc Pos fit=733.46 nm
Obj 30
Sc SBR=11.273
Sc Pos=740.64 nm
Sc Pos fit=730.06 nm
Obj 31
Sc SBR=76.214
Sc Pos=695.09 nm
Sc Pos fit=692.26 nm
Obj 32
Sc SBR=18.424
Sc Pos=725.64 nm
Sc Pos fit=728.06 nm
Obj 33
100 nm
SOP Intensity [arb.u.]
Background Intensity [arb. u.]
0.00
0.05
0.10
0.15
0.20
500
600
700
800
wavelelength [nm]

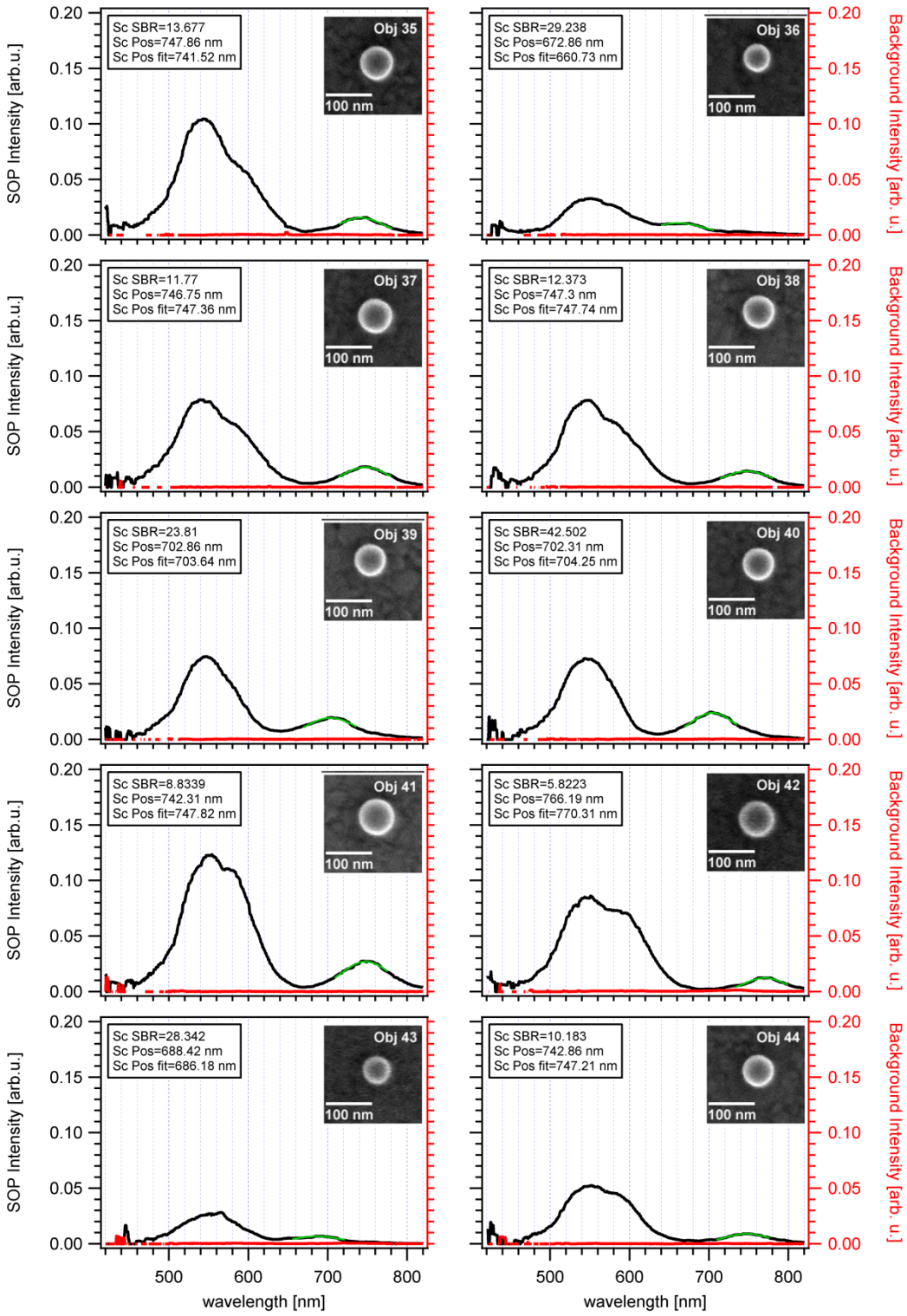
Sc SBR=13.677
Sc Pos=747.86 nm
Sc Pos fit=741.52 nm
Obj 35
100 nm
Sc SBR=29.238
Sc Pos=672.86 nm
Sc Pos fit=660.73 nm
Obj 36
100 nm
Sc SBR=11.77
Sc Pos=746.75 nm
Sc Pos fit=747.36 nm
Obj 37
100 nm
Sc SBR=12.373
Sc Pos=747.3 nm
Sc Pos fit=747.74 nm
Obj 38
100 nm
Sc SBR=23.81
Sc Pos=702.86 nm
Sc Pos fit=703.64 nm
Obj 39
100 nm
Sc SBR=42.502
Sc Pos=702.31 nm
Sc Pos fit=704.25 nm
Obj 40
100 nm
Sc SBR=8.8339
Sc Pos=742.31 nm
Sc Pos fit=747.82 nm
Obj 41
100 nm
Sc SBR=5.8223
Sc Pos=766.19 nm
Sc Pos fit=770.31 nm
Obj 42
100 nm
Sc SBR=28.342
Sc Pos=688.42 nm
Sc Pos fit=686.18 nm
Obj 43
100 nm
Sc SBR=10.183
Sc Pos=742.86 nm
Sc Pos fit=747.21 nm
Obj 44
100 nm
SOP Intensity [arb.u.]
Background Intensity [arb. u.]
0.00
0.05
0.10
0.15
0.20
500
600
700
800
wavelength [nm]

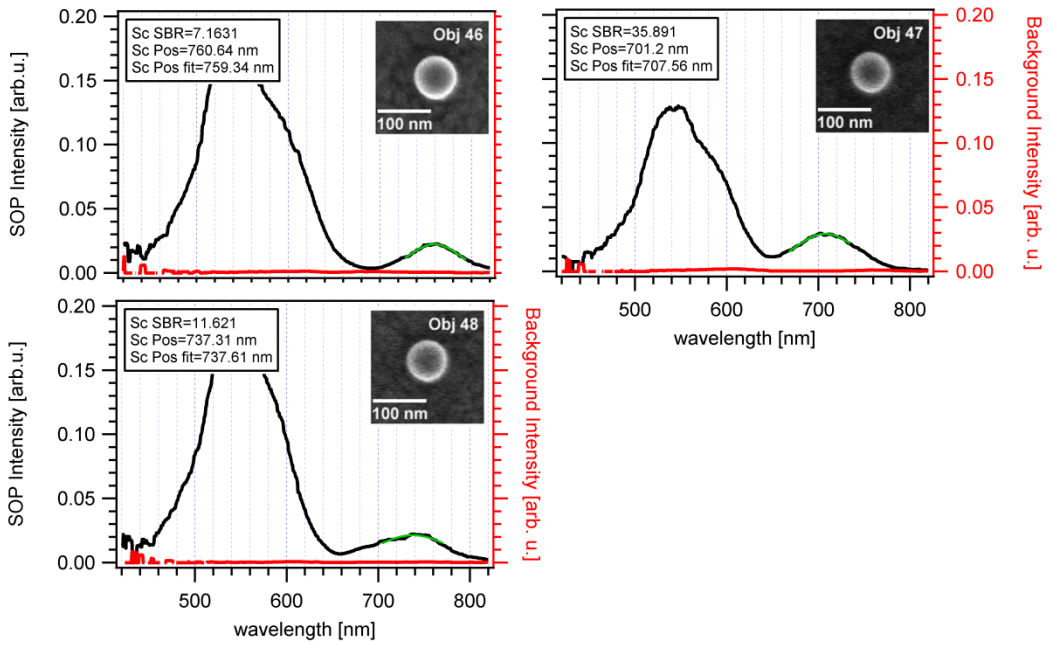

Figure 10.3: *Scattering spectra from particle positions (black), compared to the background scattering signal (black) of the film for the irradiated particles on evaporated gold. The curves are all scaled to the same maximum value and show the scattering signal of the particles which are presented top right.*

All extracted information for the particle details is summarized in the following Table 10.2. The numbers in the brackets of the height indicate how many values were determined for the mean value. The volume for these spheres is calculated for an ellipsoid with three axis determined by SEM and AFM measurements. The circularity is the proportion of the area and the perimeter (4π area/perimeter^2) and gives an indication of the two dimensional roundness of the considered particle from the SEM images.

Table 10.2: determined dimensions of the presented gold spheres on evaporated gold

Particle	x-axis [nm]	y-axis [nm]	Height [nm]	Area [nm^2]	Volume [nm^3]	Circularity
Obj1	112	48	41 (6)	4720	114321	0.720
Obj2	63	62	62 (6)	3268	126157	0.912
Obj3	68	68	65 (5)	3772	157518	0.893
Obj4	63	61	58 (8)	3148	116191	0.899
Obj5	54	54	53 (12)	2364	81041	0.897
Obj6	58	58	58 (6)	2864	101356	0.913
Obj7	70	70	68 (6)	3968	175062	0.908
Obj8	84	84	80 (11)	5748	296535	0.904
Obj10	71	70	66 (11)	4064	172839	0.895
Obj11	66	66	62 (6)	3680	141888	0.916
Obj12	73	72	72 (6)	4360	197871	0.883
Obj13	68	68	62 (11)	3808	149680	0.892
Obj14	68	68	64 (11)	3700	154203	0.912
Obj15	66	65	64 (11)	3608	143923	0.912
Obj16	62	62	61 (11)	3024	123087	0.901

Particle	x-axis [nm]	y-axis [nm]	Height [nm]	Area [nm^2]	Volume [nm^3]	Circularity
Obj17	67	66	65 (9)	3596	150009	0.905
Obj18	74	72	72 (7)	4480	202017	0.907
Obj19	70	69	67 (10)	3936	168203	0.910
Obj20	72	72	69 (10)	4144	186963	0.904
Obj21	72	72	67 (10)	4188	182458	0.905
Obj22	72	72	72 (12)	4436	194982	0.910
Obj23	66	66	64 (8)	3588	145344	0.916
Obj24	62	60	57 (9)	3044	110468	0.918
Obj25	62	62	60 (9)	3196	120998	0.906
Obj26	73	72	70 (9)	4332	193499	0.906
Obj27	64	64	65 (9)	3468	138640	0.909
Obj29	72	72	69 (6)	4240	187968	0.895
Obj30	74	73	72 (7)	4516	203893	0.906
Obj31	66	64	65 (8)	3452	143040	0.895
Obj32	62	62	62 (9)	3048	124169	0.904
Obj33	70	70	70 (8)	4160	178889	0.912
Obj35	69	67	67 (9)	3860	161185	0.909
Obj36	56	54	51 (11)	2476	81156	0.899
Obj37	70	70	69 (7)	4068	176809	0.887
Obj38	66	68	66 (6)	3724	155172	0.899
Obj39	66	64	64 (6)	3504	142101	0.908
Obj40	66	66	65 (8)	3532	147824	0.906
Obj41	76	76	75 (7)	4772	225829	0.904
Obj42	74	72	75 (5)	4260	207835	0.899
Obj43	56	56	55 (6)	2496	89996	0.918
Obj44	66	64	66 (6)	3460	145602	0.907
Obj45	94	84	61 (6)	6216	253704	0.890
Obj46	79	79	76 (10)	5096	247502	0.900
Obj47	72	70	67 (12)	4112	176017	0.900
Obj48	76	74	73 (7)	4644	213492	0.903

In Figure 10.4 all correlation plots of the interesting parameters are shown for this sample. In most cases no clear trend is seen. The plots showing a correlation are presented and discussed in the main part of the thesis.

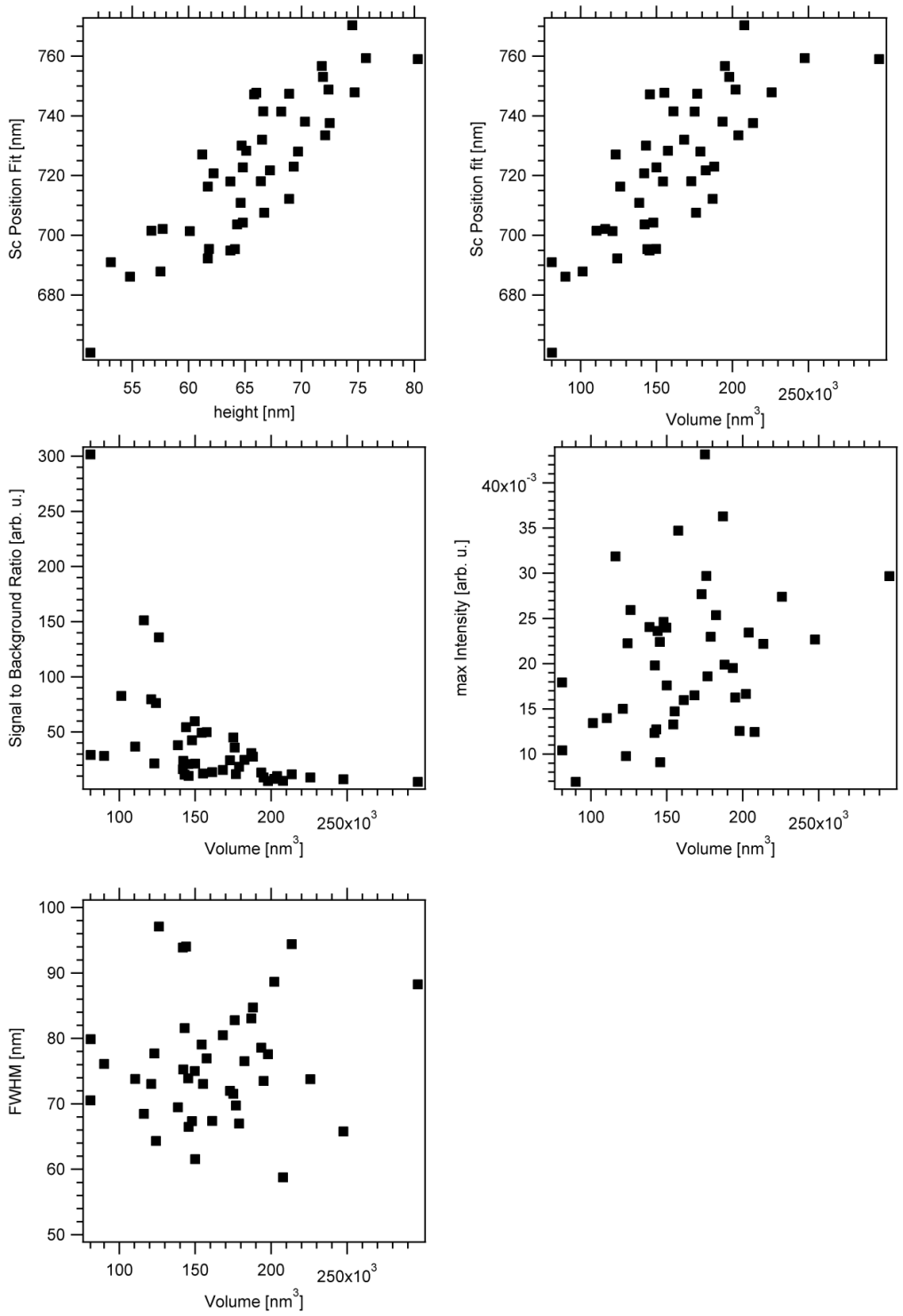

Figure 10.4: *Parameters describing the particles are plotted versus each other in the search for a correlation of data for this sample*

10.4 SOP: Template Stripped Gold (EPOTEK 377) with Irradiated Particles

All spectra for the template stripped gold sample with round spheres are shown in Figure 10.5. The reference spectra of the uncovered film show some noise above 740 nm and below 480 nm.

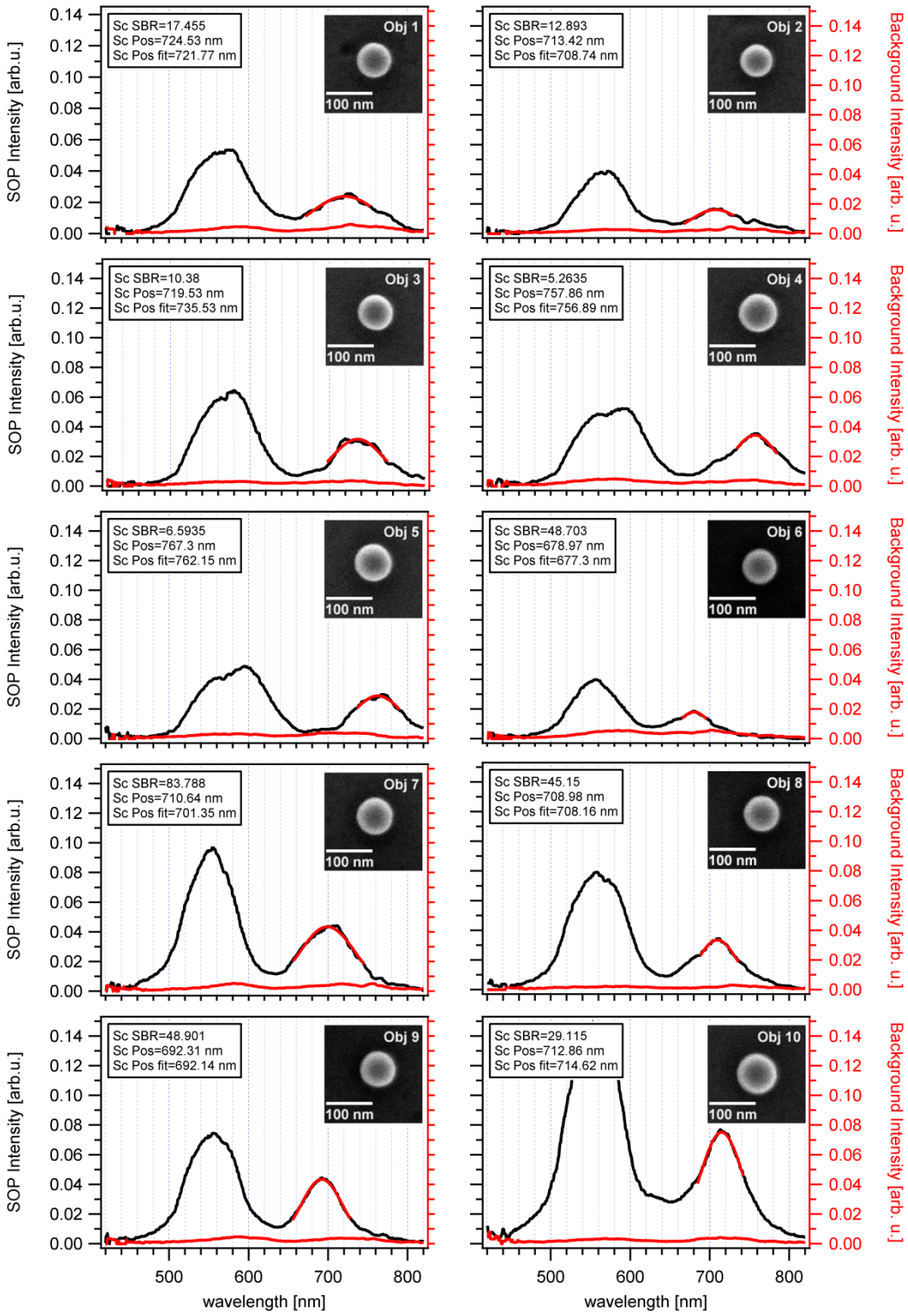
Sc SBR=17.455
Sc Pos=724.53 nm
Sc Pos fit=721.77 nm
Obj 1
Sc SBR=12.893
Sc Pos=713.42 nm
Sc Pos fit=708.74 nm
Obj 2
Sc SBR=10.38
Sc Pos=719.53 nm
Sc Pos fit=735.53 nm
Obj 3
Sc SBR=5.2635
Sc Pos=757.86 nm
Sc Pos fit=756.89 nm
Obj 4
Sc SBR=6.5935
Sc Pos=767.3 nm
Sc Pos fit=762.15 nm
Obj 5
Sc SBR=48.703
Sc Pos=678.97 nm
Sc Pos fit=677.3 nm
Obj 6
Sc SBR=83.788
Sc Pos=710.64 nm
Sc Pos fit=701.35 nm
Obj 7
Sc SBR=45.15
Sc Pos=708.98 nm
Sc Pos fit=708.16 nm
Obj 8
Sc SBR=48.901
Sc Pos=692.31 nm
Sc Pos fit=692.14 nm
Obj 9
Sc SBR=29.115
Sc Pos=712.86 nm
Sc Pos fit=714.62 nm
Obj 10
100 nm
SOP Intensity [arb.u.]
Background Intensity [arb. u.]
wavelength [nm]
0.00
0.02
0.04
0.06
0.08
0.10
0.12
0.14
500
600
700
800

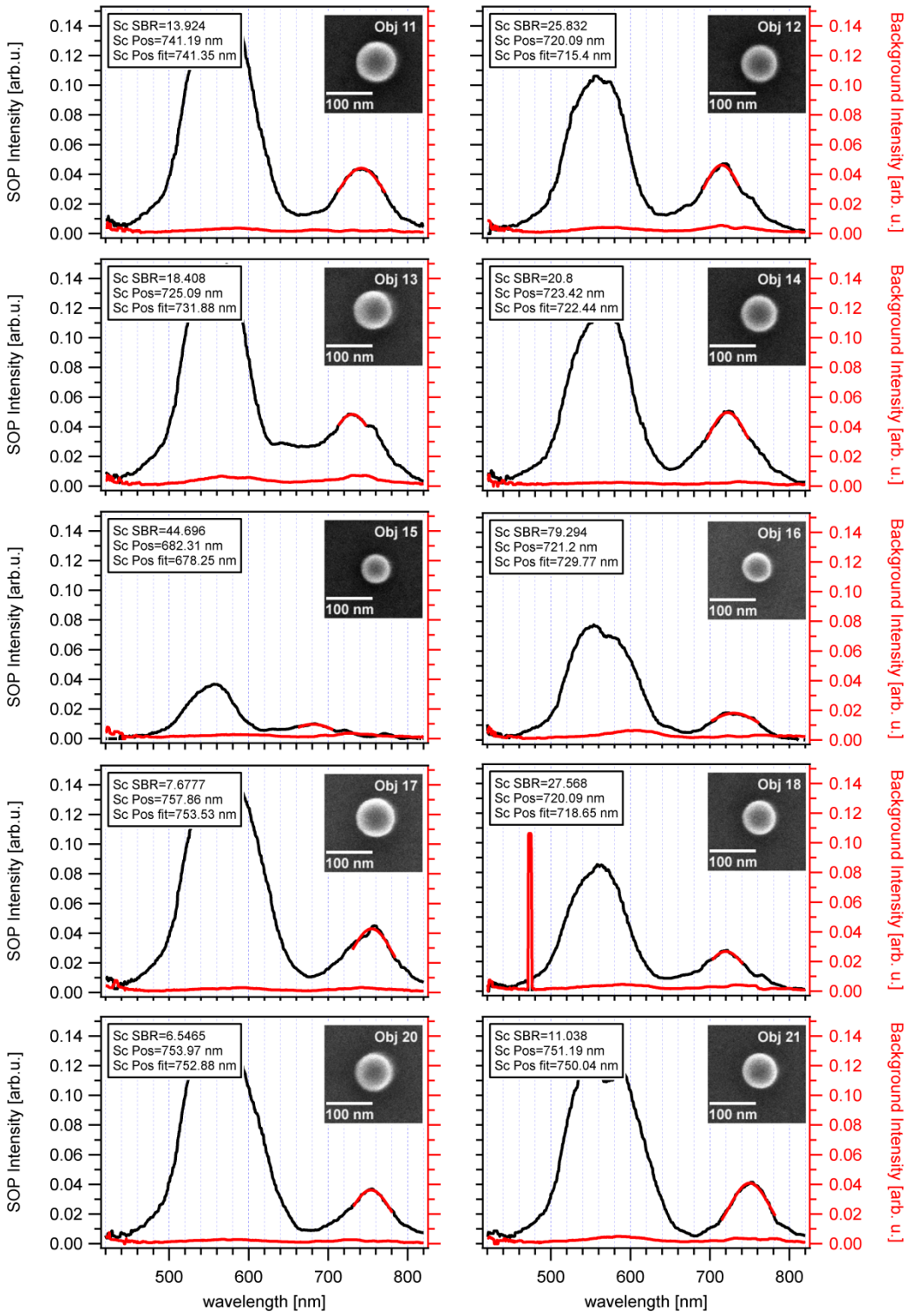

Figure 10.5: *Scattering spectra from particle positions (black), compared to the background scattering signal (black) of the film for the irradiated particles on template stripped gold. The curves are all scaled to the same maximum value and show the scattering signal of the particles which are presented top right.*

The data derived from AFM and SEM measurements is presented for all the particles in the following Table 10.3. The numbers in the brackets of the height indicate how many values were determined for the mean value. The volume for these spheres is calculated for an ellipsoid with three axis determined by SEM and AFM measurements. The circularity is the

proportion of the area and the perimeter (4π area/perimeter^2) and gives an indication of the two dimensional roundness of the considered particle from the SEM images.

Table 10.3: determined dimensions of the presented gold spheres on TSG 377

Particle	x-axis [nm]	y-axis [nm]	Height [nm]	Area [nm^2]	Volume [nm^3]	Circularity
Obj1	66	65	63 (18)	3412	142372	0.904
Obj2	61	61	58 (18)	2912	112682	0.913
Obj3	71	70	69 (28)	3940	179879	0.911
Obj4	76	76	74 (20)	4693	222302	0.901
Obj5	73	73	70 (16)	4160	194816	0.897
Obj6	56	55	53 (20)	2426	85025	0.912
Obj7	69	67	63 (20)	3637	153103	0.892
Obj8	64	64	61 (23)	3296	130625	0.889
Obj9	63	62	59 (20)	3170	121095	0.897
Obj10	75	74	72 (18)	4567	208273	0.906
Obj11	74	74	72 (17)	4449	206064	0.894
Obj12	68	67	65 (16)	3647	154566	0.895
Obj13	75	73	72 (10)	4301	205160	0.900
Obj14	71	69	67 (15)	3964	172247	0.898
Obj15	51	50	50 (19)	2042	66230	0.896
Obj16	61	60	59 (19)	2978	113214	0.898
Obj17	76	75	73 (23)	4732	218904	0.896
Obj18	65	63	64 (22)	3245	136612	0.899
Obj19	122	107	34 (22)	10562	233466	0.885
Obj20	76	73	74 (28)	4527	215582	0.901
Obj21	72	70	69 (10)	4016	183084	0.895

In Figure 10.6 the correlation plots for this TSG sample are shown.

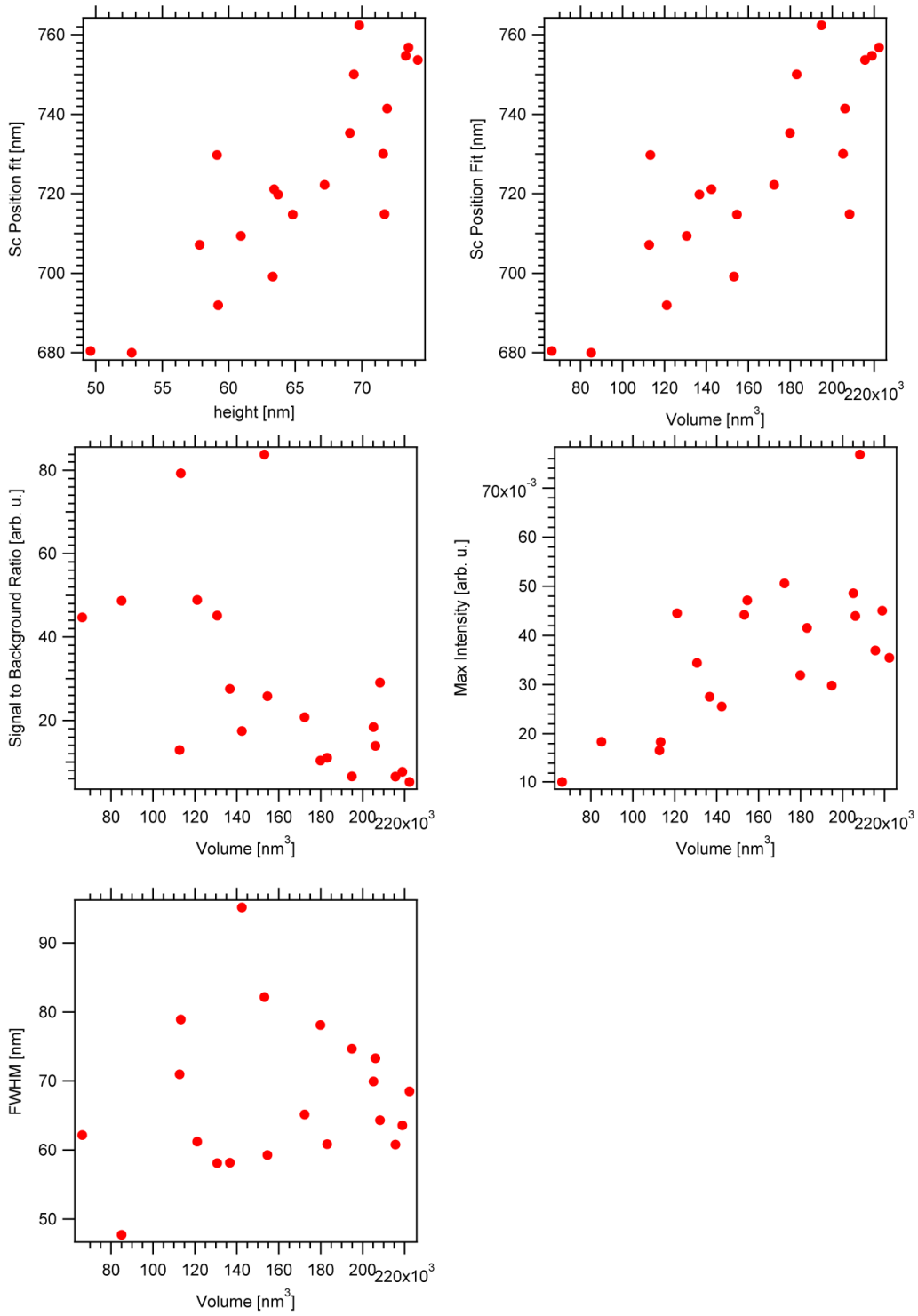

Figure 10.6: *Parameters describing the particles are plotted versus each other in the search for a correlation of data for this sample*

10.5 SOP: Template Stripped Gold (EPOTEK 353 ND-4) with Irradiated Particles

A second template stripped gold sample was prepared in order to illustrate the influence of the glue layer on the optical measurements. All obtained spectra for this sample with round spheres are shown in Figure 10.7. In all spectra the scattering response of a resonator is

shown in black, while the background signal of the gold film is displayed in red. The blue curve shows the response of the resonator without background subtraction. The consequences of the different glues are discussed in the main part of the corresponding chapter.

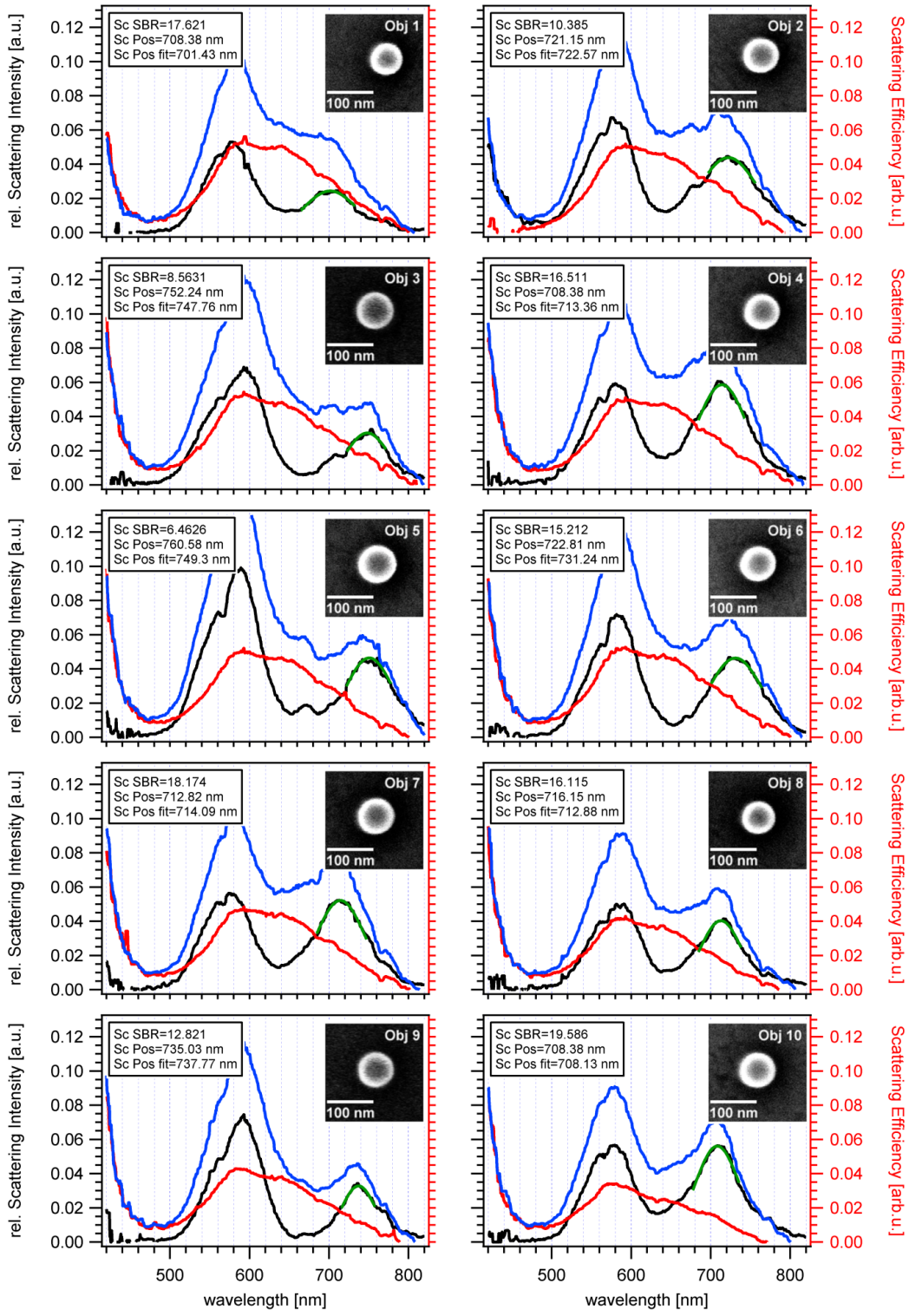

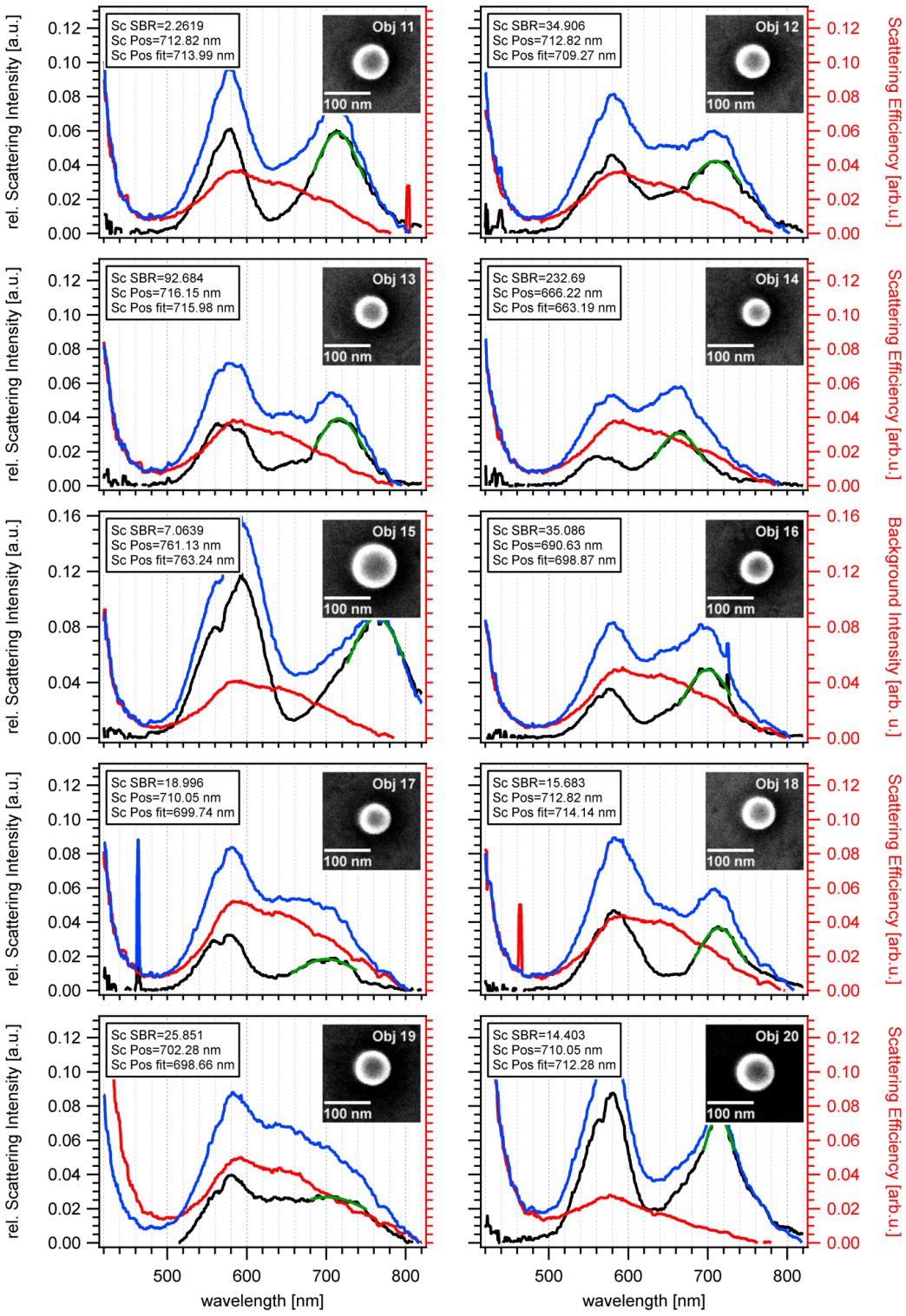
Sc SBR=2.2619
Sc Pos=712.82 nm
Sc Pos fit=713.99 nm
Obj 11
Sc SBR=34.906
Sc Pos=712.82 nm
Sc Pos fit=709.27 nm
Obj 12
Sc SBR=92.684
Sc Pos=716.15 nm
Sc Pos fit=715.98 nm
Obj 13
Sc SBR=232.69
Sc Pos=666.22 nm
Sc Pos fit=663.19 nm
Obj 14
Sc SBR=7.0639
Sc Pos=761.13 nm
Sc Pos fit=763.24 nm
Obj 15
Sc SBR=35.086
Sc Pos=690.63 nm
Sc Pos fit=698.87 nm
Obj 16
Sc SBR=18.996
Sc Pos=710.05 nm
Sc Pos fit=699.74 nm
Obj 17
Sc SBR=15.683
Sc Pos=712.82 nm
Sc Pos fit=714.14 nm
Obj 18
Sc SBR=25.851
Sc Pos=702.28 nm
Sc Pos fit=698.66 nm
Obj 19
Sc SBR=14.403
Sc Pos=710.05 nm
Sc Pos fit=712.28 nm
Obj 20
100 nm
rel. Scattering Intensity [a.u.]
Scattering Efficiency [arb.u.]
Background Intensity [arb. u.]
wavelength [nm]

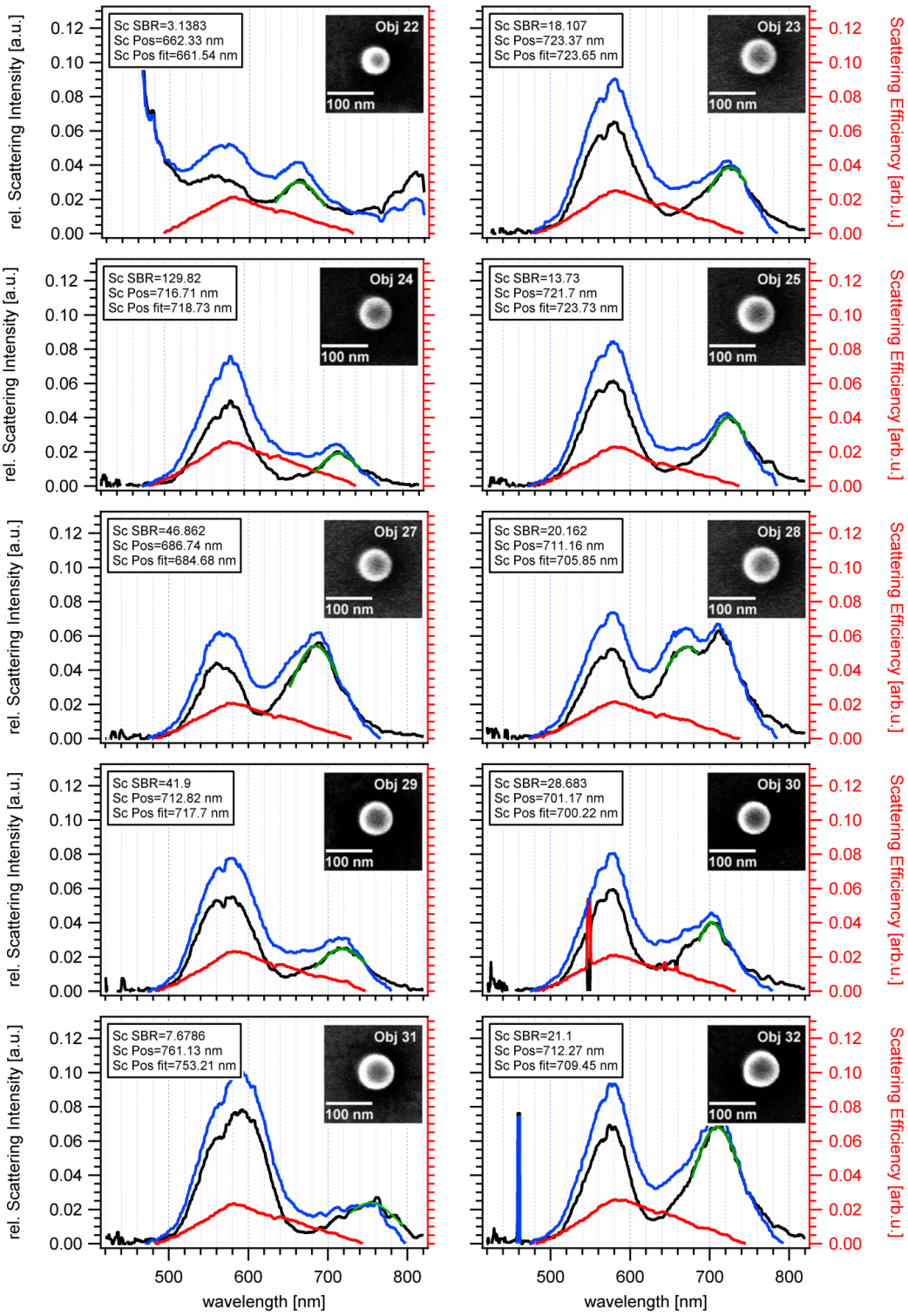
Sc SBR=3.1383
Sc Pos=662.33 nm
Sc Pos fit=661.54 nm
Obj 22
100 nm
Sc SBR=18.107
Sc Pos=723.37 nm
Sc Pos fit=723.65 nm
Obj 23
100 nm
Sc SBR=129.82
Sc Pos=716.71 nm
Sc Pos fit=718.73 nm
Obj 24
100 nm
Sc SBR=13.73
Sc Pos=721.7 nm
Sc Pos fit=723.73 nm
Obj 25
100 nm
Sc SBR=46.862
Sc Pos=686.74 nm
Sc Pos fit=684.68 nm
Obj 27
100 nm
Sc SBR=20.162
Sc Pos=711.16 nm
Sc Pos fit=705.85 nm
Obj 28
100 nm
Sc SBR=41.9
Sc Pos=712.82 nm
Sc Pos fit=717.7 nm
Obj 29
100 nm
Sc SBR=28.683
Sc Pos=701.17 nm
Sc Pos fit=700.22 nm
Obj 30
100 nm
Sc SBR=7.6786
Sc Pos=761.13 nm
Sc Pos fit=753.21 nm
Obj 31
100 nm
Sc SBR=21.1
Sc Pos=712.27 nm
Sc Pos fit=709.45 nm
Obj 32
100 nm
rel. Scattering Intensity [a.u.]
Scattering Efficiency [arb.u.]
0.00
0.02
0.04
0.06
0.08
0.10
0.12
500
600
700
800
wavelength [nm]

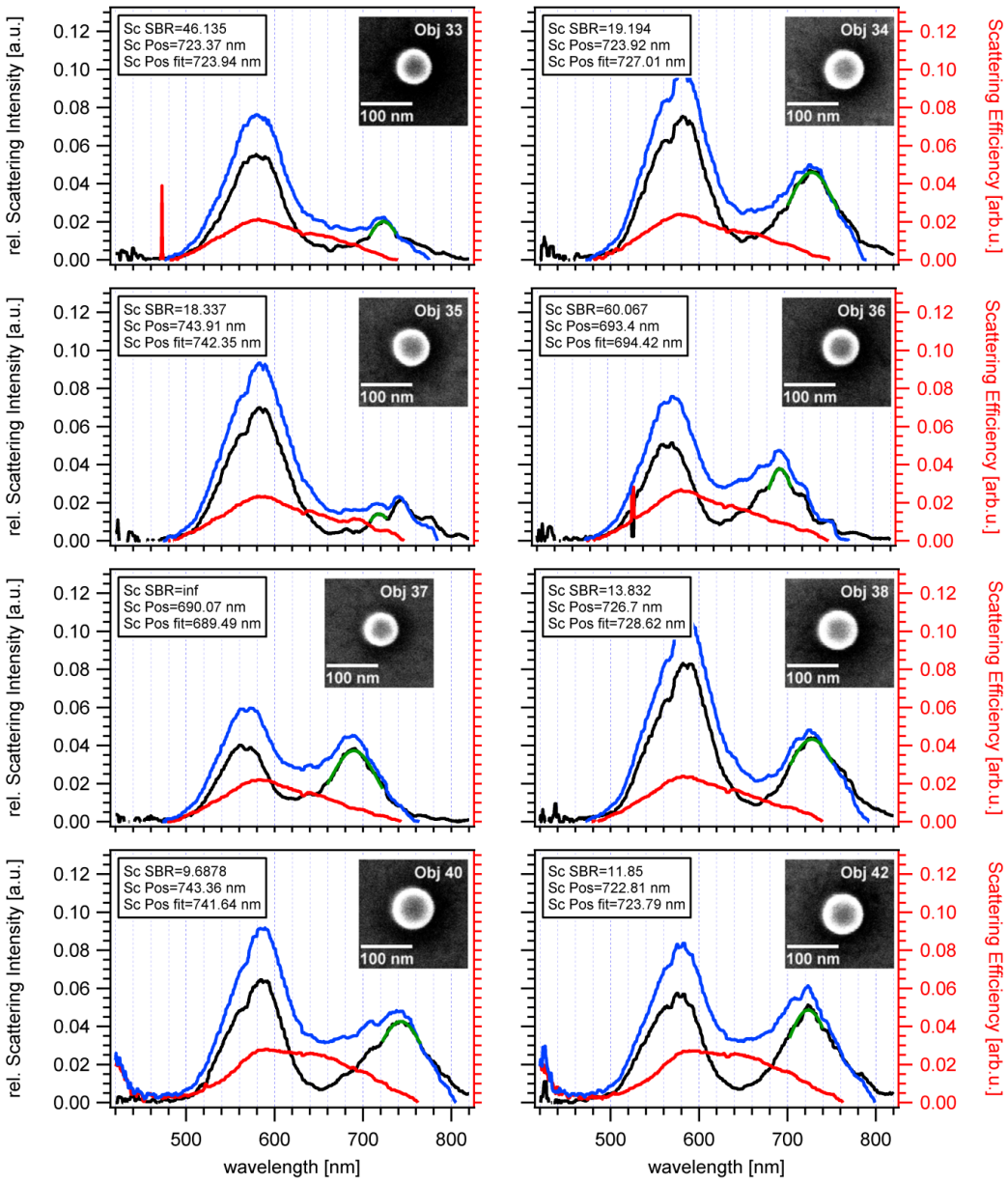

Figure 10.7: *Scattering spectra of particles in red and reference spectra for the film in red, the used glue was Epotek 353 ND*

For this template stripped gold sample all particle details are presented in the following Table 10.4.

Table 10.4: determined dimensions of the presented gold spheres on TSG 353

Particle	x-axis [nm]	y-axis [nm]	Height [nm]	Area [nm^2]	Volume [nm^3]	Circularity
Obj1	64	64	63 (5)	3416	134427	0.899
Obj2	72	72	68 (5)	4252	185009	0.901
Obj3	74	72	70 (6)	4320	196397	0.907
Obj4	72	72	70 (7)	4288	188840	0.905
Obj5	78	78	78 (7)	5104	250022	0.909
Obj6	76	76	69 (7)	4576	208236	0.906
Obj7	78	76	70 (9)	4728	215962	0.903

Particle	x-axis [nm]	y-axis [nm]	Height [nm]	Area [nm^2]	Volume [nm^3]	Circularity
Obj8	68	68	67 (9)	3852	162484	0.907
Obj9	72	72	65 (9)	4140	177729	0.890
Obj10	67	65	69 (8)	3554	157624	0.905
Obj11	72	72	69 (10)	4804	187642	0.856
Obj12	72	72	66 (11)	4156	179418	0.890
Obj13	66	68	63 (8)	3584	148817	0.902
Obj14	56	56	54 (9)	2604	88353	0.885
Obj15	96	96	93 (8)	7280	448167	0.886
Obj16	68	68	60 (5)	3756	146395	0.903
Obj17	61	61	58 (7)	3172	112746	0.910
Obj18	68	68	63 (5)	3916	151611	0.896
Obj19	72	72	67 (6)	4228	181815	0.905
Obj20	74	73	73 (13)	4380	206610	0.903
Obj21	104	56	57 (11)	5072	172299	0.799
Obj22	54	55	48 (13)	2500	75031	0.880
Obj23	71	71	67 (13)	4264	178022	0.904
Obj24	65	65	62 (13)	3476	137482	0.901
Obj25	74	76	68 (13)	4568	198791	0.904
Obj27	66	66	64 (11)	3564	145251	0.897
Obj28	72	72	69 (9)	4320	185992	0.916
Obj29	66	66	67 (10)	3624	152973	0.912
Obj30	68	66	65 (11)	3532	152296	0.912
Obj31	73	74	74 (10)	4444	208289	0.912
Obj32	72	72	71 (12)	4180	193894	0.878
Obj33	65	64	63 (9)	3432	137370	0.909
Obj34	75	74	74 (13)	4540	213924	0.907
Obj35	68	68	65 (12)	3856	157877	0.904
Obj36	68	68	66 (13)	3800	159254	0.891
Obj37	61	62	63 (13)	3156	125045	0.915
Obj38	74	74	74 (9)	4420	212143	0.903
Obj40	78	77	76 (10)	4832	237648	0.907
Obj42	75	75	71 (10)	4720	209642	0.905

The numbers in the brackets of the height indicate how many values were determined for the mean value. The volume for these spheres is calculated for an ellipsoid with three axis determined by SEM and AFM measurements. The circularity is the proportion of the area and the perimeter (4π area/perimeter^2) and gives an indication of the two dimensional roundness of the considered particle from the SEM images.

In Figure 10.8 correlation plots are shown for this TSG sample. The two top plots showing a correlation of the resonance position against the height and volume respectively are the most important ones

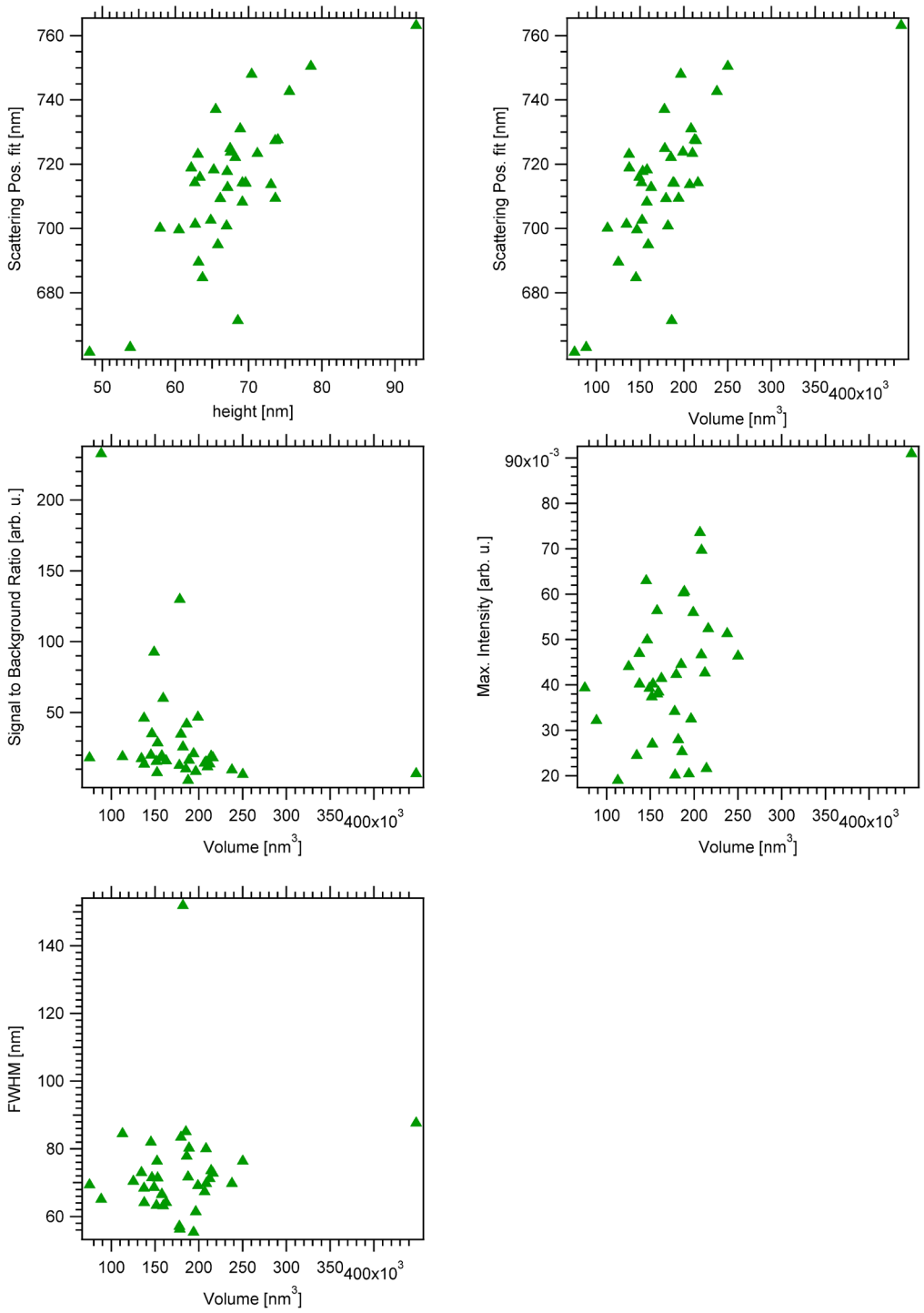

Figure 10.8: *Parameters describing the particles are plotted versus each other in the search for a correlation of data for this sample*

10.6 Emission Spectra for a Silver Sphere-On-Plane System

In Figure 10.9 the emission spectra (red) of 36 individuals measured with an excitation wavelength of 532 nm are displayed.

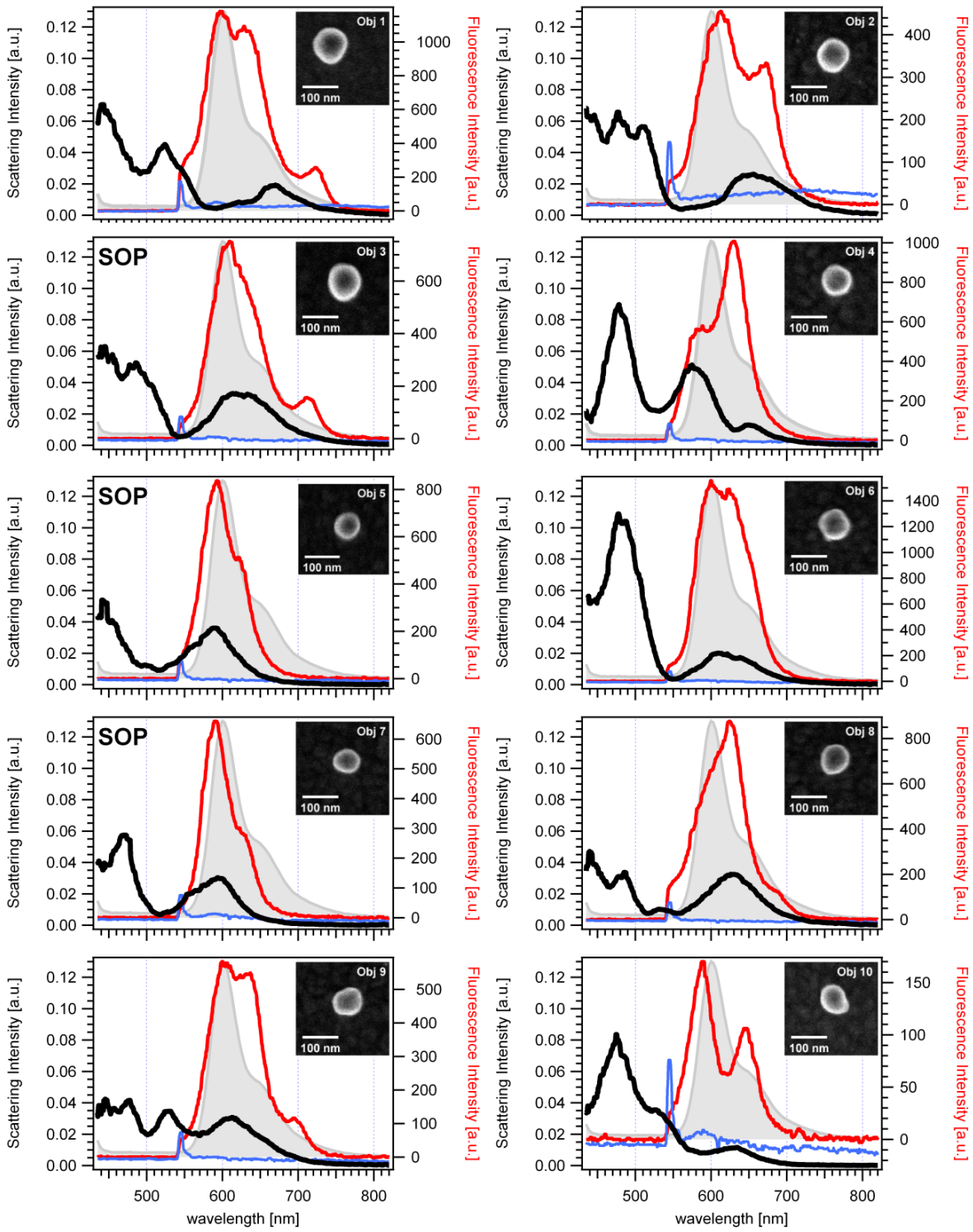
Obj 1
Obj 2
SOP
Obj 3
Obj 4
SOP
Obj 5
Obj 6
SOP
Obj 7
Obj 8
Obj 9
Obj 10
100 nm
Scattering Intensity [a.u.]
Fluorescence Intensity [a.u.]
wavelength [nm]

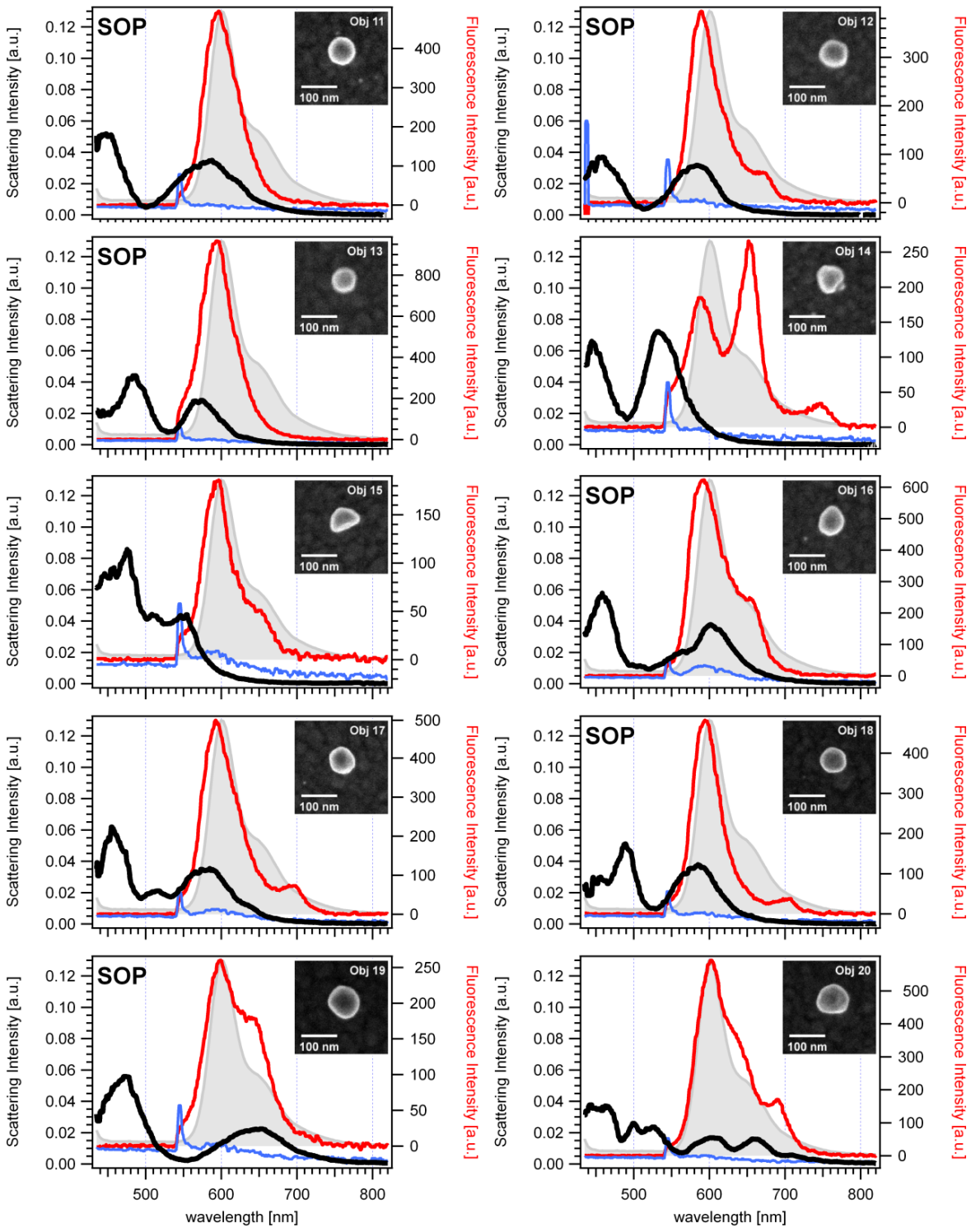
SOP
Obj 11
Obj 12
Obj 13
Obj 14
Obj 15
Obj 16
Obj 17
Obj 18
Obj 19
Obj 20
100 nm
Scattering Intensity [a.u.]
Fluorescence Intensity [a.u.]
wavelength [nm]

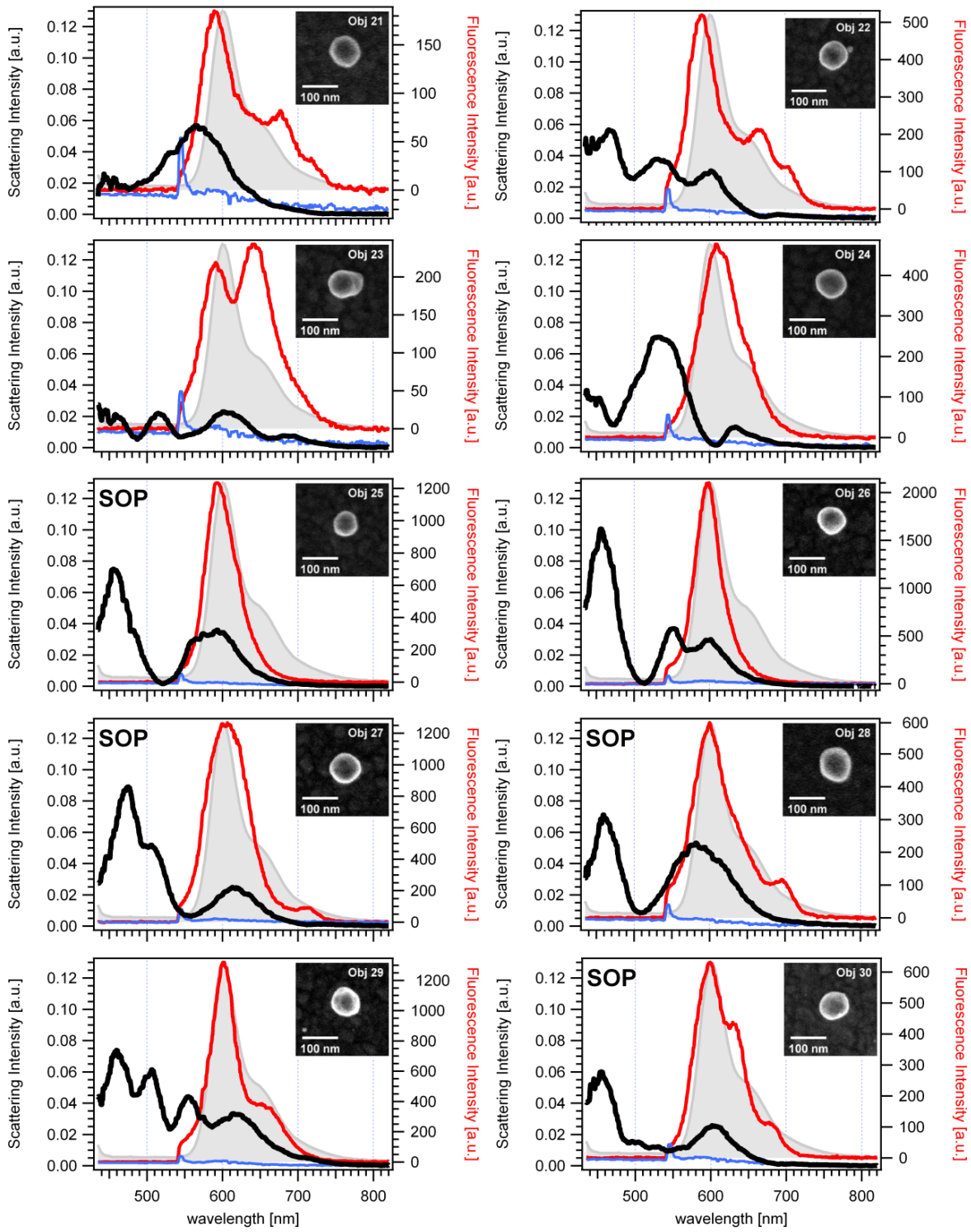
Obj 21
Obj 22
Obj 23
Obj 24
SOP
Obj 25
Obj 26
SOP
Obj 27
SOP
Obj 28
Obj 29
SOP
Obj 30
100 nm
Scattering Intensity [a.u.]
Fluorescence Intensity [a.u.]
wavelength [nm]

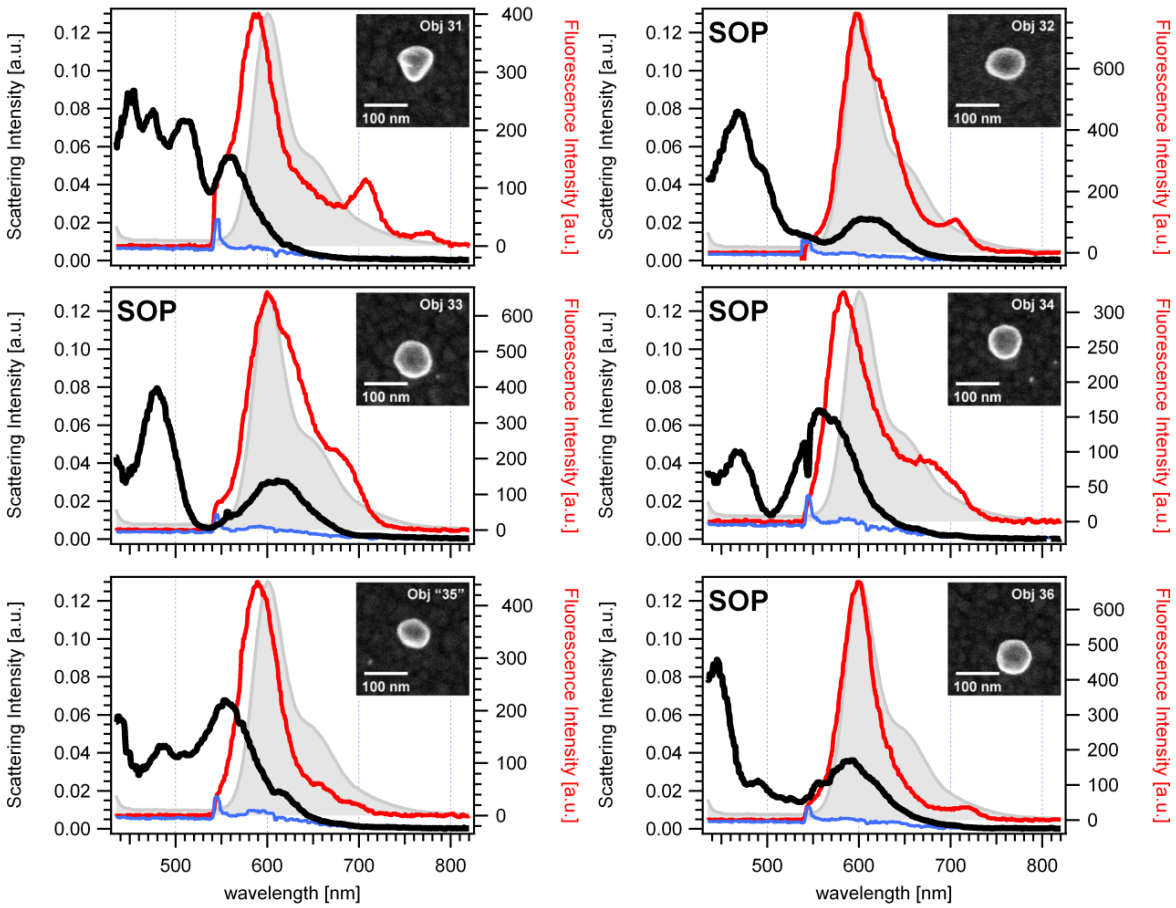

Figure 10.9: *Fluorescence spectra from particle positions (red), compared to the background fluorescence signal (blue), the emission spectrum from the dye in solution at an excitation wavelength of 405 nm is shown in gray. The black curves are all scaled to the same maximum value and show the scattering signal of the particles which are presented top right. Resonators classified as "SOP-like" are marked in the graphs.*

The SOP-like resonators are identified by visual inspection of the scattering signal (black). Since the optical properties of the silver film vary strongly through the visible spectral region, the scattering signal obtained in the plasmon-mediated dark field microscopy is wavelength dependent. Resonators with a single resonance at around 600 nm and a clear minimum on the blue side which separates strictly the higher mode resonances at much shorter wavelength are classified as SOP-like. These properties apply to 17 of 36 individuals. They are indicated by the label "SOP" in the related graphs.

In Figure 10.10 all correlation plots of the available parameters are shown. In most cases no clear trend is seen. The plots showing a correlation are presented and discussed in the main part of the thesis.

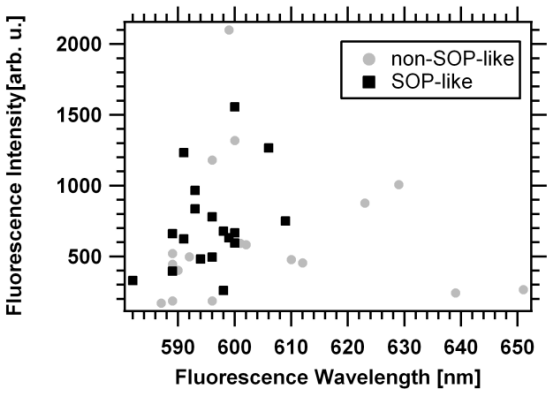
Fluorescence Intensity[arb. u.]
Fluorescence Wavelength [nm]
non-SOP-like
SOP-like

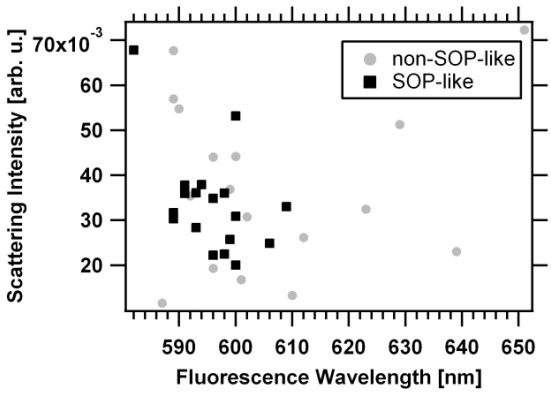
Scattering Intensity [arb. u.]
70x10-3
Fluorescence Wavelength [nm]
non-SOP-like
SOP-like

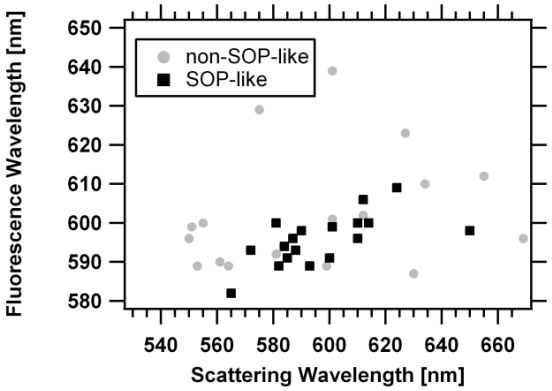
Fluorescence Wavelength [nm]
Scattering Wavelength [nm]
non-SOP-like
SOP-like

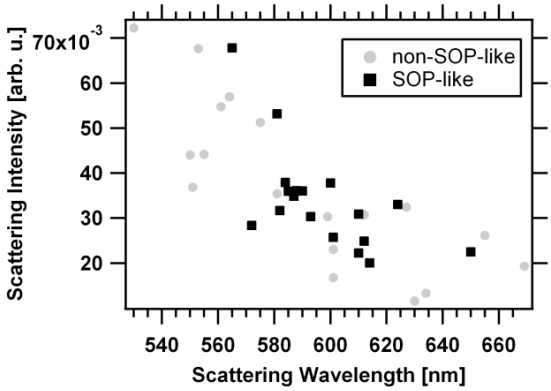
Scattering Intensity [arb. u.]
70x10-3
Scattering Wavelength [nm]
non-SOP-like
SOP-like

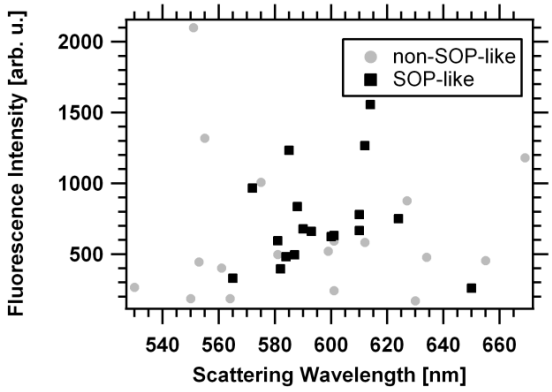
Fluorescence Intensity [arb. u.]
Scattering Wavelength [nm]
non-SOP-like
SOP-like

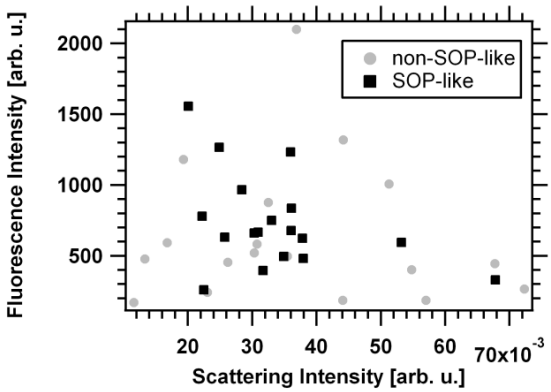
Fluorescence Intensity [arb. u.]
Scattering Intensity [arb. u.]
70x10-3
non-SOP-like
SOP-like

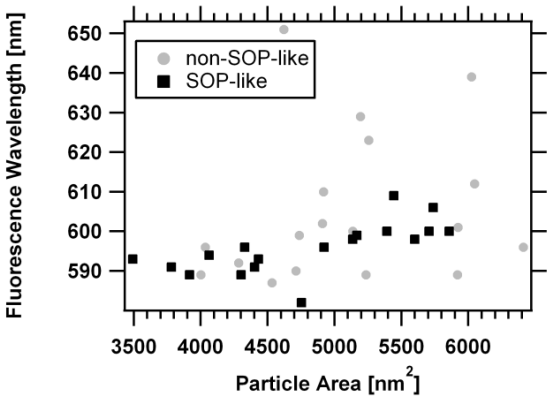
Fluorescence Wavelength [nm]
Particle Area [nm2]
non-SOP-like
SOP-like

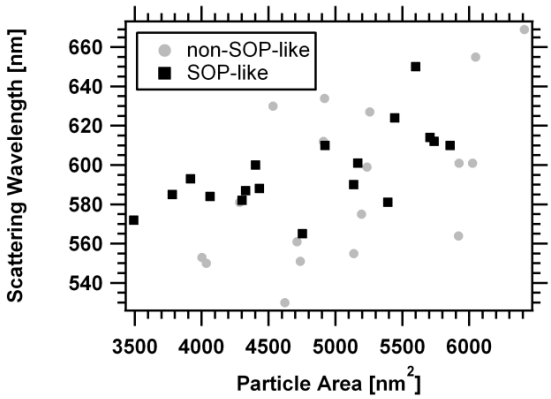
Scattering Wavelength [nm]
Particle Area [nm2]
non-SOP-like
SOP-like

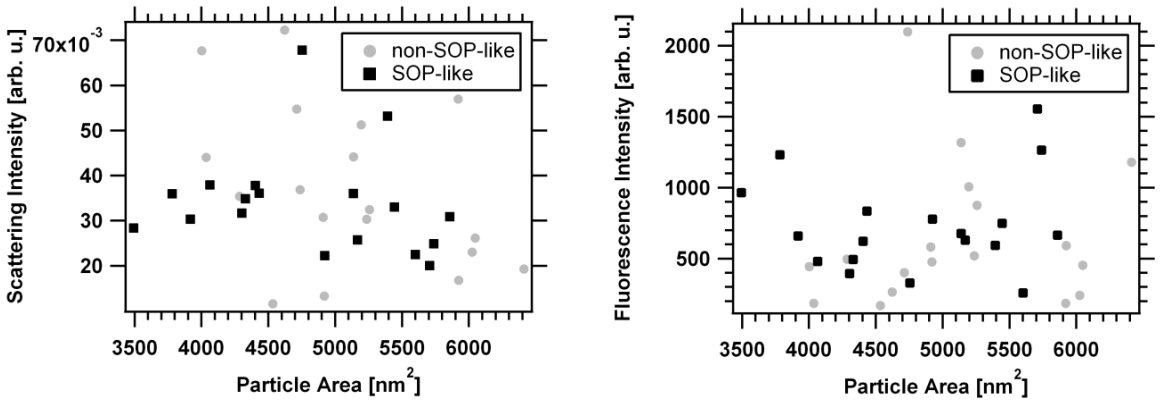

Figure 10.10: *Parameters describing the particles are plotted versus each other in the search for a correlation of data*

Acknowledgments

[in printed version available]

[in printed version available]

[in printed version available]

Curriculum Vitae

[in printed version available]

Wissenschaftliche Veröffentlichungen

Aus dieser Arbeit:

1. "Plasmon Mediated Darkfield Microscopy", M.Schmelzeisen, J. Austermann and M. Kreiter, Optics Express, 16 (**2008**), 17826.17841
2. "Fluorescence Enhancement of Individual Plasmonic Gap Resonances", M.Schmelzeisen, Y. Zhao, M. Klapper, K. Müllen and M. Kreiter", ACS Nano, 4 (**2010**), 3309-3317
3. "Individual Plasmonic Gap Resonances", M. Schmelzeisen, M. Kreiter, **in preparation**
4. "Coupling of Mie Resonances to Surface Plasmons", M. Schmelzeisen, M. Stemmler, M. Kreiter, **in preparation**

Nicht im Zusammenhang mit dieser Arbeit

1. "Synthetic Control over Substituent Location on Carbon-Chain Polymers Using Ring-Opening Polymerizations of Small Cycloalkanes", J. Penelle, T. Xie, L Kagumba, M. Schmelzeisen, M. Tibi and G. Menges, *Polymeric Materials Science and Engineering,* 80 (**1999**), 437-438
2. "Near Field Lithography by Two-Photon Induced Photocleavage of Organic Monolayers", M. Alvarez, A. Best, A. Unger, J. Alonso, A. del Campo, M. Schmelzeisen, K. Koynov and M. Kreiter, Advanced Functional Materials, 20 (**2010**), 4265-4272
3. "Visible Mie Scattering in Non-Absorbing Hollow Sphere Powders", M. Retsch, M. Schmelzeisen, H. J. Butt, T. Edwin, Nano Letters, 11 (**2011**), 1389-1394
4. "Near- and Far-Field Investigations of Individual Sub-Nanometer Plasmonic Gap Resonances", F. Schertz, M. Schmelzeisen, R. Mohamadi, H. J. Elmers, M. Kreiter, G. Schönhense, **in preparation**

[in printed version available]